ABSTRACT

Title of Dissertation:	STUDY OF PHASE EQUILIBRIA AND DIFFUSION IN SEVERAL BINARY AND MULTINARY ALLOY SYSTEMS
	Chuangye Wang, Doctor of Philosophy, 2023
Dissertation directed by:	Professor Ji-Cheng Zhao, Department of Materials Science and Engineer

This study leveraged the high-throughput experiments and high-throughput calculations to study the thermodynamic and kinetic behaviors, and mechanical properties of different alloy systems. CALculation of PHAse Diagrams (CALPHAD) and machine learning (ML) are two computational approaches to predict the phase equilibria of alloys and were adopted to study the phase formation of 2436 high-entropy alloys (HEAs). HEAs were found to form 100% BCC at VEC < 6.87 and form essentially 100% FCC at VEC > 9.16 experimentally, this is consistent with the CALPHAD calculations (VEC = valence electron concentration). ML trained models can reach more than 90% accuracy in predicting BCC/B2, BCC/B2 + FCC, and FCC phases. An autonomous materials search engine (AMASE) method was developed by collaborators to map the phase diagram of the thin-film Sn-Bi system in a closed-loop method, which speeds up the phase diagram mapping and thermodynamic assessment processes over the traditional grid mapping. In the NSF sponsored project, the diffusion-multiple approach was employed to map the phase diagrams of the ternary subsystems of the Cr-Fe-Ni-Nb system. Wavelength-dispersive

spectroscopy (WDS) mapping was adopted to measure the compositions in the triple-junction areas of diffusion multiples, leading to improve the efficiency of constructing phase diagrams in comparison with the previous practice of using electron probe microanalysis (EPMA) line scans. The WDS mapping method was demonstrated in the experimentally determined ternary phase diagram of Fe-Nb-Ni at 1100 °C. The measured tie-line data was then provided to collaborators to obtain more accurate predictions of the phase stability of topologically close-packed (TCP) phases for future improvement of the Ni-based thermodynamic databases. Besides thermodynamic calculations, mobility assessments of 25 binary systems with single-phase BCC or FCC structure were performed using the 1-parameter Z-Z-Z binary diffusion model. The data will be useful input to robust diffusion coefficient (mobility) databases. Hardness testing was performed to study the solid solution hardening effects on eight Mg-X (X = Al, Ca, Ce, Gd, Li, Sn, Y, Zn) binary systems using liquid-solid diffusion couples and on three binary systems (Mo-Nb, Mo-Ta, and Nb-Ta) of refractory elements using novel macro-gradient samples made by electron beam welding of stacked wedge-samples.

STUDY OF PHASE EQUILIBRIA AND DIFFUSION IN SEVERAL BINARY AND MULTINARY ALLOY SYSTEMS

by

Chuangye Wang

Dissertation submitted to the Faculty of the Graduate School of the
University of Maryland, College Park, in partial fulfillment
of the requirements for the degree of
Doctor of Philosophy
2023

Advisory Committee:
Professor Ji-Cheng Zhao, Chair
Professor Alison B. Flatau
Professor Ichiro Takeuchi
Professor Sreeramamurthy Ankem
Dr. Ursula R. Kattner

Acknowledgements

First and foremost, I would like to thank my advisor, Dr. Ji-Cheng Zhao, for his outstanding teaching, support, and help. I've learned tremendously from him in materials science during my five-year Ph.D. study. His brilliance, wisdom, and enthusiasm have provided many farseeing ideas for my experimental and computational work. He is very patient with me, although I made many mistakes in experiments. His depth of knowledge and scientific thinking have profoundly impacted me. He is successful not only as a scientific leader for the science of metals and alloys, but also as a great and kind mentor for students. Without his generous and kind support, I could not have had the opportunity to conduct various research and pursue a Ph.D. degree. I am also greatly thankful to other committee members: Dr. Alison Flatau, Dr. Ichiro Takeuchi, Dr. Sreeramamurthy Ankem, and Dr. Ursula Kattner.

I am grateful to all the people who provided technical help to my research. I want to thank Ms. Julie Barkman and Dr. John Donovan at the University of Oregon for performing electron probe micro-analysis (EPMA) and wavelength-dispersive spectroscopy (WDS) measurements. I want to thank Valerie Brogden at the University of Oregon for preparing foils using the focused ion beam (FIB). I am thankful to Audaldo Ponce who trained me on using the nanoindentation machine - TriboIndenter and Robert Joseph Bonenberger for giving me access to all the equipment in Kim Engineering Building 1135 lab. I am thankful to Bruce Rowley from the machine shop and Leroy Phillips from AIM Inc. for EDM cutting of samples. I thank Dr. Peter Y. Zavalij at X-ray Crystallographic Center for helping X-ray diffraction (XRD) experiments. I would like to thank Dr. Jiancun Rao, who trained me in using scanning electron microscope

(SEM) and energy dispersive spectroscopy (EDS) and taught me a lot to determine crystal structures from diffraction patterns.

I would like to thank the collaborators of several projects, Haotong Liang, Dr. Ichiro Takeuchi, Hui Sun, Dr. Zi-Kui Liu, and Dr. Wissam Abdo Saidi. Haotong is extremely good at programming and integrating different techniques to conduct experiments. Hui Sun is an expert in doing thermodynamic modeling and first-principle calculations. I enjoy the talks with them and am glad to learn about programming and modeling from them. I believe they will become excellent researchers or professors.

I would like to thank Dr. Shutong Zhang, who is like my older brother. He encouraged me when I was depressed and provided helpful suggestions for my growth and development. I want to thank Dr. Wei Zhong, who helped me greatly in my research and life. I enjoy and appreciate the time with Dr. Po-Hsien Chu and miss the fried shrimp with crumbs he cooked. I want to thank Simeng Yang, my good friend since high school, for sharing our lives in two different countries. I want to thank Fengping Zhao for her loving care and company, and I am delighted and grateful to have her by my side. I also want to thank many other friends who have experienced much with me, even though their names are not listed here.

I want to thank all the colleagues in Dr. Zhao's group: Dr. Wei Zhong, Dr. Ella Pek, Dr. Zhangqi Chen, Dr. Yi Li, Dr. Xinpeng Du, Dr. Siwei Cao, Dr. Qiaofu Zhang, Dr. Noah Kohlhorst, Dr. Meysam Akbari, Christian Sanjurjo-Rodriguez, Alex Butler, Jess Garnett, Dinh Huynh, Katelyn Howe, Justin Cheng. They are great colleagues for creating a perfect atmosphere in the office to stay in and study. I enjoy our experiences in many aspects, such as conducting experiments, having meals, playing games, during my Ph.D. period.

Lastly, I would like to express my gratitude to my mother and father for their unconditional support and love. They kept supporting my education in school even during their hardest time. They work very hard, and I hope to make our lives easy and comfortable in the future. I am also grateful to my maternal and paternal grandparents for their meticulous care and love, especially when I was young. My maternal grandmother and paternal grandparents would be happy to see the completion of my Ph.D. journey.

Publications

Chuangye Wang, Wei Zhong, and Ji-Cheng Zhao. "Insights on phase formation from thermodynamic calculations and machine learning of 2436 experimentally measured high entropy alloys." *Journal of Alloys and Compounds* 915 (2022): 165173.

Chuangye Wang, Wei Zhong, and Ji-Cheng Zhao. "High-Throughput Evaluation of Hardening Coefficient of Eight Alloying Elements in Magnesium" (Under preparation)

Chuangye Wang and Ji-Cheng Zhao. "Experimental determination of isothermal sections of Co-X-Y (X = Cr, Ni, Y = Ta, W) ternary systems" (Under preparation)

Chuangye Wang and Ji-Cheng Zhao. "A novel method to study the structure-property-composition relationship in refractory binary systems" (Under preparation)

Haotong Liang, **Chuangye Wang**, Heshan Yu, Dylan Kirsch, Rohit Pant, Austin McDannald, Aaron Gilad Kusne, Ji-Cheng Zhao, and Ichiro Takeuchi. "Real-time autonomous experiment-computational prediction interaction for closed-loop materials science" (Under preparation)

Hui Sun, **Chuangye Wang**, Shun-Li Shang, Allison M. Beese, Ji-Cheng Zhao, and Zi-Kui Liu. "Thermodynamic modeling of binary Fe-Nb and ternary Fe-Nb-Ni supported by first-principles calculations and key experiments" (Under preparation)

Table of Contents

List of Tables

List of Figures

List of Abbreviations

AI	Artificial Intelligence
AMASE	Autonomous materials search engine
ANN	Artificial Neural Network
α	Body centered cubic structure
γ	Face centered cubic structure
ψ	Thermodynamic factor
BCC	Body-centered cubic
BSE	Backscattered electron
CALPHAD	CALculation of PHAse Diagrams
D^*	Tracer diffusion coefficient
D^I	Intrinsic diffusion coefficient
D_A^B	Impurity diffusion coefficient of element A in matrix B
D_A^A	Self diffusion coefficient of element A
DT	Decision Tree
EBSD	Electron backscattered diffraction
EBW	Electron beam welding
EDM	Electro-discharge machining
EDS	Energy dispersive spectroscopy
EPMA	Electron probe microanalysis
FCC	Face-centered cubic
HCP	Hexagonal close-packed
HEAs	High entropy alloys
ICME	Integrated computational materials engineering
KNN	K-nearest neighbors

LSDC	Liquid-solid diffusion couple
MGI	Materials Genome Initiative
ML	Machine learning
NSF	National Science Foundation
Q	Activation Energy
R	Gas constant, R = 8.314 J/(mol·K)
SEM	Scanning electron microscopy
SSH	Solid solution hardening
SVM	Support Vector Machine
TEM	Transmission electron microscopy
VEC	Valence electron concentration
WDS	Wavelength-dispersive spectroscopy
XRD	X-ray diffraction

Chapter 1: Introduction

Humankind has benefited greatly from various materials from the early bronze age to the current information age. Materials properties or structures can now be predicted by implementing theories into computer programming. The Materials Genome Initiative (MGI) is a U.S. government-funded program launched in 2011 with the goal of accelerating the design and development of new materials in shorter time and with lower materials development cost by integrating the computational capabilities with experimental tests [1]. MGI aims to bring together researchers from industry, academia, and government to work collaboratively to speed up the materials development process on new advanced materials. Its materials innovation infrastructure includes computational tools, experimental tools, and digital data aimed at improving human welfare, national security, clean energy, and next generation workforce, as shown in **Fig. 1.1**. High-throughput experiments along with the combinatorial analysis help save time and cost compared with the traditional trial and error method that requires a lot of time and labor [2–5]. Computational tools such as thermodynamic modeling, molecular dynamics, first-principle calculations, and machine learning that are developed on theory and/or validated by experiments can optimize the experimental parameter settings for the next iteration experiments, and thus accelerate the whole materials design and maturation processes [6–10]. By making the digital data more open and accessible as a public resource, researchers don't need to repeat the experimental or calculation process and could easily use the shared data for their research and development.

The motivation of this dissertation is to study the phase equilibria, and the composition-structure-property relationships in many binary and multinary systems by combining the high-

throughput experiments with computations. This dissertation includes six different studies that have been done during the dissertation work either individually or through collaborations with

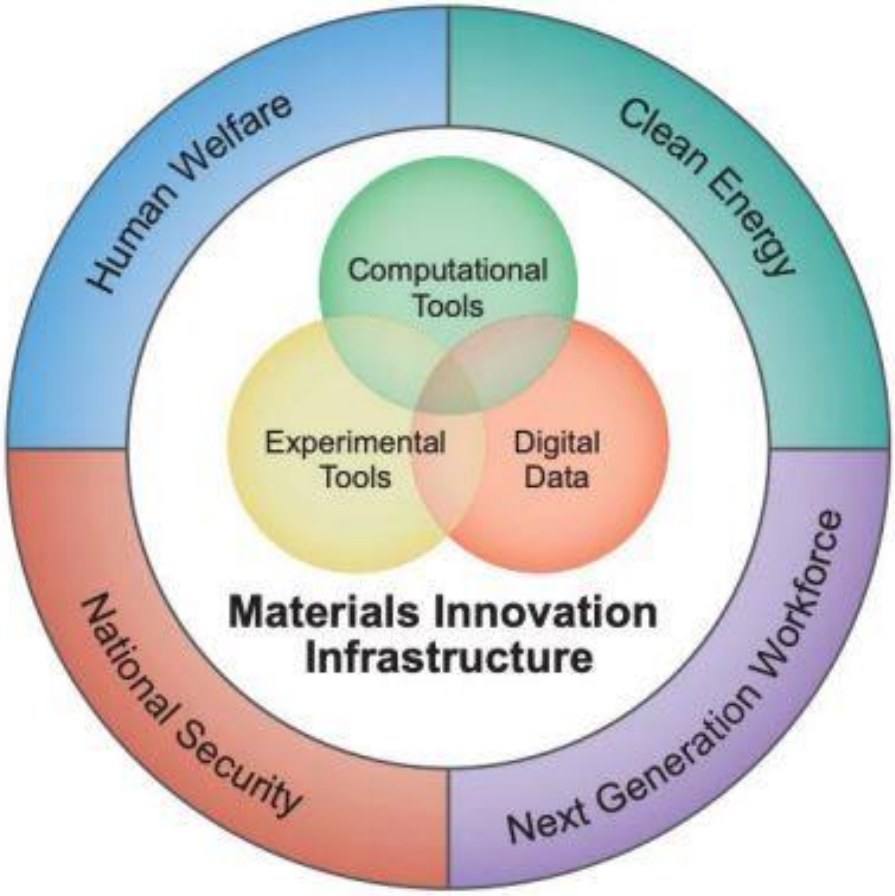

Figure 1.1 The founding conceptual structure of MGI [1].

other research groups. The effects of solid solution hardening (SSH) were studied on eight Mg-X (X = Al, Ca, Ce, Gd, Li, Sn, Y, Zn) binary systems via nanoindentation scanning on the composition gradients formed in liquid-solid diffusion couples (LSDCs). The hardening coefficients for different solutes will be very useful for the future design of Mg-based alloys. While LSDCs work well for the Mg-based binary systems, it is hard to make diffusion couples of refractory binary systems that require a very long time and high temperature to create a large

diffusion zone. A novel method was designed and developed using the electron beam welding (EBW) technique to prepare the macro-gradient samples over millimeter-scale distance, enabling the high-throughput measurements of composition-dependent materials properties of the refractory binary systems.

Artificial intelligence (AI), a way to mimic the human intelligence that makes human decisions in programmed machines, can be used to accelerate the experimental process. A real-time autonomous and closed-loop experiment-computational interaction was constructed in studying the phase diagram of thin-film Sn-Bi binary system by integrating the on-the-fly thermodynamic modeling and rapid experimental characterization.

In the project of improving the prediction ability of phase stability of topologically close-packed (TCP) phases in Ni-based superalloys, sponsored by National Science Foundation (NSF), isothermal sections of several ternary systems at different temperatures were obtained using diffusion multiples and wavelength-dispersive spectroscopy (WDS) mapping. These measured data along with other collected literature data were sent to our collaborators at Penn State University for the thermodynamic modeling and reassessment of the pertinent TCP-containing ternary systems for future improvement of the thermodynamic databases of Ni-based superalloys.

In addition to studying the phase equilibrium of low-order systems, this dissertation used thermodynamic calculations and machine learning (ML) models to predict the phase equilibria of experimental high entropy alloys (HEAs) and provide useful phase selection rules for the phase classification of HEAs.

Thermodynamics and kinetics are both important in materials science. The kinetic assessments were performed on the diffusivity data of 25 binary systems with a single-phase

BCC or single-phase FCC phase and using the newly developed Z-Z-Z binary diffusion model. The fitted binary interaction parameters were fed into the ML models to improve the ML training process and obtain a more reliable ML model for future diffusivity predictions for unassessed binary systems.

Many techniques including computational tools and experimental methods were employed in this dissertation research. Thermodynamic modeling, kinetic modeling, and machine learning are the three main computational approaches used in this study. The experimental methods include diffusion multiples, LSDCs, electron-beam welded stack-wedge macro-gradient samples, SEM, EPMA, TEM, XRD, and nanoindentation. Some of these techniques will be described in the following sections.

1.1 Computational modeling

1.1.1 Thermodynamic modeling

1.1.1.1 Gibbs energy models

The general model for the molar Gibbs energy G_m^θ for a phase (θ) in a multicomponent system has three main parts:

$$G_m^\theta = G^o + G^{ideal} + G^{xs} \qquad (1.1)$$

where G^o is a mechanical (linear) mixture of the constituents, G^{ideal} is the contribution from entropy of ideal mixing, and G^{xs} is the excess term including the interaction between atoms, magnetic effect and other factors that affect Gibbs energy of the phase.

The substitutional *regular* solution model for the molar Gibbs energy of a phase θ in a binary system can be expressed as [11–13]:

$$G_m^\theta = x_A {}^oG_A + x_B {}^oG_B + RT[x_A ln(x_A) + x_B ln(x_B)] + x_A x_B L_{AB} \qquad (1.2)$$

where x_A and x_B are the mole fraction of element A and B, R is the gas constant, ${}^oG_i$ is the Gibbs energy of the pure element i (i = A or B) whose value can be written as a power series of temperature T in the following general equation by selecting a reference state denoted by stable element reference (SER) for the *i*th element at 298.15K:

$${}^oG_i = a_0 + a_1 T + a_2 T ln(T) + a_3 T^2 + a_4 T^{-1} + a_5 T^3 + \cdots, T_1 < T < T_2 \quad (1.3)$$

L_{AB} describes the binary interaction between element A and B, and the expression built on Redlich-Kister (RK) polynomial is [12]:

$$L_{AB} = \sum_{v=0}^{k} (x_A - x_B)^v \cdot {}^vL_{AB} = \sum_{v=0}^{k} (x_A - x_B)^v \cdot ({}^va + {}^vb\,T) \qquad (1.4)$$

where v is the polynomial order, ${}^va$ and ${}^vb$ are two constants. It is temperature-independent when ${}^vb$ is zero for all v values. By plugging Eq. (1.4) into Eq. (1.2), the equation of G_m^θ becomes:

$$G_m^\theta = x_A {}^oG_A + x_B {}^oG_B + RT[x_A ln(x_A) + x_B ln(x_B)] + x_A x_B \sum_{v=0}^{k} (x_A - x_B)^v \cdot ({}^va + {}^vbT) \quad (1.5)$$

It becomes an ideal substitutional solution when no interaction of mixing constituents exists.

For a binary stoichiometric phase, no random mixing exists in the phase. The formula of Gibbs energy model is:

$$G_m^\theta = x_A^o G_A + x_B^o G_B + \Delta G^f \qquad (1.6)$$

where ΔG^f is the Gibbs energy of formation, the excess term in Gibbs energy model.

For *ordered* binary solution phases, a more complex *sublattice* model integrating substitutional and stoichiometric models is used [7,14]:

$$G_m^{\theta} = x_A^o G_A + x_B^o G_B$$

$$+ RT\left[a^1\left(y_A^1 ln(y_A^1) + y_B^1 ln(y_B^1)\right) + a^2\left(y_A^2 ln(y_A^2) + y_B^2 ln(y_B^2)\right)\right]$$

$$+ y_A^1 y_A^2 G_{AA}^o + y_A^1 y_B^2 G_{AB}^o + y_B^1 y_A^2 G_{BA}^o + y_B^1 y_B^2 G_{BB}^o$$

$$+ y_A^1 y_B^1 y_A^2 \sum_{i=0}^{n_{2A}} L_{2A}^i (y_A^1 - y_B^2)^i$$

$$+ y_A^1 y_B^1 y_B^2 \sum_{i=0}^{n_{2B}} L_{2B}^i (y_A^1 - y_B^1)^i$$

$$+ y_A^1 y_A^2 y_B^2 \sum_{i=0}^{n_{1A}} L_{1A}^i (y_A^2 - y_B^2)^i$$

$$+ y_B^1 y_A^2 y_B^2 \sum_{i=0}^{n_{1B}} L_{1B}^i (y_A^2 - y_B^2)^i$$

$$+ y_A^1 y_B^1 y_A^2 y_B^2 L_{12AB} \qquad (1.7)$$

where y_A^1, y_B^1, y_A^2, and y_B^2 are the compositions of element A and B on the sublattices 1 and 2 with the relation that $a^1 y_A^1 + a^2 y_A^2 = x_A$, $a^1 y_B^1 + a^2 y_B^2 = x_B$, $y_A^1 + y_B^1 = 1$, $y_A^2 + y_B^2 = 1$. a^1 and a^2 are the site fraction of the sublattices 1 and 2. The remaining terms excluding the first three terms refers to the excess term in the Gibbs energy model. Four coefficients G_{AA}^o, G_{AB}^o, G_{BA}^o, and G_{BB}^o can be regarded as the Gibbs energies of the four end-member phases AA, AB, BA, and BB. L_{1A}^i, L_{2A}^i, L_{1B}^i, L_{2B}^i, and L_{12AB} are the interaction parameters between the atoms in the two sublattices.

1.1.1.2 Calculation of phase diagram

With the Gibbs energy function, the chemical potential, μ_n^θ, of a component n in phase θ can be derived and used to establish the equilibrium conditions in a multicomponent system. The chemical potential of each phase obeys the following rule at equilibrium:

$$\mu_i^\alpha = \mu_i^\beta = \cdots = \mu_i^\theta \qquad (1.8)$$

where i corresponds to the *i*th element in the system, meaning that the chemical potential of any element i is the same in all phases (α, β, θ…) of the system. Finding the equilibrium is a process of minimizing the total Gibbs energy of the system. An example of using Gibbs energy to determine the two-phase equilibrium of the Mg-Cu system at 1123 K is shown in **Fig. 1.2**. The common tangent line is drawn in red color for the Gibbs energy of the liquid and FCC phases. Between the two points of tangency, the Gibbs energy of the mixed two phases is smaller than that of each individual phase, stabilizing the two-phase region. To the left of the left purple dashed line, the system is represented by the liquid phase whose Gibbs energy is lower than that of the FCC phase. And vice versa on the right side of right purple dashed line. The equilibrium of the system is then plotted in the temperature-versus-composition diagram (phase diagram) as indicated by the horizontal black line. By calculating all the phase equilibria at various temperatures, the phase diagram of Mg-Cu can be constructed.

1.1.1.3 Optimization of thermodynamic parameters

As shown in the formula of Gibbs energy model for a binary system, interaction parameters can be optimized to describe the system via comparing the model-predicted values with experimental data. Experimental data include chemical potential, activity of component, enthalpy, the (T, x, phase) info of phase equilibrium, and so on. In magnetic systems, the Curie

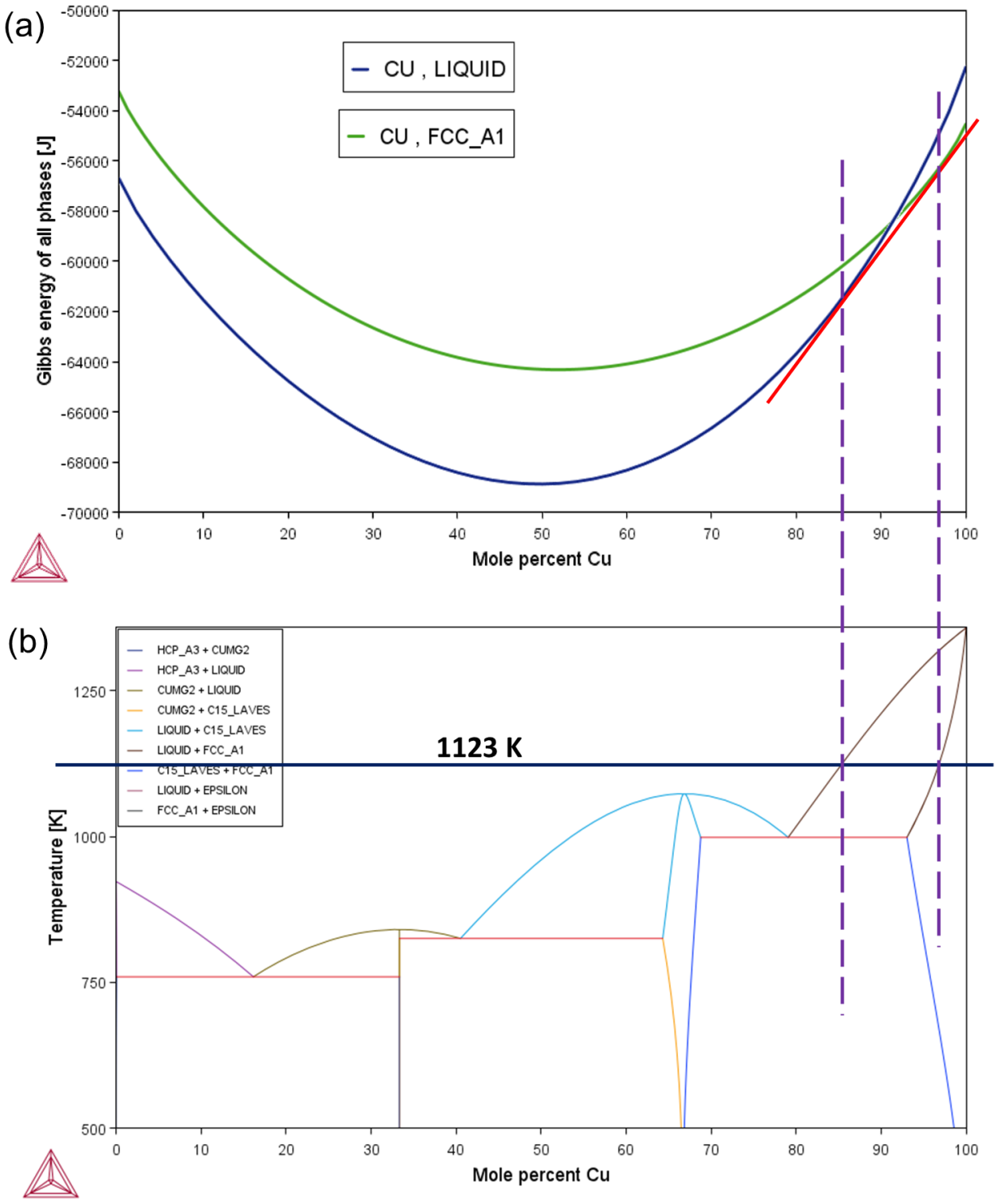

Figure 1.2 The process of mapping phase diagram from Gibbs energy functions in Mg-Cu. (a) Gibbs energy function of the liquid and FCC phase at 1123K. (b) The phase diagram.

temperature and Bohr magneton number are two important parameters to optimize the model to simulate the magnetic transition process.

The optimization can be performed with different software like Thermo-Calc, Pandat, and ESPEI; and Thermo-Calc is mainly used in this dissertation. To perform optimization using PARROT module in Thermo-Calc, the first step is creating a POP file containing all the relevant experimental data [15,16]. Then, a setup file containing the information of system definition, model parameters, optimizing variables, and a series of PARROT commands that performs optimization should be created. Setting weights for data is important because the quality of data is not the same from different measurement techniques and research groups. Some data could be more reliable than others, and therefore they can be given a larger weight. Dropping optimized variables from the interaction parameters is feasible in the case that evaluated values for these variables have large standard deviations. By going through changing weights and variables, better agreement between calculations and experimental data could be achieved. The optimization process for ternary systems and high-order systems has similar steps. **Fig. 1.3** shows the framework of CALPHAD using the Gibbs energy model [7]. Assessed parameters in the excess term of G of binary systems are used in the G of ternary systems directly without the need to reassess them. Then, other interaction parameters in the ternary system are optimized by fitting the experimental data. Following this strategy, assessed parameters from (n-1)-component systems will be added to the thermodynamic description of n-component system. This strategy saves computational sources used in the optimization since it has fixed parameters originating from lower-order systems. In general, the database of high-order (> 4 components) system extrapolated form binary and ternary systems could predict the experimental data reasonably and no correction or minor corrections need to be considered.

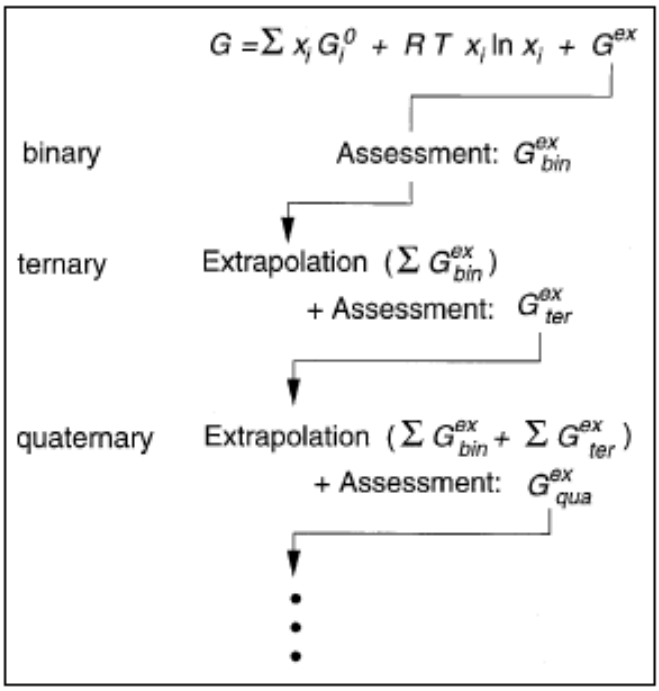

Figure 1.3 The framework of CALPHAD method. The model of high-order systems relying on the extrapolation of low-order systems [7].

1.1.2 Kinetic modeling

Diffusion occurs when mixing two or more materials together, and diffusion coefficients are crucial in understanding these diffusion behaviors and are helpful for materials design, especially in the simulation of kinetic processes such as homogenization, precipitation, and creep deformation. This part introduces diffusion models. Composition-dependent diffusion coefficients can be extracted from composition-versus-distance profiles obtained from a diffusion couple according to Fick's second law:

$$\frac{\partial C}{\partial t} = \frac{\partial}{\partial x}\left(D(C)\frac{\partial C}{\partial x}\right) \qquad (1.9)$$

where D is the diffusion coefficient, C is composition, *x* is distance, and t is the time. This equation can be solved using the Boltzmann-Matano method to obtained the interdiffusion (chemical) diffusion coefficient [17]:

$$D(C') = \left(\frac{1}{2t}\frac{dx}{dC}\right)|_{C'} \int_{C_L}^{C'} (x - x_M) dC \qquad (1.10)$$

where C' is a composition at a specific location x'. x_M is the position of the Matano plane, which can be calculated by

$$\int_{-\infty}^{x_M} [C(x) - C_L] dx = \int_{x_M}^{+\infty} [C_R - C(x)] dx \qquad (1.11)$$

C_L and C_R are the two compositions at the far left and far right end of the diffusion couple. Other extraction methods include the Sauer-Freise method [18], Wagner method [19], Hall method [20], and forward-simulation analysis (FSA) [21] which was developed and implemented in both Matlab and Python codes by Dr. Qiaofu Zhang and Dr. Zhangqi Chen when they were pursuing their doctorates in Prof. Zhao's group. FSA integrates all the advantages of previous methods and can be applied to the entire composition range to extract reliable interdiffusion coefficients and *impurity* coefficients with reduced errors caused by experimental data fluctuation (scattering). The extracted interdiffusion coefficients using FSA from a Co-Ni diffusion couple are shown in **Fig. 1.4**, which are smooth and reliable over the full composition space compared with diffusion coefficients calculated using other methods [22].

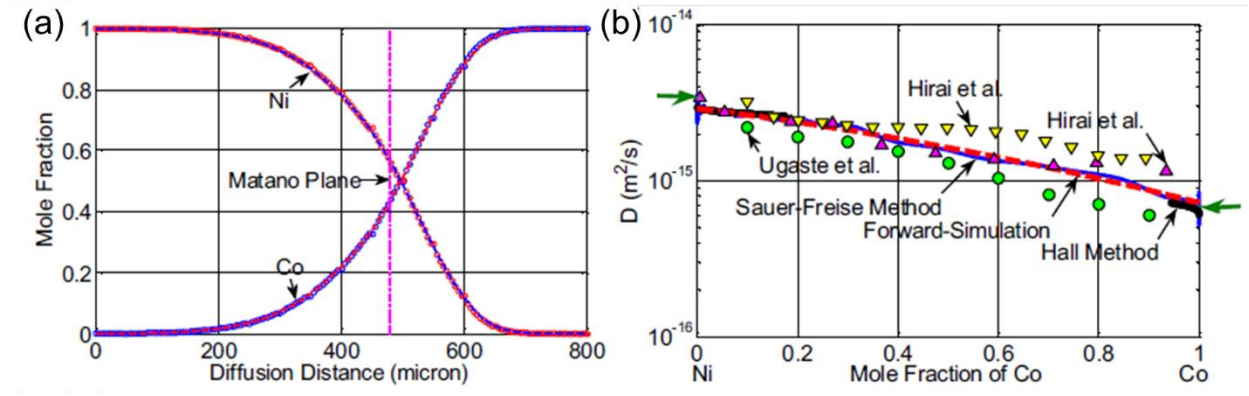

Figure 1.4 (a) Diffusion profiles of Ni and Co after annealing at 1100 °C for 1000 hours. (b) Comparison among extracted interdiffusion coefficients using different methods [22].

Diffusion coefficients have different types, including self-diffusion, impurity diffusion, tracer diffusion, intrinsic diffusion, and interdiffusion coefficients. The temperature-dependent diffusion coefficient of element i in element j, D_i^j, can be expressed using the Arrhenius equation:

$$D_i^j = D_{0_i}^j exp\left(-\frac{Q_i^j}{RT}\right) \qquad (1.12)$$

where $D_{0_i}^j$ is the pre-exponential factor, Q_i^j is the activation energy, and T is the absolute temperature. D_i^j is the impurity diffusion coefficient of *i* in *j* when $i \neq j$ and is self-diffusion coefficient of *i* when $i = j$. The interdiffusion coefficient is correlated with tracer diffusion and intrinsic diffusion through Darken's equations [23]:

$$D_A^I = D_A^*\psi, \quad D_B^I = D_B^*\psi \qquad (1.13)$$

$$\widetilde{D} = x_B D_A^I + x_A D_B^I = (x_B D_A^* + X_A D_B^*)\psi \qquad (1.14)$$

where D_i^I corresponds to intrinsic diffusion coefficient of element *i* (*i* = A or B), D_i^* corresponds to tracer diffusion coefficient of element *i*, ψ corresponds to the thermodynamic factor, $\widetilde{D}$ corresponds to interdiffusion coefficient in a binary A-B system. The interdiffusion coefficient $\widetilde{D}$ becomes impurity coefficient D_A^B when the composition of element A approaches 0. ψ is related to the second derivative of the molar Gibbs energy function with respect to composition, and can be calculated using thermodynamic databases or CALPHAD software:

$$\psi = 1 + \frac{dln\gamma_i}{dlnx_i} = \frac{x_i}{RT}\frac{d\mu_i}{dx_i} = \frac{x_A x_B}{RT}\frac{d^2G}{dx_B^2} \qquad (1.15)$$

where γ_i is the activity coefficient, μ_i is the chemical potential of element i, G is the molar Gibbs energy.

A connection between the diffusion coefficient and the atomic mobility M_i is described according to Einstein's relation:

$$M_i = \frac{D_i^*}{RT} = \frac{D_{0i}^*}{RT} exp\left(\frac{-Q_i}{RT}\right) = \frac{1}{RT} exp\left(\frac{RT\ lnD_{0i}^* - Q_i}{RT}\right) = \frac{1}{RT} exp\left(\frac{\Phi_i}{RT}\right) \qquad (1.16)$$

where D_{0i}^* and Q_i are the pre-factor and activation energy of tracer diffusion coefficient D_i^*. Atomic mobility parameter, Φ_i, with a formula $\Phi_i = RTlnD_{0i}^* - Q_i$, can be expressed in an equation considering the individual contribution of end members and the interaction among atoms in a multicomponent system [12,24]:

$$\Phi_i = \sum_j x_j \Phi_i^j + \sum_j \sum_{k>j} x_j\, x_k \left[\sum_{r=0}^{n} {}^r\Phi_i^{j,k}\left(x_j - x_k\right)^r\right]$$

$$+ \sum_j \sum_{k>j} \sum_{l>k} x_j\, x_k x_l \left[\sum_{s=j,k,l} v_{jkl}^s \cdot {}^s\Phi_i^{j,k,l}\right] \qquad (1.17)$$

where x_j is the mole fraction of element j. Φ_i^j is the atomic mobility parameter to describe the diffusion coefficient D_i^j (i in j) of end members. ${}^r\Phi_i^{j,k}$ is the binary mobility interaction

parameter at $i = j$ or $i = k$. And it is called cross-binary mobility interaction parameter when $i \neq j$ or $i \neq k$, which describes the impurity diffusion coefficient of a third element in the diffusion matrix lattice of other two elements in a ternary solid solution. r is the polynomial order in the second term. v_{jkl}^{s} is prefactor coefficient before ${}^{s}\Phi_{i}^{j,k,l}$ term that is the ternary interaction parameter, with a relation to compositions, $v_{jkl}^{s} = x_s + \left(1 - x_j - x_k - x_l\right)/3$. General assessments for diffusivity refer to assessment of mobility and then derive the diffusion coefficients from the mobility parameters. It follows a similar strategy that can be used in the optimization or assessment of interaction parameters in the Gibbs energy model. Reliable assessments or extrapolation to higher-order systems rely on good assessments of lower-order subsystems, especially binary and ternary subsystems.

1.1.3 Machine learning (ML) models

1.1.3.1 Decision Tree (DT)

The DT model splits the data at each parent node into the left child node and the right child node in a binary tree [25,26]. Assume we have a dataset denoted by Q with n samples and the data at node m denoted by Q_m with n_m samples. x_i is the vector of ith feature, and y is the label vector. The data can be partitioned into two subsets, $Q_{left}(\theta)$ at the left child node and $Q_{right}(\theta)$ at the right child node for each candidate split $\theta = (j, t_m)$ that stands for feature j and threshold t_m:

$$Q_m^{left}(\theta) = (x, y)|x_j \leq t_m \qquad (1.18)$$

$$Q_m^{right}(\theta) = Q_m \setminus Q_m^{left}(\theta) \qquad (1.19)$$

The t_m can be median or mean of a feature or other quantities. The information loss at each split of node *m* can be computed using Shannon's entropy:

$$H(Q_m) = -\sum_k p_{mk} log(p_{mk}) \qquad (1.20)$$

or Gini impurity:

$$H(Q_m) = \sum_k p_{mk}(1 - p_{mk}) \qquad (1.21)$$

where p_{mk} stands for the proportion of class *k* in Q_m. The DT algorithm minimizes the function

$$G(Q_m, \theta) = \frac{n_m^{left}}{n_m} H\left(Q_m^{left(\theta)}\right) + \frac{n_m^{right}}{n_m} H\left(Q_m^{right(\theta)}\right) \qquad (1.22)$$

where n_m^{left} and n_m^{right} are the number of samples in the left child and the right child of node *m*, respectively. This algorithm achieves most information gain or least information loss with the best split θ^* for each node *m* that minimizes $G(Q_m, \theta)$. By iterating the splitting at each node and its child nodes, the decision tree is constructed. An example of classifying a dataset with two features and two classes is presented in **Fig. 1.5**. The DT model finds feature 1 < x1 as the best splitting strategy in the first split for the whole dataset. Feature 2 > y1 and feature 2 < y2 are the two best splitting strategies for the two subsets at left child node and right child node, respectively. From this example, we can see that the depth of the tree and samples size at each node are important hyperparameters that affect the prediction accuracy of the model.

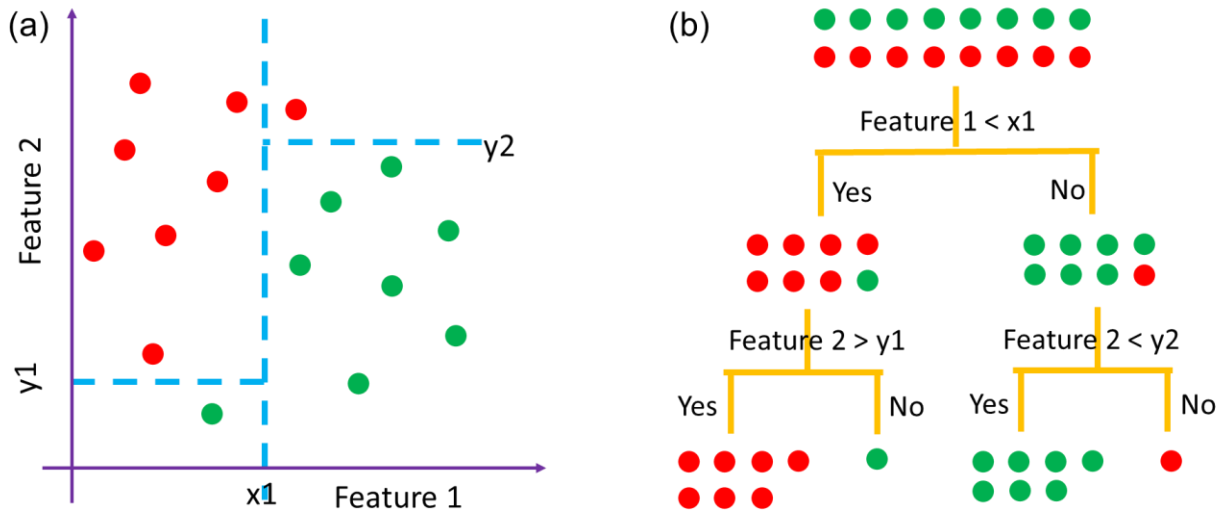

Figure 1.5 (a) The dataset plotted in dimensions of x1 and y1. (b) The splitting strategy using if-else conditions in a binary-tree structure. The two classes are presented by the red and green colors.

1.1.3.2 K-nearest neighbors (KNN)

KNN utilizes a voting mechanism by k nearest neighbors to a query sample [27,28]. In this way, the query sample is assigned to the class with major votes among k nearest neighbors. When the weight of voting for every nearest neighbor is the same, then KNN uses a uniform weight. However, the voting weight is often different for every voter since the voting power of every voter is not same. The distance weights are proportional to the inverse of distance between training sample and query sample and are used here because the contributions of nearer neighbors are regarded as more important than farer neighbors, which is based on the calculation of the standard Euclidean distance [29], $d(p,q) = \sqrt{\sum_{i=1}^{n}(p_i - q_i)^2}$, where p is a training vector and q is the query vector. By iterating the process of assigning each sample to the class with

major votes, the assigned class of each sample will converge and reach a stable status. Predicting the class of a query sample using 5 nearest neighbors in a dataset with two classes and two features is shown in **Fig. 1.6**. The query sample has 2 neighbors in the red color and 3 neighbors in the green color, therefore it is predicted to be in the same class of green data points.

The weight of a nearest neighbor and the number of nearest neighbors affects the prediction results and can be used to optimize the KNN model. The value k cannot be too small, otherwise it will cause a strong bias by not considering the effects of other nearest neighbors. It degrades the performance of the model severely if k is too large, because all the predicted results will be very similar under a similar set of nearest neighbors. This is an easy-to-understand model, which has only a few hyperparameters to tune in contrast with the other ML models.

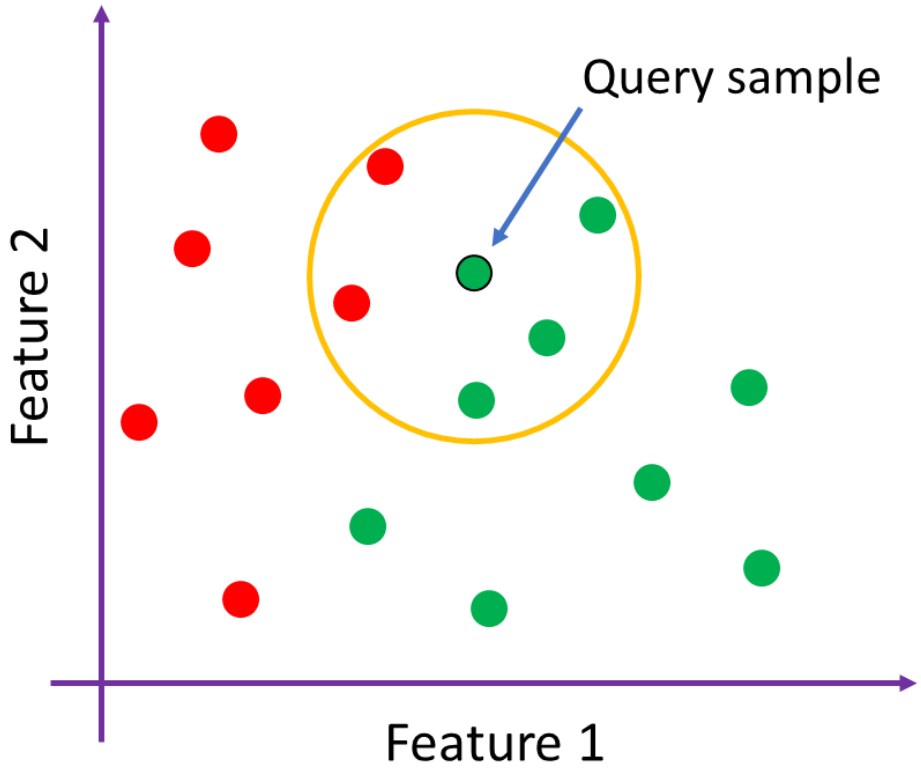

Figure 1.6 The visualization of assigning the class to a query sample based on its 5 nearest neighbors.

1.1.3.3 Support vector machine (SVM)

The goal of an SVM is to find the hyperplane in a high-dimensional space that maximally separates the data points of different classes. The distance from the hyperplane to the nearest data points is known as the margin. SVM aims to maximize the margin to give best generalization or prediction to unlabeled data. In the case of a linear SVM, the hyperplane is a simple linear decision boundary that separates the data into two classes. For non-linearly separable data, SVM

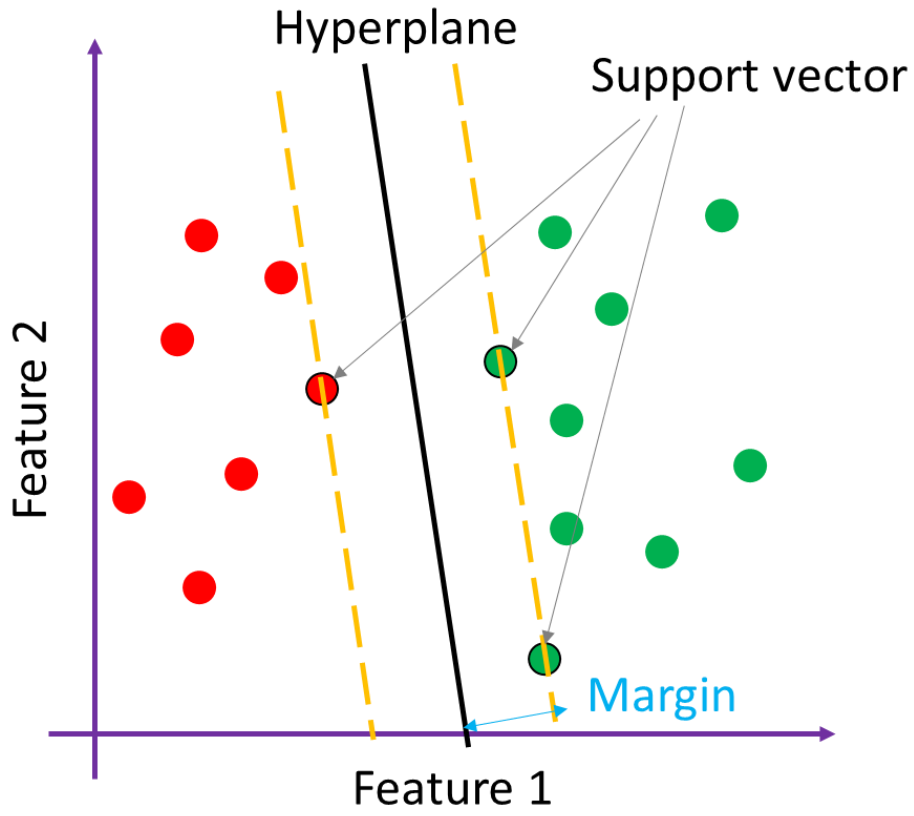

Figure 1.7 Linear kernel for classifying a dataset with two classes marked in red and green colors, with some important concepts.

can use the so-called "kernel trick" to map the data to a higher-dimensional space in which it becomes linearly separable. Some common kernels used in SVMs include the linear kernel, the polynomial kernel, sigmoid kernel, and the radial basis function (RBF) kernel. The maximal margin for classifying two classes using a linear kernel is shown in **Fig. 1.7**. The optimal line to separate two classes is called hyperplane and the data points on the hyperplane is called support vectors.

The SVM model implements one-versus-one or one-versus-rest strategy for multi-class classification [30]. The radical basis function $k(x_i, x_j) = e^{-\gamma|x_i - x_j|^2}$ is one of the kernel functions, where x_i and x_j are the features of ith and jth samples, and γ is the kernel coefficient in this study. γ is also an indicator of the degree of effect of a training sample on other samples. A sample with larger γ has lower influence on other samples. Another penalty parameter C (Parameter C is not in the above equation and thus undefined here!!!) is also critical to control the tradeoff between the overfitting and simplicity of the decision surface. A large C could increase misclassification of samples in the training process and cause underfitting, while a small C could improve the training accuracy but may lead to overfitting for the training samples. Hence the appropriate parameters γ and C of the SVM model can be tuned to obtain optimal training and test outcomes.

1.1.3.4 Artificial neural network (ANN)

ANN simulates the decision-making process of human mind by constructing artificial neurons in the model [31,32], whose architecture is illustrated in **Fig. 1.8**. ANN usually contains an input layer of the exploring features that are fed into separate neurons, hidden layers whose quantity and number of neurons are affected by the complexity of data and number of classes, and an output layer including the classified outcomes in each neuron. The input features propagate

forward to each neuron in each hidden layer with fitted weights, then the fitting values are

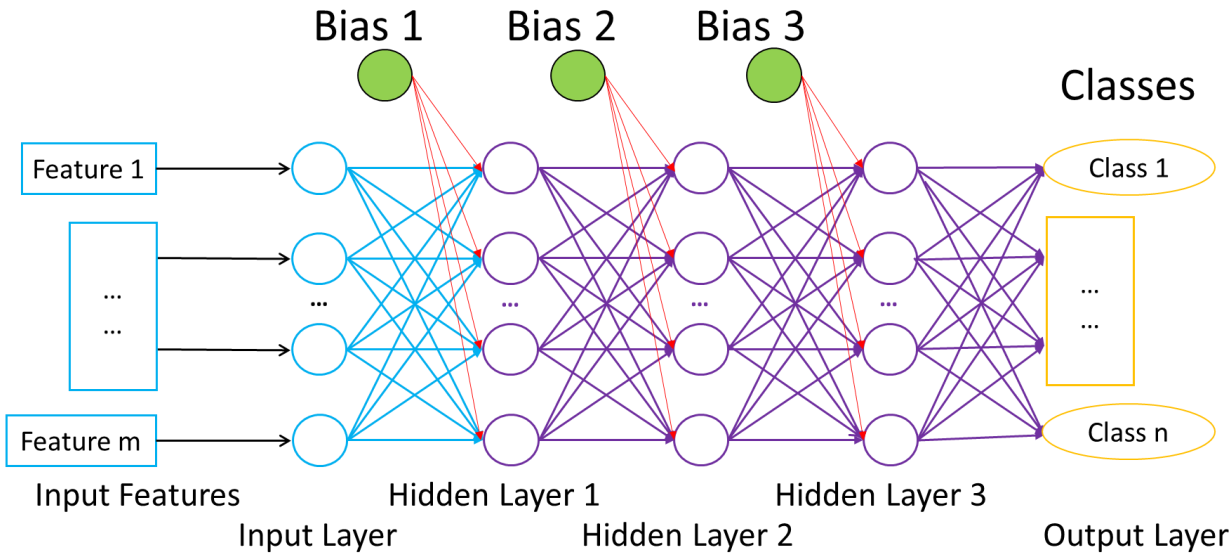

Figure 1.8 The architecture of neural network.

transformed by an activation function. Commonly used activation functions include rectified linear unit (ReLU), sigmoid, tanh, and softmax. At each hidden layer, a bias is introduced and propagates together with the transformed fitting values to the next layer. In the final output layer, the softmax function is often used to calculate the probability of one sample that belongs to each class at each neuron. Then the sample will be assigned to be the class with highest calculated probability.

Compared with other ML models, the neural network can be a more complex model with many parameters, such as large number of neurons at each layer and multiple hidden layers. The learning rate is an important hyperparameter in the implemented batch gradient descent to search for the best parameter set of weights and biases for the ANN model. Other hyperparameters such

as drop-out rate, batch size, epoch times, and activation function also impact the prediction accuracy of the ANN model.

1.2. Experimental techniques

1.2.1 Diffusion multiple approach

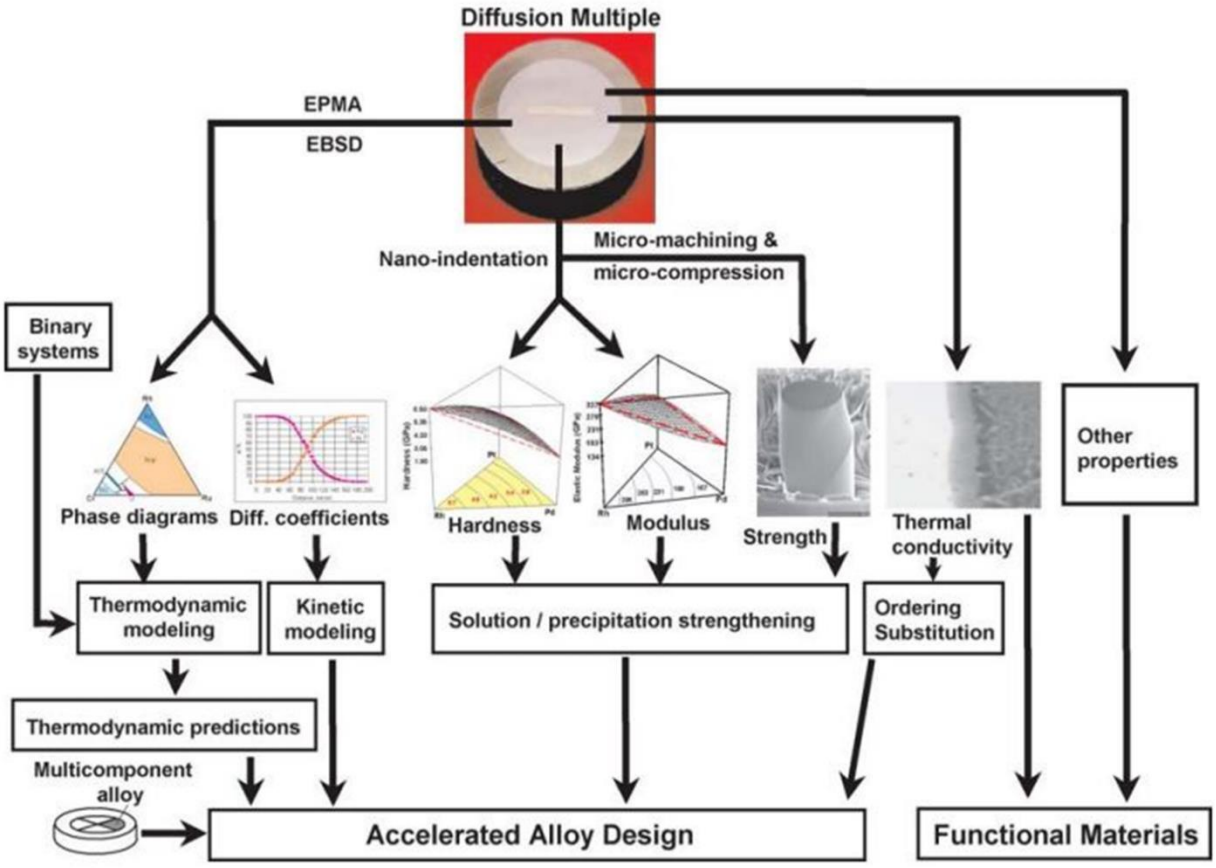

Figure 1.9 The applications of diffusion multiples in alloy design and discovery of structural or functional materials [33].

A diffusion multiple is an assembly of multiple metal pieces with close interfacial contact between pieces, which are subjected to diffusion annealing at a high temperature to form solid

solutions and intermediate phases [2,5,34–37]. Hence, multiple binary and ternary systems co-exist in one diffusion multiple, saving the raw materials cost and time compared to preparation of individual diffusion couples or diffusion triples. The extensive applications of diffusion multiples are summarized in **Fig 1.9** [2]. First, the diffusion multiple is very helpful to map phase diagrams of ternary systems in the triple junction areas and multiple phase diagrams at different temperatures can be obtained with a good design and preparation of the diffusion multiples. The tie-line data of two-phase or three-phase equilibrium can be extracted from the composition versus distance profiles measured using EPMA technique under the assumption of local equilibrium. In addition to phase equilibrium data, diffusion coefficients of binary systems can also be obtained from the diffusion profiles. All these data are valuable to the establishment of thermodynamic and kinetic databases to assist the alloy design using the Integrated Computational Materials Engineering (ICME) approach [38,39]. Properties can be measured at different locations locally for various compositions to construct the composition-structure-property relationship, such as compositional dependence of hardness, elastic modulus, strength, thermal conductivity using nanoindentation, micro-compression, and time-domain thermoreflectance (TDTR) techniques. Other properties like magnetic and electrical properties can also be measured on diffusion multiples. The high-throughput way of measuring properties of the diffusion-annealing induced composition gradients is much more efficient than the traditional way that prepares multiple bulk alloys of individual compositions in terms of time and raw materials cost. The design process of new structural or functional materials can be accelerated with the open-source data and improved computational modeling based on extracted data from this approach.

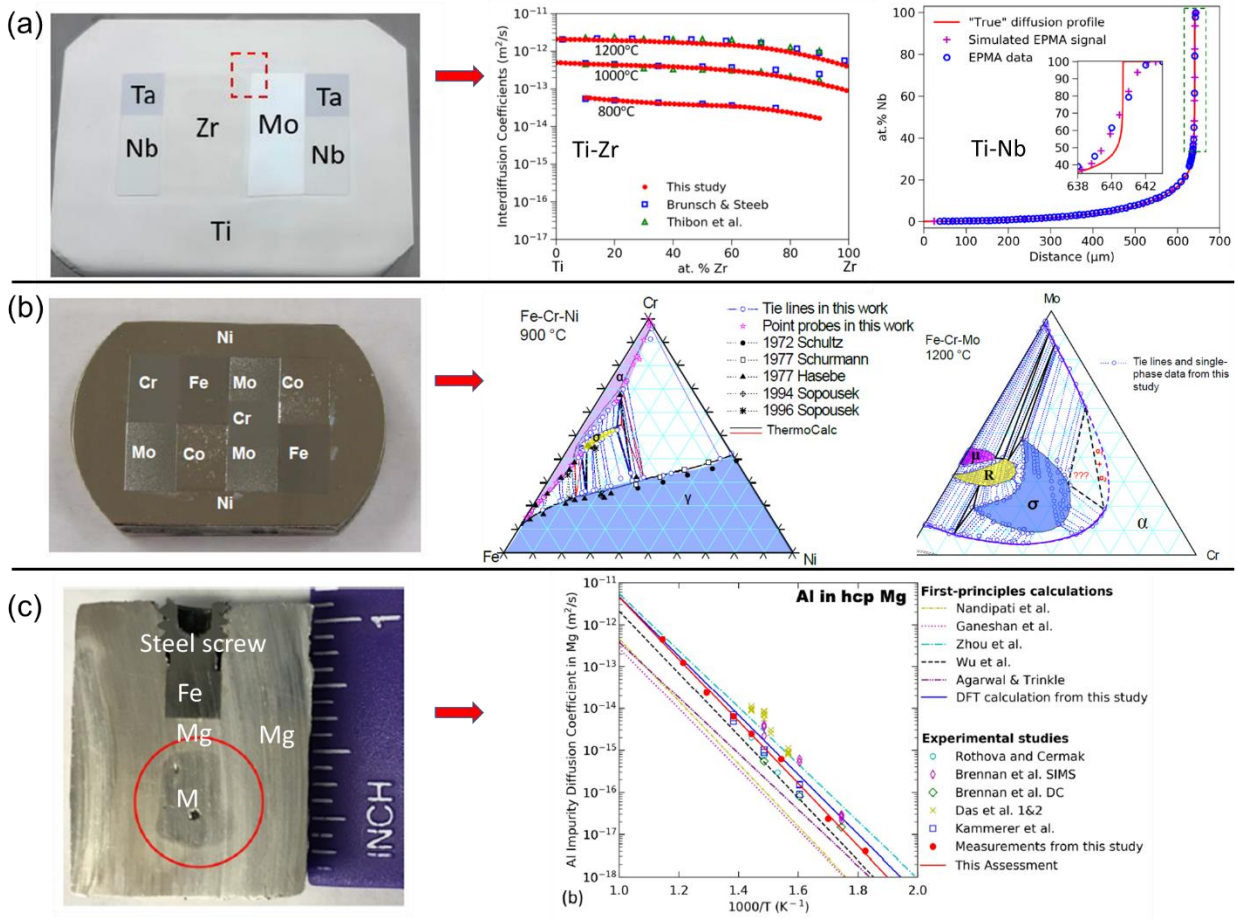

Figure 1.10 Examples of research work conducted by previous group members using the diffusion-multiple approach and a liquid-solid diffusion couple (LSDC). (a) Zhangqi Chen's diffusion multiple for the Ti-Mo-Nb-Ta-Zr system [40]. (b) Siwei Cao's dual-anneal diffusion multiple for the Ni-Cr-Nb-Ta-Fe system [41]. (c) Wei Zhong's Mg-based LSDC [42].

Prof. Zhao's group has performed large amount of research in studying the thermodynamic and kinetic behavior of binary systems and ternary systems using the diffusion-multiple technique. Examples of work from previous group members using diffusion multiples under the guidance of my advisor are presented in **Fig. 1.10**. Zhangqi Chen prepared the Ti-Mo-Nb-Ta-Zr diffusion multiple to study the interdiffusion coefficients of Ti-based and Zr-based binary

systems using the forward-simulation analysis shown in **Fig. 1.10(a)** [43]. He also investigated the effect of steep composition gradient on the extraction of interdiffusion coefficients caused by the relatively large X-ray interaction volume in the EPMA measurement and suggested the upper limit of composition gradient of 1 at.% per μm for reliable extraction of diffusion coefficients from diffusion profiles [44]. Siwei Cao prepared dual-anneal diffusion multiples (DADMs) that underwent two stages of annealing, as presented in **Fig. 1.10(b)** [45,46]. The first annealing of DADM is at a high temperature to form solid solutions and intermetallic compounds and the second one is at an intermediate temperature to generate precipitates from the supersaturated solid solutions. Isothermal sections of Cr-Fe-Mo and Cr-Fe-Ni at 1200 °C, 900 °C, 800 °C, and 700 °C were mapped. Wei Zhong developed a novel liquid-solid diffusion couple (LSDC) to study the diffusion coefficients above the eutectic point in Mg-based binary systems (**Fig. 1.10(c)**) [47–51]. The metal block M is either a pure element or a master alloy, and it is surrounded by Mg metal cartridge and a Mg metal piece. Since Fe has no solubility in Mg, the iron block miminizes the interdiffusion between Mg and the carbon steel screw. The carbon steel screw is used to provide the initial intimate contact among the metal pieces and the Mg cartridge. Using this approach, multiple interdiffusion coefficients of Mg-based binary systems were obtained and a robust Mg-based mobility database was established [52].

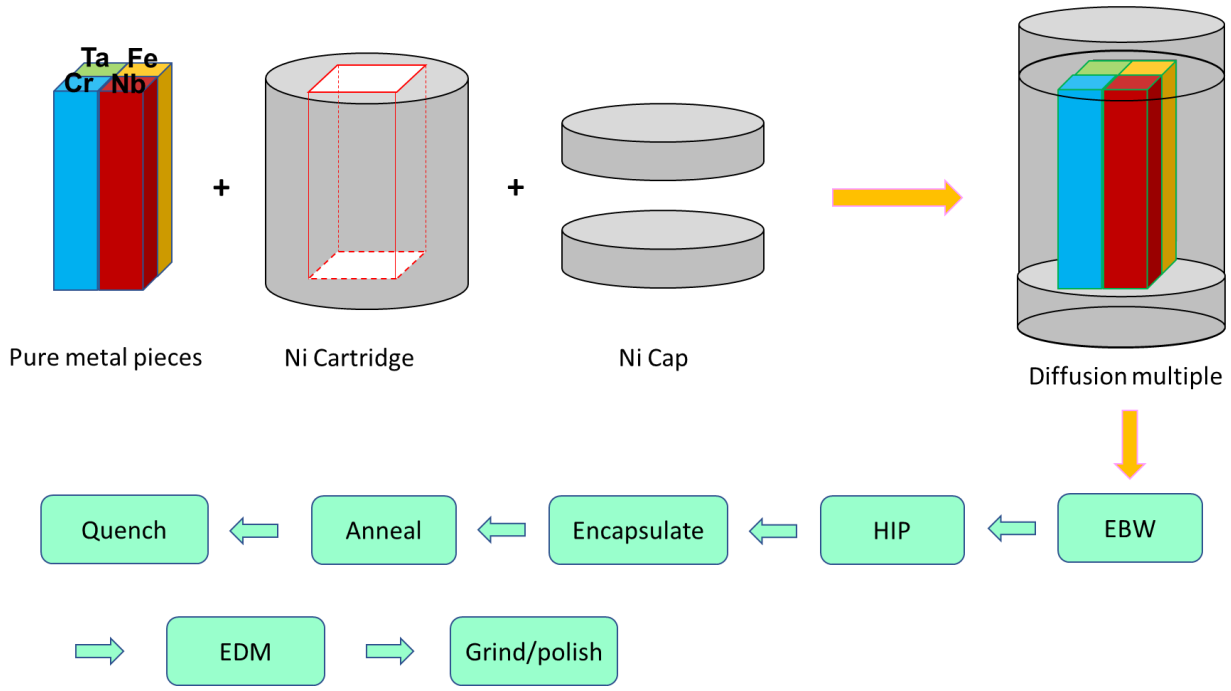

Figure 1.11 The workflow of fabricating a diffusion multiple sample.

Fig. 1.11 shows the general steps of preparing a Ni-Cr-Nb-Ta-Fe diffusion multiple. Four pieces of pure elements Cr, Nb, Ta, Fe were cut into bars with a square cross-section on the ends. The Ni cartridge had a hollow interior whose width is twice that of the width of the pure metal pieces, this allowed the pure metal pieces to fit into the Ni cartridge. Two Ni caps were aligned at the top and bottom of Ni cartridge. All the components were ground using 1200 SiC grits before assembly. The two Ni caps were welded to the Ni cartridge along the outer circular edges of the Ni cartridge. Then the hot isostatic pressing (HIP) was performed to squeeze the piece from the outside to provide an intimate contact at each interface. After HIP, the diffusion multiple was encapsulated into a quartz tube with an argon environment and some Ta foil was put inside the tube to serve as an oxygen getter. The diffusion multiple was then annealed at 1100 °C for 1000 hours. Upon finishing the annealing, the quartz tube was taken out of the

furnace and was broken into a bucket of water for quenching. A slice parallel to the circular side was cut using electro-discharge machining (EDM) and went through the mounting, grinding, and polishing to a final step using 0.05 silica suspension. Then the prepared sample is ready for characterization and measurement of properties.

1.2.2 Characterization techniques

A scanning electron microscope (SEM) is an instrument that uses a high-energy beam of electrons to produce high resolution images of the surface of a sample. The electrons emitted from a gun travel through two or more electromagnetic lenses in a column and hit spots on the sample surface. When the electrons hit the surfaces, secondary electrons are emitted by atoms that interact with the electron beam. They are collected using a secondary electron detector to create an image of the surface as the electron beam scans across the sample surface. SEM could have a high magnification up to 300,000x, presenting a large advantage over optical microscope with a magnification of usually up to 1000x [53]. A lot of micro- or nanoscale details could be detected on the sample surface using SEM. SEM can also be applied to analyze the chemical composition of a sample using an installed EDS. Backscattered electrons (BSE) are the electrons reflected by the sample due to elastic scattering interactions, and they are helpful in detecting the brightness contrast of areas with different chemical compositions and crystal structures. The area with heavy elements is brighter since heavy atoms reflect more electrons than light atoms. The SEM BSE image is employed heavily in my study to determine the phase boundaries for phase diagram mapping using diffusion multiples. Tescan GAIA and XEIA FEG SEM in AIMLAB inside the Kim Engineering Building on campus were mostly used for the SEM images.

A transmission electron microscope (TEM) uses a beam of electrons emitted from an electron gun and transmitted through a thin sample to form an image. The resulting image is

formed by the interaction of the electrons with the thin foil sample. The thickness of the sample is usually less than 100 nm, enabling electrons passing through the sample to collect enough signals. Careful sample preparation is required to get the thin foil piece from a bulk material sample. Preparation techniques for metallic samples include mechanical milling, chemical etching, ion etching, and ion milling. The focused ion beam (FIB) is used for the ion milling. The TEM foils in this work were prepared using FIB with the help of CAMCOR at University of Oregon. High-resolution images were taken using the JEM 21000 FEG TEM/STEM at UMD.

TEM has two image modes, the bright field mode and the dark field mode. In the bright field mode, the transmitted electrons are selected, and the scattered electrons are blocked. The area with heavy atoms or masses appears darker in the image since it is harder for electrons to pass through the sample area with heavy atoms and most electrons are scattered back. This phenomenon is inversed in the dark field mode with the selected scattered electrons and blocked transmitted electrons. There is a diffraction mode to observe a diffraction pattern of samples. With careful analysis of different diffraction patterns taken at the same grain but different orientations, the crystal structure could be determined. The TEM can also be used to measure the compositions at high-resolution mode with the assistance of EDS.

Electron probe microanalysis (EPMA) is designed to determine the elemental composition of materials at the microscopic level using WDS instead of EDS. EPMA system is a more dedicated SEM with WDS detectors in addition to most SEM units that have EDS capabilities only. An EPMA system also uses of a beam of high-energy electrons with an accelerating energy usually from 10 to 20 keV to probe the surface of a sample through interaction in a small-size volume and generate characteristic X-ray emissions that are specific to each element existing in the sample. X-rays are then collected using the WDS detectors and analyzed to determine the

compositions of each element in the sample through well-established X-ray florescence correction methods developed decades ago. EPMA has a high spatial resolution of around 1 micron, which gives precise measurement of the compositions in a small area. WDS is also an important technique to perform composition mapping of an area rather than point analysis in as in the case of EPMA scans. WDS mapping is usually performed by reducing the X-ray collection time on both peak positions and background positions in order to form a composition image at a reasonable amount of time. In this study, WDS was used in mapping the composition distribution in a triple junction area of a diffusion multiple, which speeds up the data collection and analysis for the construction of phase diagrams. Cameca SX100 machine at CAMCOR was employed to perform the EPMA and WDS measurements.

X-ray powder diffraction (XRD) is a very powerful tool to analyze the crystal structure of materials. It usually uses the characteristic X-rays of Cu K_α (= 1.5406 Å) generated by impinging an electron beam on a pure Cu target. The Cu K_α X-ray beam strikes a sample and is reflected by the crystallographic planes of the sample. The intensity of the reflected X-rays is recorded by a detector as the sample is rotated relatively to the direction of emitted X-rays in a range of angles to record the intensity peaks reflected of different crystal planes. After collecting enough signals or intensity from the detector, the intensity-2θ plot could be generated to reveal the peaks at different angles. Bragg's law is used to analyze crystal structures of the sample. The XRD experiments of this dissertation were performed at the X-ray Crystallographic Center at UMD.

1.2.3 Nanoindentation

Nanoindentation is a useful tool to measure two important mechanical properties, hardness and elastic modulus of materials [54,55]. It involves two processes, loading and unloading. The typical behavior with a Berkovich triangular indenter is shown in **Fig. 1.12(a)**. The unloading

curve is used for data analysis assuming that only elastic deformation is recovered in the initial unloading process. And the corresponding contact geometry during unloading is presented in **Fig. 1.12(b)**. In contrast, it is assumed that both elastic and plastic deformation occurs during loading, especially in the late part of loading.

Contact stiffness, the slope of unloading curve at the initial stage of unloading can be expressed in $S = \frac{dP}{dh}$, where P and h are the load and displacement relative to the initial surface after loading. To calculate S, a power law function of h is used in describing P:

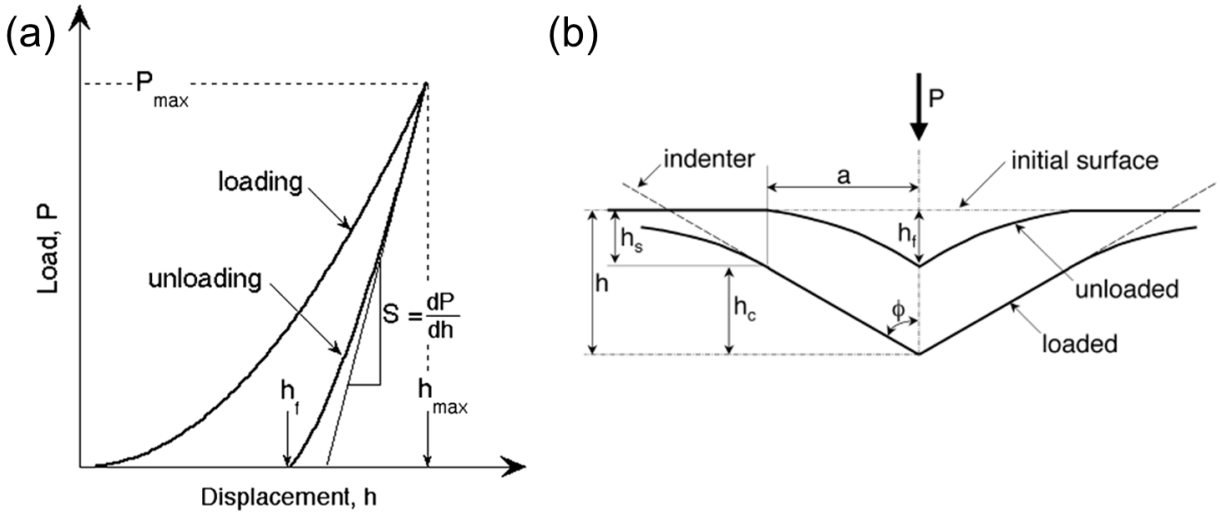

Figure 1.12 (a) Schematic illustration of typical load-displacement curve with important measured parameters. (b) Schematic illustration of the unloading with characterizing parameters for the contact geometry [55].

$$P = \alpha\left(h - h_f\right)^m \qquad (1.23)$$

where α and m are two fitting constants, and h_f is the permanent depth of penetration measured at the end of unloading. The sink-in amount (the area not touched by indenter) caused by loading, h_s, is related to maximum load P_{max} and S:

$$h_s = \epsilon \frac{P_{max}}{S} \qquad (1.24)$$

where ϵ is a constant affected by the geometry of indenter. The vertical displacement of the contact periphery, h_c, can be easily derived by h_s subtracted from h_{max}.

$$h_c = h_{max} - h_s = h_{max} - \epsilon \frac{P_{max}}{S} \qquad (1.25)$$

The contact area, A, describing the projected area of indenter at a distance d back from its tip, can be presented in a power law function of h_c:

$$A = \sum_{n=0}^{8} C_n (h_c)^{2-n} = C_0 h^2 + C_1 h + C_2 + C_3 h^{1/2} + C_4 h^{1/4} + \cdots + C_8 h^{1/128} \qquad (1.26)$$

where C_n are the fitting parameters calibrated on the standard specimen. Then the hardness can be calculated by:

$$H = \frac{P_{max}}{A} \qquad (1.27)$$

The elastic modulus, which is correlated to the elastic modulus of the sample and the indenter, can be determined through the equation:

$$\frac{1}{E_{eff}} = \frac{1-v^2}{E} + \frac{1-v_i^2}{E_i} \qquad (1.28)$$

where v and E are the Poisson's ratio and Young's modulus of sample, v_i and E_i are the Poisson's ratio and Young's modulus of the indenter. E_{eff} corresponds to the effective elastic

modulus determined by $E_{eff} = \frac{S\sqrt{\pi}}{2\beta\sqrt{A}}$ with β related to all physical processes. Thus, the elastic modulus can be obtained once other quantities are known in **Eq. (1.28)**.

From **Eq. (1.27)**, the hardness value depends on the maximum load and contact area (or h_c). It's important to compare the hardness of different materials under the same experimental settings such as maximum load and indenter type. Other indenters with axisymmetric geometry including conical or spherical indenters are also useful in measuring mechanical properties of materials. The MTS Nanoindenter XP at the Ohio State University was employed to explore the hardening effect in Mg-based binary alloys and the TI-900 TriboIndenter at UMD was used in studying the compositional dependence of hardness in refractory binary alloys.

Chapter 2: High-Throughput Evaluation of Hardening Coefficients of Eight Alloying Elements in Magnesium

2.1 Introduction to solid solution hardening

Magnesium alloys are used in automobiles and biomaterials due to their low density and good bio-compatibility [56–58]. Despite multiple applications, their disadvantages of low elastic modulus, high chemical reactivity, limited strength, and low creep resistance at elevated temperatures have impeded their widespread utilities. To enhance the mechanical behaviors of Mg-based alloys, strain hardening, solid solution hardening (SSH), and precipitation hardening are feasible approaches [59–61].

The hardening mechanism strongly depends on grain orientation (crystallographic orientation), grain size, strain rate, temperature, dislocation characteristics, and composition of solid solutes [62–65]. Sahoo et al. revealed that the hardness of annealed pure magnesium decreases in planes when the degree of deviation relative to basal orientation increases [62]. Both higher indentation strain-rates and lower temperatures could increase the hardness of Mg alloys, according to Somekawa and Schuh's work [63]. SSH is a common method to improve hardness by introducing other solutes into alloys. Previous experiments performed by microindentation testing have shown that adding solutes Al, Gd, Sn, Y, and Zn to pure magnesium can improve the hardness by an amount that is proportional to c, where c is the composition of solutes [66–71]. Since the hardness was measured on bulk alloys with different compositions, only a few experimental data points were obtained, mainly due to the time of needed to prepare individual alloys and samples. Each diffusion couple (DC) contains a diffusion zone with composition

variations after sufficient diffusion time, from which multiple useful data points can be obtained by measuring along the composition gradient. To reduce the effect of the short diffusion length and increase accuracy of using measured composition at each indent, we employed nanoindentation instead of microindentation to make small indents and fully use the space of the diffusion zone [72].

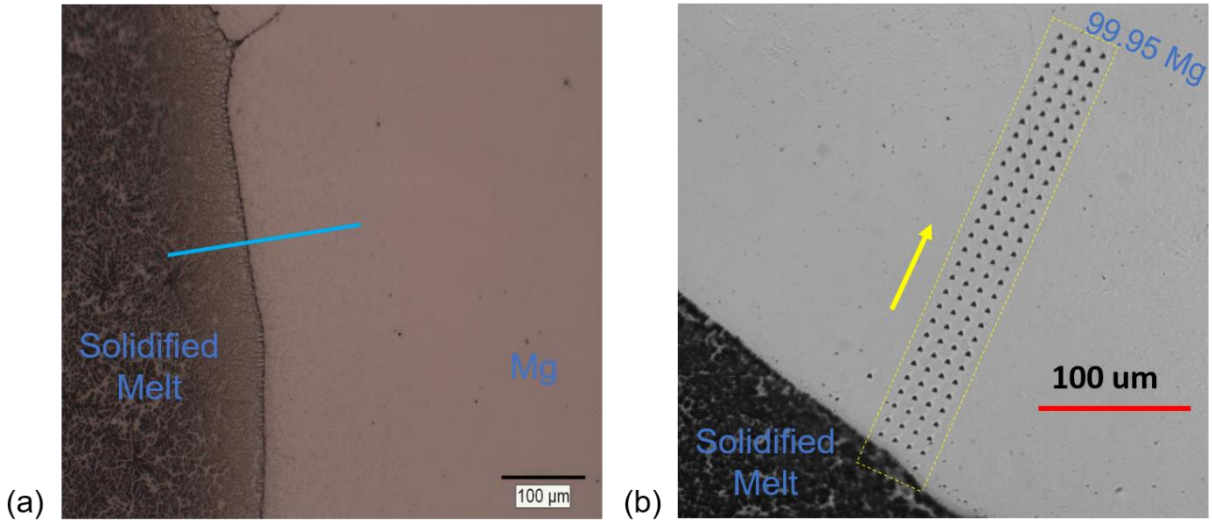

Figure 2.1 Optical images of EPMA scan line in (a) and nanoindentation indents in (b) on the surface of a Mg-Zn LSDC.

This study investigated the effects of eight solutes, Al, Ca, Ce, Gd, Li, Sn, Y, and Zn, on magnesium's hardness. The eight Mg-X (X = Al, Ca, Ce, Gd, Li, Sn, Y, Zn) liquid-solid diffusion couples (LSDCs) prepared for the extraction of diffusion coefficients by Dr. Wei Zhong were utilized for hardness measurements [47–51]. To evaluate SSH effects, the classical Labusch model, Fleisher model, and linear model were tested [73,74]. The shear modulus, elastic modulus, and atomic size difference affect the hardness in alloys, and these parameters

were explored to understand hardening behavior. The yield strength of materials is closely correlated with hardness, and the solid solution effect can lead to an increase in both yield stress and hardness [67,75]. Different solutes exhibited various hardening coefficients (indicator for hardening ability) in Mg alloys. These hardening coefficients were further compared with the first-principles calculated data and experimental data on strengthening potency related to critical resolved shear stress (CRSS) to understand the correlation between CRSS and hardness [76].

2.2 Experimental methods

To obtain a wide range of solute composition variation for these eight Mg-based binary systems, the LSDCs with high solubilities of solutes were selected. The heat treatment temperatures for LSDCs with Al, Ca, Ce, Gd, Li, Sn, Y, and Zn solutes were 500, 530, 605, 570, 550, 550, 590, and 500 °C, respectively. The processes to measure the composition and perform nanoindentation on the Mg-Zn LSDC are illustrated in **Fig. 2.1**. The diffusion composition profile of the Mg-Zn LSDC was quantitatively measured following the blue line in **Fig. 2.1(a)** using EPMA with a CAMECA SX100 electron microprobe operated at 15kV accelerating voltage and a 40° take-off angle. The step size of the EPMA scan varied from 1 μm to 5 μm depending on the thickness of phases in the diffusion zone. The hardness test was performed using the NanoIndenter XP system with a Berkovich indenter under a load of 5 mN, a loading time of 15 s, a holding time of 5 s at peak load, and at room temperature. Four nanoindentation scans were made on the sample surface as shown in **Fig. 2.1(b)**. The indents were enclosed by the yellow dashed lines and was made following the direction of the yellow arrow from the Mg-solidified melt (liquid) interface to pure magnesium. This direction was tilted by a small angle

relative to the perpendicular direction of Mg-solidified melt interface to make more indents along the composition gradient, which is effective to gather more available hardness-composition data. Based on the load-displacement curve, the hardness, H, can be determined by the peak load, P_{max}, and contact area, A, where $H = \frac{P_{max}}{A}$ according to Oliver-Pharr method [55,72].

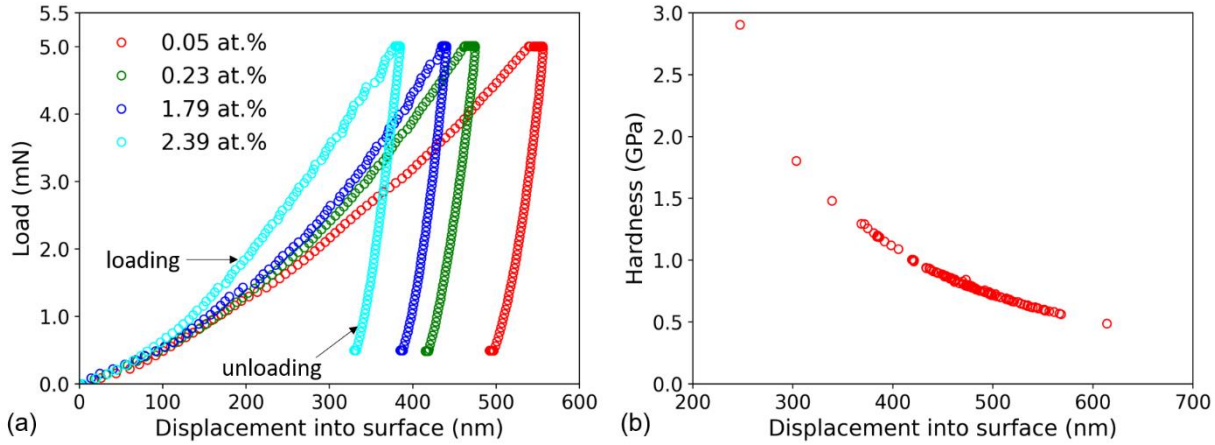

Figure 2.2 (a) Typical load-displacement curves measured at 0.05, 0.23, 1.79, and 2.39 at.% Zn in the Mg-Zn LSDC; and (b) The hardness versus displacement relationship.

2.3 Hardening coefficients of Mg-based binary systems

During the nanoindentation test, the load-displacement profiles at different indentation locations on the Mg-Zn LSDC were collected to determine the hardness. As shown in **Fig. 2.2(a)**, h_{max} (the final displacement after unloading) reduces with increasing amount of Zn, indicated by the higher resistance to deformation caused by indenter. The serration or pop-ins seen in loading curves could be caused by the nucleation and/or propagation of dislocations [77,78]. The indent with shallower h_{max} means higher hardness at the location of this indent, as illustrated in **Fig. 2.2(b)**. The hardness and composition data as a function of

distance, extracted along the blue line of the EPMA scan in **Fig. 2.1(a)** are displayed in **Fig. 2.3(a)**. With these two datasets, the composition for each indent was calculated by interpolation, and the corresponding hardness-composition data are presented in **Fig. 2.3(b)**. As shown in the plot, the higher concentration of Zn increases the hardening effect in the Mg-Zn alloys. Following the described procedures above, all hardness-composition profiles in eight Mg-based LSDCs were extracted.

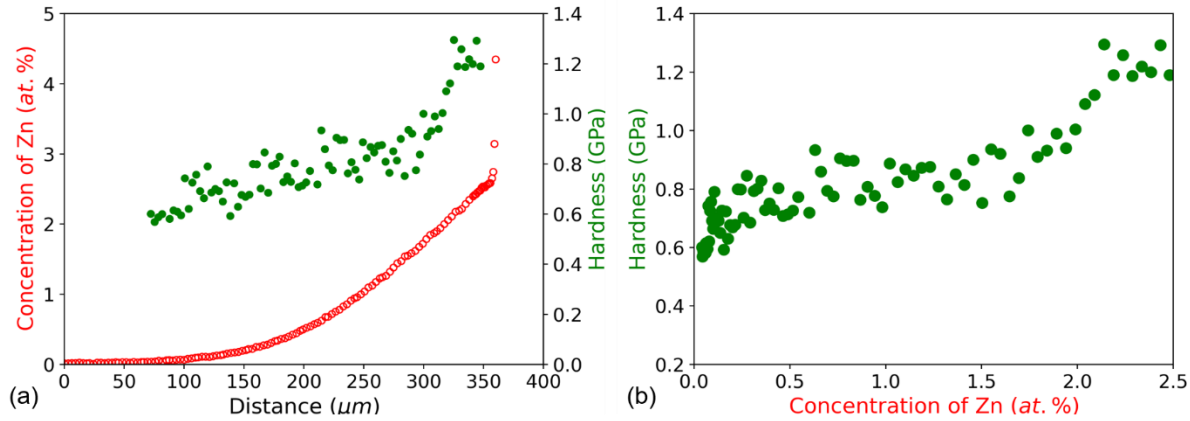

Figure 2.3 (a) The profiles of composition of Zn versus distance (red circles) and hardness versus distance (green dots); (b) The extracted hardness-composition profile for the Mg-Zn LSDC.

The experimental data for Al, Gd, Y, and Zn solutes are compared with the measurements performed under 5mN load by Kammerer [59] in **Fig. 2.4**. The hardness increases appreciably in our measurement for dilute Mg-Al solid solutions, while there exists a softening phenomenon in the observation of Kammerer at low compositions of Al. The hardening rates from 1 to 6 at.% Al obtained in our work is similar to Kammerer's work. In the Mg-Gd system, the two measurements are in good agreement. In the Mg-Y solid solutions, the experimental hardness

and the hardening rate are larger than that from the literature. For Mg-Zn system, the hardness of the solid solutions increases with a higher composition of Zn, which agrees well with the previous work.

The SSH mechanism can be described by the relationship between hardness and composition of solutes as:

$$H = H_0 + Kc^b, \qquad (1)$$

where H and H_0 are the hardness after and before adding other solutes in a pure metal, K is the hardening coefficient or hardening rate, and b is an exponent that depends on models. This equation was derived based on the Tabor factor and Taylor factor for conversion between normal stress to indentation hardness, and conversion between shear stress and normal stress [75,79]. There are two classical models, Fleischer model and Labusch model, to explain the hardening mechanisms of solutes atoms. In the Fleischer model [74], ΔH $(= H - H_0)$ is proportional to $c^{1/2}$ by taking the solute atoms as individual point defects. In contrast, Labusch model [73] considers the collective interaction of dissolved atoms with mobile dislocations and uses $\Delta H \propto c^{2/3}$. The Labusch-type weak-pinning model developed the Labusch model, which is applicable to arbitrary compositions and multiple-component systems [64,80]. These two models and a linear model (b = 1) were employed to study the SSH with the hardness-composition data.

The experimental data for hardness versus composition and the corresponding fitting curves based on the Labusch model are presented in **Fig. 2.5**. These data points were pre-processed by excluding the data measured in the solidified melt region. From these figures, the hardness of Mg

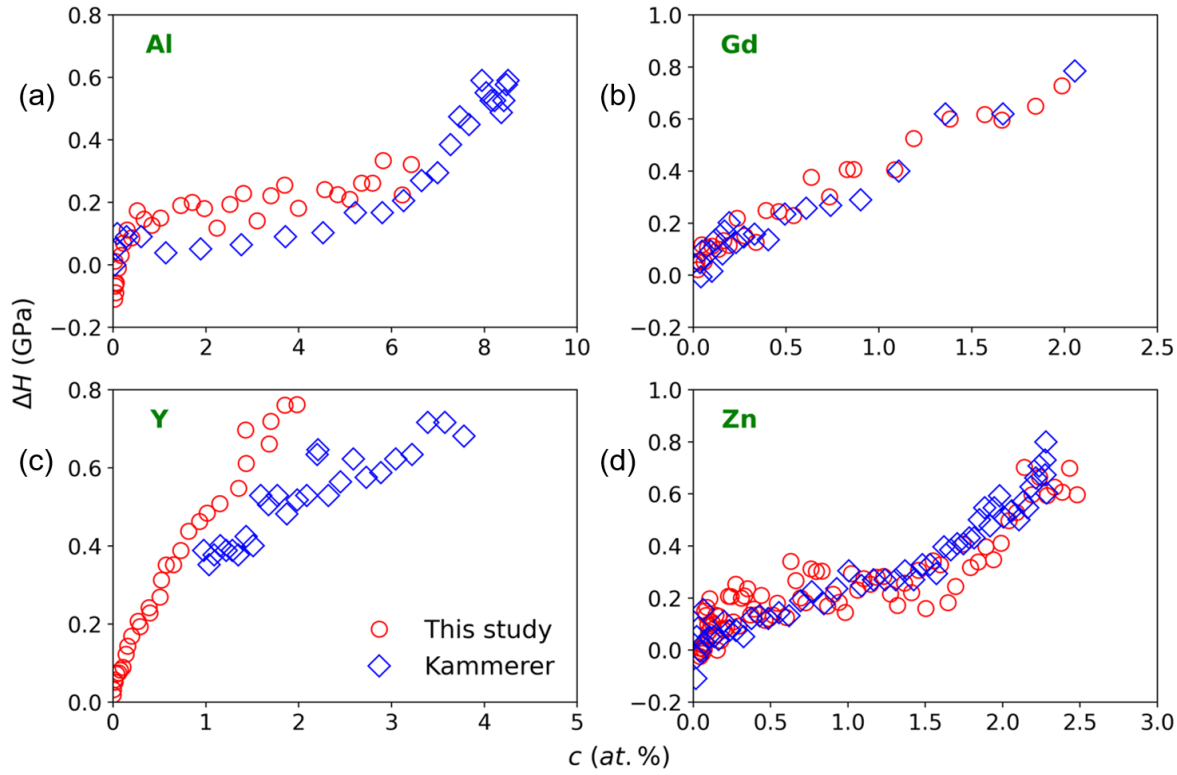

Figure 2.4 The increase of hardness-composition comparison between experiment and literature data for (a) Al, (b) Gd, (c) Y, and (d) Zn. The data in red circles are from this study and data in blue diamonds are from Kammerer [59].

alloy increases with a larger composition of solutes, demonstrating that all these eight solutes have positive effects on hardening Mg. The solute Al and Sn have a similar hardening coefficient, and the hardness of Mg alloys increases fast with a small amount of Al, as shown in **Fig. 2.5(a)**. The hardening ability of Gd is very close to that of Y in Mg alloys, as presented in **Fig. 2.5(c)**. All these fitting curves are summarized and plotted in **Fig. 2.5(f)**. Based on this figure, the solubility of solutes presented in open circles and the hardening coefficients in Mg are quite extensive. Though Mg can only dissolve about 0.13 at.% Ce, Ce is the most efficient in

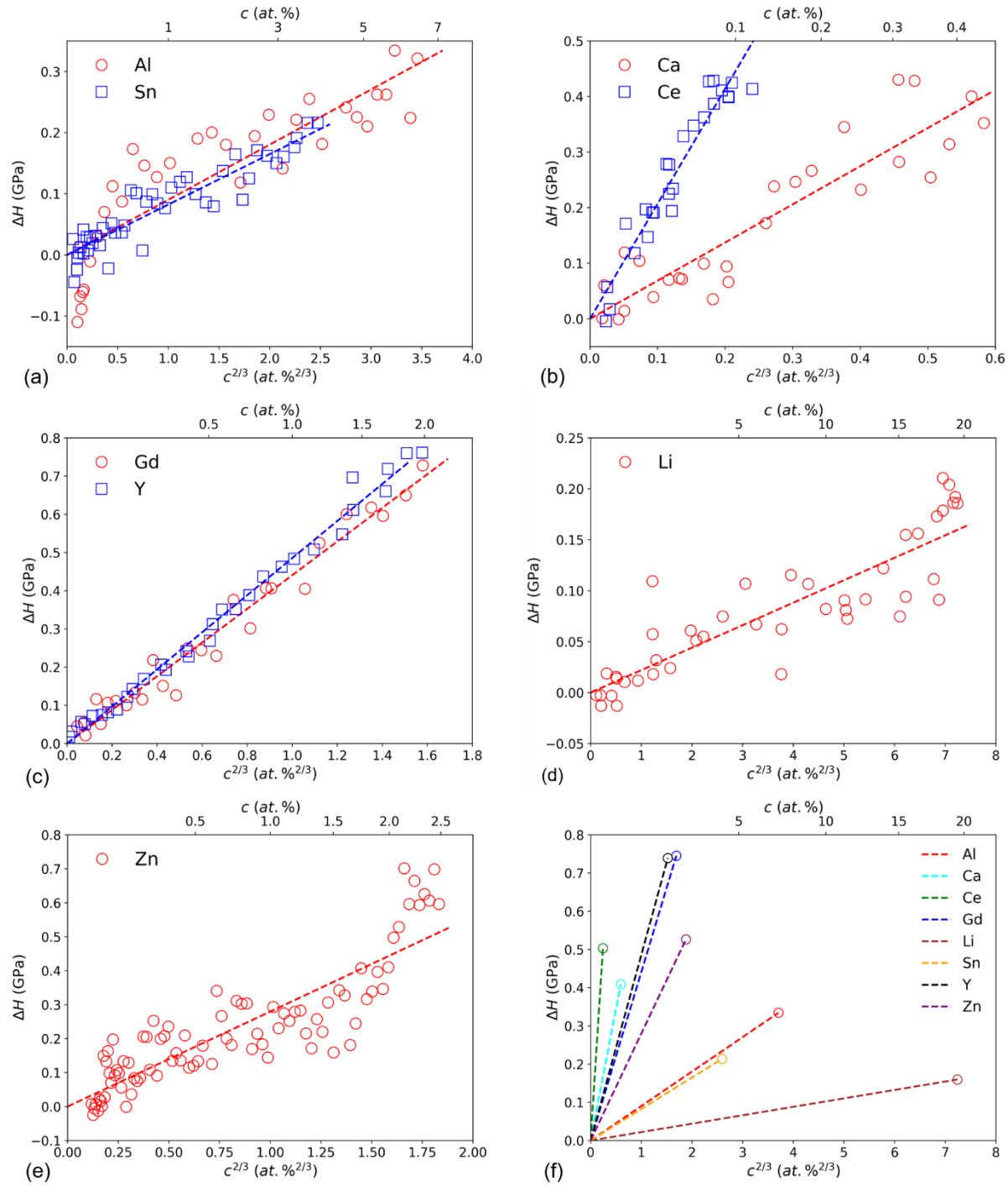

Figure 2.5 Hardness-composition data is shown in this figure with $\mathbf{c^{2/3}}$ as bottom x-axis, c as top x-axis, and increase of hardness as y-axis. The dashed lines are the fitting results based on the Labusch model. (a) Al and Sn solutes; (b) Ca and Ce solutes; (c) Gd and Y solutes; (d) Li

solute; (e) Zn solute; (f) Fitting curves are plotted and the compositions shown as open circles are the solubility limits for solutes.

hardening Mg. In contrast, Li exhibits the weakest ability in hardening Mg despite having the highest solubility limit among these eight solutes. The hardening ability of Ce, Ca, Y, Gd, Zn, Al, Sn, and Li declines from Ce to Li in Mg-based binary systems. The fitting results based on three models are evaluated by R-squared (R^2) in each LSDC, as shown in **Table 2.1**. By comparing R^2 values, the fitting result based on the Labusch model is better than that of the Fleischer model and linear model at explaining the SSH mechanism due to the fast-increasing hardness at low compositions of solutes.

The SSH models are built on the interaction mechanism between solute atoms and dislocations, which is correlated with atomic size misfit parameter, $\delta = (da/dc)/a$, and shear modulus misfit parameter, $\eta = (dG/dc)/G$, where a is the lattice parameter and G is shear modulus [81]. Consequently, the effects of these two misfits are summarized in one misfit parameter $\epsilon = (\eta^2 + \alpha^2\delta^2)^{1/2}$, where α is an adjustable number. The value of η can be calculated by formula $\eta = 2(G_1 - G)/(G_1 + G)$ if the relation between G and c is unclear [82]. In some studies, the effect of elastic modulus rather than shear modulus misfit is considered in ϵ [83]. The misfit parameter becomes $\epsilon_E = \left(\epsilon_y^2 + \alpha^2\delta^2\right)^{1/2}$, where $\epsilon_y = \epsilon_u/(1 + |\epsilon_u|/2)$, elastic modulus misfit, $\epsilon_u = \Delta E/E_{PS}$, ΔE is the elastic modulus difference between pure solvent and solute, and E_{PS} is the elastic modulus of pure solvent. α and δ are the same as described above. To study the relationship between hardening coefficients and misfit parameters in Mg alloys, all mentioned misfit parameters for Al, Zn, Gd, Y, Ce, Ca, Sn, and Li, and corresponding

hardening coefficients are summarized in **Table 2.2**.

Table 2.1 The fitting parameters H_0, K and R^2 are listed at b = 1/2, 2/3, and 1. The R^2 marked in red are the best fitting results obtained by a comparison among all three models for each solute.

	b = 1/2 (Fleischer model)			b = 2/3 (Labusch model)			b = 1 (Linear model)		
Solute	H_0	K	R^2	H_0	K	R^2	H_0	K	R^2
Al	0.727	0.132	0.804	0.759	0.090	0.761	0.792	0.045	0.679
Ca	0.424	0.633	0.822	0.464	0.687	0.832	0.506	0.863	0.816
Ce	0.498	1.597	0.931	0.566	2.070	0.919	0.639	3.843	0.872
Gd	0.435	0.516	0.950	0.502	0.441	0.968	0.573	0.343	0.964
Li	0.578	0.038	0.760	0.592	0.022	0.769	0.607	0.008	0.772
Sn	0.540	0.108	0.860	0.559	0.082	0.856	0.578	0.052	0.825
Y	0.415	0.560	0.972	0.480	0.485	0.990	0.555	0.380	0.978
Zn	0.539	0.345	0.733	0.593	0.230	0.753	0.647	0.203	0.781

Table 2.2 Misfit parameters for Al, Ca, Ce, Gd, Li, Sn, Y, and Zn solutes in Mg. The hardening coefficient K (GPa/ at.%$^{2/3}$) obtained by the Labusch model is used. $\boldsymbol{\alpha}$ is 16 for $\boldsymbol{\epsilon}$ and $\boldsymbol{\epsilon_E}$.

solute	δ	η	ε_u	ε_y	ε_E	ε	K
Al	-14%	0.419	0.556	0.435	2.282	2.279	0.090
Ca	23.10%	-0.789	-0.556	-0.435	3.721	3.779	0.687
Ce	13.70%	-0.230	-0.244	-0.218	2.203	2.204	2.070
Gd	11%	0.247	0.222	0.200	1.771	1.777	0.441
Li	-3%	1.208	-0.891	-0.616	0.781	1.300	0.022
Sn	1.25%	0.057	0.111	0.105	0.226	0.208	0.082
Y	11%	0.404	0.422	0.349	1.794	1.806	0.485
Zn	-17%	0.867	1.400	0.824	2.842	2.855	0.230

Table 2.3 Hardening coefficients derived from linear model by nanoindentation (K_n in MPa/at.%) and Vickers tester (K_{v5} in MPa/at.%) for solutes Y, Gd, Zn, Al, and Sn in Mg.

Atom	Y	Gd	Zn	Sn	Al
K_n	380.13	342.68	202.83	51.53	45.47
K_{v5}	129.44	137.28	88.25	67.47	32.36

The rank of hardening ability of these solute atoms is $K_{Ce} > K_{Ca} > K_{Y} > K_{Gd} > K_{Zn} > K_{Al} > K_{Sn} > K_{Li}$ in both Labusch model and Fleischer model. The absolute value of size misfit gives $r_{Ca} > r_{Zn} > r_{Al} > r_{Ce} > r_{Y} = r_{Gd} > r_{Li} > r_{Sn}$ that is quite different from the hardening coefficient rank, showing a deficiency of only using size misfit to explain SSH mechanism. Kadambi et al. found that hardening coefficient K increases with larger ϵ_E in Ni binary face-centered cubic (FCC) alloys Ni-Co, Ni-Fe, Ni-Pt, Ni-Mo, and Ni-Ta, and in Co binary FCC alloys Co-Ni, Co-Fe, Co-Pt, and Co-Mo, respectively [83]. However, the hardening coefficient is not totally dependent on δ, η, ϵ, ϵ_u, ϵ_E for these eight solid solutions, which indicates that other influential factors should be considered besides these misfit parameters. Chen et al. pointed out that the hybridization of valence electrons calculated by electron localized functions affects SSH, and the bond strength between Mg and Y is stronger than that of Mg-Al and Mg-Zn [84], which leads to stronger hardening result by Y than Al and Zn. The order of chemical bonds obtained by Chen et al. is that strong covalent bond > polarized covalent bond > ionic bond. Polarized covalent bonds formed between rare earth elements (Gd, Ce) and Mg atoms are stronger than ionic bonds formed in Mg-Sn system, rendering stronger hardening effect with addition of rare elements in Mg alloys. The SSH could be affected by other misfits, such as slip misfit ϵ_s correlated to stacking fault energy in the structure [76].

Besides the nanoscale hardness tests, there was hardness measured by the microindentation in prior research [66–70]. These tests were carried out by a Vickers tester with a load of 500g (about 4.9 N) and a holding time of 15s on Mg-based systems with the addition of Y, Gd, Zn, Al, and Sn solutes, respectively. The hardening coefficients extracted by the linear model from nanoindentation, and the Vickers tester are listed in **Table 2.3**. There exists a difference in these two groups of measured hardening coefficients for each solute, which could be attributed to the

effects of indent geometry and indentation size [85,86]. The ranks of hardening coefficients from these two tests are in good agreement except that the hardening effect of Y is slightly stronger than that of Gd based on the data obtained by nanoindentation, which is reversed in the microindentation results.

2.4 Relationship between hardening coefficients and strengthening potency

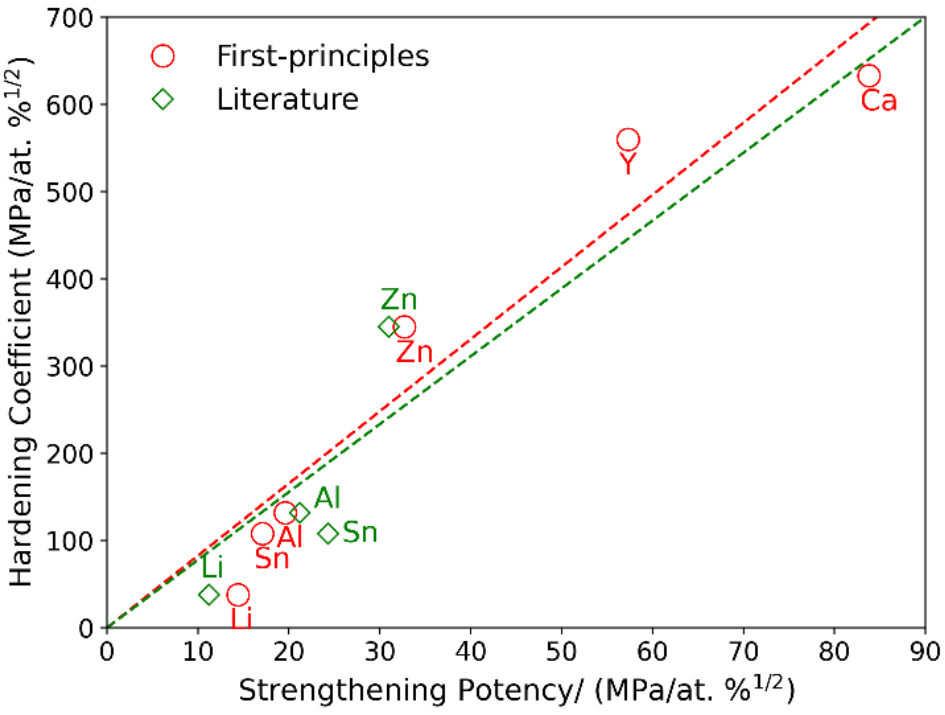

Figure 2.6 Solid solution hardening coefficient versus strengthening potency and the corresponding fitting curves (dashed lines). The value of y-axis is the experimental hardening coefficient, and the value of x-axis is strengthening potency from two sources, one is the literature first-principles calculations (red open circles and red line), another is the literature experimental data (green open diamonds and green line).

There exists a correlation between hardness and critical resolved shear stress (CRSS) as described in Tabor relation since both could stand for materials' resistance ability to plastic deformation. Yasi et al. obtained composition-independent strengthening potency at 0K, which is the pre-factor in describing the relationship between CRSS and composition by the Fleischer model, via quantum-mechanical first-principles calculations considering the size and chemical misfits in Mg-based binary systems [76]. Strengthening potency from first-principles calculations for solute Al, Ca, Li, Sn, Y, and Zn and from experimental data for Al, Li, Sn, and Zn [87–90] are collected. The correlation between strengthening potency of the solutes and the hardening coefficients extracted by the Fleischer model are presented in **Fig. 2.6**. The correlation data indicate that the hardening coefficient is positively correlated with strengthening potency. Per Tabor relation, the linear fitting is applied to hardening coefficient versus calculated and experimental strengthening potency, respectively. The equations for the two linear fits in red and green are:

$$\begin{cases} K = 8.3K_s & (2) \\ K = 7.8K_s & (3) \end{cases}$$

where K is hardening coefficient, and K_s is the strengthening potency. Based on these two equations, the hardening coefficient has a strong linear relationship with strengthening potency of solutes in Mg-based binary systems.

2.5 Conclusion

In conclusion, the hardening coefficients of eight solutes in Mg alloys are extracted and analyzed from the experimental hardness-composition data. The rank of hardening ability of

these solutes are $K_{Ce} > K_{Ca} > K_{Y} > K_{Gd} > K_{Zn} > K_{Al} > K_{Sn} > K_{Li}$ in both Labusch and Fleischer model. The misfit parameters related to atomic size, shear modulus, and elastic modulus cannot fully explain the SSH mechanism in Mg alloys, which requires introducing other factors such as valency electrons and stacking fault energy. The rank of hardening coefficients obtained by nanoindentation is in good agreement with that obtained by microindentation for Y, Gd, Zn, Al, and Sn solutes in Mg. The hardening coefficient increases linearly with increasing strengthening potency, showing a strong correlation between hardness and critical resolved shear stress. Therefore, knowing either one of the properties can give us a good picture of both properties.

Chapter 3: Real-time autonomous experiment-computational prediction interaction for closed-loop materials science

Note: This study was led by Prof. Ichiro Takeuchi's group at UMD and Dr. A. Gilad Kusne at the National Institute of Standards and Technology (NIST). My contribution to this study is mainly on integrating the thermodynamic parameter optimization and phase diagram calculations into the overall artificial intelligence (AI) algorithm and approaches.

3.1 Introduction

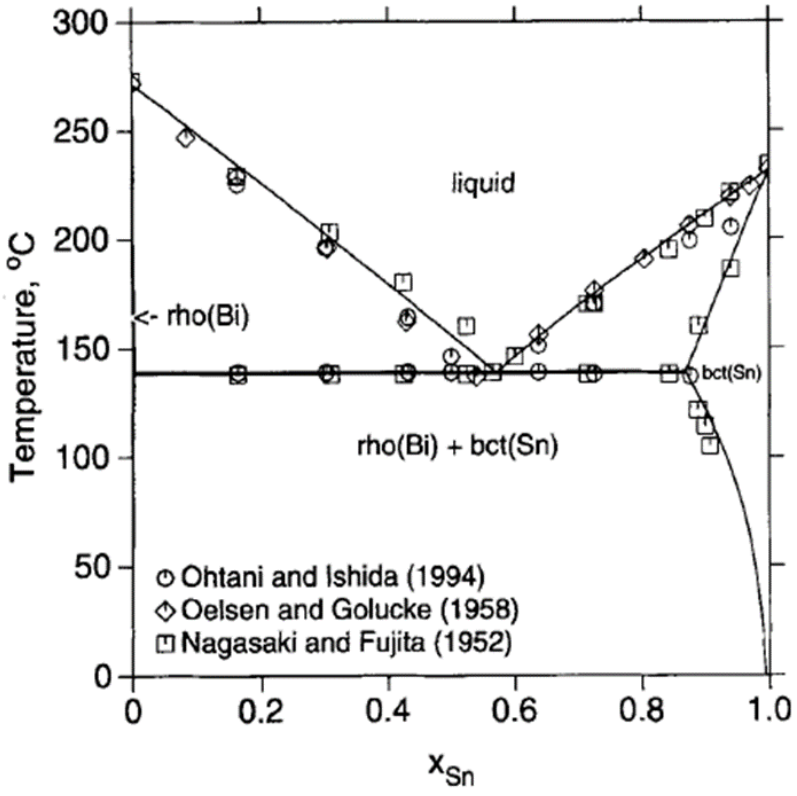

Figure 3.1 Assessed Sn-Bi phase diagram with experimental data [91].

Developing Pb-free solder alloys to replace the Pb-Sn solder is important as excessive Pb could contaminate the water. The Sn-based alloys is promising in solving this problem by introducing other alloying elements such as Zn, Bi, Sb, and In into the alloys to replace and eliminate the Pb. The phase diagram of bulk Sn-Bi system has been well studied and assessed by many researchers [91–94]. However, the phase diagram of the thin-film Sn-Bi system has never been explored, which can serve as a guidance to the design of thin-film devices incorporating superconductor $Sn_{1-x}Bi_x$ [95,96]. The thin films display significant departure in thermodynamic behavior from their bulk counterparts because of the fast evaporation rate, stress from the substrate, and their inherent two-dimensional structure. Therefore, their phase diagram could be different from the phase diagram of bulk systems.

One way to map the phase diagram of the Sn-Bi system is by making different thin film samples with a composition spread and measure the crystal structures on the samples at different temperatures (grid mapping). This could take several days to accomplish the whole measurement. Instead of conducting experiments manually, an autonomous materials search engine (AMASE) method was developed together with our collaborators from Prof. Takeuchi's group and Dr. A. Gilad Kusne of NIST. This method could be applied to detect the eutectic point of the phase diagram through real-time experimental observations and computational predictions. In the phase diagram of the bulk system, the eutectic point of Sn-Bi is at around 138 °C and both melting points of Sn and Bi are below 275 °C. This is an ideally simple system with a low eutectic point and no intermetallics to be explored to demonstrate the AMASE method. The AMASE system performs threaded cyclical tasks of composition selection via active learning, XRD measurement and its analysis, thermal processing of samples, and it is regularly interspersed with Gaussian Process (GP) classification for phase boundary determination and

thermodynamic calculations. The contribution our group has made in this method is the thermodynamic modeling part to provide the predicted thin-film Sn-Bi phase diagram. The continuously-updating live computation of Gibbs energies combined with Bayesian autonomous experiments helps us to map the complete phase diagram of thin-film with measuring small-size sampled compositions from the whole composition space. This is a fully closed-loop experiment and takes just above five hours to complete the Sn-Bi thin-film phase diagram, which is around 30-fold faster than the exhaustive and time-consuming grid mapping, decreasing the experimental time greatly.

3.2 Methodology

Variable-temperature XRD experiment is conducted on samples with thin-film composition spread which covers most part of the phase diagram. The You Only Look Once (YOLO)-based model developed in Prof. Takeuchi's group is employed to determine the phase or crystal structure on various locations of sample by identifying diffraction peaks and monitoring the phase shifting in a series of diffraction patterns. This model is reliable in detecting the low-intensity peak signals with noise-reducing technique. GP model helps to search for the composition that is closest to the phase boundary between two phase regions from many candidate compositions. The Thermo-Calc (TC), one of the CALPHAD software packages, is used to optimize the thermodynamic parameters in the self-built Sn-Bi database and predict the phase diagram. Before describing how the whole experiment runs, the thermodynamic modeling using TC (my major contribution) is described below.

Under a given temperature, pressure, and composition, the alloy system reaches phase equilibrium when the chemical potential μ of each component in each phase is the same. This enables the system to stay in the state with minimal Gibbs energy. Therefore, the process of calculating the phase diagram can be regarded as solving multiple differential equations derived from Gibbs energy functions since chemical potential is essentially the Gibbs energy per mole of substance. The substitutional regular solution model for the molar Gibbs energy of a phase θ in a binary system can be expressed using **Eq. (1.5)**, which is rewritten here for the Sn-Bi system:

$$G_m^{\theta} = x_{Bi}{}^{o}G_{Bi} + x_{Sn}{}^{o}G_{Sn} + RT[x_{Bi}ln(x_{Bi}) + x_{Sn}ln(x_{Sn})]$$

$$+x_{Bi}x_{Sn}\sum_{v=0}^{k}(x_{Bi} - x_{Sn})^{v} \cdot ({}^{v}a + {}^{v}bT) \qquad (3.1)$$

where x_i denotes the mole fraction of element i, ${}^{o}G_i$ is the molar Gibbs energy of the element i. $\sum_{v=0}^{k}(x_1 - x_2)^{v} \cdot ({}^{v}a + {}^{v}bT)$ is the Redlich-Kister (RK) polynomial expansion where v is the order of the polynomial, ${}^{v}a$ and ${}^{v}b$ are two parameters that could be adjusted during optimization. Parameters with 0,1,2 order in the Gibbs energy functions usually are sufficient to generate accurate predictions for the binary systems. Only the 0-order ($v = 0$) and 1-order ($v = 1$) are used for the binary interaction parameters of solid phases. In assessing the liquid phase of the Sn-Bi bulk system, one more parameter of the 2-order ($v = 2$) is used because liquidus cannot be predicted accurately without using the 2-order parameter when assessing the phase diagram of the Sn-Bi bulk system. The only experimental data available is the phase boundary information. Since there is no experimental data on other thermodynamic properties, we can simplify the number of parameters in the optimization by keeping just one adjustable constant ${}^{v}a$ and removing the temperature-related ${}^{v}b$ term.

Due to the microstructure and melting point difference between the thin film and bulk alloys, the Gibbs energy function of pure elements varies. A single constant parameter is added to the Gibbs energy function of the βSn phase to adjust the melting point of βSn in the thin film form, which can better explain the thermodynamic behavior in the thin-film Sn-Bi system. Therefore, we have a total of eight adjustable parameters to be optimized. Gibbs energy expressions containing these eight parameters in the setup file for optimization are:

ENTER-PARAMETER G(bct,Sn) 298.15 -5855.135+65.443315*T-15.961*T*LN(T)-0.0188702*T**2+3.121167E-6*T**3-61960*T**(-1) + V10; 505.07 Y; 2524.724+4.005269*T-8.2590486*T*LN(T)-0.016814429*T**2+2.623131E-6*T**3-1081244*T**(-1)-1.2307E25*T**(-9) + V10; 800 N

ENTER-PARAMETER G(LIQUID,Sn,Bi;0) 298.15 V1; 800 N

ENTER-PARAMETER G(LIQUID,Sn,Bi;1) 298.15 V3; 800 N

ENTER-PARAMETER G(LIQUID,Sn,Bi;2) 298.15 V20; 800 N

ENTER-PARAMETER G(bct,Sn,Bi;0) 298.15 V5; 800 N

ENTER-PARAMETER G(bct,Sn,Bi;1) 298.15 V7; 800 N

ENTER-PARAMETER G(rho,Sn,Bi;0) 298.15 V9; 800 N

ENTER-PARAMETER G(rho,Sn,Bi;1) 298.15 V11; 800 N

The V10, V1, V3, V20, V5, V7, V9, and V11 are all parameters to be optimized. The closed-loop cycle is shown in a block diagram in **Fig. 3.2(a)**. Before starting the experiment, we used CALPHAD as implemented in the Thermo-Calc (TC) software to calculate the phase diagram of Sn-Bi with all initialized interaction parameters set to 0. In other words, we used the ideal phase diagram of Sn-Bi bulk alloy system to generate initial phase diagram and provide initial

compositions for the experiment to measure. We measured the phase for the initialized compositions at an initial temperature in the solid-phase region. The process at each temperature took approximately 30 mins for performing X-ray diffraction test at automatically selected few locations on a thin-film composition spread. We then used GP classification to identify the solvus composition. The converged composition is considered as the phase boundary at current experimental temperature if its neighboring compositions show drastic changes in phase composition. Otherwise, a new sample with a randomly selected composition is measured to update the GP modeling and generate new predicted phase boundary composition. After we got the composition for solvus, the next temperature chosen was determined autonomously via active learning. AMASE is aimed to utilize a composition spread focused on the Sn-rich region (Sn atomic %65-95) to map the partial phase diagram, as shown in **Fig. 3.2(b)**.

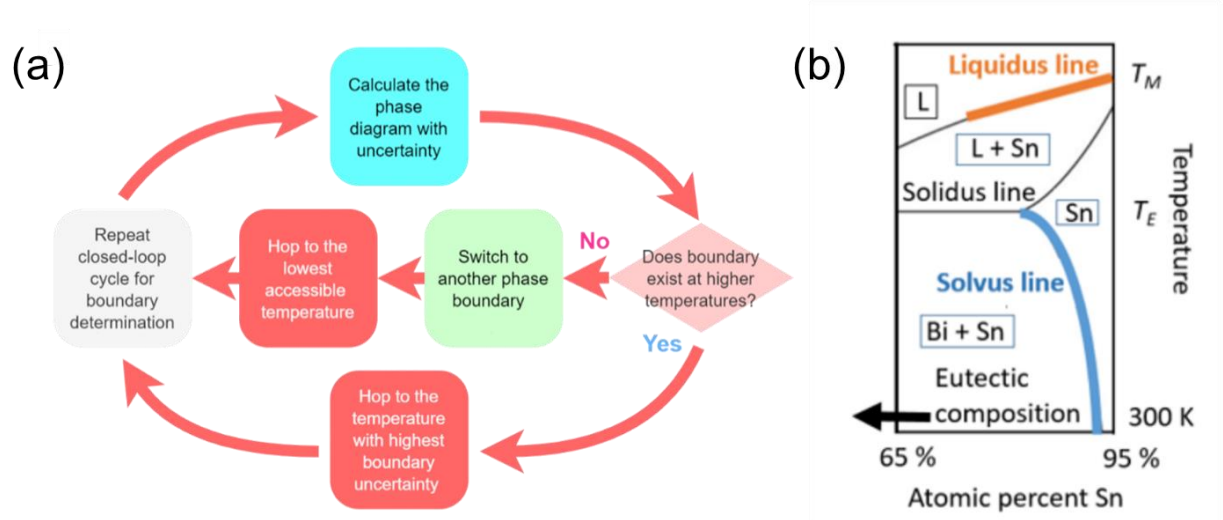

Figure 3.2 AMASE (autonomous materials search engine). (a) The workflow showing the steps in the closed-loop cycles starting at room temperature. (b) The composition range of Sn from 65 at.% to 95 at.% with some important annotations used to understand the thin-film eutectic binary

(Sn-Bi) phase diagram. T_E and T_M are the eutectic temperature and the melting point of Sn, respectively.

Once the solvus composition is experimentally identified, we populated the experimental dataset in POP file to run the thermodynamic assessment (i.e. optimizing the eight binary interaction parameters) to update the thermodynamic database. At this moment, the binary interaction parameters for two solid phases were adjustable, but we fixed all interaction parameters of the Gibbs energy function of liquid to 0. The updated database was then used to predict a new Sn-Bi phase diagram which provides the phase boundary information for the unexplored composition-temperature region in the experiment. The uncertainty of the new prediction is quantified by sampling multiple phase boundaries from the randomized model parameters generated by TC. Here, these randomized parameters were sampled using the Gaussian distribution with the mean and standard deviation value from the linear optimizer. The uncertainty of a phase boundary is defined as:

$$U^{\xi}(T) = \sum_{i=1}^{n} \left(\tau_i^{\xi}(T) - \bar{\tau}^{\xi}(T) \right)^2 \qquad (2)$$

Where $U^{\xi}(T)$ is the uncertainty of the phase boundary ξ at temperature T, $\tau_i^{\xi}(T)$ is the *i*th sampled TC-predicted composition of the phase boundary ξ at temperature T. The uncertainty describes the discrepancy among n = 10 sampled phase diagrams.

Once the phase boundary at current experimental temperature is experimentally determined, the system temperature will be adjusted to explore phase boundaries at other temperatures. Since raising temperature causes irreversible change to the sample, the system temperature cannot be

decreased to measure the phase boundaries at temperature lower than current experimental temperature. To decrease the uncertainty of predictions from the thermodynamic modeling, it jumps to the temperature with highest uncertainty $U^{\xi}(T)$ to perform the next round of measurement. The subsequent composition of phase boundary measured at this new selected temperature is believed to reduce the uncertainty in the TC predictions using reassessed database.

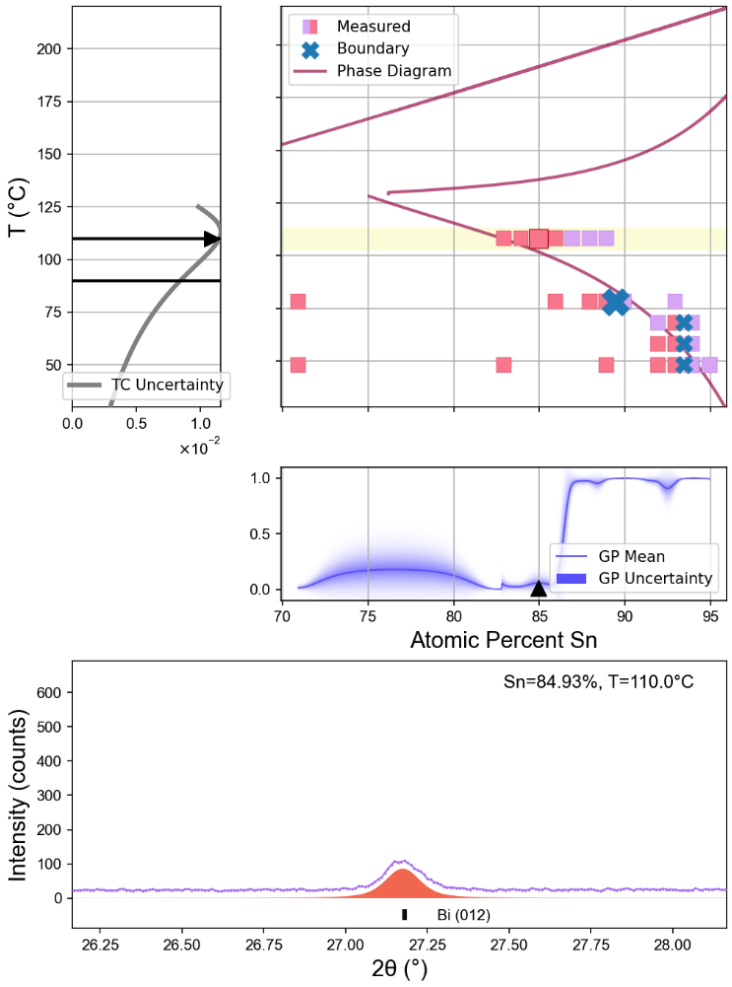

Figure 3.3 The left panel shows our TC uncertainty values at each temperature, and two horizontal lines show the allowed search range. The top right panel shows our experimentally measured data points. Red color represents the Sn + Bi phase. Purple color represents the pure Sn

phase. And blue color is the finally determined phase boundary point. The middle panel shows the Gaussian Process classification mean and uncertainty prediction in the blurry-colored region. The XRD pattern and the fitted peak model are shown in the bottom panel.

An example of AMASE at work is shown in **Fig. 3.3**. In this example, the system searches for the Bi-βSn solvus at the current temperature (110 °C) with highest uncertainty by autonomous measurement and analysis of the Bi (012) peak shown in the bottom panel. The measured point, shown as a highlighted red square, indicates the 012 peak or the Bi phase appears at this composition (in the lower graph of **Fig 3.3**). The sharp transition of the GP mean curve suggests that the phase boundary would appear at around $x_{Sn} = 87\%$. The experimental observation validated this prediction; thus, the phase boundary is determined at this temperature. At higher temperatures, the solvus disappears and liquidus could show up. Once the liquidus is confirmed in the experiment, the thermodynamic assessment process will take the 3 binary interaction parameters in the Gibbs energy function of liquid phase into account and performs the optimization with previous interaction parameters together.

3.3 Results and conclusion

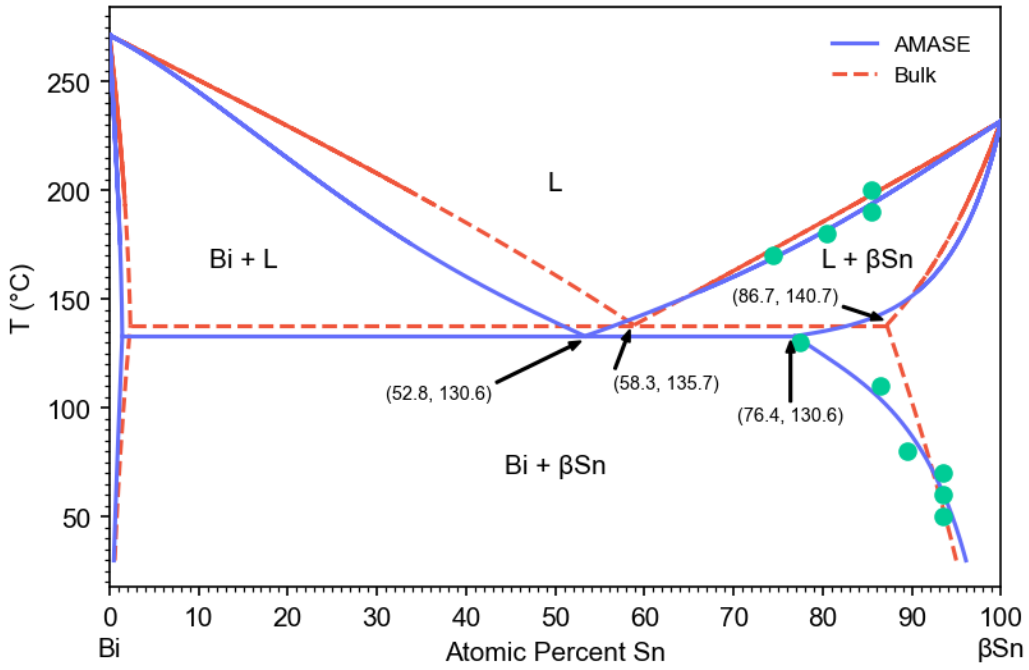

Figure 3.4 The comparison of bulk vs. thin film phase diagram. Green dots correspond to the AMASE experimentally determined compositions at phase boundaries. The thin-film Sn-Bi phase diagram evaluated from the AMASE live run is shown in solid blue line, while the bulk Sn-Bi phase diagram is shown in red dashed lines [93].

The final predicted thin-film Sn-Bi phase diagram and the measured data points at phase boundaries along with the well-assessed phase diagram of bulk system are shown in **Fig. 3.4**. The phase diagram of thin-film Sn-Bi was successfully mapped using the AMASE strategy, and is consistent with the experimentally measured data. The thin-film phase diagram exhibits a shift from Sn side towards Bi side compared with the phase diagram of bulk system. The final predicted eutectic point is at (52.8 at.%, 130.6 °C) whose Sn composition is 5.5 at.% lower and

temperature is 5.1 °C lower than the eutectic point (58.3 at.%, 135.7 °C) of bulk system. The phase diagram mapping of thin-film Sn-Bi binary system provides significant references for the design of superconducting systems containing Sn and Bi rather than relying on the bulk system's phase diagram.

This work firstly realized the completely autonomous experiments to map the phase diagram (especially solvus and liquidus) of thin-film Sn-Bi. This shows the possibility of using AMASE for fast exploration of other binary and even ternary thin-film systems. The AMASE approach works by integrating different techniques such as active learning, XRD measurement and its analysis, thermal processing of samples, Gaussian Process (GP) classification and thermodynamic calculations. A holistic and robust database could be constructed using Gibbs energy functions with well assessed parameters based on future experiments that excavates multiple phase diagram data of other systems, which would definitely accelerate the development and application of thin film in superconductor field.

Chapter 4: Machine learning and thermodynamic calculations on phase equilibria of high entropy alloys

4.1 Introduction

High entropy alloys (HEAs) typically consist of five or more principal elements with composition between 5 and 35 at.% [97,98]. HEAs open up vast composition spaces for designing and discovering new alloys for ever-increasing demands of new materials for energy, environment, and daily well-being.

To accelerate the discovery of novel and advanced materials, the CALculation of PHAse Diagrams (CALPHAD) approach has often been employed to predict and investigate phase formation of HEAs [7,99–106]. In addition to CALPHAD, phase selection rules were developed by various research groups to help predict phases of HEAs via studying the existing experimental data. Such empirical rules are built by presenting the formation of phases in one-dimensional histograms or two-dimensional plots whose axes are usually thermodynamic and physical parameters. For instance, the Hume-Rothery rules depict the effects of atomic size ratio and electrochemical properties on solid solution (SS) formation [107]. Guo et al. revealed that single-phase FCC forms at a valence electron concentration (VEC) > 8 and single-phase BCC forms at VEC < 6.87, while Jiang's work added some constraints based on the alloys they designed and showed that this formation rule applies under the conditions of ΔS_{mix} > 12.47, -7.27 < ΔH_{mix} < 4 kJ/mol, and δ < 4.27%, where ΔS_{mix}, ΔH_{mix}, and δ are the mixing entropy, mixing enthalpy, and difference in atomic sizes, respectively [108,109]. Yang et al. recently developed a new VEC selection rule for predicting SS phases based on high-throughput

CALPHAD calculations in the Al-Co-Cr-Fe-Ni system [110]. Other parameters such as -22 $\leq \Delta H_{mix} \leq$ 7 kJ/mol, $0 \leq \delta \leq 8.5$, and $11 \leq \Delta S_{mix} \leq 19.5$ kJ/mol are found to be conditions for the formation of SS [111]. According to the evaluation of Senkov et al. of over 130,000 alloys, the increasing number of alloying elements in a system beyond 3 results in a reduced likelihood of occurrence of SS [112]. Inoue summarized the conditions to form bulk metallic glasses (BMGs) in terms of the number of elements, atomic size ratios, and mixing heat of atomic pairs [113]. Both $\Omega \geq 1.1$ and $\delta \leq 6.6\%$ were shown by Yang and Zhang to be conditions for the formation of SS phases, and BMGs form in regions of smaller Ω and larger δ as compared to HEAs, where Ω is a parameter related to the ΔH_{mix}, ΔS_{mix}, and melting temperature (T_m) of constituent elements [114]. A single dimensionless thermodynamic parameter ϕ which is correlated with ΔH_{mix}, ΔS_{mix}, T_m, and excessive entropy was defined and HEAs were found to be single-phase SS (SPSS) at $\phi > 20$ based on the analysis of nearly 50 types of HEAs [115]. All these phase selection rules can be used to guide the future design of HEAs; however, most of the rules were developed from small experimental datasets. Li and Tsai collected 100 selected HEAs from the literature and assessed eight published formation rules; they found that the overall accuracy is only ~ 72% in predicting SPSSs and intermetallics (IM) [116]. Therefore, it is highly desirable to test and expand these rules using large, consistent datasets.

Machine learning (ML) holds great promise for future materials design and discovery [117,118]. Unlike CALPHAD that was built upon semi-empirical physical models, ML makes predictions using data-driven strategies with unique algorithms [119–121] that learn from training datasets with input patterns and an optimization target, and then extracts the implicit insights hidden in the datasets. For phase prediction using ML, the properties of alloys or constituent atoms will be taken as input features, and the crystal structures of the phases are

the corresponding targets. Since ML can explore different features simultaneously, it is able to overcome the limitations of traditional strategies in studying phase selection rules [122–124]. For example, phase selection rules were explored via support vector machine (SVM) and artificial neural network (ANN) on two separate groups of features - compositions of HEAs and physical parameters of HEAs, respectively, showing that the accuracies of learning obtained from these two groups of input features are similar and high for HEAs when 4 or 5 physical parameters were employed [125,126]. The Gaussian process statistical analysis was performed on 322 alloys based on a combination of 9 physical parameters, which provided robust predictions for the formation of SPSSs [127]. Krishna et al. utilized six ML approaches with 5 input features to study the classification of SS and SS + Intermetallics (IM) with a dataset of 636 compositions, and they found that the trained ANN reached 80% prediction accuracy and can correctly predict the crystal structures of newly designed alloys [128]. Zhao et al. recently studied 3 categories (SS, IM, SS + IM) using five ML models and achieved 87% prediction accuracy through ANN with 5 selected features [129]. Pei et al. put forward a new parameter λ related to bulk modulus, melting temperature, volume, and configurational entropy with the help of performing ML and found that SPSS forms at $\lambda \geq 1$ with 73% accuracy and it can increase to 81% with a constraint of $\delta \leq 6\%$. They further applied their new formation rule to new compositions that are SPSSs predicted by CALPHAD, and the consistency reached 94% [130]. In addition to studying phase formation separately, a study applied the eXtreme Gradient Boosting (XGBoost) model to explore > 300,000 equilibrium data of HEAs generated by CALPHAD calculations and built more comprehensive and superior phase selection rules for single-phase FCC and BCC based on the 5 ML-selected features [131]. Machaka applied 6 ML models to 896 SPSSs and 101 dual-phase SSs and did feature selection using 36 dataset

features [132]. The accuracy reaches 95% with the top-most identified 13 features. Zhang et al. used a model of SVM combined Kernel Principal Component Analysis to classify a dataset of 556 entries including SS, amorphous (AM), the mixture of SS and IM, and IM, and obtained 97% accuracy with 4 selected features [133]. Zhou et al. performed various experiments on the $(FeCrNi)_{10-x}(ZrCu)_x$ system to verify the ability of the trained ML models, and they achieved good agreements for bulk alloys made by arc melting and ribbon samples through vacuum melt spinning. The thin films made via co-sputtering presented a transition from a crystalline to an amorphous structure as x in $(FeCrNi)_{10-x}(ZrCu)_x$ increases, which is consistent with their ML predictions [134].

Table 4.1 Summary of experimental alloys classified by the phases [135]**.**

Phase	Number
BCC	604
B2	158
FCC	553
BCC + FCC	441
B2 + FCC	5
BCC + Amorphous	71
FCC + Amorphous	145
BCC + FCC + Amorphous	34
Amorphous	192
Intermetallic compound (σ and/or more)	233

A lot of research has been done on predicting phase formation of HEAs using CALPHAD or machine learning, proving the efficiency of these two methods in helping materials design with targeting crystal structure. Therefore, these two methods will be used in studying the phase formation of HEAs. Regarding the data source, experimental data of 2,436 quinary HEAs with different mixtures of Al, Cr, Mn, Fe, Co, Ni, Cu from Kube et al. [135] is employed in this study to perform an extensive test of CALPHAD predictions and ML capabilities. The phase categories and their corresponding numbers of alloys are listed in **Table 4.1**. CALPHAD is utilized to calculate the phase equilibrium of 1,761 SS HEAs from a full dataset of 2,436 HEAs, and the CALPHAD predictions are analyzed and compared with experimental data. Phase selection rules based on different parameters are investigated using traditional methods and ML models as well.

4.2 Methods

4.2.1 CALPHAD calculations

A program is written to predict the phase equilibrium of the 1,761 SS alloys using TC-Python, a python language-based software development kit (SDK) that allows Thermo-Calc to perform high throughput calculations. The computation settings were: TCHEA4 database, only BCC and FCC phases were entered (explained in the Results section), and 1100 °C which is the temperature at which all high-throughput thin film libraries were made.

4.2.2 Parameters for phase selection

Nine parameters are selected for studying the phase selection rules among 2,436 alloys: the mixing entropy (ΔS_{mix}), the mixing enthalpy (ΔH_{mix}), melting temperature (T_m), atomic size difference (δ) [136], Ω that links mixing entropy, mixing enthalpy and melting

temperature [114,137], valence electron concentration (VEC) [107,108], the FCC-BCC-index (FBI) [135], number of itinerant electrons (e/a) [107,138], and the difference in Pauling electronegativity $\Delta\chi$ [139,140]. These parameters are defined as followings.

$$\Delta S_{mix} = -R\sum_{i=1}^{N} c_i ln c_i \,, \qquad (4.1)$$

$$\Delta H_{mix} = \sum_{i=1, i\neq j}^{N} \Omega_{ij}\, c_i c_j \,, \qquad (4.2)$$

$$T_m = \sum_{i=1}^{n} c_i (T_m)_i \,, \qquad (4.3)$$

$$\delta = 100\sqrt{\sum_{i=1}^{n} c_i (1 - r_i/\bar{r})^2} \,, \qquad (4.4)$$

$$\Omega = \frac{T_m \Delta S_{mix}}{|\Delta H_{mix}|} \,, \qquad (4.5)$$

$$VEC = \sum_i c_i VEC_i \,, \qquad (4.6)$$

$$FBI = \sum_i c_i \varphi_i \,, \qquad (4.7)$$

$$e/a = \sum_{i=1}^{N} c_i (e/a)_i \,, \qquad (4.8)$$

$$\Delta\chi = \sqrt{\sum_{i=1}^{N} c_i (\chi_i - \bar{\chi})^2} \,, \qquad (4.9)$$

where c_i, $(T_m)_i$, r_i, VEC_i, $(e/a)_i$, χ_i, $\bar{r}(=\sum_{i=1}^{n} c_i\, r_i)$, $\bar{\chi}(=\sum_{i=1}^{n} c_i\, \chi_i)$ are the mole fraction, melting temperature, atomic radius, valence electron concentration, number of itinerant electrons, electronegativity of element i, average atomic radius, average electronegativity of an alloy. N is the number of elements in an alloy system, and *R* is the gas constant. $\Omega_{ij}(= 4\Delta H_{mix}^{AB})$ is the regular solution interaction parameter between elements i and j [141], and ΔH_{mix}^{AB} is the mixing enthalpy of A-B binary liquid alloys whose values can be found in Refs. [142,143]. φ_i is +1 for element i with either the FCC or HCP crystal structure, and φ_i is -1 for elements i with the BCC crystal structure. The crystal structure, atomic radius, melting

temperature, VEC, φ, e/a, and electronegativity of Al, Cr, Mn, Fe, Co, Ni, Cu in **Table 4.2** are used to calculate the nine parameters listed above for HEAs.

Table 4.2 Summary of crystal structure, atomic radius r, T_m, VEC, **φ**, e/a, χ of each element involved in this study (Data from Ref. [140]).

Element	Structure	*r* (Å)	T_m (K)	VEC	φ	*e/a*	χ
Al	FCC	1.4317	933	3	1	3	1.61
Cr	BCC	1.2491	2180	6	-1	1	1.66
Mn	Cubic	1.3500	1519	7	±0	2	1.55
Fe	BCC	1.2412	1811	8	-1	2	1.83
Co	HCP	1.2510	1768	9	1	2	1.88
Ni	FCC	1.2459	1728	10	1	2	1.91
Cu	FCC	1.2780	1358	11	1	1	1.90

4.2.3 Machine learning

With these nine parameters as input features, four supervised ML algorithms, decision tree (DT), k-nearest neighbor (KNN), support vector machine (SVM), and artificial neural network (ANN), were employed to predict the phase formation of the HEAs [32,144–147]. These four algorithms are implemented using the scikit-learn package, a machine learning library in Python [148]. Each algorithm has different hyperparameters that are used to adjust the training model. Five-fold cross-validation (CV) was employed to evaluate the performance of predictions, which can reduce overfitting and underfitting issues in ML. The dataset is split

randomly into five disjoint subsets of nearly the same size. The models were trained with 4 subsets and tested 5 times with the remaining subset. The 5-fold CV accuracy is the average of the 5 test accuracies and is referred as the CV accuracy for simplicity.

Each machine learning model has unique hyperparameters to tune in order to get higher training accuracy during the model training process. However, it can easily lead to overfitting or underfitting (test accuracy is low) if training accuracy is too high or too low. Therefore, it is necessary to control the hyperparameters to obtain the best prediction results. The DT model employs the best splitting strategies at each child node in a binary tree. Minimum number of samples at a node and maximal depth of a tree are tuned to regularize the size of constructed trees. KNN utilizes a voting mechanism by k nearest neighbors. Thus, number of nearest neighbors is the hyperparameter to be adjusted for KNN model in the training process. SVM aims to find meaningful hyperplanes to classify the data, and the hyperplanes can be controlled by the regularization parameter γ, and penalty parameter C. ANN simulates the decision-making process of the human mind by constructing artificial neurons in the model, and the number of neurons in each hidden layer are used to adjust the model performance.

Since the effects of the initial eight input features on phase prediction are likely very different, it is valuable to perform a systematic screening of the features and find those that are more critical phase selection criteria. The forward selection is applied with a three-step procedure for each model [118,149–151]. The first step is training these features separately and creating an initial empty feature pool. The feature with the highest CV accuracy is added to the initial pool of features. The second step is finding the next feature that increases the CV accuracy most from the remaining features. And then adding this feature to the previous feature pool until all the features are sorted by their feature importance and stored in the feature pool. Therefore, a pool of

features is ranked by their importance to ML models in datasets. The last step is selecting a cutoff point from the ordered optimal pool for each ML model, where the increase in the CV accuracy by adding a new feature to the pool becomes smaller than the standard deviation of the CV accuracy.

4.3 Calculation results and discussion

4.3.1 CALPHAD results

4.3.1.1 Comparison between experimental data and CALPHAD predictions

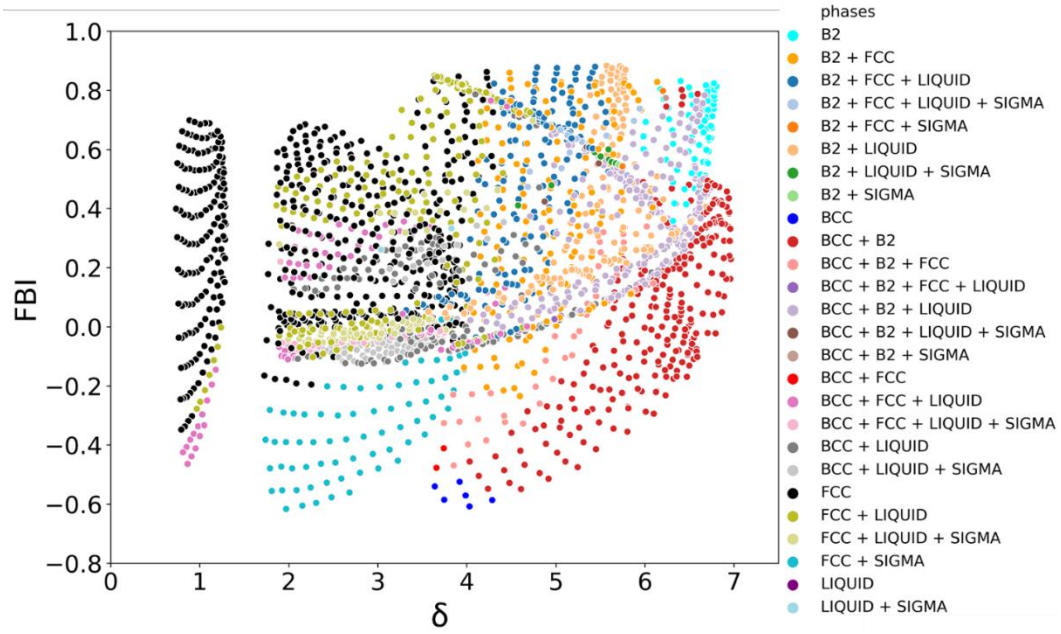

Figure 4.1 The CALPHAD calculations of 2436 alloys under unconstrained conditions.

We first performed unconstrained high-throughput thermodynamic calculations of the equilibrium phases at the experimental temperature (1100 °C) for the 2,436 HEAs using the

Thermo-Calc software and its associated TCHEA4 thermodynamic database, and the calculations are presented **Fig. 4.1 and 4.2**. The results are very different from the experimental observations reported by Kube et al., including the formation of IMs in far more alloys than experimental observations as well as the formation of liquid in a large number of alloys. Since the liquid phase was not observed during the experimental co-sputtering process of the combinatorial films, it is thus excluded in subsequent thermodynamic calculations in this study. The experimental IM consists of Sigma and other possible unidentified phases, making it hard to compare with thermodynamic calculations. We performed constrained calculations for the 233 alloys with the IM phase from experiments after excluding the liquid phase; 146 SS and 87 Sigma + SS alloys were predicted, which deviates significantly from the experimental observations, as shown in **Fig. 4.3(a)** and **4.3(b)**. The prediction of the IM formation is also beyond the capabilities of the current TCHEA4 database, similar to the situation in Ni-based superalloys [152]. Thus, IMs are also excluded in further calculations, and we focused on calculating and analyzing the phase formation of the SS alloys.

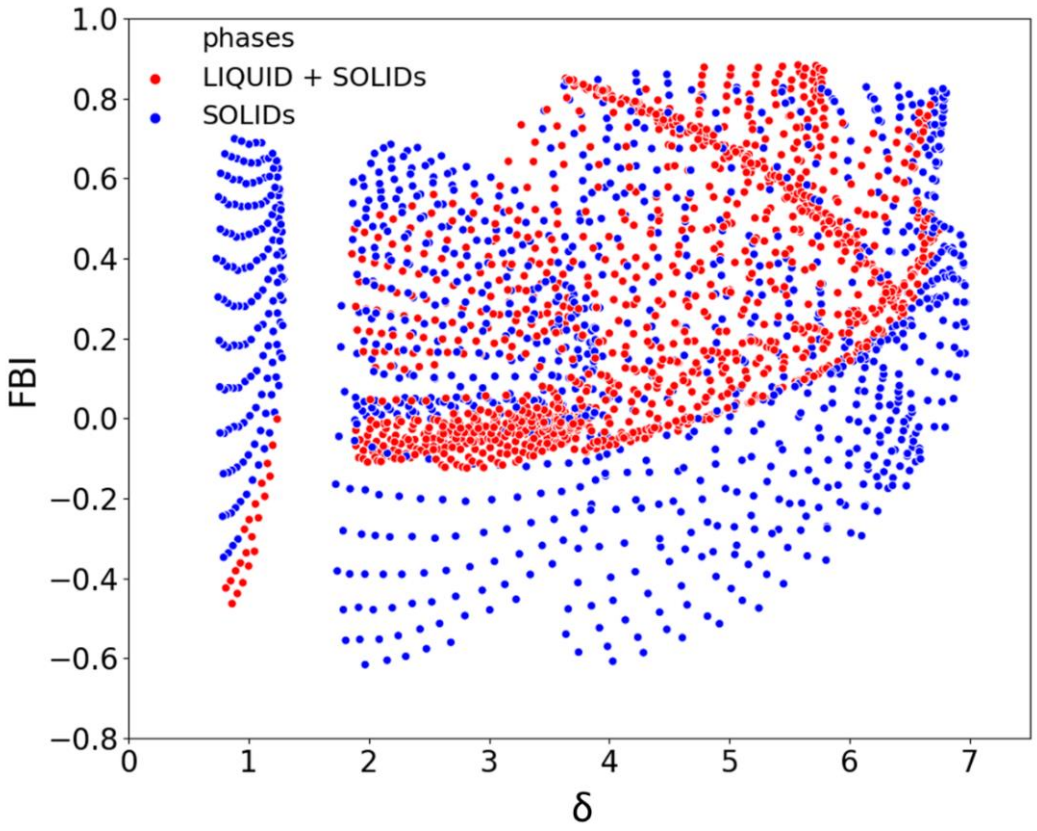

Figure 4.2 The CALPHAD calculations of 2436 alloys under unconstrained conditions, the phases are divided into two categories, one is SOLIDs (1294 alloys, solid phases without liquid), and another is LIQUID + SOLIDs (1142 alloys).

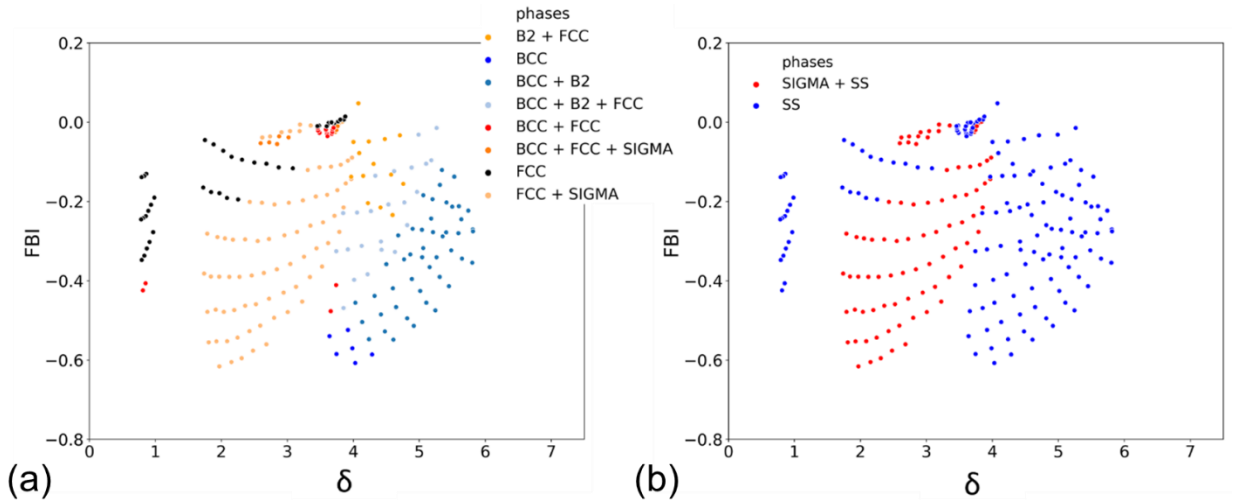

Figure 4.3 The CALPHAD calculations of 233 alloys under constrained conditions (excluding liquid) are presented in (a) and (b). The phases are divided into two categories, one is SS (solid solutions) (146 alloys) in (a), and another is SIGMA+SS (87 alloys) in (b).

Calculations using the TCHEA4 database predicted far more alloys with the B2 phase and B2 associated two-phase cases (B2+FCC and BCC+B2) as well as the BCC+B2+FCC three-phase cases than the experimental observations, as shown in **Fig. 4.4(a)**. Far few single-phase BCC alloys were predicted at the expense of forming the B2 phase for most of the experimental compositions. The TCHEA4 database calculations predicted the number of single-phase FCC alloys close to experimental observations, but the overall consistency with experimental observations (including all the matched predictions of BCC, B2, BCC+FCC, and B2+FCC phases) is only 28.2%. When the single-phase B2 and single-phase BCC phases are regarded as one BCC-based single phase (BCC/B2), the agreement between the Thermo-Calc results and experimental observations is much better and reaches 61.4%, **Fig. 4.4(b)**, showing less single-phase BCC/B2 and single-phase FCC, and more BCC/B2 + FCC two-phase cases. It is very

likely that the Thermo-Calc database TCHEA4 does not have accurate enough thermodynamic parameters for the B2 phase whose Gibbs free energy is very close to the disordered BCC phase and thus hard to be modeled accurately, especially for multicomponent HEAs.

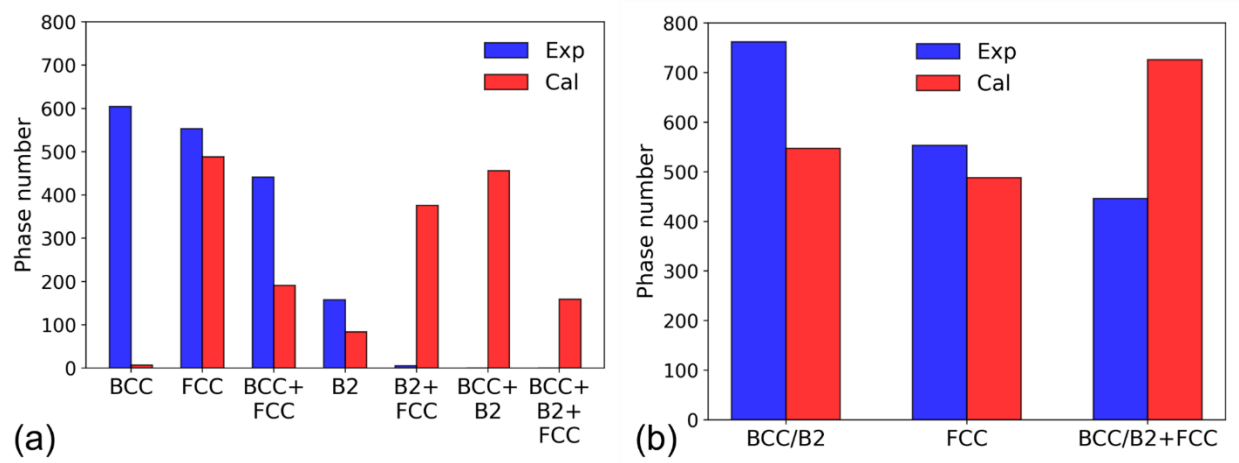

Figure 4.4 Bar graphs showing the total number of HEAs with different phases: (a) B2 and BCC are treated as separate phases in CALPHAD calculations, and (b) B2 and BCC are treated as the same BCC-based phase (BCC/B2). The experimental data and CALPHAD predictions are presented in blue and red bars, respectively.

Since the CALPHAD thermodynamic databases are built from the thermodynamic parameters of the binary and ternary systems (and usually without quaternary assessments), it is necessary to go through all the pertinent binary systems to see how good the thermodynamic parameters of the B2 phase can reproduce the experimental binary phase diagrams and other measured quantities such as specific heat capacity if available. Re-assessments will be necessary if substantial discrepancies are observed between the computed and experimental results. If no thermodynamic parameters for the B2 phase are available in the literature for some binary

systems involving the BCC/B2 transition, it is necessary to perform assessments to obtain the thermodynamic parameters. Completion of all or most of the pertinent binary systems will substantially improve the overall database performance. It is very likely that experimental ternary phase diagrams are incomplete or not measured for some pertinent ternary systems. Completion of thermodynamic assessments of the ternary systems whose experimental data are available will be an important next step in improving the overall thermodynamic databases of multicomponent HEAs. Effective employment of first-principles data, if available, as well as ML results are also recommended, especially for the binary and ternary systems whose experimental data are still missing or incomplete.

The major factor leading to the disparity between the CALPHAD predictions (representing the phases of bulk alloys) and the experimental data from the sputtered (thick) film compositions is very likely the poorly assessed thermodynamic parameters for the B2 phase in the TCHEA4 database, as explained above. Some non-equilibrium nature of the sputtering process may also contribute to this disparity. One can see from **Fig. 4.4(a)** that far more B2 cases were predicted from CALPHAD than experimental observations, suggesting the possibility of a sluggish BCC → B2 transition to reach thermodynamic equilibrium. A thermo-kinetic model with kinetic coefficients appropriate for the sputtering process would need to be established to evaluate the BCC → B2 transformation kinetics. Such a model may be a topic of a future study and is beyond the scope of the current study.

Fig. 4.5 compares the experimental observations in the left column (a) with the CALPHAD results in the middle column (b) by plotting the number of alloys in each category against VEC, showing again a higher number of the computed BCC/B2 + FCC two-phase alloys than experimental observations. The difference is also compared in **Fig. 4.5(c)**, the right column,

where one can see that quite a number of the single-phase BCC/B2 alloys observed in experiments show up as the BCC/B2 + FCC two-phase alloys – the red part of the bottom panel of **Fig. 4.5(c)**. The red part of the top panel of **Fig. 4.5(c)** represents alloys that were observed as single-phase FCC experimentally but showed up as two-phase BCC/B2 + FCC in CALPHAD calculations. As represented by the blue part of the middle panel of **Fig. 4.5(c)** of the experimentally observed 2-phase (BCC/B2 + FCC) alloys, only a few alloys were computed as single-phase BCC/B2. Similarly, the green part of the middle panel in **Fig. 4.5(c)** represents the experimentally observed 2-phase (BCC/B2 + FCC) alloys which were predicted to be single-phase FCC.

Fig. 4.5 also shows a clear trend that alloys with higher VEC prefer FCC over BCC/B2 in both experimental observations and CALPHAD predictions. A previous study has found that the FCC and BCC phases tend to be stable at higher VEC (> 8) and lower VEC (< 6.87), respectively [108]. The rule of VEC < 6.87 for single-phase BCC/B2 formation holds well with respect to the 1,761 SS HEAs, as shown in **Fig. 4.5**. The VEC > 8 rule also holds well for the formation of single-phase FCC, but at 8 < VEC < 9.16, there are also substantial number of alloys with BCC/B2 + FCC two-phase structure. Only when VEC > 9.16, the single-phase FCC is formed with only a few exceptions in the CALPHAD predictions. At VEC < 6.87 and VEC > 9.16, the predicted phase formation is in good agreement with experimental observations, which illustrates the excellent ability of CALPHAD in calculating phase equilibrium of HEAs, especially for single-phase solid solution SPSS. Yang et al. found that more than 90% of the compositions have single-phase BCC structures at $5.7 \leq VEC \leq 7.2$, and the pure FCC structure at VEC > 8.4 in Al-Co-Cr-Fe-Ni system by high-throughput calculations using

CALPHAD [110]. The new rules revealed from this study and that of Kube et al. [135] should be more reliable due to the large number of experimental HEAs covering more elements.

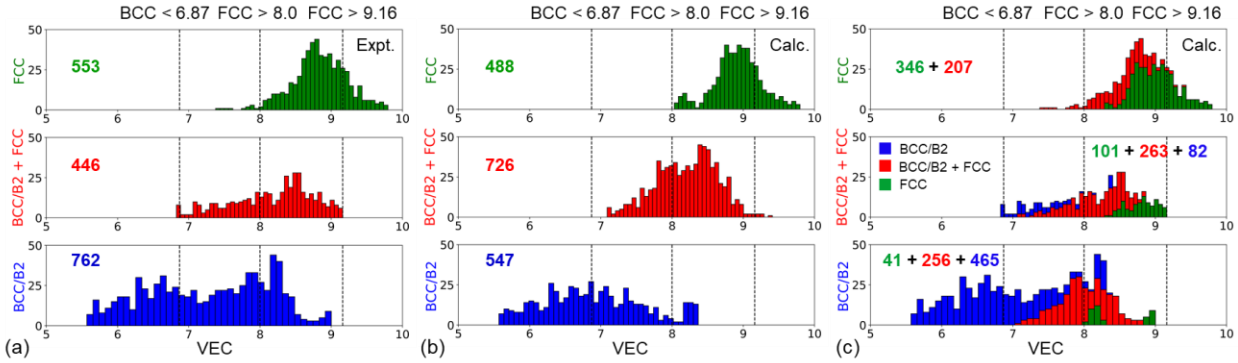

Figure 4.5 VEC histograms based on experimental data in (a) and CALPHAD results in (b). (c) is plotted to show how alloys with different phases vary from experimental observations to the CALPHAD predictions.

4.3.1.2. FBI, ΔH_{mix}, and δ selection rules for SS alloys

Two alloy examples of how to calculate ΔS_{mix}, T_m, ΔH_{mix}, and Ω are presented here.

Alloy 1: $Al_{18.1}Fe_{23.7}Co_{12.1}Ni_{16.3}Cu_{29.8}$

$$\Delta S_{mix} = -R\sum_{i=1}^{N} c_i ln c_i = -8.314 * [0.181 * ln(0.181) + 0.237 * ln(0.237) + 0.121 * ln(0.121) + 0.163 * ln(0.163) + 0.298 * ln(0.298)] = 12.991$$

$$T_m = \sum_{i=1}^{n} c_i (T_m)_i$$

$$= 0.181 * 933 + 0.237 * 1811 + 0.121 * 1768 + 0.163 * 1728 + 0.298 * 1358$$

$$= 1498.356$$

$$\Delta H_{mix} = \sum_{i=1, i\neq j}^{N} \Omega_{ij}\, c_i c_j \;=\; \sum_{i=1, i\neq j}^{N} 4\Delta \mathrm{H}_{mix}^{ij}\, c_i c_j$$

$$= 4 * \{\, 0.181 * [(-11 * 0.237) + (-19 * 0.121) + (-22 * 0.163) + (-1 * 0.298)]$$

$$+0.237 * [\,(-11 * 0.181) + (-1 * 0.121) + (-2 * 0.163) + (13 * 0.298)]$$

$$+0.121 * [(-19 * 0.181) + (-1 * 0.237) + (0 * 0.163) + (6 * 0.298)]$$

$$+0.163 * [(-22 * 0.181) + (-2 * 0.237) + (0 * 0.121) + (4 * 0.298)]$$

$$+0.298 * [(-1 * 0.181) + (13 * 0.237) + (6 * 0.121) + (4 * 0.163)]\,\}$$

$$= -2.945$$

$$\Omega = \frac{T_m \Delta S_{mix}}{|\Delta H_{mix}|} = \frac{1498.356\ K * 12.993\ J/K/mol}{|-2.945|\ kJ/mol} = 6.609$$

Alloy 2: $Al_{19.6}Cr_{20.6}Co_{11.3}Ni_{14.5}Cu_{34}$

$$\Delta S_{mix} = -R \sum_{i=1}^{N} c_i ln c_i = -8.315 * [0.196 * ln(0.196) + 0.206 * ln(0.206) + 0.113 *$$

$$ln(0.113) + 0.145 * ln(0.145) + 0.34 * ln(0.34)] = 12.787$$

$$T_m = \sum_{i=1}^{n} c_i (T_m)_i$$

$$= 0.196 * 933 + 0.206 * 2180 + 0.113 * 1768 + 0.145 * 1728 + 0.34 * 1358$$

$$= 1544.012$$

$$\Delta H_{mix} = \sum_{i=1, i\neq j}^{N} \Omega_{ij}\, c_i c_j \;=\; \sum_{i=1, i\neq j}^{N} 4\Delta \mathrm{H}_{mix}^{ij}\, c_i c_j$$

$$= 4 * \{\, 0.196 * [(-10 * 0.206) + (-19 * 0.113) + (-22 * 0.145) + (-1 * 0.34)]$$

$$+0.206 * [(-10 * 0.196) + (-4 * 0.113) + (-7 * 0.145) + (12 * 0.34)]$$

$$+0.113 * [(-19 * 0.196) + (-4 * 0.206) + (0 * 0.145) + (6 * 0.34)]$$

$$+0.145 * [(-22 * 0.196) + (-7 * 0.206) + (0 * 0.113) + (4 * 0.34)]$$

$$+0.34 * [(-1 * 0.196) + (12 * 0.206) + (6 * 0.113) + (4 * 0.145)] \}$$

$$= -4.404$$

$$\Omega = \frac{T_m \Delta S_{mix}}{|\Delta H_{mix}|} = \frac{1544.012\ K * 12.789\ J/K/mol}{|-4.404|\ kJ/mol} = 4.484$$

Representative 2D plots are shown in **Fig. 4.6** in which the left-hand side and right-hand side columns plot the experimental results and the CALPHAD results, respectively, for comparison. One can see from **Fig. 4.6(a)** and **(b)** that at $\delta < 5$ based on the experimental data and $\delta < 4$ based on the computed data, the FCC phase forms at higher FBI values, which is the direct consequence of the definition of FBI, **Eq. (4.7)**. For experimental data at $\delta > 6$, the FBI effect breaks down, and almost all alloys form single-phase BCC irrespective of the FBI values, showing the overwhelming effect of δ in dictating the formation of BCC when δ value is high. This phenomenon is also verified and is more evident in the CALPHAD calculations. Formation of BCC/B2 over FCC with increasing size difference δ was attributable to the lower packing density of BCC/B2 and higher ability to accommodate atoms with different sizes than FCC structure [135].

Guo and Liu [111] found that ΔH_{mix} and δ for the formation of SS should satisfy $-22 \leq \Delta H_{mix} \leq 7$ kJ/mol, $0 \leq \delta \leq 8.5$, and $11 \leq \Delta S_{mix} \leq 19.5$ simultaneously. Our study, covering far more alloy compositions than Guo and Liu, shows that the ΔH_{mix} range for the formation of FCC is similar to that of Guo and Liu, but it can be expanded from –33.6kJ/mole to 17.5 kJ/mol for forming single-phase BCC/B2, **Fig. 4.6(c)** and **(d)**. Single-phase BCC can form at a negative ΔH_{mix} and larger δ values, which agrees with the work of Raghaven et al. [153] and Agarwal and Rao [126]. Our results also agree with the observation of Agarwal and Rao that BCC can

coexist with FCC at a lower δ and FCC preferentially forms at a negative ΔH_{mix} while BCC prefers to form at a positive ΔH_{mix}. The CALPHAD results show similar trend but more pronounced separations of the phase formation regions, **Fig. 4.6(d)**. These phase selection rules are useful for predicting alloy crystal structures and compositions, but more effective rules are still highly desired; thus, we will subsequently explore the capabilities of ML in improving the phase predictions.

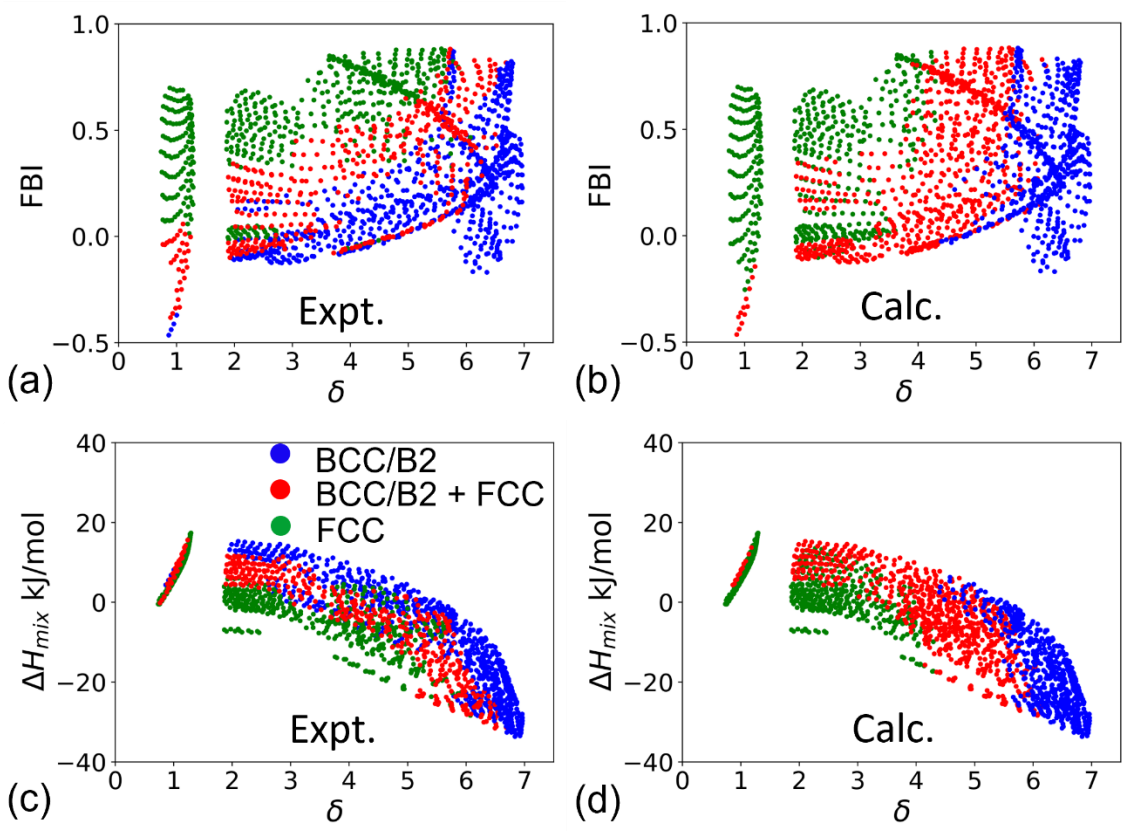

Figure 4.6 FBI and ΔH_{mix} versus δ plot based on experimental data in (a) and (c); as well as CALPHAD predictions in (b) and (d).

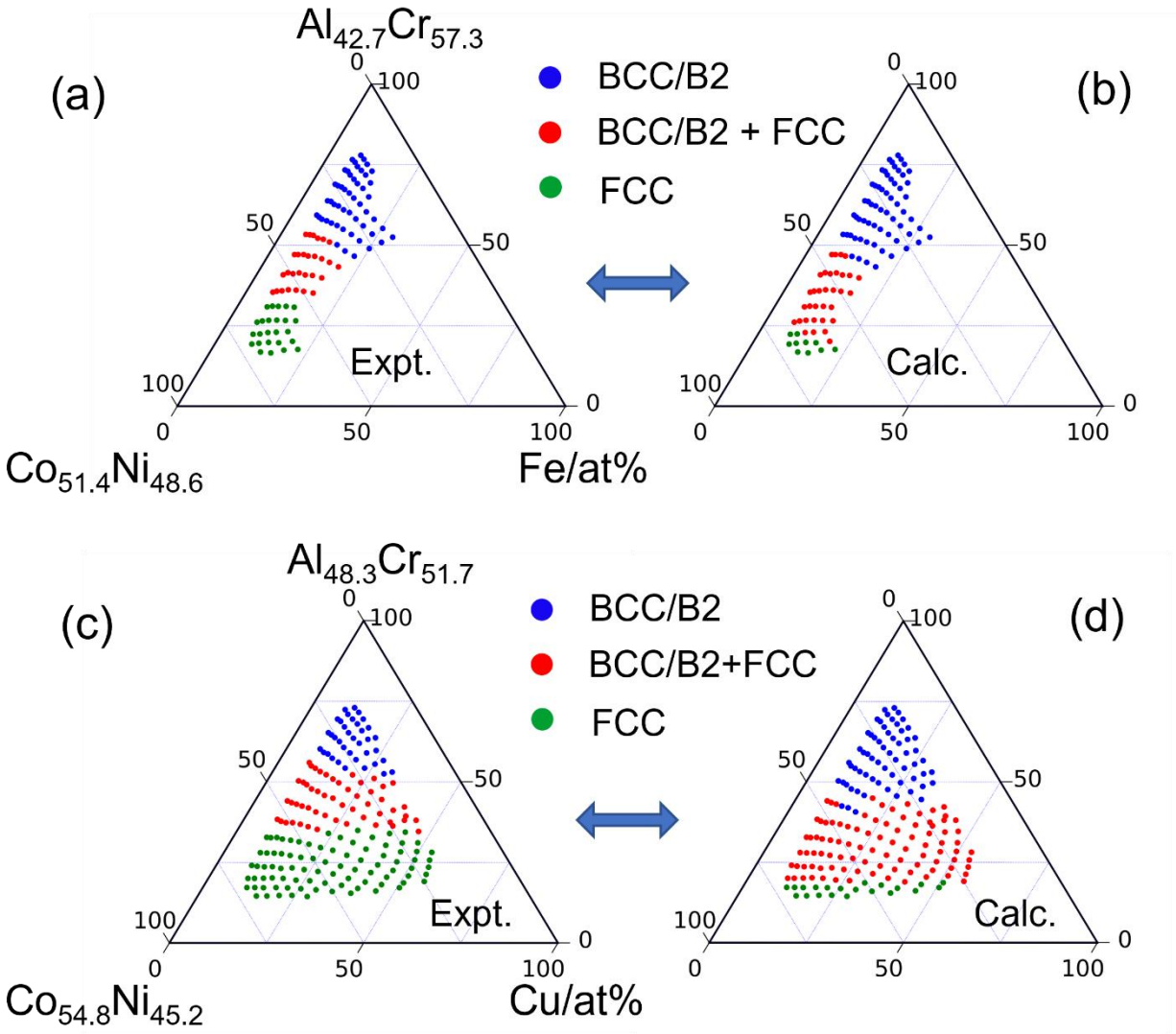

Figure 4.7 Comparison of phase formation between experimental and computational (CALPHAD) results in the pseudo-ternary Fe – $Co_{51.4}Ni_{48.6}$ – $Al_{42.7}Cr_{57.3}$ system shown in (a) and (b) as well as the pseudo-ternary Cu – $Co_{54.8}Ni_{45.2}$ – $Al_{48.3}Cr_{51.7}$ system in (c) and (d).

4.3.1.3 Examples of phase formation in specific systems

Different HEA libraries cover different regions of the multicomponent HEA composition space. The agreements between experimental and computational results can be very different.

Two examples are shown in **Fig. 4.7** to illustrate the degree of agreements for both the Al-Cr-Co-Ni-Fe and Al-Cr-Co-Ni-Cu systems. **Fig. 4.7(a)** and **(b)** show that for the compositions covered by a pseudo-ternary Fe – $Co_{51.4}Ni_{48.6}$ – $Al_{42.7}Cr_{57.3}$ system, the agreement is good except for a smaller single-phase FCC region and slightly larger BCC/B2 + FCC two-phase region from CALPHAD. A more pronounced difference was observed in **Fig. 4.7(c)** and **(d)** for the compositions covered by the pseudo-ternary Cu – $Co_{54.8}Ni_{45.2}$ – $Al_{48.3}Cr_{51.7}$ system. Such comparisons may also help identify the specific systems where CALPHAD assessments need improvement.

4.3.2 Machine learning results

Two groups of datasets are analyzed using ML, and one is the SS only dataset with 1,761 HEAs, the other is the full dataset with 2,436 HEAs. Similar to the analysis using CALPHAD, the SS is divided into three categories, BCC/B2, BCC/B2 + FCC, FCC, which are the targets of the ML models. The predictions from ML in the SS dataset are further compared with the experimental observations. The full dataset is classified into four classes, SS, AM, SS + AM, and IM as the output of the ML models. It is noted that IM is used here to refer to alloys with an intermetallic compound (mostly the σ phase) identified from XRD and some alloys contain additional phases in addition to IM. The ML models are optimized by adjusting their parameters first. Then the best feature sets are screened by their contributions towards improving the CV accuracy of predictions for each ML model, which provides information for the relative importance among these input features.

4.3.2.1 ML for classifying BCC/B2, BCC/B2 + FCC, FCC phases

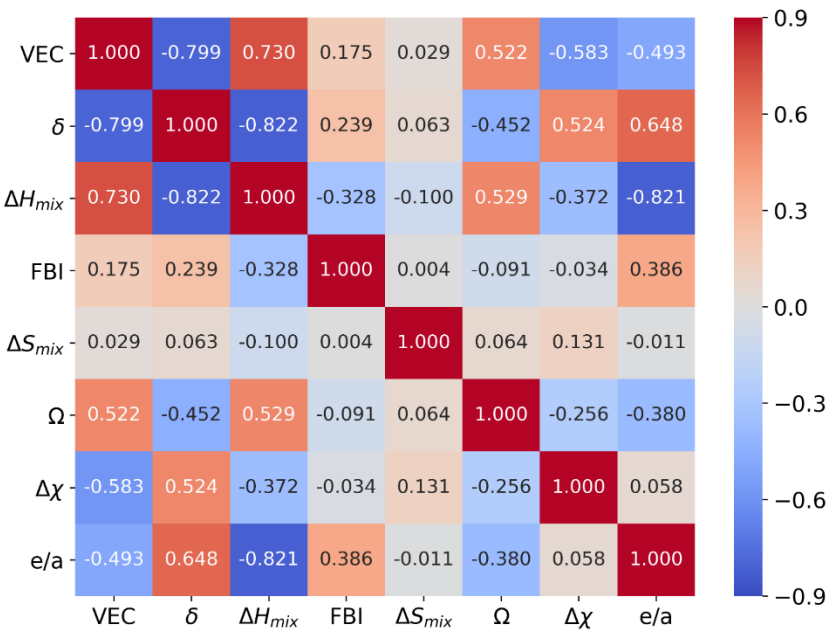

Figure 4.8 The heat-map of the correlation matrix between any pair of features. The value at each cell is the calculated coefficient.

Before training the ML model and making predictions, it is essential to look into the correlation among these features because adding collinear features will not provide more valuable information and will increase the time of training and could even degrade the performance of the models. The Pearson correlation coefficient is used for the quantitative assessment of the correlation between any pair of features, and it is calculated with the following formula,

$$r_{xy} = \frac{\sum_{i=1}^{n}(x_i - \overline{x})(y_i - \overline{y})}{\sqrt{\sum_{i=1}^{n}(x_i - \bar{x})^2}\sqrt{\sum_{i=1}^{n}(y_i - \bar{y})^2}}$$

where x, y are the two variables/features, x_i and y_i are the x and y values of ith sample, $\bar{x}$ and $\bar{y}$ are the mean values of x and y, and n is the sample size of both x and y [154]. Using this formula, the correlation between any pair of features is shown in **Fig. 4.8**, indicating that all input features can be kept and further used in the ML models since there is no high correlation coefficient between any two features.

The ML models can be modified by tuning parameters and then judged by the CV accuracy. Here, the grid search method was employed to adjust parameters for each model with all the nine features, and the optimized results are shown in **Fig. 4.9**. The max_depth parameter is identified as the main factor in determining the quality of the DT model, and the min_samples_leaf parameter has negligible effect, **Fig. 4.9(a)**. The CV accuracy of the DT model reaches the highest when max_depth is 9 and stays stable after 9; thus min_samples_leaf = 3 and max_depth = 9 were selected for the final DT model. The parameter n_neighbors = 3 is best for the KNN model in **Fig. 4.9(b)**. For SVM, a parameter set of $\gamma = 10^p$ and $C = 2^q$ is created, where $-6 \leq p \leq 4$ and $1 \leq q \leq 10$. Both γ and C affect the accuracy of the SVM model, and both cannot be too large or too small; otherwise, they would lead to inefficiency. The pair of γ = 1 and C = 32 (p = 0, q = 5) achieved a high CV accuracy from the parameter sets, **Fig. 4.9(c)**. The neural network was built with three hidden layers that contain n_1, n_2, n_3 neurons in each hidden layer, and the corresponding CV result is shown in **Fig. 4.9(d)**. For each third hidden layer with neurons changing from 5 to 50 (interval 5), the combination of three layers' neurons with the highest CV accuracy is marked as the black dot, so there are 10 highest CV accuracies shown in 10 black dots. Finally, the combination n_1 = 45, n_2 = 25, n_3 = 20 is chosen from these 10 CV accuracies.

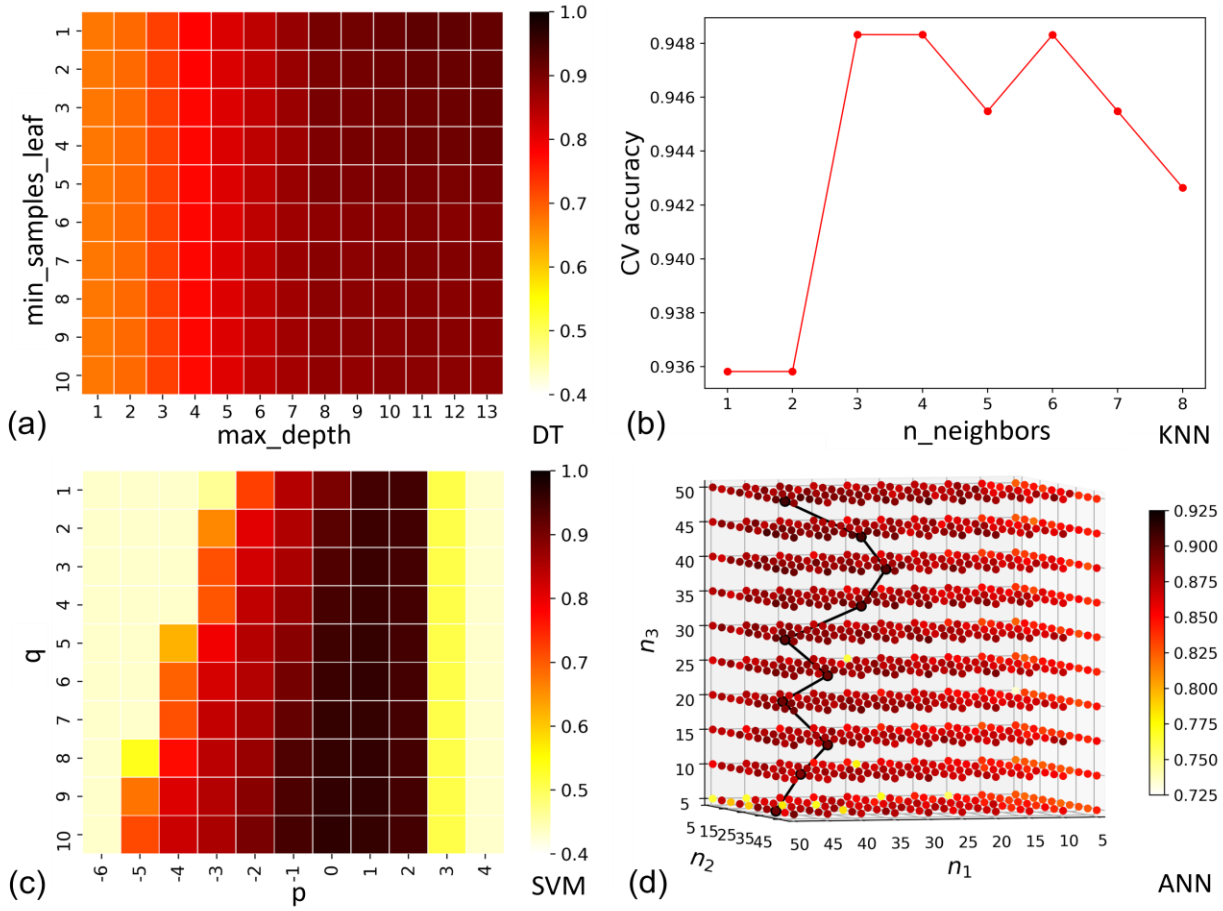

Figure 4.9 The grid search method for tuning input hyperparameters to obtain the high CV accuracy in each ML model: (a) DT, (b) KNN, (c) SVM, (d) ANN, respectively.

The results of feature selections for the four ML models are shown in **Fig. 4.10**. The CV accuracy increases first rapidly, then stays stable or decreases when more input features are employed for the ML models, **Fig. 4.10(a)**, indicating that more features are not always helpful in ML because they could lead to overfitting in the training process and decreasing CV accuracy. The order of precedence of the features in each ML model are shown in **Fig. 4.10(b)**, and the best feature sets for different ML models are colored for easier visualization. The {VEC, ΔH_{mix},

e/a, FBI} set is the best feature combination for DT, KNN, and ANN, achieving a CV accuracy of 90.4%, 94.1%, and 89.7%, respectively. For the SVM model, the prediction accuracy reaches 93.8% with the best feature set of {VEC, ΔH_{mix}, e/a, FBI, $\Delta\chi$ }. In all four feature sets, the VEC feature has the highest order of precedence, thus is the most influential among these nine features in determining SS formation. It is noted that the CV accuracy obtained by using only the VEC feature is comparable to or even better than the prediction accuracy from CALPHAD; and the CV accuracy is higher than 85% after training with the first three best features in each ML model, showing advantages of phase predictions over the current state of thermodynamic calculations. The other features that are helpful for enhancing the prediction accuracies are ΔH_{mix}, e/a, and FBI. In the DT, KNN, and ANN models, the two features that could degrade the performance of predictions are $\{\Delta S_{mix}, \Delta\chi\}$, $\{\Delta\chi, \Delta S_{mix}\}$, and {$T_m$, δ}, respectively. Li and Guo also found that VEC is the most important feature in classifying BCC, FCC, and NSP (not forming SPSS) with the SVM model, and the CV accuracy reaches 90.7% under the input of {VEC, δ, T_m, ΔH_{mix}, ΔS_{mix}} feature set [149]. A study by Zeng et al. explored >300,000 phase equilibria generated by CALPHAD calculations in 3 classes (single-phase FCC, single-phase BCC, and other phases) using XGBoost [131]. They achieved > 99% accuracy on both the training set and the test set and predicted 155 experimental phases with 81% accuracy through the selection of 5 most important features {equilibrium temperature, average atomic radius, VEC difference, VEC, $\Delta\chi$}. A feature set of 13 top-ranked features was screened in classifying BCC, FCC, and BCC + FCC by Machaka, and VEC was found to have the highest relative importance [132]. His models can reach 97.5%, 95.8%, 94.35%, and 94.0% using random forest (RF), SVM, KNN, and ANN, which is slightly higher than the current study, possibly due to the larger set of features used in his study. Zhang et al. utilized a genetic algorithm with ANN and

also found that the VEC criterion is important in classifying BCC, FCC, and dual-phase HEAs [151]. Their classification accuracy achieved 91.3% with a feature set containing VEC, the core electron distance, Δχ, the mismatch in compression modulus. Their CV accuracy is comparable to ours in ANN learning. Overall, the accuracy could reach higher than 89% for these four models, making the application of ML in phase prediction significant.

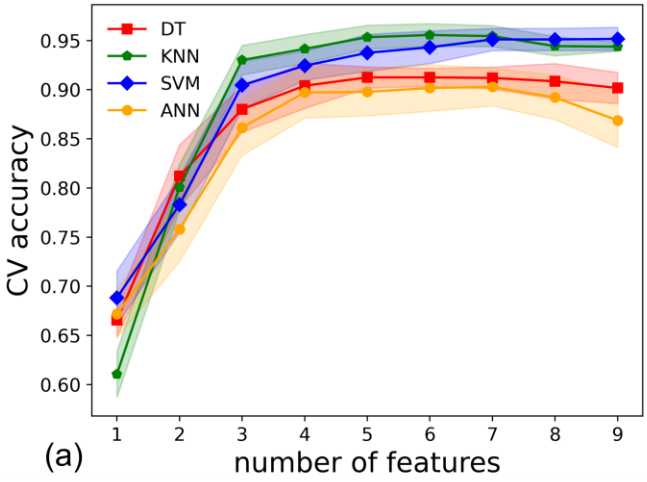

DT	KNN	SVM	ANN
VEC	VEC	VEC	VEC
ΔH_{mix}	ΔH_{mix}	ΔH_{mix}	ΔH_{mix}
e/a	e/a	e/a	e/a
FBI	FBI	FBI	FBI
T_m	δ	Δχ	Ω
δ	T_m	ΔS_{mix}	Δχ
Ω	Ω	T_m	ΔS_{mix}
ΔS_{mix}	Δχ	Ω	T_m
Δχ	ΔS_{mix}	δ	δ

Figure 4.10 (a) Feature selection process to increase the CV accuracy in each ML model for classifying the BCC/B2, BCC/B2 + FCC, FCC phases of the solid-solution only compositions. (b) Corresponding features based on the order of precedence from top to bottom after each selection step. The colored features are the best sets that achieve the performance of the ML models.

Since ML has found both VEC and ΔH_{mix} as the two most significant features to predict the SS phases, VEC-vs-ΔH_{mix} plots are made based on experimental results in **Fig. 4.11(a)** and SVM ML predictions in **Fig. 4.11(b)**. All alloys with BCC/B2 + FCC two phases are located in the middle region shaded in red in **Fig. 4.11(a)**. Towards the left side of this region is single-

phase BCC/B2 and single-phase FCC is on the right side. By counting the correct phases predicted by this division strategy, the accuracy is 67.1% in **Fig. 4.11(a)**, which is much more efficient than relying on the VEC only (VEC < 6.87 for BCC/B2 and VEC > 9.16 for FCC). The colored areas in **Fig. 4.11(b)** are the predicted phases by SVM, and the boundaries for

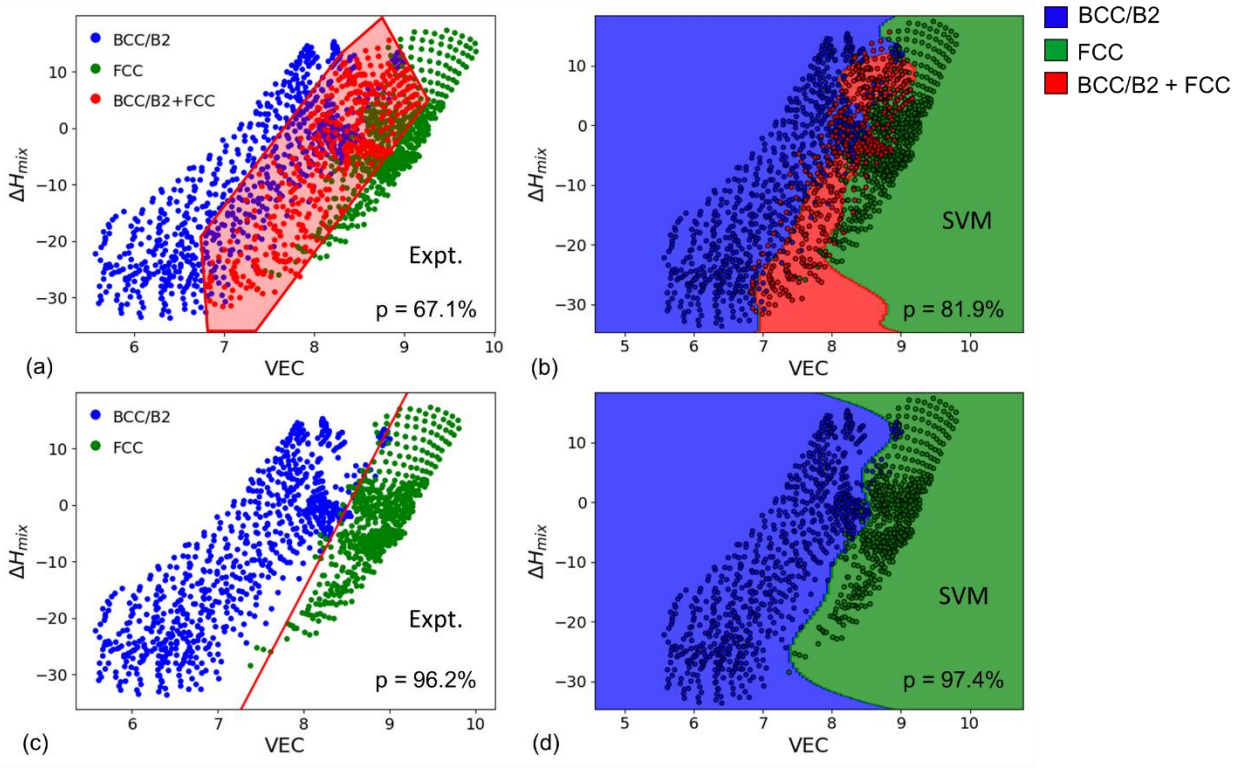

Figure 4.11 VEC vs ΔH_{mix} plots for the SS data in (a) and (b), and the SPSS data in (c) and (d), respectively. The experimental data are plotted in circle points and predictions by SVM are plotted as colored areas in (b) and (d), where the blue, red, and green area manifests predicted BCC/B2, BCC/B2 + FCC, and FCC phases, respectively. The p value refers to the prediction accuracy in (a) and (c), and the CV accuracy in (b) and (d).

classification are curves rather than straight lines. When experimental data points are in the area with the same color, then the predictions for phases agree with experiments (Note some of the red color points are outside the red region). The CV accuracy achieves 81.9% by SVM based on VEC and ΔH_{mix}, exhibiting the advantages of ML in predicting the correct phases over traditional strategies. We also used the ML models to study the classification for BCC, B2, FCC, BCC + FCC, and B2 + FCC phases (having B2 and BCC separately) and found that VEC is still the most important feature in every ML model as shown in **Fig. 4.12**.

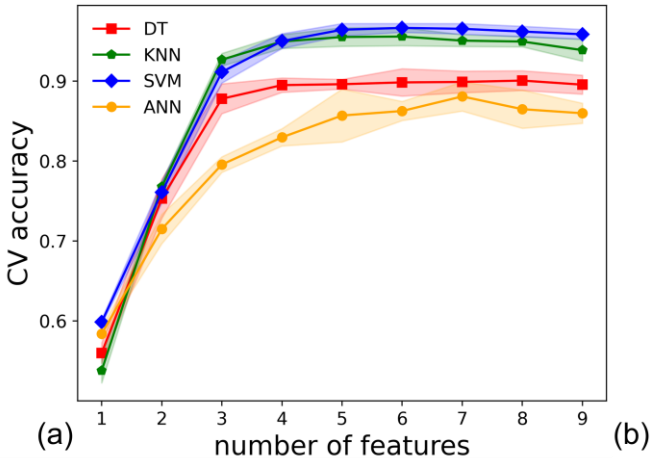

(b)

DT	KNN	SVM	ANN
VEC	VEC	VEC	VEC
FBI	T_m	ΔH_{mix}	FBI
T_m	FBI	e/a	T_m
Ω	e/a	T_m	ΔH_{mix}
e/a	Δχ	Δχ	e/a
Δχ	Ω	FBI	ΔS_{mix}
ΔS_{mix}	ΔH_{mix}	Ω	Δχ
ΔH_{mix}	δ	δ	Ω
δ	ΔS_{mix}	ΔS_{mix}	δ

Figure 4.12 Feature selection process measured by the CV accuracy in each ML model for predicting BCC, B2, FCC, BCC+FCC, and B2+FCC.

The VEC-vs-ΔH_{mix} plots are far more accurate in predicting the single-phase BCC/B2 and single-phase FCC solid solutions without considering the BCC/B2 + FCC two-phase alloys, as shown in **Fig. 4.11(c)** and **(d)**. Even a simple plot of experimental data only, a simple straight line of $\Delta H_{mix} = 29 \times VEC - 247$ can achieve 96.2% accuracy, which is simply remarkable, **Fig. 4.11(c)**. The CV accuracy of 96.4%, 97.0%, 97.4%, and 96.5% achieved for DT, KNN, SVM, and ANN, respectively, is not significantly better than the predicted results determined by

the straight line, and **Fig. 4.11(d)** shows the SVM results only. Even though the simple plot of experimental data, **Fig. 4.11(c)**, achieves excellent abilities to predict the single-phase formation, it is ML that helps identify these two critical parameters (VEC and ΔH_{mix}) for the plot.

With these well-trained models, we applied them to predict the selected alloy systems (containing 13 elements) that were tested in the study of Zeng et al. [131]. Compositions, experimentally determined phases, ML-predicted phases, and CALPHAD-predicted phases are shown in **Table 4.3**. ANN beats other ML models with the highest overall prediction accuracy 80.3%, demonstrating the feasibility of using trained ANN with thin film data to predict the phase formation of bulk alloys. The CALPHAD prediction accuracy is 78.8% without a constrained limit and 86.4% with constrained input of only BCC and FCC phases. The prediction accuracy of ANN lies in between the two CALPHAD predictions, exhibiting a comparable prediction ability of ANN with CALPHAD. There exists an apparent advantage of using ANN over CALPHAD in predicting the phase equilibria of bulk alloys whose elements are not available in the TCHEA4 or other HEA CALPHAD database.

Table 4.3 The compositions and experimentally determined phases with single BCC/B2 or BCC/B2 + FCC or single FCC phases [131]. The predictions from four ML models are also listed. CALPHAD1 is the CALPHAD calculations under unconstrained conditions and CALPHAD2 is the CALPHAD calculations under constrained input of only BCC, FCC phases. The number 1, 2 and 3 stands for BCC/B2, BCC/B2 + FCC, FCC, respectively. The number 0 in CALPHAD1 column indicates that there are other phases beyond SS in the predictions.

Alloys	**Phases**	**DT**	**KNN**	**SVM**	**ANN**	**CALPHAD1**	**CALPHAD2**
$Al_{0.25}CoCrFeNi$	2	3	1	2	2	2	2
$Al_{0.375}CoCrFeNi$	3	3	1	2	2	3	3

$Al_{0.5}CoCrFeNi$	3	3	1	3	2	3	3
$Al_{0.75}CoCrFeNi$	3	3	1	3	3	3	3
$Al_{0.875}CoCrFeNi$	3	2	3	3	3	3	3
$Al_{1.0}CoCrFeNi$	3	2	1	3	3	3	3
$Al_{1.25}CoCrFeNi$	1	1	1	3	3	1	1
$Al_{1.5}CoCrFeNi$	1	1	1	1	1	1	1
$Al_{2.0}CoCrFeNi$	1	1	1	1	1	1	1
$Al_{0.7}Co_{0.3}CrFeNi$	3	3	3	3	3	3	3
$Al_{0.3}CoCrFeNi$	2	3	1	2	2	3	3
$Al_{0.7}CoCrFeNi$	3	3	1	3	3	3	3
$Al_{0.9}CoCrFeNi$	3	2	1	3	3	3	3
$Al_{0.7}CoCrFeNi_{1.3}$	1	3	1	3	3	3	3
$Al_{0.6}CoCrFeNi$	3	3	1	3	3	3	3
CrFeCoNi	2	2	3	2	2	2	2
$Al_{0.3}CoCrCu_{0.3}FeNi$	2	3	1	3	2	0	3
AlCoCrFeNi	3	2	1	3	3	0	1
$Al_{0.3}CoCrFeNi$	2	3	1	2	2	2	2
$AlCo_{0.25}Cu_{0.25}Fe_{0.25}Ni_{0.25}$	1	1	1	1	1	1	1
AlTiCrMo	1	1	1	1	1	1	1
$Co_{0.2}Cr_{0.1}Fe_{0.6}Ni_{0.1}$	2	1	3	1	2	2	2
$Co_{0.2}Cr_{0.2}Fe_{0.5}Ni_{0.1}$	2	1	1	2	2	2	2
$Co_{0.2}Cr_{0.3}Fe_{0.4}Ni_{0.1}$	3	3	1	2	2	0	2
$Co_{0.2}Cr_{0.3}Fe_{0.1}Ni_{0.4}$	2	2	2	2	2	2	2
$Co_{0.2}Cr_{0.2}Fe_{0.1}Ni_{0.5}$	2	2	2	2	2	2	2
$Co_{0.2}Cr_{0.1}Fe_{0.1}Ni_{0.6}$	2	2	2	2	2	2	2
$Co_{0.2}Cr_{0.1}Fe_{0.5}Ni_{0.2}$	2	3	3	2	2	2	2
$Co_{0.2}Cr_{0.2}Fe_{0.4}Ni_{0.2}$	2	2	3	2	2	2	2
$Co_{0.2}Cr_{0.3}Fe_{0.3}Ni_{0.2}$	2	3	1	2	2	2	2
$Al_{0.5}CoCrFeMo_{0.3}Ni$	2	3	1	3	3	0	3
$Al_{0.5}CoCrFeMo_{0.4}Ni$	2	3	1	3	3	0	3
$Al_{0.5}CoCrFeMo_{0.5}Ni$	2	3	1	3	3	0	3
NbTiVZr	1	1	1	1	1	1	1
$Co_{0.1}Cr_{0.225}Fe_{0.225}Mn_{0.225}Ni_{0.225}$	2	3	1	3	2	0	2

$Co_{0.2}Cr_{0.2}Fe_{0.2}Mn_{0.2}Ni_{0.2}$	2	3	1	3	2	2	2
$Co_{0.3}Cr_{0.175}Fe_{0.175}Mn_{0.175}Ni_{0.175}$	2	3	1	3	2	2	2
$Co_{0.5}Cr_{0.125}Fe_{0.125}Mn_{0.125}Ni_{0.125}$	2	3	1	2	2	2	2
$Co_{0.25}Fe_{0.25}Mn_{0.25}Ni_{0.25}$	2	3	3	2	2	2	2
$Co_{0.238}Cr_{0.05}Fe_{0.238}Mn_{0.238}Ni_{0.238}$	2	3	1	2	2	2	2
$Co_{0.213}Cr_{0.15}Fe_{0.213}Mn_{0.213}Ni_{0.213}$	2	3	1	3	2	2	2
$Co_{0.188}Cr_{0.25}Fe_{0.188}Mn_{0.188}Ni_{0.188}$	2	3	1	3	2	2	2
$Co_{0.25}Cr_{0.25}Mn_{0.25}Ni_{0.25}$	2	3	1	2	2	2	2
$Co_{0.225}Cr_{0.225}Fe_{0.1}Mn_{0.225}Ni_{0.225}$	2	3	1	3	2	2	2
$Co_{0.175}Cr_{0.175}Fe_{0.3}Mn_{0.175}Ni_{0.175}$	2	3	1	3	2	2	2
$Co_{0.125}Cr_{0.125}Fe_{0.5}Mn_{0.125}Ni_{0.125}$	2	1	1	1	2	2	2
$Co_{0.225}Cr_{0.225}Fe_{0.225}Mn_{0.1}Ni_{0.225}$	2	3	1	3	2	2	2
$Co_{0.175}Cr_{0.175}Fe_{0.175}Mn_{0.3}Ni_{0.175}$	2	3	1	3	2	2	2
$Co_{0.125}Cr_{0.125}Fe_{0.125}Mn_{0.5}Ni_{0.125}$	2	1	1	1	3	2	2
$Co_{0.1}Cr_{0.1}Fe_{0.1}Mn_{0.1}Ni_{0.6}$	2	2	2	2	2	2	2
$Co_{0.02}Cr_{0.02}Fe_{0.02}Mn_{0.02}Ni_{0.92}$	2	2	2	1	2	2	2
FeNiCoCrMn	2	3	1	3	2	2	2
FeNiCo	2	2	2	2	2	2	2
FeNiCr	2	3	1	2	2	2	2
FeNiMn	2	2	2	2	2	2	2
NiCoCr	2	2	2	2	2	2	2
NiCoMn	2	2	2	2	2	2	2
$AlCo_{0.5}Cr_{0.5}Fe_{0.5}MnNiV$	1	1	1	2	3	0	1
$AlCo_{0.5}Cr_{0.5}Fe_{0.5}MnNiV_{0.5}$	1	1	1	2	3	0	1
$Al_{0.3}CoCrFeNi$	2	3	1	2	2	0	3
$CoCr_{1.25}FeMn_{0.25}Ni$	2	3	1	2	2	0	2
$CoCr_{0.75}FeMn_{0.75}Ni$	2	3	1	3	2	0	2
$CoCrFe_{0.5}Mn_{0.5}Ni_{1.5}$	2	2	1	2	2	2	2
$Co_{1.5}Cr_{0.5}FeMn0.5Ni$	2	2	2	2	2	2	2
$Al_{1.17}CoCrFeNi$	1	3	1	3	3	1	1
VNbMoTa	1	1	1	1	1	1	1

4.3.2.2 ML for classification of SS, AM, SS + AM, and IM phases

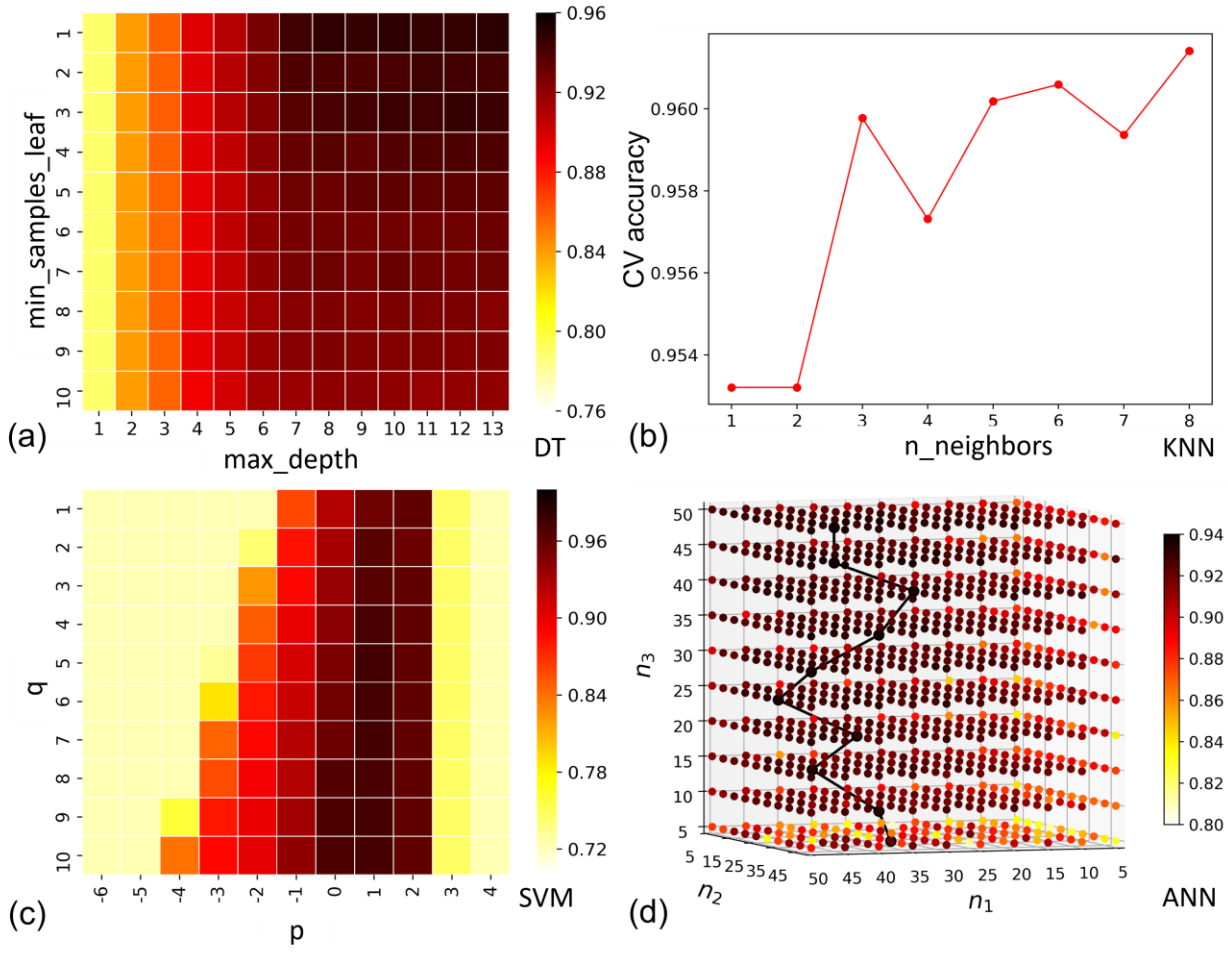

Figure 4.13 The grid search method for tuning input parameters to obtain the high CV accuracy in each ML model: (a) DT, (b) KNN, (c) SVM, (d) ANN, respectively. The targets of these models are SS, AM, SS+AM, and IM.

In addition to analyzing the classification of SS into BCC/B2, BCC/B2 + FCC, and FCC, ML was applied to distinguish SS from other phases, such as AM, SS + AM, and IM. Such information is very beneficial for the design of new materials, especially when it is necessary to avoid the additional phases. The process of tuning parameters for SS, AM, SS + AM, IM phases

are the same as that for the SS phases in the above discussions, and the corresponding plots are presented in **Fig. 4.13**. The best conditions are min_samples_leaf = 2 and max_depth = 7 for the DT model, n_neighbors = 3 for KNN, γ = 10 and C = 16 for SVM, and n_1 = 40, n_2 = 40, n_3 = 20 for ANN. The feature selection process and the corresponding CV accuracy values are shown in **Fig. 4.14**.

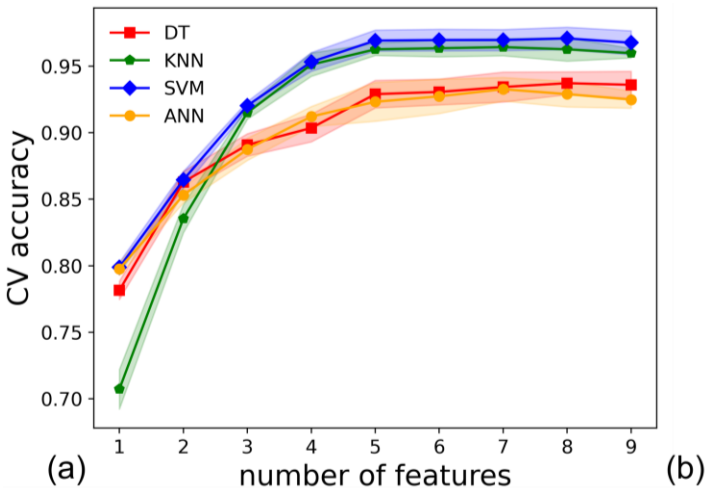

DT	KNN	SVM	ANN
Δχ	Δχ	Δχ	Δχ
FBI	FBI	FBI	FBI
ΔS_{mix}	δ	ΔH_{mix}	ΔH_{mix}
ΔH_{mix}	ΔH_{mix}	VEC	δ
T_m	VEC	ΔS_{mix}	ΔS_{mix}
VEC	e/a	Ω	e/a
e/a	T_m	e/a	VEC
δ	Ω	T_m	T_m
Ω	ΔS_{mix}	δ	Ω

Figure 4.14 Feature selection process measured by the CV accuracy in each ML model for predicting SS, AM, SS+AM, and IM.

The best four feature sets are {Δχ, FBI, ΔS_{mix}, ΔH_{mix}, T_m}, { Δχ, FBI, δ, ΔH_{mix}, VEC}, {Δχ, FBI, ΔH_{mix}, VEC, ΔS_{mix}}, {Δχ, FBI, ΔH_{mix}, δ, ΔS_{mix}} with a CV accuracy of 92.9%, 96.3%, 96.9%, 92.3% for DT, KNN, SVM, ANN, respectively. The CV accuracies of these ML models are very high and very close to one another. The two best features for predicting the phases here are Δχ and FBI, which is different with VEC as the best feature in classifying BCC/B2, BCC/B2 + FCC, and FCC phases. Islam et al. found that VEC and ΔS_{mix} are the most and the least important features, respectively, in classifying AM, SS, and IM, by performing singular value

decomposition on the weight matrix in the first hidden layer of ANN [122]. Our results also show the positive effect of VEC and ΔS_{mix} in helping classify phases, but they are not the most important feature. To separate SS and IM, King et al. proposed a new parameter Φ related to mixing enthalpy of both SS and IM by means of Miedema's model [155]. They found that $\Phi > 1$ favors SS and almost all IM forms when $\Phi < 1$, which forecasts more accurately than using Ω. Zhou et al. reported that their trained ANN, convolutional neural network (CNN), and SVM can reach around 95% accuracy with 13 features and reach around 89% with 4 features $\{\Delta S_{mix}$, δ, ΔH_{mix}, $\Delta\chi\}$ in predicting AM, IM, and SS. The 4 top-ranked features they selected are amongst our selected feature sets. The CV accuracy with only Δχ and FBI as the two input features can reach more than 80% for the four ML models, which motivates us explore the Δχ-vs-FBI plot as a potential useful phase selection rule.

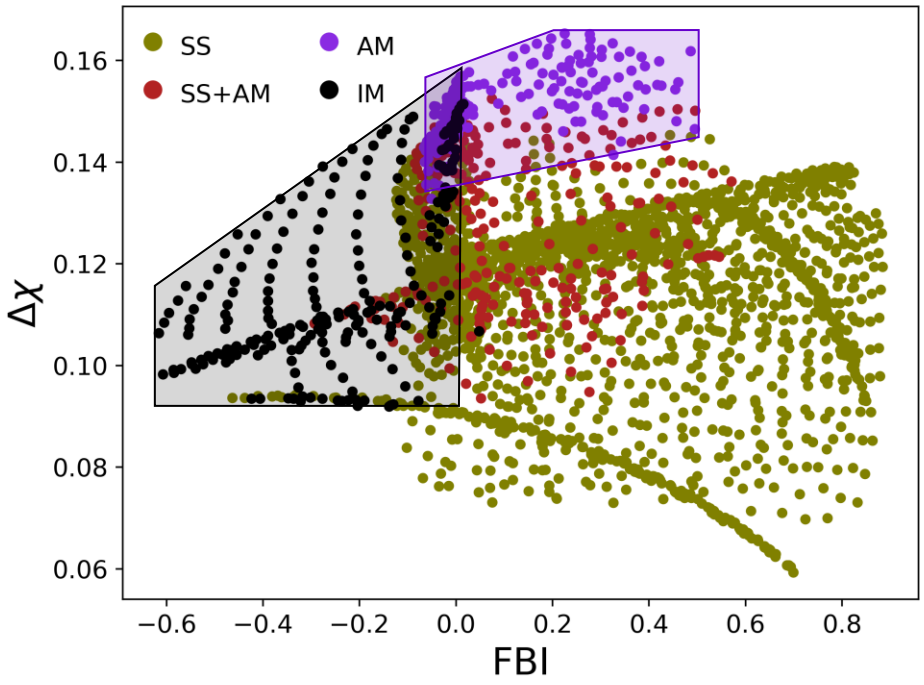

Figure 4.15 FBI-vs-**Δχ** plot for identification of SS, AM, SS+AM, and IM. Most IM-containing alloys are in the black shaded area in the left-hand side with only one exception.

In the Δχ-vs-FBI plot shown in **Fig. 4.15**, all amorphous alloys are in the purple shaded area, where $-0.065 \leq \text{FBI} \leq 0.5$ and $0.13 \leq \Delta\chi \leq 0.165$. All intermetallics with only one exception are in the black shaded area, in which $\text{FBI} \leq 0.015$ and $\Delta\chi \geq 0.09$. These two shaded areas only have a small, overlapping area of which the most SS alloys form in the lower right area. Therefore, these two areas could be used as phase selection rule for screening amorphous alloys and intermetallics, respectively. The ML methods are also applied to classify BCC, B2, FCC, BCC+FCC, B2+FCC, BCC+AM, FCC+AM, BCC+FCC+AM, AM, and IM phases (having B2 and BCC separately) and FBI and δ are found to be the two best features in improving the CV accuracies rather than Δχ and FBI.

4.4 Conclusions

High-throughput CALPHAD calculations were performed on 2,436 experimental HEAs and compared the results with experimental observations. Both CALPHAD predictions and experimental results show that alloys prefer BCC/B2 over FCC at larger atomic size difference which is understandable since BCC is less constrained than FCC, and alloys tend to form FCC structure at higher FBI, negative ΔH_{mix}, and small δ. Alloys exhibit single-phase BCC/B2 at VEC < 6.87 and FCC at VEC > 9.16, which agrees with prior findings for BCC/B2, but the range has been expanded beyond VEC > 8 for FCC as reported in the literature.

Four ML models were applied to two different datasets, one with the 1,761 solid solution only HEA compositions and the other with the entire 2,436 HEAs containing amorphous (AM) and/or intermetallic compounds (IMs). The best feature sets were identified using the five-fold cross validation method and achieve 90.4%, 94.1%, 93.8%, 89.7% for classifying BCC/B2, BCC/B2 +

FCC, FCC with DT, KNN, SVM, and ANN models, respectively. These trained models were applied on predicting the phase structures of 66 selected bulk alloys, and the ANN model achieved 80.3% prediction accuracy, which is comparable to CALPHAD predictions. For classification of SS, AM, SS + AM, IM phases, the CV accuracy reaches 92.9%, 96.3%, 96.9%, 92.3% in DT, KNN, SVM, and ANN models, respectively. The CV accuracies for both datasets are very high, which shows the effectiveness of ML in phase predictions of HEAs. In the ranked feature sets, VEC is identified as the most important feature in determining phase formation of SS. ML identified both ΔH_{mix} and VEC as two dominating factors for predicting the SS phase; and based on this learning, a simple straight line of $\Delta H_{mix} = 29 \times VEC - 247$ was found to be able to predict single-phase BCC/B2 and single-phase FCC at a 96.2% accuracy, which is simply remarkable, **Fig. 4.11(c)**.

Both $\Delta\chi$ and FBI are the two best features that improve the performance of ML models in predicting the formation of SS, AM, SS + AM, and IM phases. In the $\Delta\chi$-vs-FBI plot shown in **Fig. 4.15**, all amorphous alloys are in the area shaded in purple, where $-0.065 \leq \text{FBI} \leq 0.5$ and $0.13 \leq \Delta\chi \leq 0.165$. All the intermetallic-containing alloys with only one exception are in the area shaded in black, in which $\text{FBI} \leq 0.015$ and $\Delta\chi \geq 0.09$. All these phase selection rules will be very valuable for future design of advanced HEAs for challenging applications.

Chapter 5: Experimentally determination of ternary phase diagrams at different temperatures using diffusion multiple

5.1 Introduction

Ni-based superalloys are extensively used in the aerospace field including gas turbines, rocket engines due to their high strength, creep resistance, and resistance to oxidization and corrosion at high temperature [156–164]. They consist of multiple compositions and usually contain refractory components such as Cr, Mo, Re, W, Nb, and Ta, which contribute to their excellent properties for a wide range of applications. However, the amount of refractory elements should be carefully controlled in Ni-based superalloys since most topologically close-packed (TCP) phases can form at high temperature and stress, and these phases can degrade the performance through robbing refractory elements serving as solid solution strengtheners in the Ni-based γ (FCC) or γ' ($L1_2$) matrix. For example, the formation of TCP σ phase, in the Co and Ti modified Ni-based Rolls-Royce superalloy (RR1000), degrades the creep rupture life at 750 °C, compared with the regular RR1000 [162]. Thus, there exists a tradeoff between the formation of TCP phases and properties optimization with the addition of refractory elements, and it is critical to predict and control the formation of TCP phases in designing Ni-based superalloys.

To accelerate the design of new superalloys with high performance, a combination of computer-assisted high-throughput calculations and high-throughput experiments can be employed. The integrated method will increase the efficiency in terms of saving time and cost on laborious experiments using traditional approaches. CALPHAD is a useful tool in predicting the phase equilibrium of alloys by utilizing databases with optimized thermodynamic parameters [6,166,167]. It calculates the phase equilibrium of high-order systems by

extrapolating the assessed descriptions of binary and ternary systems. According to the study on the ability of CALPHAD in predicting Ni-based superalloys, CALPHAD databases still need significant improvement for calculating the phase equilibrium of TCP phases [152,168,169]. So, it is necessary to enhance the predictive ability for phase equilibria of CALPHAD in low-order systems, especially the phase equilibrium with TCP phases, to help the design of new Ni-based superalloys, and this requires large amount of experimental data and reassessment of pertinent binary and ternary systems.

Hasebe et al. prepared Fe-Nb-Ni bulk alloys with arc melting, and obtained the partial phase diagram partly below 50% Nb at 1100 °C and 1200 °C [170]. More experiments are needed to study the equilibrium between μ phase and other phases with composition of Nb greater than 50%. Also, the phase region of ε-Fe_2Nb in their assessed phase diagram is larger than their experimentally determined phase diagram at 1100 °C, because no data for the two-phase equilibrium of ε-Fe_2Nb + μ data were measured, as shown in **Fig. 5.1(a)** and **(b)**. Therefore, more experiments need to be conducted to map the phase boundary of ε-Fe_2Nb TCP phase in the Fe-Nb-Ni system. In the Cr-Nb-Ni system, very few available phase equilibrium data can be found in the literature [171–173].

Because of lack of experimental data of TCP phases and demands for well-assessed databases to predict the phase stability of TCP phases, our research objective is to make diffusion multiples, collect phase equilibrium data, and map the phase diagram of Ni-based ternary systems. We then provided the collected literature data and new experimental data to research group at Penn State University (PSU) for CALPHAD assessment using the open ESPEI (Extensible, Self-optimizing Phase Equilibrium Infrastructure) platform.

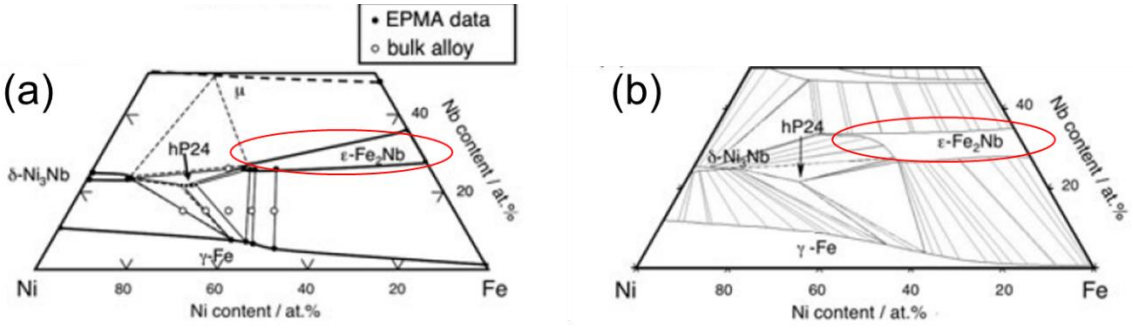

Figure 5.1 (a) and (b) are experimentally determined and calculated isothermal sections using assessed database in literature [170], respectively.

5.2 Methods

5.2.1 Diffusion multiple preparation

A diffusion multiple was assembled by combining several metal or alloy blocks arranged in a designed geometry with intimate interfacial contact that enables the thermal interdiffusion to form solid solutions and intermetallic compounds at high temperatures [34,36,37,174,175]. In this study, isothermal sections of Cr-Nb-Ni and Fe-Nb-Ni at 1100 °C, and Co-Cr-Ta, Co-Cr-W, Co-Ni-Ta, and Co-Ni-W at 700 °C are investigated using this diffusion multiple approach, whose geometries are shown **Fig. 5.2**.

The interfaces of blocks were well polished with SiC paper up to 1200 grit before assembling them. And then, these blocks were assembled and treated using hot isostatic pressing (HIP) to ensure the close interfacial contact between metal blocks. The sample was then encapsulated into quartz tube along with Ta foils to reduce the possibility of oxidation. The sealed quartz tube was annealed at 1100 °C for 1000 hours, with subsequent water quenching to ambient temperature. After annealing, a slice was cut using EDM and then mounted and polished with a final step of

using 0.05μm silica suspension. Then the sample was ready for the characterization and property test using a series of techniques.

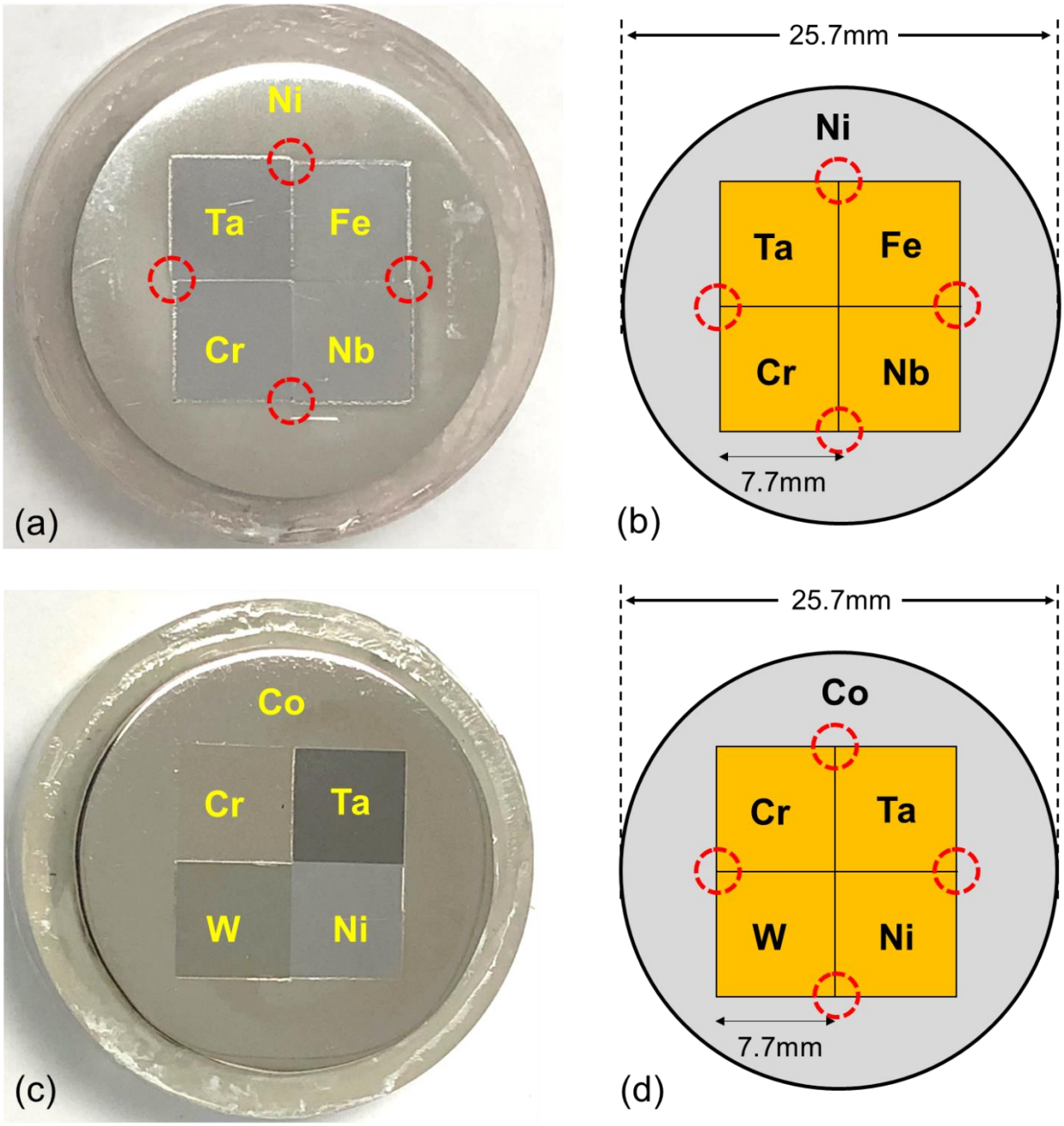

Figure 5.2 Photograph (a) and schematic diagram (b) of a slice cut from the diffusion multiple including Cr-Fe-Nb, Cr-Fe-Ta, Cr-Ni-Nb, and Cr-Ni-Ta ternary systems after heat treatment at

1100 °C for 1000 hours. (c) and (d) are for the diffusion multiple including Co-Cr-Ta, Co-Cr-W, Co-Ni-Ta, and Co-Ni-W ternary systems after annealing at 700 °C for 3000 hours.

With the prepared sample, the SEM BSE on XEIA3 TESCAN was used to observe the phase morphology in each ternary system in the triple junction area. WDS mapping was performed on the desired triple junction area with an accelerated voltage of 20 keV and a beam current of 50 nA on the Cameca SX100 machine. With these measurements, the composition information of each ternary system can be mapped, and tie-line data can be extracted by studying the composition versus distance profiles near phase interfaces using the methods discussed in the following section.

5.2.2 Tie-line Extraction

To obtain tie-line data from any composition-distance profile across the phase interfaces, a package is developed using Python (https://github.com/Chuangye-Wang/TernaryPlot). The programming is tested to be very robust, and we will briefly describe how to extract tie-line using the developed package.

The method using diffusion multiple and EPMA line scans has been well developed and widely used to construct the phase diagram of ternary systems. It is efficient to map multiple phase diagrams by including many binary and ternary systems in one diffusion multiple that undergoes the diffusion annealing process. Constructing a phase diagram generally takes several steps after preparing the samples. Firstly, the SEM BSE image is taken of the triple junction area of interest. Different phases with different masses exhibit various intensities of brightness which

helps identify these phases under SEM BSE mode. Secondly, the plan for EPMA line scans is designed by placing line segments across the important phase interfaces in the BSE image. Thirdly, EPMA line scans are performed to measure the composition along the designed lines. Lastly, tie-line data is extracted by processing the composition-distance profiles and composition-composition ternary diagram.

The successful phase diagram mapping requires a well-designed EPMA line scan plan; otherwise, the phase diagram can only be partially constructed because of not fully taking advantage of the composition information available in the triple junction area. Also, multiple cycles of loading and unloading the samples into the EPMA machine might have to be done if more critical tie-line data needs to be obtained. To avoid the necessity of a careful design plan of EPMA line scans and to prevent long experimental cycles, we can use the WDS mapping to get all the composition data in the triple junction area.

The WDS mapping technique scans the sample pixel by pixel instead of using a single-point scanning strategy, which only takes a few hours to complete composition mapping of the targeted area. Due to the increased measurement precision of EPMA equipment and the computational ability to analyze the collected intensities information, the result of WDS composition mapping is close to and comparable to the single-point measured composition. By taking a composition average of neighboring pixels, the measured composition will be closer to the composition obtained through the single-point analysis. The WDS mapping approach was used to map the phase diagram of the Ni-Ta-NiAl system on the specimen after annealing at 1200 C for 100 hours [176]. The authors found some binary intermetallic compounds, such as Ni_3Ta, Ni_2Ta, and Ni_3Al, and two ternary compounds in the system. However, no tie-line information on the two-phase equilibria was studied in their work. Therefore, our study will

establish a robust method to extract the tie-line data whose procedures are elaborately described in the following part.

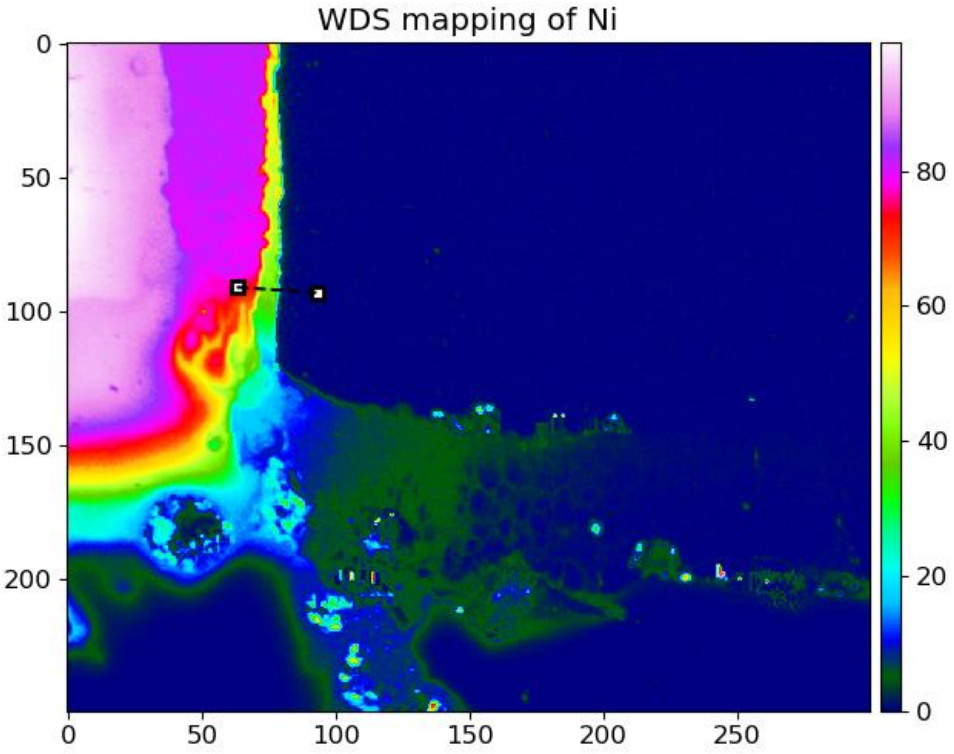

Figure 5.3 Composition mapping of Ni in Co-Ni-W system. The unit for the x- and y-axis is μm, and the color bar on the right represents the atomic percentage of Ni.

The tie-line data can be extracted from the diffusion profiles across the phase interfaces under the assumption of local equilibrium. **Fig. 5.3** is the composition map of Ni in the Co-Ni-W triple junction area and is taken as an example to show how to extract tie-lines from composition maps. Two locations are selected in the composition map, forming a line segment containing composition information across two phase interfaces by connecting these two locations. The composition-composition ternary diagram and three composition versus distance profiles along this line segment for Co, Ni, and W are plotted in **Fig. 5.4**. Three different phases are identified

as there exists a drastic composition jump from one phase to the other phase. In **Fig. 5.4(b)**, **(c)**, and **(d)**, the purple dashed lines stand for the phase interface, and the composition data from single-phase region are extrapolated to the phase interface location using a straight line. Subsequently, the yellow points contain the composition information of the tie-line. Following this approach of extracting tie-line, multiple line segments can be placed on the composition heatmap to generate multiple tie-line data for the establishment of the phase diagram.

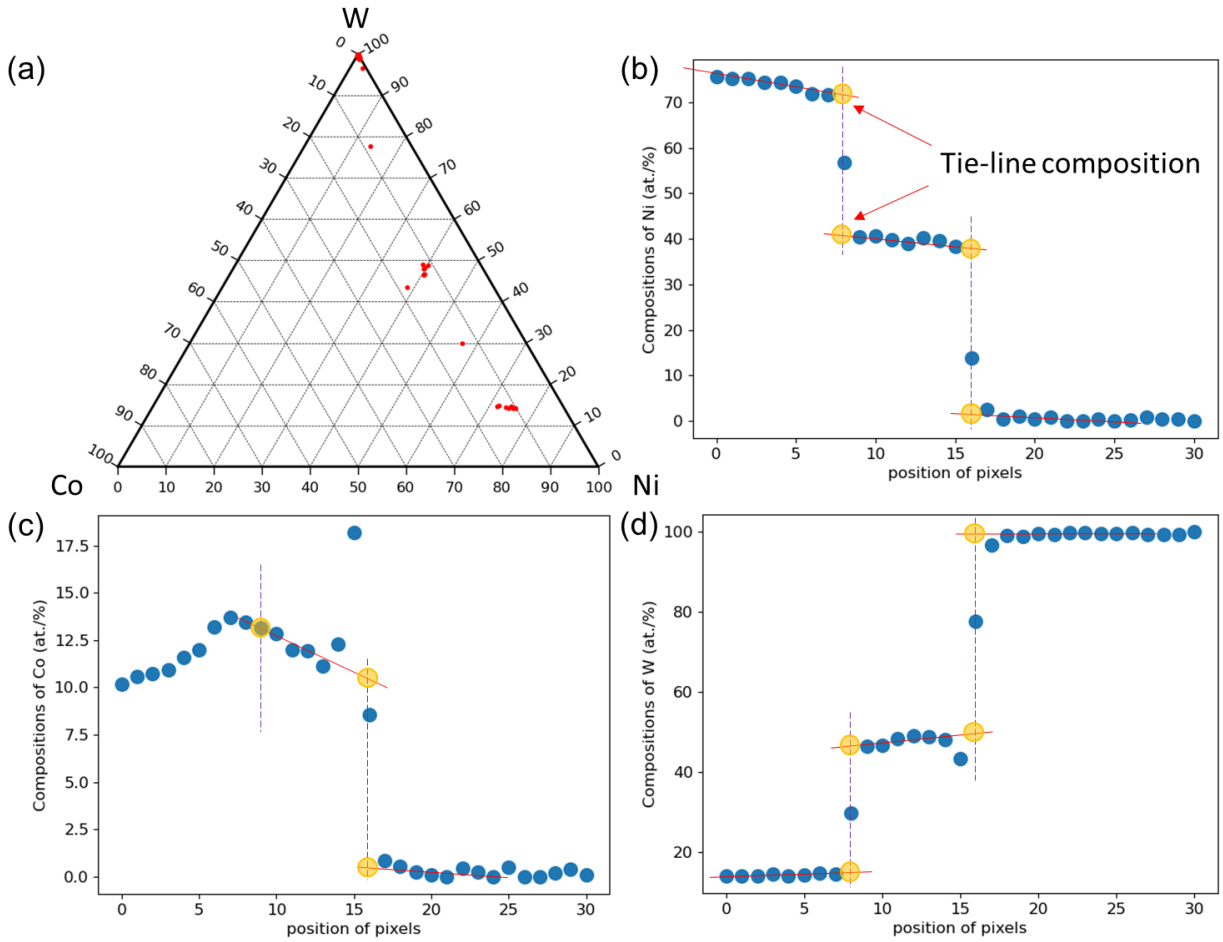

Figure 5.4 (a) is the composition-composition ternary diagram along the marked line in **Fig. 5.3**. (b), (c), and (d) are the composition versus distance profiles for Ni, Co, and W, respectively.

5.3 Results and Discussion

5.3.1 Fe-Nb-Ni

The SEM BSE image and composition mapping of Fe-Nb-Ni triple area after annealing at 1100 °C for 1000 hours is shown in **Fig. 5.5**. Near the Fe-Nb binary region in the upper left side of **Fig. 5.5(a)**, two layers of phases were observed and identified as ε-Fe_2Nb (C14 Laves phase), and μ-Fe_7Nb_6, based on the WDS-mapped compositions and the existing Fe-Nb binary phase diagram. In the Fe-Ni binary region, it is purely a single-phase FCC. The phase analysis is complex for Nb-Ni binary area due to the occurrence of $NiNb_2$ phase, which is nitrogen-stabilized intermetallic phase according to the work of Kodentsov et al. [177]. It is worthy to note that some readings in the composition mapping are inaccurate and should be analyzed along with the BSE image because they were measured at cracks in **Fig. 5.5(a)**. As shown in the lower area of **Fig. 5.5(b)**, the blue and green areas are alternatively distributed in the Nb-Ni region, which were identified as the $NiNb_2$ and the μ-Ni_7Nb_6 phase, respectively. Another identified phase is the δ-Ni_3Nb. A ternary compound was found to be hP24 in the area enclosed by irregular shape based on previous literature with XRD analysis [178]. The brightness of Nb in the enclosed area is close to that of δ-Ni_3Nb, as shown in **Fig. 5.5(b)**, making it hard to distinguish it from other phases. However, according to **Fig. 5.5(c)** and **5.5(d)**, the amount of Fe and Ni in the enclosed area is quite different from that in ε-Fe_2Nb and δ-Ni_3Nb, indicating that this phase is different from other phases.

The tie-lines information was extracted based on the composition-distance profiles along black dashed lines across phase interfaces in **Fig. 5.5(b)** and another composition mapping near the Fe-Nb binary side (not shown to save space). With the extracted tie-line data, the isothermal section of Fe-Nb-Ni excluding $NiNb_2$ phase at 1100 °C is constructed and presented in **Fig. 5.6**. Two

sets of tie-line data from EPMA line scans and WDS mapping are consistent with each other, indicating the validity and robustness of establishing phase diagram with WDS mapping.

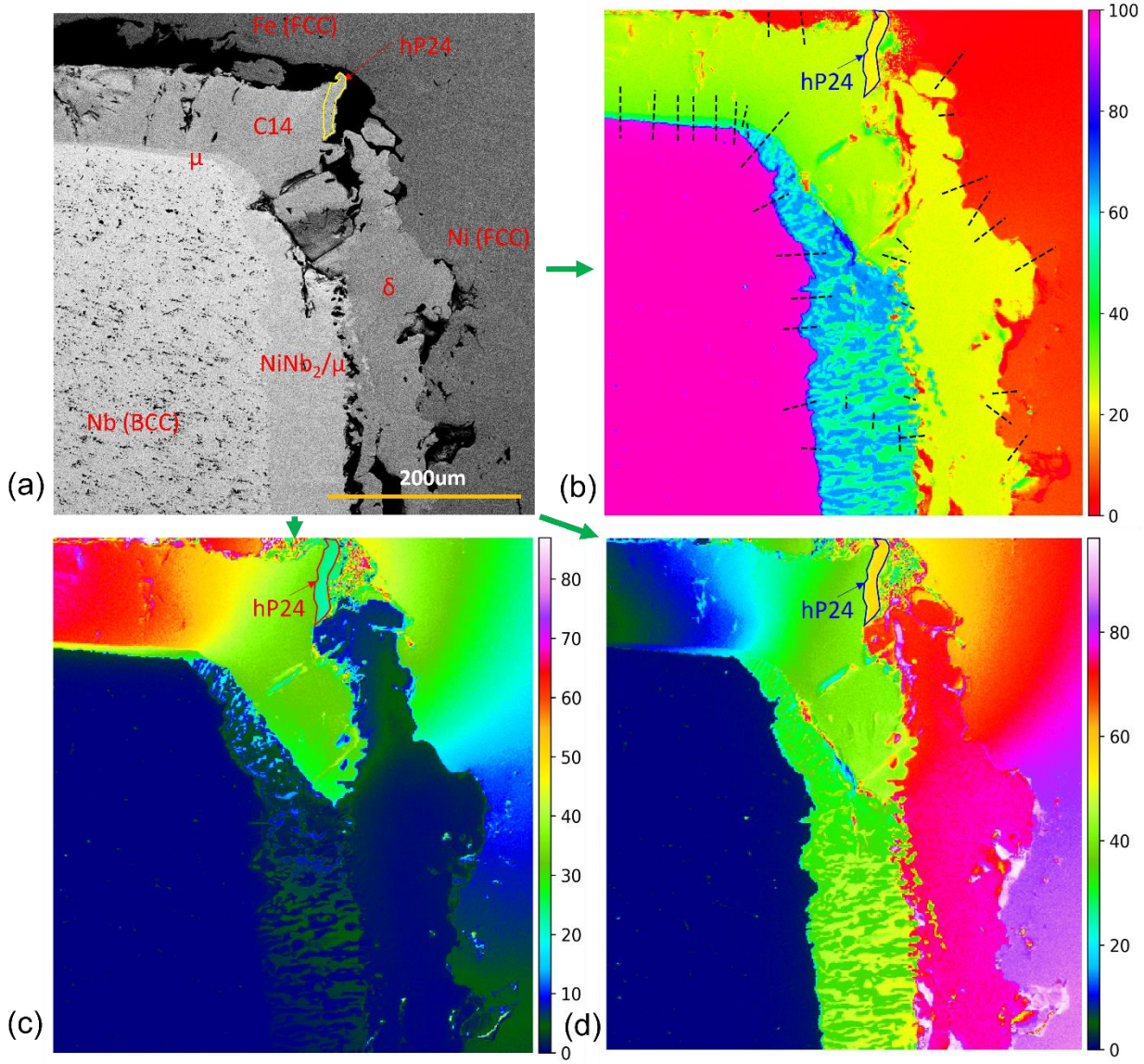

Figure 5.5 (a) The SEM BSE image of the Fe-Nb-Ni system. (b), (c), and (d) are the heatmap of compositions. The area in (a) is mapped using the WDS technique, and the composition mapping of Nb, Fe, and Ni are presented in (b), (c), and (d), respectively. The color bar stands for the composition of each element in atomic percent. The black dashed lines across phase interfaces in

(b) are where the tie-lines were extracted based on the information of both BSE image and composition heatmap.

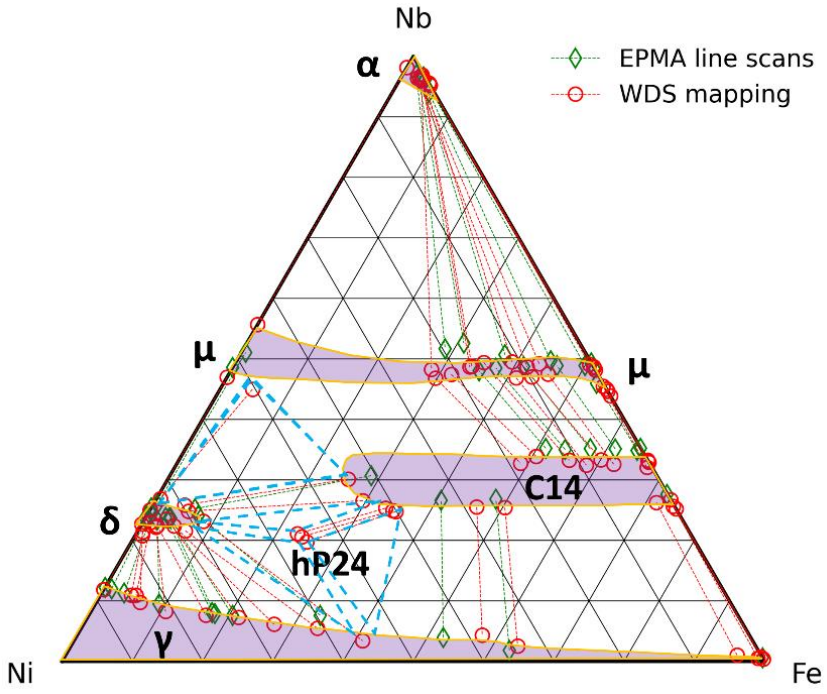

Figure 5.6 The isothermal section of Fe-Nb-Ni at 1100 °C. The green-colored tie-line data is from EPMA line scans, and the red-colored tie-line data is from WDS mapping. The purple-shadowed area with an orange boundary represents a single-phase region. The cyan-colored triangle is the ternary phase region. The ternary diagram is plotted in at.% with numbers on the axes removed for simplicity.

The solubility of Fe in δ-Ni_3Nb is around 8.5%, and the ε-Fe_2Nb extends deeply towards Ni, up to 44.5%. Ni primarily replaces Fe in the ε-Fe_2Nb structure, and the formula of ε-Fe_2Nb becomes ε-$(Fe, Ni)_2Nb$. The ternary compound, hP24, consists of about 22.9% Fe, 21% Nb, and

56.1% Ni, which is in good agreement with the reported composition Fe-21.5Nb-(56.8-59.8)Ni in the literature [178]. The μ-Fe_7Nb_6 has a significant solubility for Ni, up to 23.4%. Due to the formation of $NiNb_2$, the solubility of Fe in μ-Ni_7Nb_6 was reduced and separated into the μ-Fe_7Nb_6 and μ-Ni_7Nb_6 regions. The $NiNb_2$ + ε-Fe_2Nb phase equilibrium hinders the growth of μ-Ni_7Nb_6 towards Fe-Nb binary side, thus resulting in the formation of three ternary phase regions, $NiNb_2$ + μ-Ni_7Nb_6 + ε-Fe_2Nb, $NiNb_2$ + μ-Fe_7Nb_6 + ε-Fe_2Nb, and $NiNb_2$ + μ-Fe_7Nb_6 + α, as shown in the ternary diagram with $NiNb_2$ phase in **Fig. 5.7(a)**.

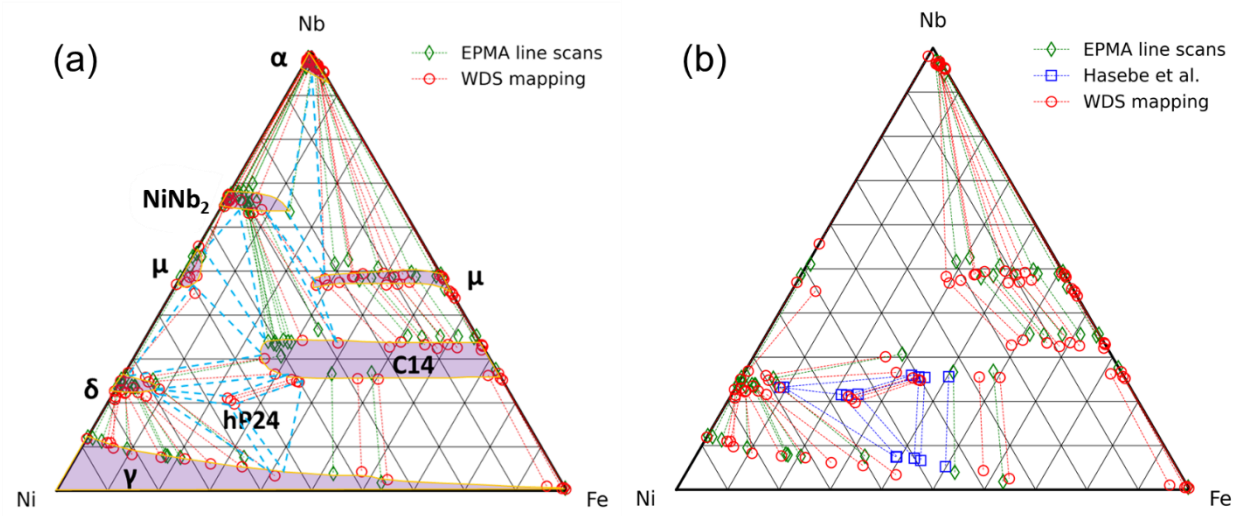

Figure 5.7 The isothermal section of Fe-Nb-Ni at 1100 °C, compared with literature data [178].

Our experimental data and the collected literature data of the Fe-Nb-Ni system at 1100 °C are presented in **Fig. 5.7(b)**. Overall, the experimental tie-line data agrees well with the literature data. Our constructed isothermal section is comprehensive because of the large amount of extracted tie-line data for all the phases in the system. The upper boundary of C14 Laves is clearly mapped, which agrees with the assessed phase diagram in **Fig. 5.1(b)**. Also, the μ phase and its equilibria with other phases are well constructed, which would be highly beneficial for

reassessment of the Ni-based databases and improvement of the prediction accuracy of phase equilibrium with TCP phases.

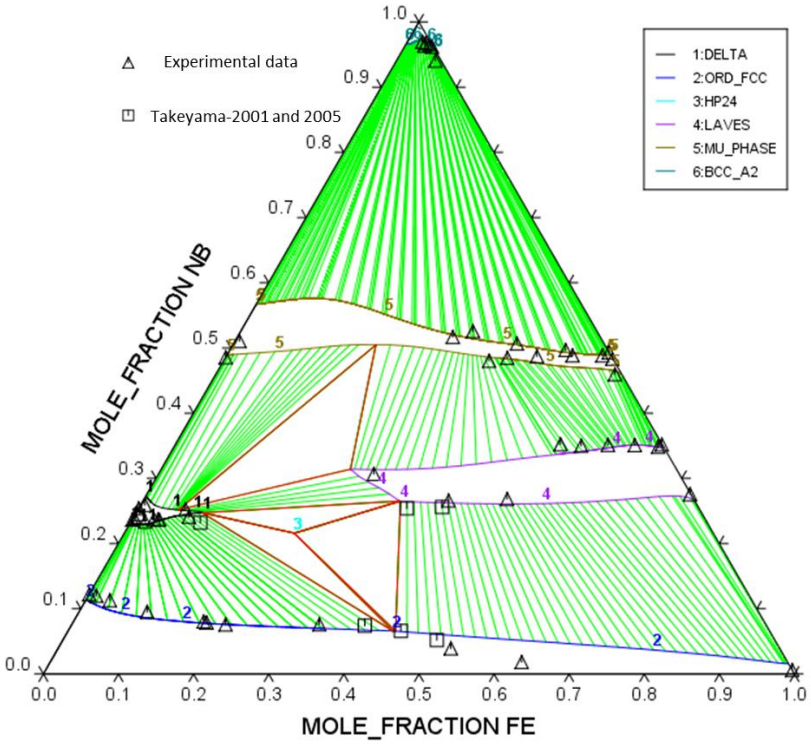

Figure 5.8 The calculated Fe-Nb-Ni phase diagram using the reassessed database.

The phase diagram of Fe-Nb-Ni at 1100 °C calculated using the reassessed database is presented in **Fig. 5.8**. This part of work is done by the collaborators in PSU, especially Hui Sun, who did most part of the assessment. The assessment of this ternary Fe-Nb-Ni system took the well assessed interaction parameters from binary systems as the basis and optimized the ternary interaction parameters. Four three-phase regions and six two-phase regions are predicted, which agrees well with the experimental data.

5.3.2 Cr-Nb-Ni

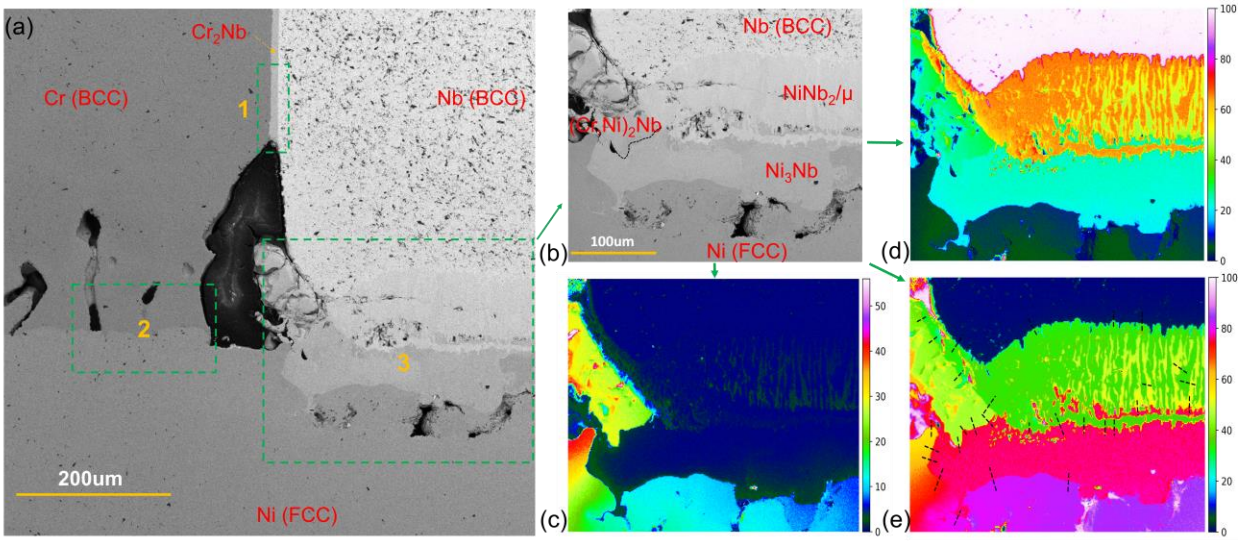

Figure 5.9 (a) and (b) The SEM BSE image of the Cr-Nb-Ni system. (c), (d), and (e) are the heatmap of compositions of Cr, Nb, and Ni, respectively.

Fig. 5.9(a) and **(b)** present the SEM BSE images of Cr-Nb-Ni triple junction area after heat treatment at 1100 °C for 1000 hours. Two layers of intermetallic compounds formed in the Nb-Ni binary side. The $NiNb_2$ and μ are alternatively distributed as shown in **Fig. 5.9(d)** and **(e)**. Kodentsov and Loo found that the ternary compound with approximately 33 at.% Nb composition is the high-temperature (HT) modification of $NbCr_2$. The increasing Ni-content in $NbCr_2$ leads to the phase transition from low-temperature (LT) cubic phase to the HT C14 Laves phase. To verify the crystal structure of the ternary compound, TEM and FIB were employed.

Fig. 5.10 shows the major steps taken during FIB-based TEM foil preparation. Two trenches and a thin layer of foil were left after milling using the gallium ion beam, as shown in **Fig. 5.10(a)**. The length and width of the foil is roughly about 20 and 10 μm. **Fig. 5.10(c)** shows the

sample surface after taking the foil out from the sample. It can be seen that FIB needs a ~50x30 μm^2 area to make one piece of foil. **Fig. 5.11** presents the diffraction patterns of one grain with a composition of approximately 24Cr-30Nb-46Ni. The diffraction patterns were taken on the grain marked 'H' in **Fig. 5.11(a)**. Diffraction pattern (a), (b), and (c) correspond to $[1\bar{1}0]$, [031], and [010] zone axis, respectively. Based on the analysis of diffraction patterns, the crystal structure is identified to be the C14 Laves phase, which agrees with previous literature reports.

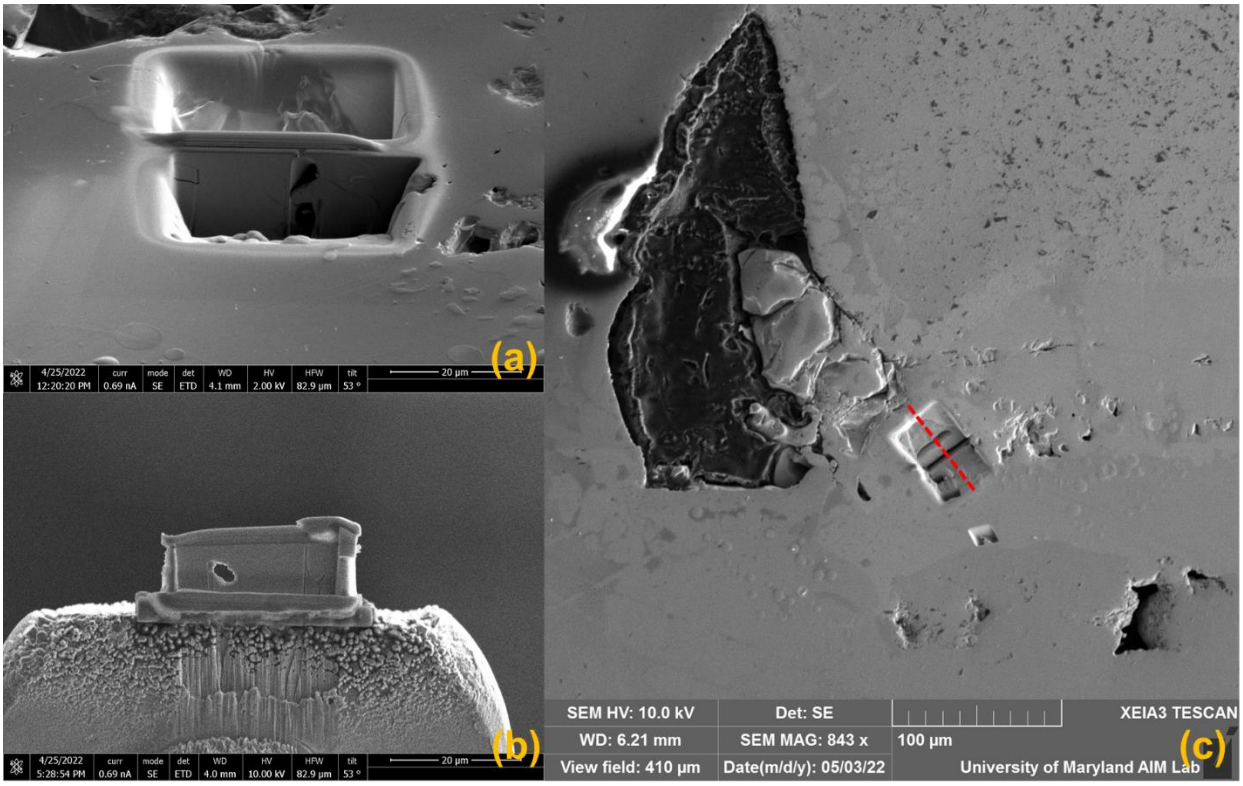

Figure 5.10 (a) The foil and two trenches in the two sides of foil. (b) TEM foil separated from the sample. (c) The surface morphology after FIB operation.

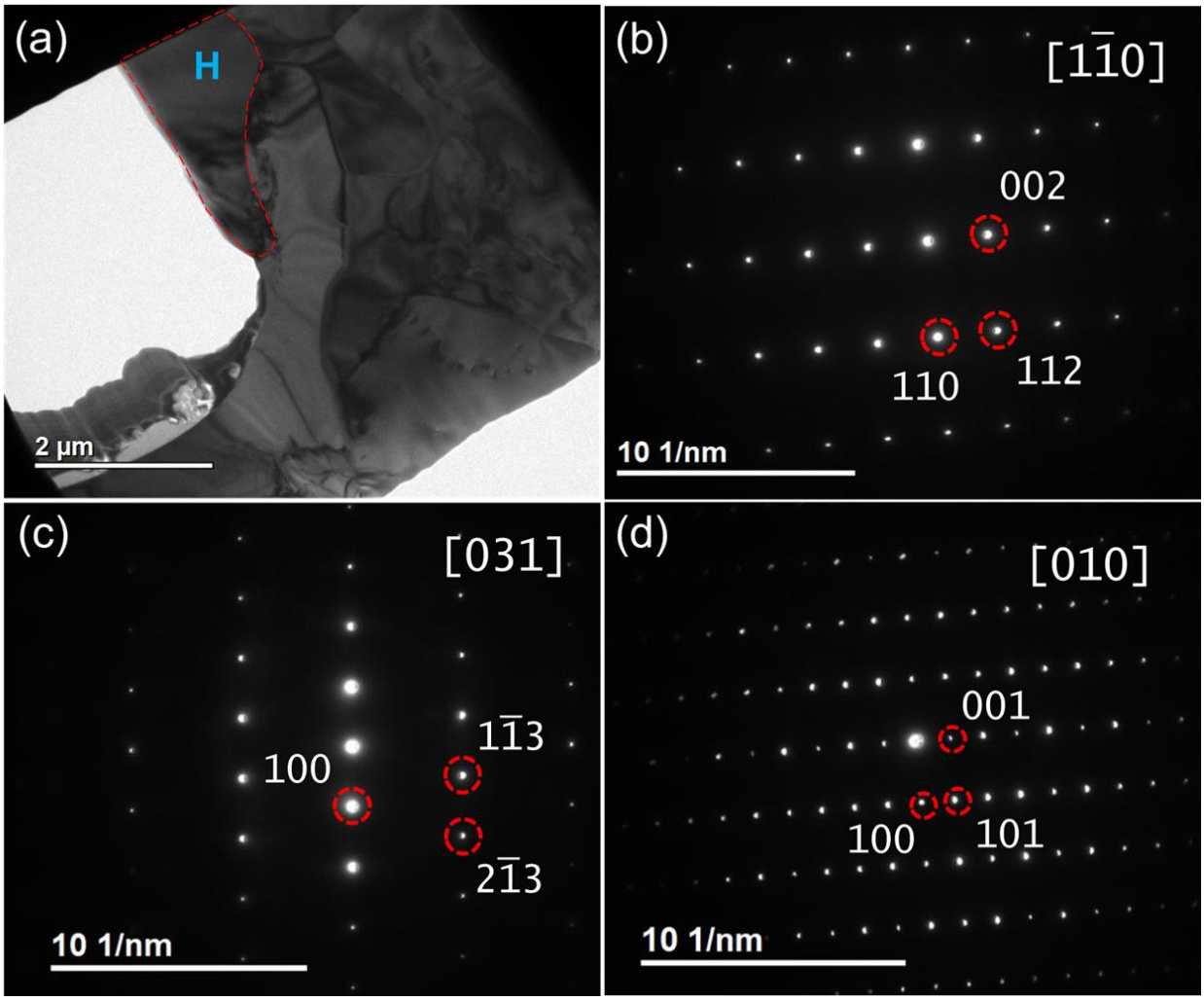

Figure 5.11 (a) TEM observation of the foil in bright field. (b), (c), and (d) are the diffraction patterns at different zone axis on the grain marked in blue 'H'.

With careful study of the phase equilibrium in the sample, the isothermal section of Cr-Nb-Ni system at 1100 °C was established, as shown in **Fig. 5.12**. The Ni solubility in C15 Laves is up to 7.5 at.%, and then is a two-phase equilibrium C15 + C14 till 13.5 at.% where stabilized C14 Laves phase appears. The C14 Laves phase extends deeply to the Ni side, up to 46 at.%. Six three-phase equilibria αCr + C14 + C15, αNb + C14 + C15, αNb + C14 + μ, C14 + μ + δ, αCr + C14 + δ, αCr + γ + δ were observed. The predicted phase diagram using reassessed database is shown in **Fig. 5.13**, which is in good consistency with experimental data.

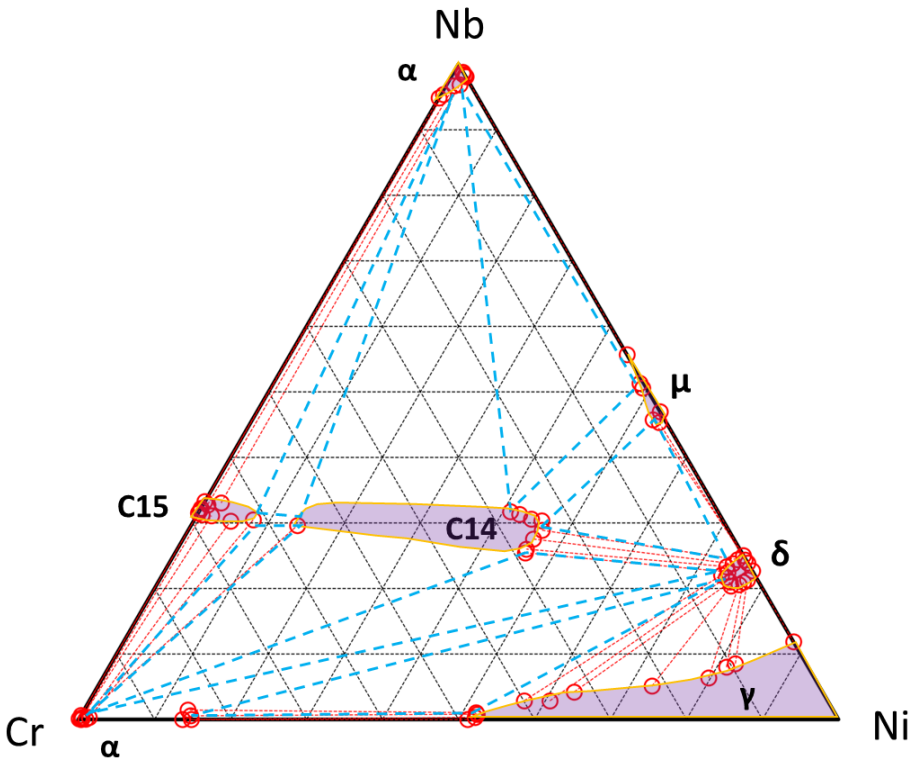

Figure 5.12 The isothermal section of Cr-Nb-Ni at 1100 °C.

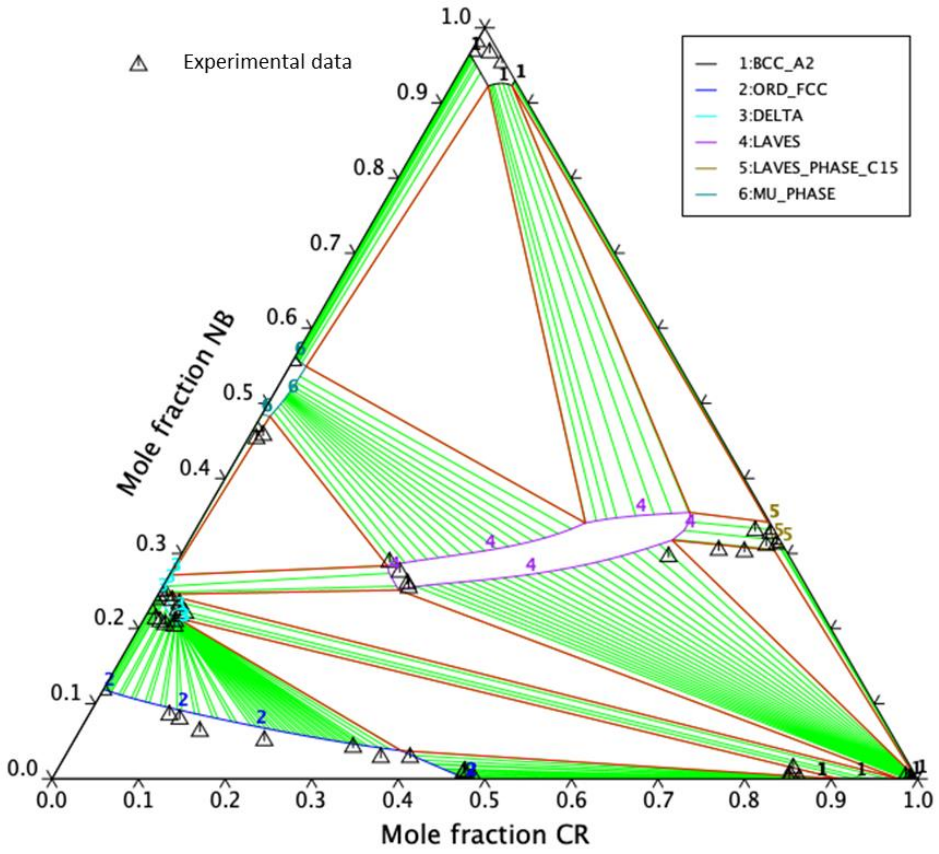

Figure 5.13 The calculated Cr-Nb-Ni phase diagram using the reassessed database.

5.3.3 Co-(Cr, Ni)-(Ta, W) systems

5.3.3.1 Co-Cr-Ta

Few studies have been done on the phase diagram of Co-Cr-Ta system. Drapier et al. presented a solubility limit of FCC (γCo) phase in Co-Cr-Ta system which does not agree with the solubility limit in Co-Cr binary system [179]. Zhao et al. prepared the samples by arc melting and annealed samples at 800 °C, 900 °C, and 1100 °C for 150 days, 140 days, and 120 days, respectively [180]. They mapped the isothermal sections at the three experimental temperatures systematically. The $(Co, Cr)_2Ta$ (C14, $MgZn_2$-type structure) phase was found to

have a wide solubility of Cr from 4 at.% to 58 at.%. And they reported a large solubility of Cr in Co_6Ta_7 phase.

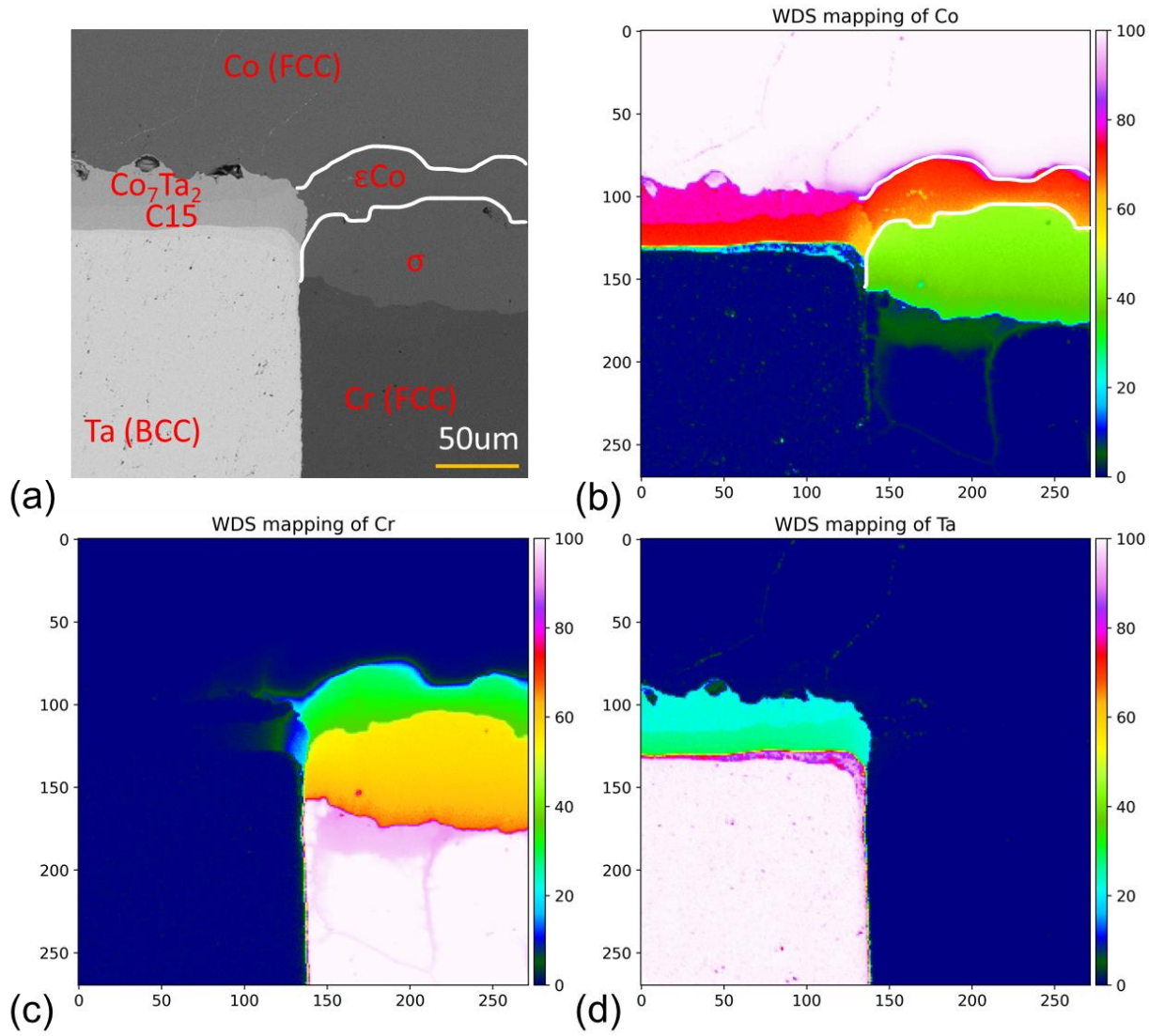

Figure 5.14 (a) SEM BSE image of Co-Cr-Ta triple junction in the diffusion multiple. (b), (c), and (d) are the composition heatmap of Co, Cr, and Ta in the Co-Cr-Ta system, respectively. The color bar stands for the composition of an element.

Table 5.1 Crystal structures of the phases in Co-X-Y (X = Cr, Ni, Y = Ta, W) ternary systems.

System	Phase	Struktur-Bericht	Pearson Symbol	Space group	Prototype	References
Pure Element	αCo	A1	*cF*4	$Fm\bar{3}m$	Cu	[181]
	Cr	A2	*cI*2	$Im\bar{3}m$	W	[181]
	αNi	A1	*cF*4	$Fm\bar{3}m$	Cu	[181]
	Ta	A2	*cI*2	$Im\bar{3}m$	W	[181]
	W	A2	*cI*2	$Im\bar{3}m$	W	[181]
Co-Cr	Co_7Cr_8	$D8_b$	*tP*30	$P4_2/mnm$	σ(Cr,Fe)	[182]
	(εCo)	A3	*hP*2	$P6_3/mmc$	$D0_{19}$	[182]
Co-Ta	Co_7Ta	$L1_2$	*cP*4	$Pm\bar{3}m$	$AuCu_3$	[183]
	Co_7Ta	-	*hR*12	$R\bar{3}m$	$BaPb_3$	[183]
	Co_2Ta	C15	*cF*24	$Fd\bar{3}m$	Cu_2Mg	[184]
	Co_2Ta	C14	*hP*12	$P6_3/mmc$	$MgZn_2$	[184]
	Co_6Ta_7	$D8_5$	*hR*13	$R\bar{3}m$	Fe_7W_6	[181]
	$CoTa_2$	C16	*tI*12	$I4/mcm$	Al_2Cu	[181]
Co-W	Co_3W	$D0_{19}$	*hP*8	$P6_3/mmc$	Ni_3Sn	[181]
	Co_3W	$D0_a$	*oP*8	*Pmmn*	Cu_3Ti	[185]
	Co_7W_6	$D8_5$	*hR*13	$R\bar{3}m$	Fe_7W_6	[181]
Cr-Ta	Cr_2Ta	C14	*hP*12	$P6_3/mmc$	$MgZn_2$	[182]
	Cr_2Ta	C15	*cF*24	$Fd\bar{3}m$	Cu_2Mg	[182]
Ni-Ta	Ni_8Ta		*tI*36	$I4/mmm$	Ni_8Nb	[186]
	Ni_3Ta	$D0_{22}$	*tI*8	$I4/mmm$	Al_3Ti	[181]
		…	*oP*8	*Pmmm*	Cu_3Ti	[181]
		…	*mP*48	$P2_1/m$	$NbPt_3$	[181]
	Ni_2Ta	C11b	*tI*6	$I4/mmm$	$MoSi_2$	[181]
	Ni_7Ta_6	D85	*hP*13	$R\bar{3}m$	Fe_7W_6	[181]
	$NiTa_2$	C16	*tI*12	$I4/mmm$	Al_2Cu	[181]
Ni-W	Ni_4W	$D1_\alpha$	*tI*10	$I4/m$	$MoNi_4$	[181]
	NiW	-	*oP*56	$P2_12_12_1$	MoNi	[187]
	NiW_2	-	*tI*96	-	-	[188]

Fig. 5.14(a) is the SEM BSE image of Co-Cr-Ta system after being annealed for 3000 hours at 700 °C. Two layers of intermetallic existed between pure Ta and pure Co, which are C15 Laves and Co_7Ta_2 phases. The μ phase was not observed in the Co-Ta diffusion area even though it is supposed to be present, according to the binary phase diagram of Co-Ta. This was possibly due to the sluggish diffusion in μ phase. In the Co-Cr binary side, two layers of phases εCo and σ were identified. The phase boundary of εCo was not easily distinguished in the SEM BSE image, but the phase boundary was clearly presented in the composition map of Co and Cr. Therefore, the phase boundary of εCo was mapped using white lines. No intermetallic was found in the Cr-Ta system. Two two-phase equilibria of σ + C15 and εCo + C15 formed at the phase interfaces.

In the composition map **Fig. 5.14(b)**, **(c)**, and **(d)**, the tie-lines can be extracted by means of exploring composition profiles across phase interfaces. The mapped isothermal section is presented in **Fig. 5.15(a)** and the corresponding calculated isothermal section from TCFE11 database is shown in **Fig. 5.15(b)**. In the experimentally determined isothermal section, four intermetallic compounds are mapped. Solubilities of Ta in both εCo and σ are very small, around 2 at.%. Co_7Ta_2 has an extremely short extension towards Cr, exhibiting the same behaviors as in the isothermal sections at 800 °C and 900 °C constructed by Zhao et al. [180]. The $(Co, Cr)_2Ta$ with $MgZn_2$ (C14) structure type was found above 800 °C and it took up a large composition space in the isothermal section. This C14 structure was not observed at our experimental temperature of 700 °C, even after a long-term period of annealing. Instead, only $(Co, Cr)_2Ta$ with Cu_2Mg (C15) structure type was observed in the sample annealed at 700 °C. The C15 Laves phase has a solubility of 18 at. % Cr. As marked in blue-dashed triangles in the isothermal section, five three-phase equilibria Co + εCo + C15, Co + C15 + Co_7Ta_2, σ + εCo + C15, αTa + σ + C15, and αCr + αTa + σ were identified.

The calculated composition area of μ has a wide range from 47 at.% Ta to 77 at.% Ta near the Co-Ta side, which heavily deviates from the composition range of μ in the binary phase diagram of Co-Ta. The C14 Laves is predicted by CALPHAD instead of the C15 Laves in the experiment, and it extends deeply into the Cr-Ta binary side. Co_7Ta_2 was not shown in the predicted isothermal section. Overall, the TCFE11 database should be reassessed by taking new phase equilibrium data of the Co-Cr-Ta system into account.

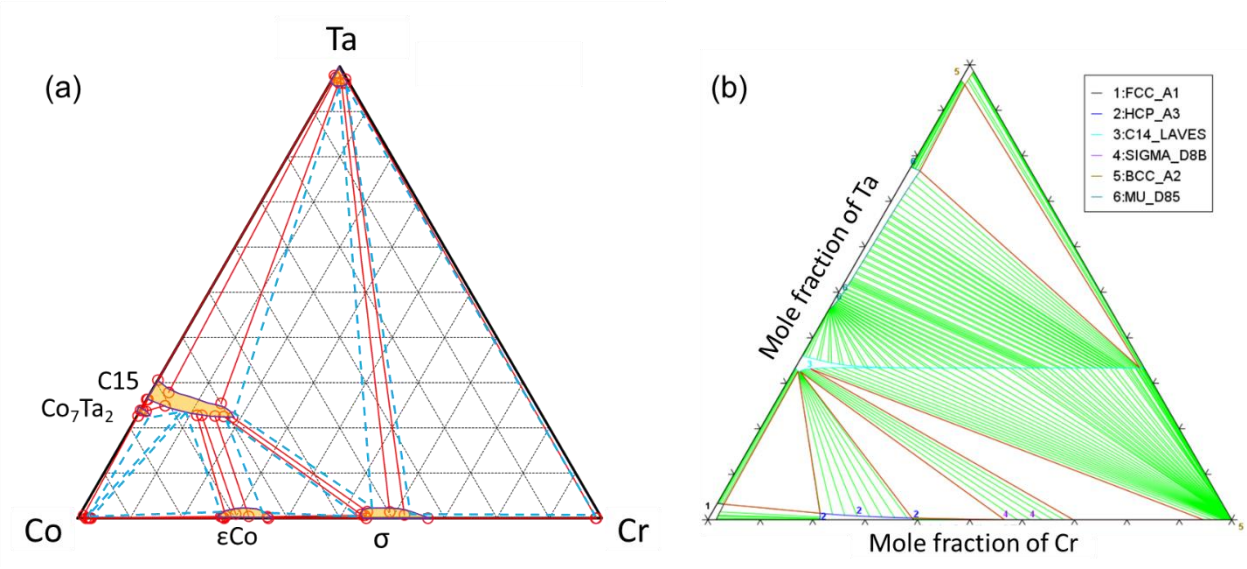

Figure 5.15 (a) Experimental and (b) calculated (using TCFE11 database) isothermal section of Co-Cr-Ta ternary system at 700 °C.

5.3.3.2 Co-Cr-W

The isothermal section of Co-Cr-W system at 1350 °C was first explored by Barrows and Newkirk and they found a new ternary intermetallic compound, R phase, with a composition around 27.7 wt.% Co, 16.4 wt.%, 55.9 wt.% by conducting EPMA and XRD experiments [189]. Gupta proposed a modified isothermal section at 1350 °C and a schematic liquidus projection

based on the experimental data in the literature and some assumptions [190]. Sato constructed the isothermal sections at 1000 °C, 1200 °C, and 1350 °C, and Yang et al. did a thermodynamic assessment using the published phase equilibrium data [191,192].

All the previous literature data only provided phase equilibria data near Co-Cr binary side (below 50% at. W), therefore a more comprehensive study was reported by Zhang et al. [193]. Bulk alloys were prepared with arc melting and heat treated at 1000 °C, 1100 °C, and 1200 °C for several weeks. And then EPMA and XRD were used to map the isothermal sections. The R phase was confirmed to exist at 1200 °C, but not at other two experimental temperatures. The Co_7W_6 was reported to have a large solubility of Cr at all the experimental temperatures. Thermodynamic assessment was performed by Kaplan et al. based on both experimental data and ab initio calculated results [194]. Since the agreement between their assessed results and experimental data can be improved, Wang et al. reassessed the system by considering the W-rich data of the μ phase [195].

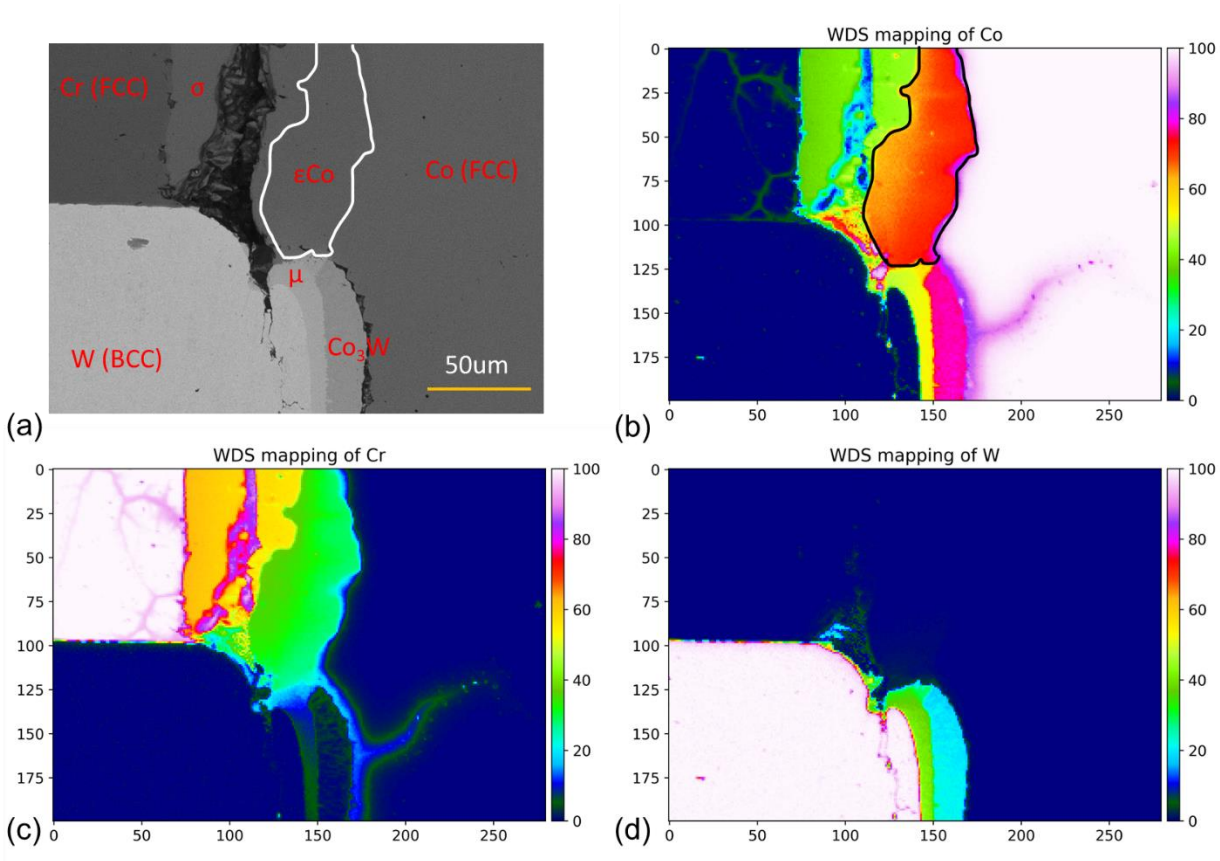

Figure 5.16 (a) SEM BSE image of Co-Cr-W triple junction in the diffusion multiple. (b), (c), and (d) are the composition heatmap of Co, Cr, and W in the Co-Cr-W system, respectively.

The SEM BSE image of Co-Cr-W triple junction after annealing process is shown in **Fig. 5.16(a)**. In the Co-Cr binary side, two layers of intermetallic compounds σ and εCo were observed with the assistance of composition maps. A crack formed in the σ phase, which did not affect phase interfaces between σ and εCo but affected the extraction of tie-lines for the phase equilibrium of σ + αW and σ + μ. The μ and Co_3W phase layers formed on the Co-W binary side. The μ grew extensively and had a two-phase equilibrium with εCo. The ternary phase R

was identified at 1200 °C and 1350 °C [189,193], but no ternary intermetallic compounds were found at 700 °C.

With composition mapping, the isothermal section of Co-Cr-W ternary system was constructed and presented in **Fig. 5.17(a)**. The solubilities of W in εCo and σ are around 4 at.% and 3 at.%, respectively, which are small. These solubility values are similar to the solubility of Ta in εCo and σ of Co-Cr-Ta system. The Co_3W phase has a solubility of 5 at.% Cr. The solubility of Cr in μ phase decreased to 28 at.%, compared with the reported solubility of Cr 42.8 at.% at 1000 °C, 44 at.% at 1100 °C, and 46.5 at.% at 1200 °C [193]. Due to the crack formation during the annealing, we did not get the tie-line information for the σ + μ equilibrium. Fortunately, it does not affect much mapping the isothermal section and two three-phase equilibrium σ + μ + εCo; σ + μ + αW can still be easily inferred and built in the isothermal section. Other three three-phase equilibria γCo + εCo + Co_3W, εCo + Co_3W + μ, αCr + αW + σ are presented in **Fig. 5.17(a)** as well.

CALPHAD predicted isothermal section at 700 °C is presented in **Fig. 5.17(b)**, and we can see that some reassessment is needed to be made on the TCFE11 database. The FCC_L12 was predicted as a ternary compound by CALPHAD, which was not found in the experiment. The Co_3W phase was not predicted while it should exist in the system. The experimentally measured composition area of μ phase is much broader than the predicted composition area.

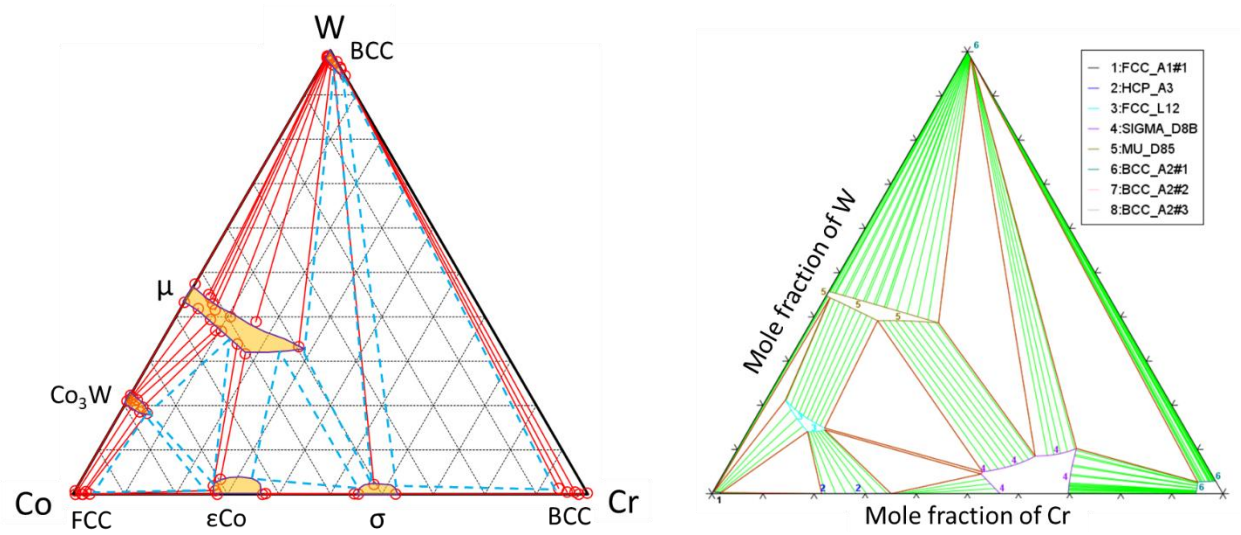

Figure 5.17 (a) Experimental and (b) calculated (using TCFE11 database) isothermal sections of Co-Cr-W ternary system at 700 °C.

5.3.3.3 Co-Ni-Ta

Nesterenko et al. constructed the schematic isothermal section of Co-Ni-Ta system at 1000 °C using equilibrated alloys [196]. Xu et al. studied the phase equilibria at 1100 °C using five different equilibrated alloys and different (Co-Ni alloy)/Ta diffusion couples [197]. The alloys were remelted five times using arc melting to improve the alloy homogeneity and then annealed at 1100 °C for 240 h. The five diffusion couples made were (Co-xNi)/Ta, where x is equal to 90, 70, 50, 30, and 10 and one ternary diffusion couple was Co-Ni/Ta. All diffusion couples were annealed at 1100 °C for 168h. After heat treatment and metallographic preparations, the specimens were characterized using scanning electron microscopy (SEM) and EPMA. The authors reported four three-phase equilibria and nonexistence of ternary compounds. And it presented that $TaCo_2$ and $TaNi_3$ phase are connected in the isothermal section. However, it was

rebutted in the research of isothermal sections at 1200 K and 1375 K by Shaipov et al. [198]. They pointed out that it is not a mono-phase in composition of $(Ni, Co)_3Ta$, instead it includes two ternary intermetallic compounds which are α′ (Mg_3Cd-structure type) and α″ ($BaPb_3$-structure type) at 1375 K. At 1200 K, the α″ phase disappeared and was absorbed into the Co_3Ta phase, but α′ remains as a ternary phase.

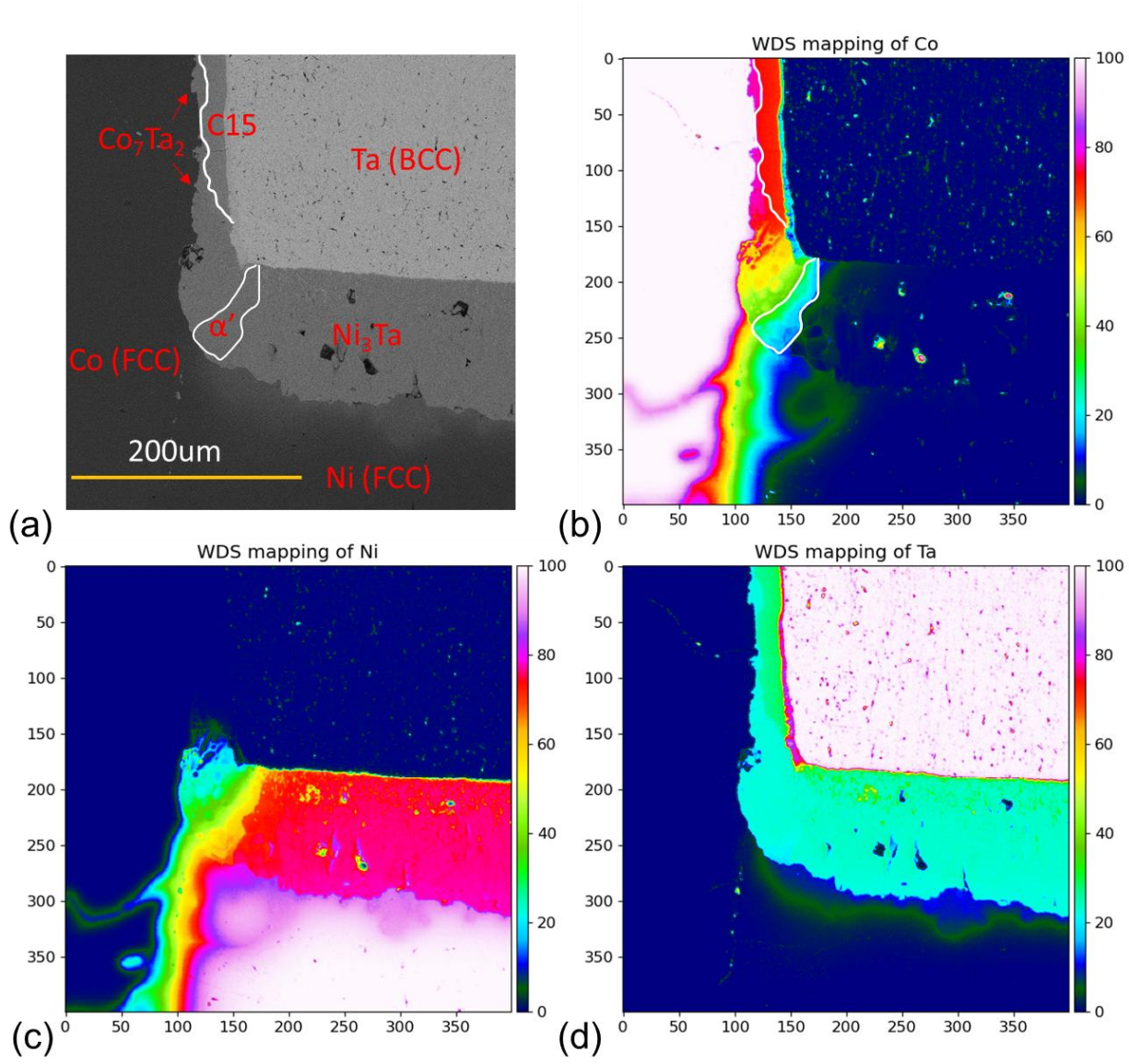

Figure 5.18 (a) SEM BSE image of Co-Ni-Ta triple junction in the diffusion multiple. (b), (c), and (d) are the composition heatmap of Co, Ni, and Ta in the Co-Ni-Ta system, respectively.

The phase evolutions in the Co-rich corner at 1000 and 1100 °C was investigated by Baheti et al. using diffusion couple technique [199]. They suggested that the Co_2Ta with C15 structure is stable in both binary and ternary systems. They also provided reliable phase equilibria data which is in good agreement with Xu et al.'s work. Besides using diffusion couples and equilibrated alloys, Zhu et al. used diffusion multiple approach to study the phase diagram of Co-Ni-X (X = W, Mo, Nb, Ta) at 800 °C and 900 °C [200]. They found a smaller phase area of α′ compared with the phase area mapped at 927 °C and 1102 °C in previous literature. A possible four-phase equilibrium was postulated between 927 °C and 900 °C since the ternary phase region C15 + α′ + Co_7Ta_2 and C15 + α′ + μ were constructed at 927 °C by Shapipov et al and C15 + Co_7Ta_2 + μ and α′ + Co_7Ta2 + μ were mapped at 900 °C by them.

After long-term annealing at 700 °C, SEM BSE image and composition heatmaps of Co, Ni, and Ta are shown in **Fig. 5.18(a)**, **(b)**, **(c)**, and **(d)**, respectively. Two layers of Co_7Ta_2 and C15 were observed in the Co-Ta binary side. According to the phase diagram of Co-Ta system, Co_6Ta_7 and $CoTa_2$ are stable at intermediate temperature. However, they were not observed using SEM and WDS mapping possibly due to the sluggish diffusion in these phases. Therefore, the diffusion multiple technique is at the mercy of kinetics and preparing equilibrated bulk alloys will be helpful to determine the phase equilibrium. The area of α′ phase was marked using the white line as shown in **Fig. 5.18(a)** and **(b)** with the help of composition mapping. On the Ni-Ta binary side, the intermetallic Ni_3Ta has a thick layer of ~ 115 μm. The other phases are Ni_2Ta, μ, and $NiTa_2$ phases, but their phase layers are very thin and can only be observed with higher resolution.

With EPMA measured compositions, the isothermal section of Co-Ni-Ta is presented in **Fig. 5.19(a)**. The solubility of Ni in Co_7Ta_2 phase reaches up to 43%, which is slightly smaller than

the measured solubility at 800 °C and 900 °C in previous work [200]. A ternary compound α′ was identified with composition range of ~50-70 at.% Ni and ~18-24 at.% Ta. The ternary compound α″ decomposed between 1102 °C and 927 °C, as reported by Shaipov et al. [198] and no α″ phase was found at 700 °C in current work. In the Ni-Ta side, only Ni_3Ta intermetallic was successfully mapped in the isothermal section and phase equilibrium of other binary intermetallic compounds were not extracted because of their phase layers are too thin to obtain reliable tie-line data. The phase regions of (Co, Ni)Ta_2, μ, Ni_2Ta, C15 Laves are tentatively mapped based on the binary phase diagram and the predicted isothermal sections at higher temperature from previous work [201].

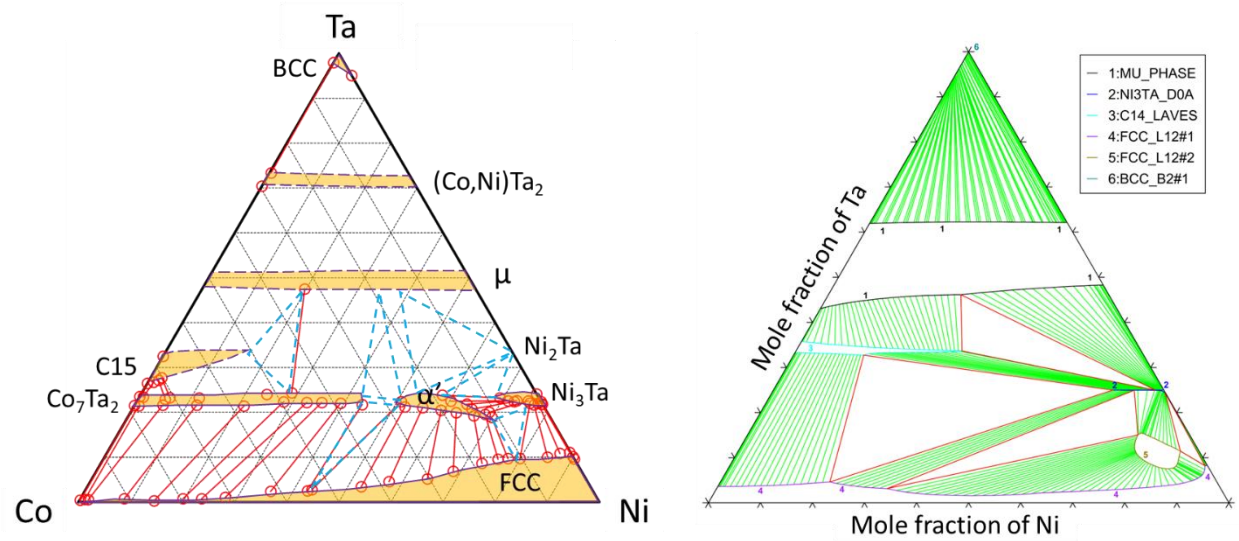

Figure 5.19 (a) Experimental and (b) calculated (using TCNI11 database) isothermal sections of Co-Ni-Ta ternary system at 700 °C.

As shown in **Fig. 5.19(a)** and **(b)**, there exists a big difference between the experimental and CALPHAD predicted isothermal section. The μ phase covers a range of 15 at.% Ta in

CALPHAD calculations, which is overpredicted when compared with the binary phase diagram of Co-Ta and Ni-Ta systems. The Co_7Ta_2 and α′ was not correctly predicted in the calculated isothermal section. Composition space of FCC phase near the Ni corner side in the experimental isothermal section is wider than that in calculated one. Based on the comparison, the TCNI11 database needs to be improved to predict the phase equilibria of Co-Ni-Ta system.

5.3.3.4 Co-Ni-W

Shipovskov et al. determined the phase equilibrium and isothermal section at 1000 °C using equilibrated alloys [202]. Jin et al. mapped the isothermal section at 1300 °C using diffusion triple technique and EPMA [203]. They reported three two-phase regions and one three-phase region α + γ + μ. The solubility of Ni in μ phase reached up to 22.3 at.%. Using the same method, Cao et al. constructed the isothermal section at 1100 °C and reported a solubility of 19.76 at.% of Ni in μ phase [204]. To study the interdiffusion and growth of phases in CoNi/W system, Divya et al. made five diffusion couples that include five diffusion path at 1300 °C [205]. They not only contributed useful diffusivity data to the Co-Ni-W system, but also provided phase equilibrium data for mapping the isothermal section at 1300 °C, which agrees well with the reported FCC region from Jin et al. in the Co-Ni side and presents a wider range of μ phase compared with Jin et al.'s work.

Zhu et al. investigated the isothermal sections of Co-Ni-W system at 900 °C and 800 °C using the same methods as mentioned in literature review of Co-Ni-Ta system [200]. They found five two-phase regions (α + μ, μ + Co_3W, γ + Co_3W, γ + μ, γ + Ni_4W), and a three-phase region (γ + μ + Co_3W). The phase equilibrium near the Ni-W binary side was not well established because of the formation of Ni_2W_4C and Ni_6W_6C carbide phases. These carbide phases hindered the growth of μ phase, which resulted in non-existence of some two and three-phase regions that

should have contributed to the phase diagram in the Ni-W binary side at both experimental temperatures. Therefore, the authors left a question mark on that area in the phase diagram. The authors found that Co_3W phase extended deeply to ~ 62 at.% Ni at 800 °C, while it only extended to ~13 at.% Ni at 900 °C. This phenomenon was later explained by Bouliez et al. [185], which is attributed to the formation of a new phase Co_3W-$D0_a$ starting from 21.5% Ni at 1000 °C by means of transmission electron microscope (TEM). They further constructed a ternary phase equilibrium Co_3W-$D0_a$ + Co_3W-$D0_{19}$ + Co_7W_6-μ in the isothermal section at 1000 °C.

The SEM BSE image of Co-Ni-W triple junction area is shown in **Fig. 5.20(a)**. Two phase layers of intermetallic compound Ni_4W and μ were formed in the Ni-W binary side after annealing. Bouliez et al. pointed out that the $(Co, Ni)_3W$ has two crystal structures from analysis on their heat-treated samples at 1000 °C for 720 hours [185]. One is the Co_3W-$D0_{19}$ with prototype Ni_3Sn and another one is the Co_3W-$D0_a$ ternary compound with prototype Cu_3Ti. As shown in **Fig. 5.21**, there exists a gap inside the red circle marked region between the two clustering of compositions, indicating that the two clustering belong to two different phases which are Co_3W-$D0_{19}$ and Co_3W-$D0_a$ in Co-Ni-W system. The phase boundary between Co_3W-$D0_{19}$ and Co_3W-$D0_a$ phases is mapped using white line in the SEM BSE image. In the Co-W binary side, the μ phase layer is narrow with only a few microns while Co_3W-$D0_{19}$ has a diffusion distance of ~ 50 μm.

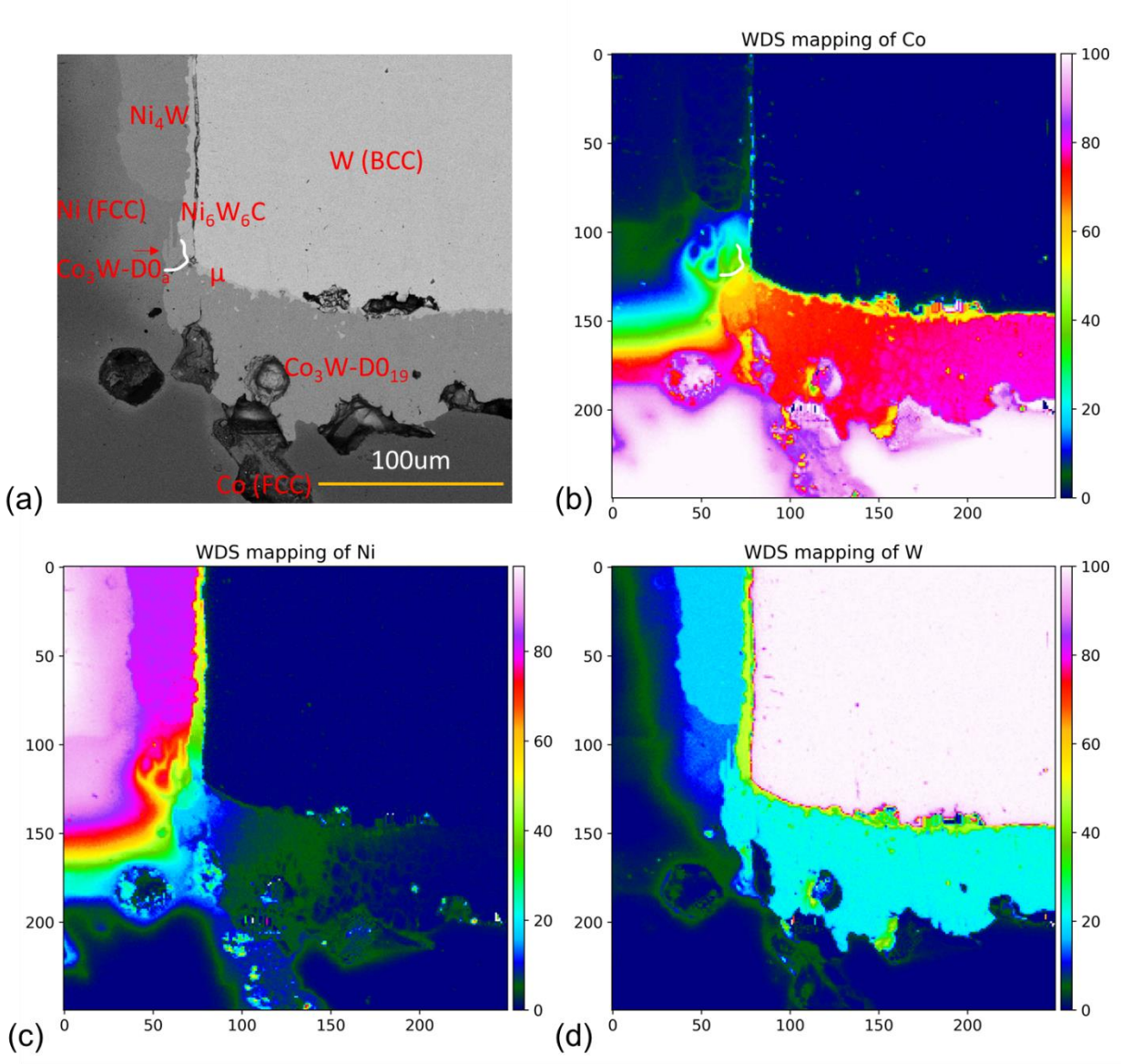

Figure 5.20 (a) SEM BSE image of Co-Ni-W triple junction in the diffusion multiple. (b), (c), and (d) are the composition heatmap of Co, Ni, and W in the Co-Ni-W system, respectively.

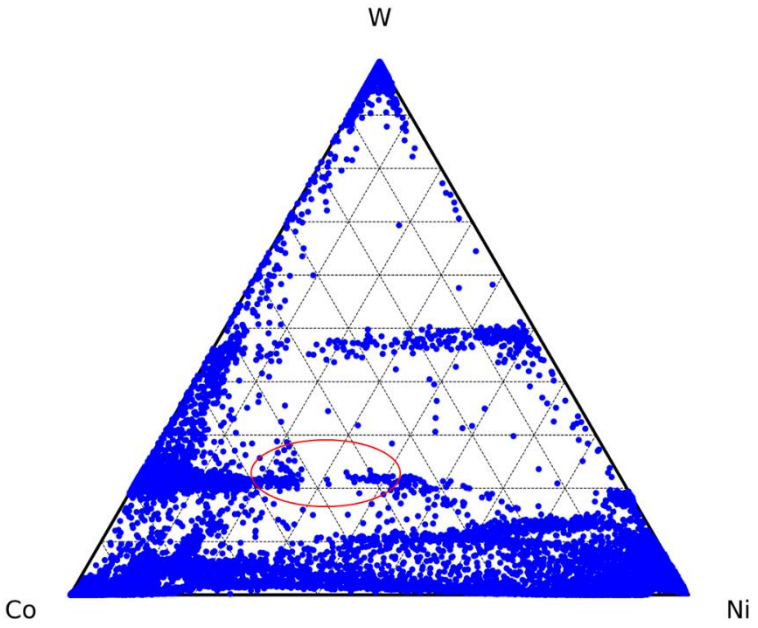

Figure 5.21 The ternary diagram with all the measured compositions in Co-Ni-W system.

With the phase and composition information, the isothermal section of Co-Ni-W at 700 °C is presented in **Fig. 5.22(a)**. The μ phase has a wide composition range, 0 to 55 at.% Co and ~ 50 at.% W from Co-W to Ni-W binary side. The Co_3W-$D0_{19}$ phase dissolves up to 24 at.% Ni, comparing with solubility of ~ 62 at.% at 800 °C and ~ 13 at.% at 900 °C in Zhu et al.' work [200]. According to the study of Bouliez et al., mislabeling Co_3W-$D0_a$ as the Co_3W-$D0_{19}$ at 800 °C could have happened in the work of Zhu et al.. The solubility of Ni in Co_3W-$D0_a$ is from 38 to 48 at.%. The Ni_4W has a limited solubility of Co, ~ 4 at.%, compared with solubility of ~ 7 at.% at 800 °C and ~ 3 at.% at 900 °C. Four ternary phase equilibria are observed, and they are FCC + Co_3W-$D0_{19}$ + Co_3W-$D0_a$, μ + Co_3W-$D0_{19}$ + Co_3W-$D0_a$, FCC + μ + Co_3W-$D0_a$, and FCC + μ + Ni_4W. The calculated isothermal section using TCNI11 database is presented in **Fig. 5.22(b)**. The predicted phase area of μ phase is very narrow compared with experimentally mapped μ phase. The Co_3W-$D0_{19}$, Co_3W-$D0_a$, and Ni_4W were not predicted in the calculated

diagram, requiring more efforts to improve the predictive ability of Ni-based database for the Co-Ni-W system.

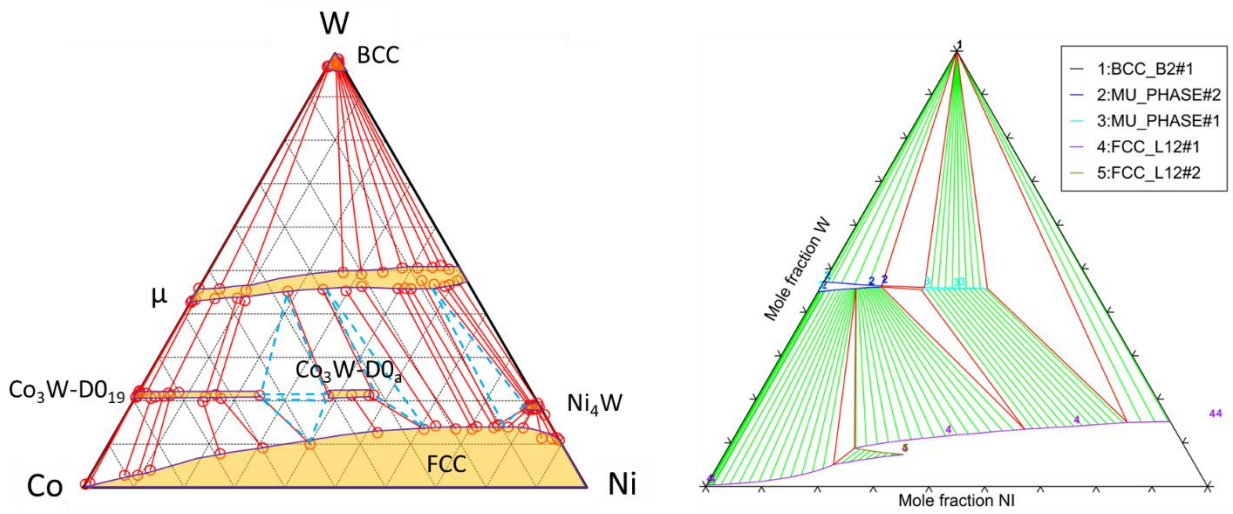

Figure 5.22 (a) Experimental and (b) calculated (using TCNI11 database) isothermal sections of Co-Ni-W ternary system at 700 °C.

5.4 Conclusions

In summary, a new developed approach to mapping phase diagram of ternary systems was developed and demonstrated using the Fe-Nb-Ni ternary system (**Fig. 5.6**). This approach was also used to explore other ternary systems such as Cr-Nb-Ni, Co-Cr-Ta, Co-Cr-W, Co-Ni-Ta, and Co-Ni-W, generating large amount of phase equilibrium data. Thermodynamic assessment was done on Fe-Nb-Ni and Cr-Nb-Ni systems, and good agreement was achieved between the predictions and experiments. Our reassessed parameters will help build a more reliable and robust Ni-based database.

Chapter 6: Assessments of diffusion coefficient and atomic mobilities of binary systems

6.1 Introduction

The 1-parameter Z-Z-Z model developed in the literature was demonstrated to be very reliable and robust based on the test of 18 binary systems covering ~9 orders of magnitude and a temperature range from ~800 °C to ~2000 °C, as summarized in **Fig. 6.1** [206]. The goal of this project is to apply the developed model to other binary systems and extract the parameters by

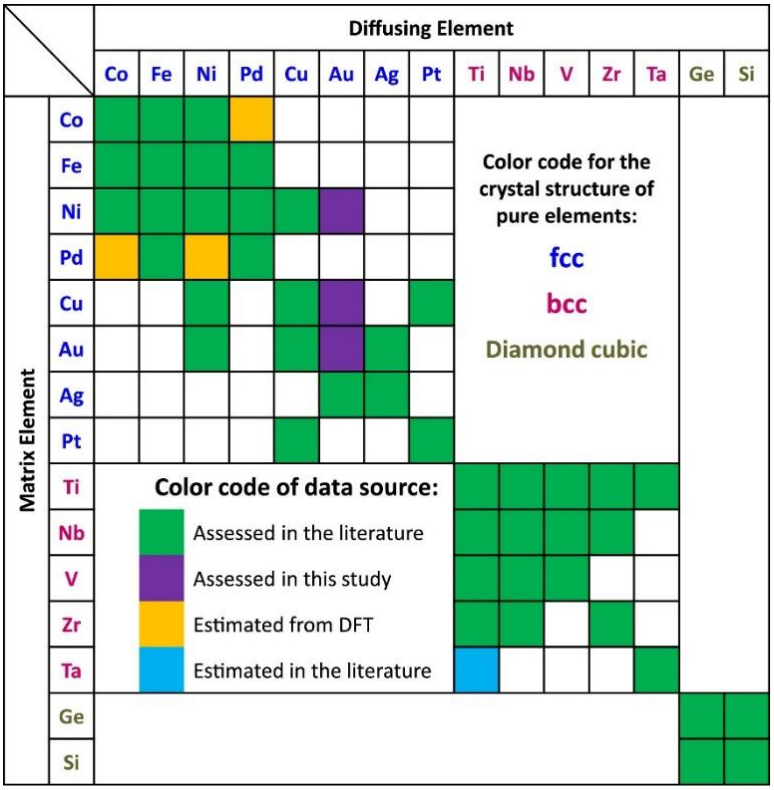

Figure 6.1 The summary of assessment of the self-diffusion and impurity diffusion coefficient of pure elements in the 18 binary systems [206].

fitting the experimental data, and then use machine learning (ML) models to make predictions for the Z-Z-Z model parameters.

6.2 Methods

The interdiffusion coefficient of a binary A-B system can be expressed using Darken's equation **Eq. (1.14)** [23], rewritten here:

$$\widetilde{D} = x_B D_A^I + x_A D_B^I = (x_B D_A^* + x_A D_B^*)\psi \qquad (6.1)$$

where $\widetilde{D}$ is the interdiffusion coefficient, D_i^* is the tracer diffusion coefficient of i (A or B), and D_i^I represents the intrinsic diffusion coefficient of i. x_A and x_B are the mole fractions of element A and B. ψ is the thermodynamic factor which can be calculated using thermodynamic databases and CALPHAD software. The tracer diffusion coefficient can be modeled using the Ågren-Andersson treatment:

$$lnD_i^* = x_A lnD_i^A + x_B lnD_i^B + x_A x_B \sum_{r=0,1,\ldots} \Phi_i^{A,B}(x_A - x_B)^r / RT \qquad (6.2)$$

where D_B^A and D_B^B are the impurity diffusion coefficient of B in A and self-diffusion coefficient of B, respectively. In the case of r = 0, **Eq. (6.2)** becomes:

$$lnD_i^* = x_A lnD_i^A + x_B lnD_i^B + \Phi_i^{A,B} x_A x_B / RT \qquad (6.3)$$

$$D_i^* = exp\left(x_A lnD_i^A + x_B lnD_i^B\right) exp((\mathrm{a_i} + b_i T)\, x_A x_B / RT) \qquad (6.4)$$

The interaction parameter $\Phi_i^{A,B} = a_i + b_i T$ is the same as the interaction parameter in the atomic mobility notation. The intrinsic and interdiffusion coefficients can be derived from the tracer diffusion coefficients from Darken's expression, **Eq. (6.1)**. The 1-parameter Z-Z-Z model treats $\Phi_A^{A,B} = \Phi_B^{A,B} = a$, and the relationship among these diffusion coefficients and whole process of

fitting for Fe-Ni binary system is illustrated in **Fig. 6.2**. Tracer diffusion coefficient serves as a bridge connecting interdiffusion and impurity coefficients. The interdiffusion coefficient $\widetilde{D}$ becomes D_{Fe}^{Ni} when composition of Ni is approaching to 100 at.%. The objective function used for fitting is a mean squared error expression:

$$F = \frac{1}{2}\sum_{i=1}^{n}\left(lnD_i^{pred} - lnD_i^{exp}\right)^2 \qquad (6.5)$$

where n is the number of input data points, D_i^{pred} and D_i^{exp} are the predicted diffusion coefficients and experimental diffusion coefficients of the *i*th data point. For each binary system, only one interaction parameter needs to be optimized.

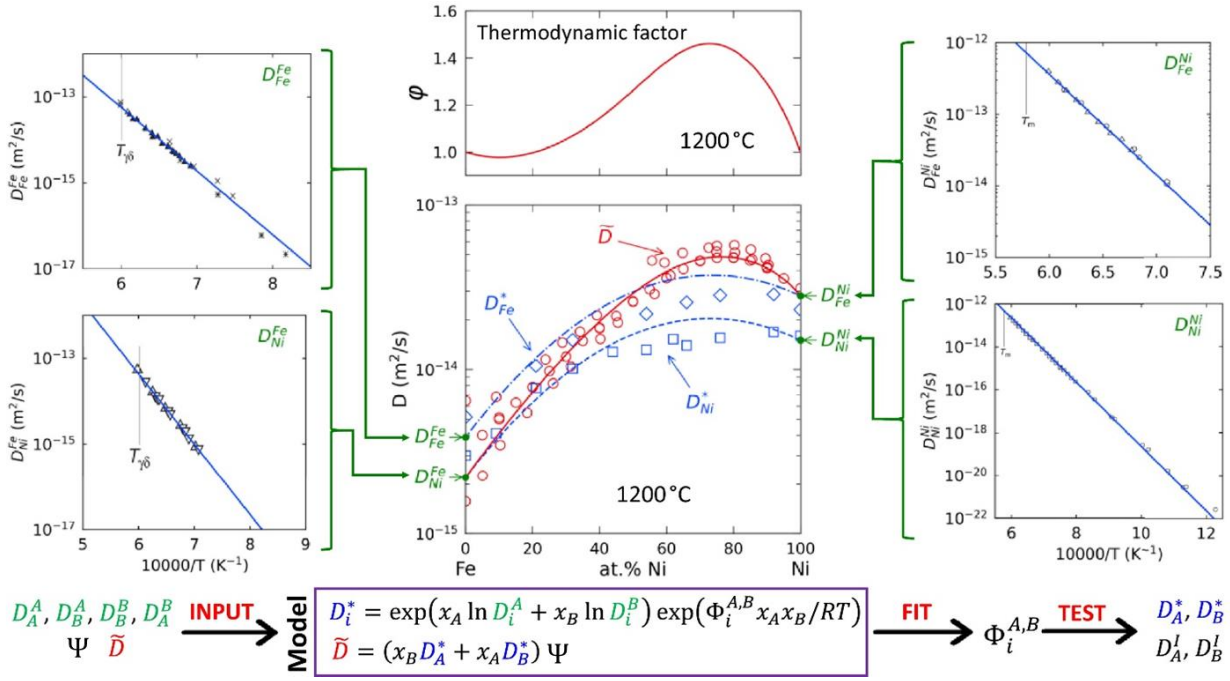

Figure 6.2 Diffusion coefficients and thermodynamic factor plot of the FCC phase in the Fe-Ni binary system [206].

In this project, additional assessments were performed of 12 binary systems with the bcc crystal structure (Cr-Ti, Hf-Ti, Hf-Zr, Mo-Nb, Mo-Ta, Mo-Ti, Mo-W, Mo-Zr, Nb-Ta, Nb-W, Ta-W, Ta-Zr) and 13 binary systems with the fcc crystal structure (Al-Co, Al-Cu, Al-Ni, Co-Cu, Co-Mn, Co-Cr, Co-Pt, Cr-Fe, Cr-Ni, Cu-Mn, Fe-Mn, Mn-Ni, Ni-Pt) using the literature data, as presented in **Fig. 6.3**. The four end members D_A^A, D_B^A, D_A^B, D_B^B in the **Eq. (6.4)** are the initial input data. For some systems, these four end members are well assessed based on reliable diffusion data; while for other systems, the end members might be assessed inadequately because of data selections or were not assessed due to lack of experimental data. In those cases, re-evaluation of the diffusion data was performed for the impurity diffusion or self-diffusion coefficient with careful evaluation of the available data or leverage the predicted values from the ML study performed by Wei et al. [207]. The newly assessed binary interaction parameters are provided to our collaborators to enhance the ML model for more reliable prediction of diffusion coefficients of binary solid solution systems.

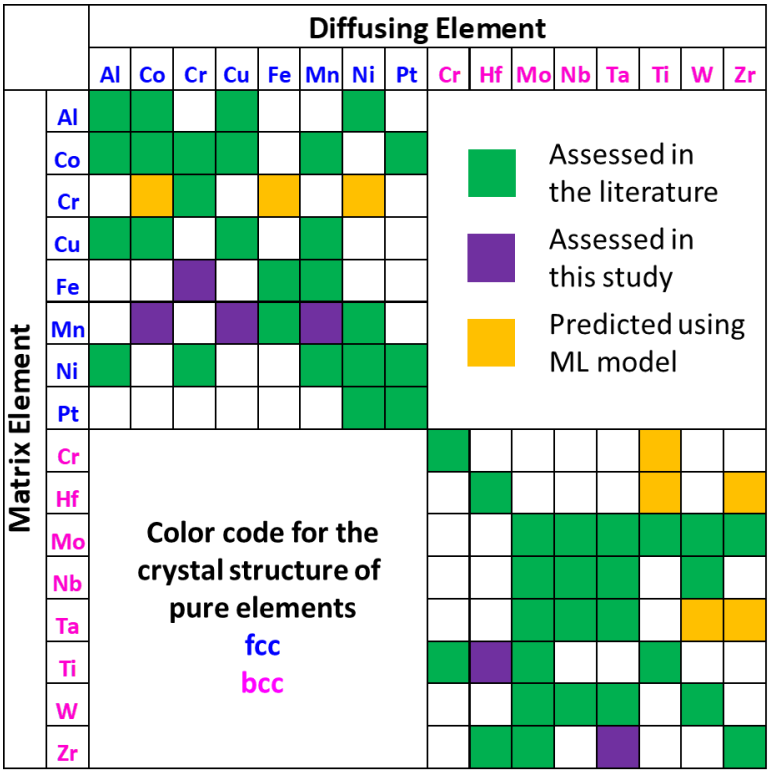

Figure 6.3 The summary of assessment of the self-diffusion and impurity diffusion coefficient of pure elements in the 12 single BCC binary systems and 13 single FCC binary systems.

6.3 Results and summary

All the 25 binary systems were assessed based on the literature data using the Z-Z-Z model. And the assessed interaction parameters for each system is summarized in **Table 6.1**. We selected three representative binary systems to show the details, including two BCC Mo-Ti, Hf-Ti systems, and one FCC Co-Mn system.

Table 6.1 Summary of assessed binary interaction parameters using the Z-Z-Z model.

BCC system	$\Phi_i^{A,B}$ (J/mol)	FCC system	$\Phi_i^{A,B}$ (J/mol)

Cr-Ti	162773.43	Al-Co	-41994.52
Hf-Ti	16879.74	Al-Cu	-3308.77
Hf-Zr	6391.45	Al-Ni	-164014.58
Mo-Nb	-111386.79	Co-Cu	-52855.45
Mo-Ta	-109889.15	Co-Mn	-20936.15
Mo-Ti	38073.87	Co-Cr	46694.51
Mo-W	-94201.69	Co-Pt	-2318.28
Mo-Zr	205209	Cr-Fe	112105.49
Nb-Ta	77630.03	Cr-Ni	58596.46
Nb-W	124353.2	Cu-Mn	97608.87
Ta-W	52090.11	Fe-Mn	-33933.49
Ta-Zr	214265.8	Mn-Ni	196125.4
		Ni-Pt	34590.51

6.3.1 Mo-Ti

The diffusion behaviors in Mo-Ti have been explored in many works [43,208–213]. Heumann and Imm investigated the interdiffusion and intrinsic diffusion of Mo-Ti at 1446 °C, showing that the intrinsic diffusion coefficients of Ti are greater than that of Mo generally [212]. Zhu et al. explored the interdiffusion at 899 °C and 1100 °C using diffusion multiple approach [210], and Chen et al. further studied the interdiffusion at 800 °C, 1000 °C, and 1200 °C [43]. Their reported results agree well with other literature data. Bian et al. studied the interdiffusion

behaviors at 1000 °C, 1100 °C, 1150 °C, and 1200 °C using four different diffusion couples [211].

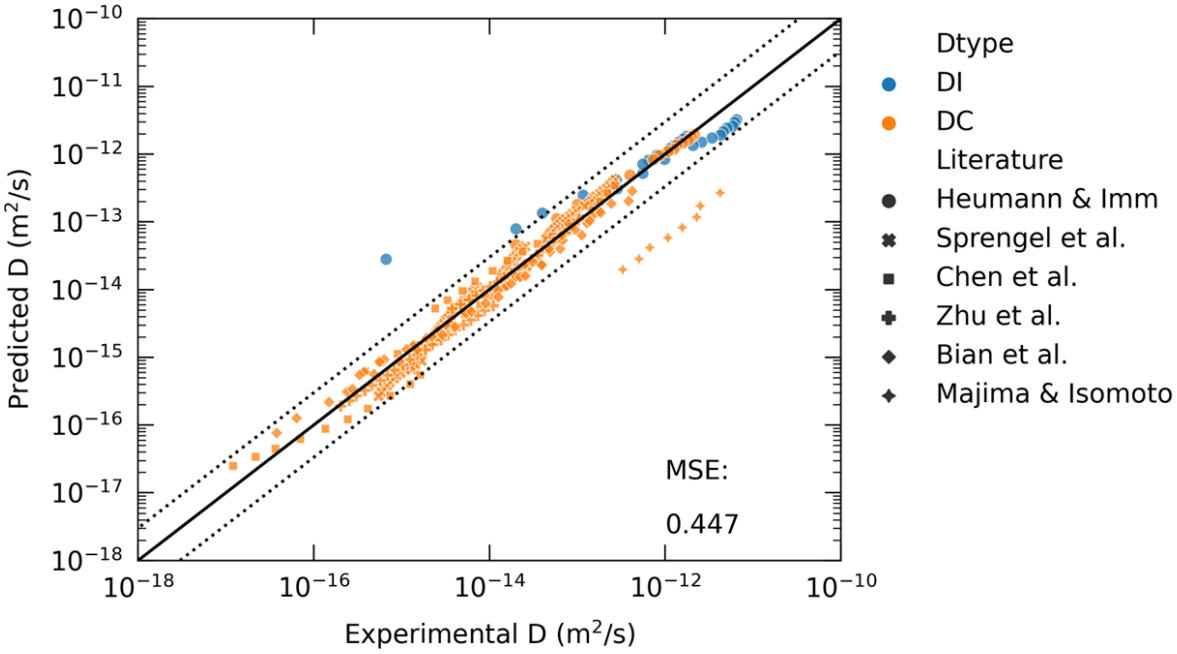

Figure 6.4 Predicted D versus experimental D for Mo-Ti system using the Z-Z-Z binary diffusion model. Color represents diffusion types and marker represents data source. The dashed line represents a deviation from the fitting results (solid line) with a factor of 3 or 1/3.

The modeling results are shown in **Fig. 6.4**. While the data from Majima and Isomoto shows a large deviation from the fitting curve, most of the data lie in the zone between two dashed lines, indicating a good fitting result. The fitting results for interdiffusion coefficients data are

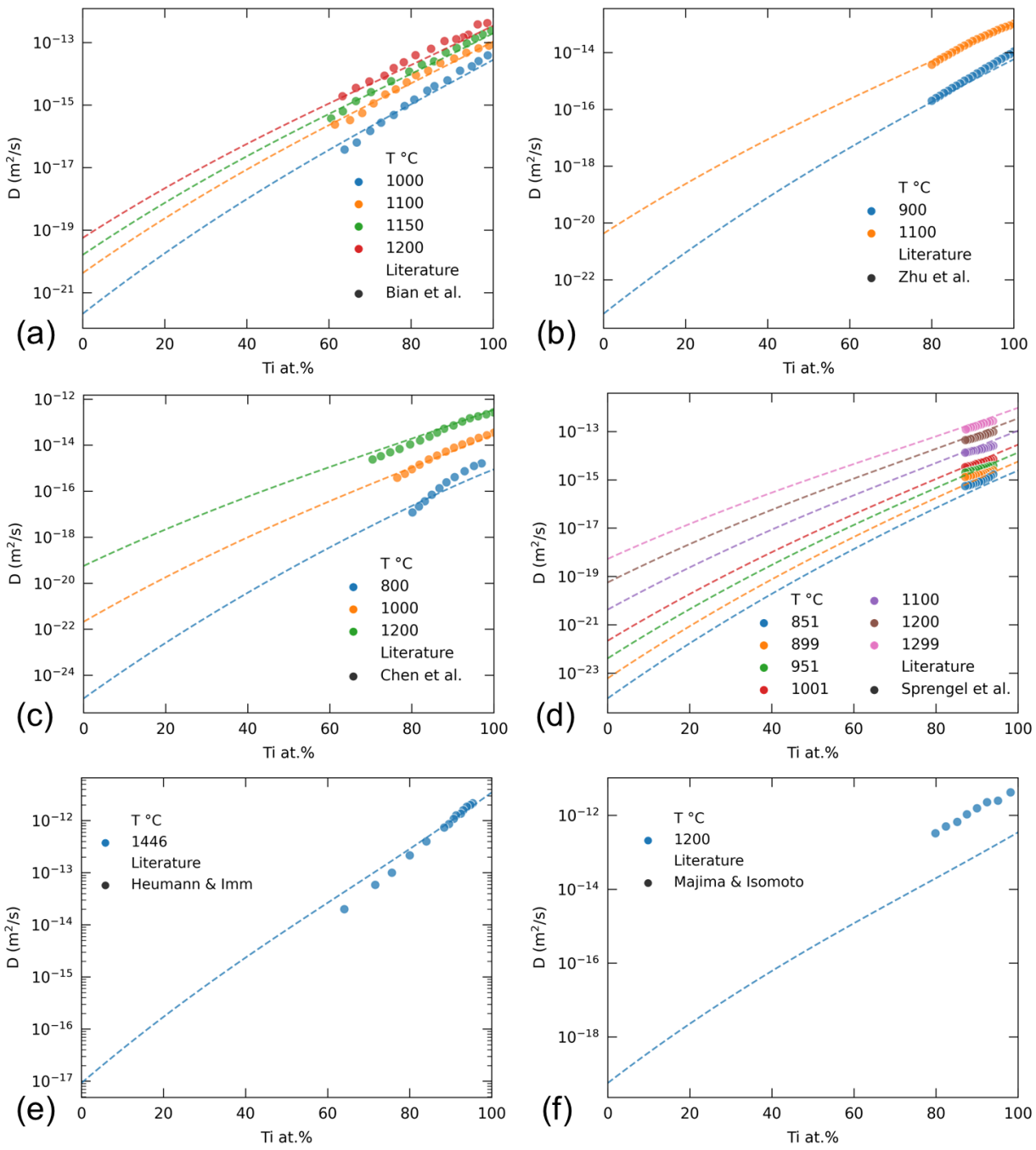

Figure 6.5 Fitting results for interdiffusion coefficients in Mo-Ti system. Dashed lines are the fitting results. (a), (b), (c), (d), (e), and (f) represents the comparison between predictions and the experimental data from different studies [43,208–212].

presented individually in D-versus-composition plot (**Fig. 6.5**). As shown in **Fig. 6.5(e)**, the fitting curve agrees well with the data from Heumann and Imm near the pure Ti side, but the fitting becomes bad towards the intermediate compositions. A clear disparity (about 1 order of magnitude) exists between the predictions and the composition-dependent interdiffusion coefficients presented in **Fig. 6.5(f)**. The fitting results for intrinsic diffusion coefficients are presented in **Fig. 6.6**. It shows good consistency at pure Ti side for Mo intrinsic diffusion coefficients and at intermediate Ti compositions for Ti intrinsic diffusion coefficients. After excluding the significantly deviating data, we refitted the model and got the assessed interaction parameter, $\Phi_i^{A,B}$ = 38073.87 J/mol.

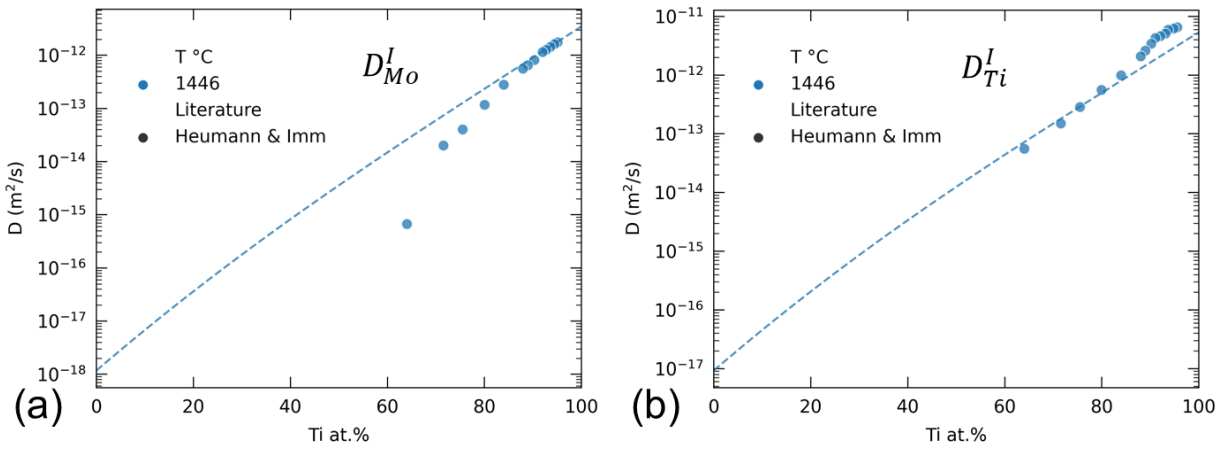

Figure 6.6 Fitting results for intrinsic diffusion coefficients in Mo-Ti system. (a). Mo intrinsic diffusion coefficient. (b) Ti intrinsic diffusion coefficient [212].

6.3.2 Hf-Ti

Gall et al. conducted diffusion annealing experiments at a series of temperatures between 1000 and 2000 °C and reported multiple interdiffusion coefficients data [214]. Zhu et al. designed diffusion multiple to extract interdiffusion coefficients after annealing at 900 °C (600 h), 1000

°C (120 h), 1100 °C (25 h), and 1200 °C (10 h) [210]. Since no impurity data of Hf in Ti is available from previous work, we adopted the extrapolated impurity coefficients from Gall et al. to fit the Arrhenius equation to obtain the pre-exponential factor and activation energy. And the fitting result with equation $D = 1.65 \times 10^{-4} exp\left(-1.2 \times 10^{5}/(RT)\right)$ is shown in **Fig. 6.7**.

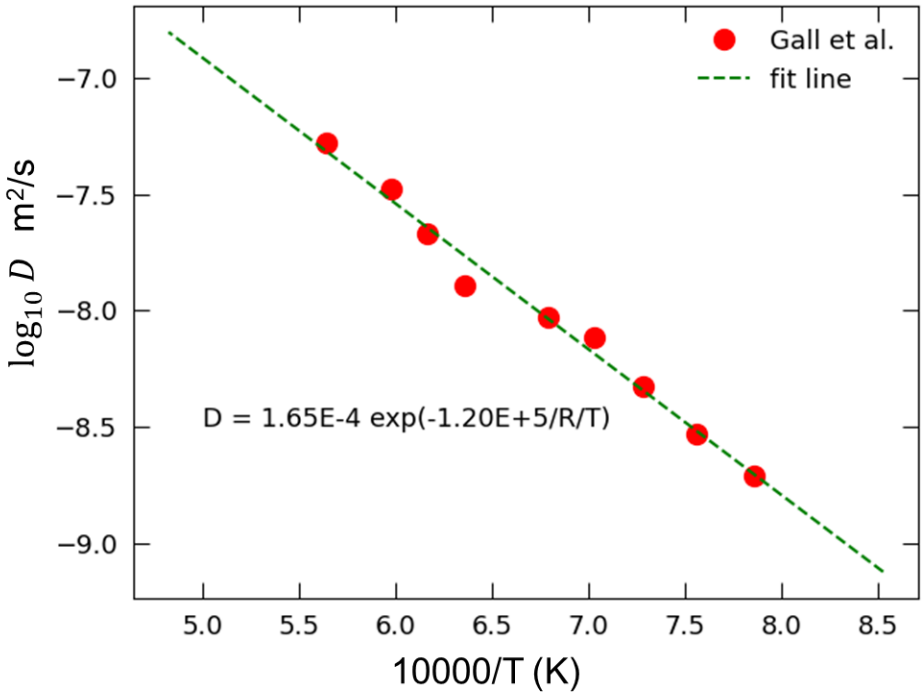

Figure 6.7 The fitting result for impurity coefficient of Hf in Ti using the extrapolated data from Gall et al. [214].

The fitting results for all collected diffusion coefficients is presented in **Fig. 6.8**. All the data are in between the two dashed lines, which shows good agreement between fitting values and literature data. As shown in **Fig. 6.9(a)**, the good fitting results for the interdiffusion coefficients near the Ti end indicates that the self-assessed pre-exponential factor and activation energy based on the extrapolated data is reliable. Using the two datasets, we got $\Phi_i^{A,B}$ = 16879.74 J/mol.

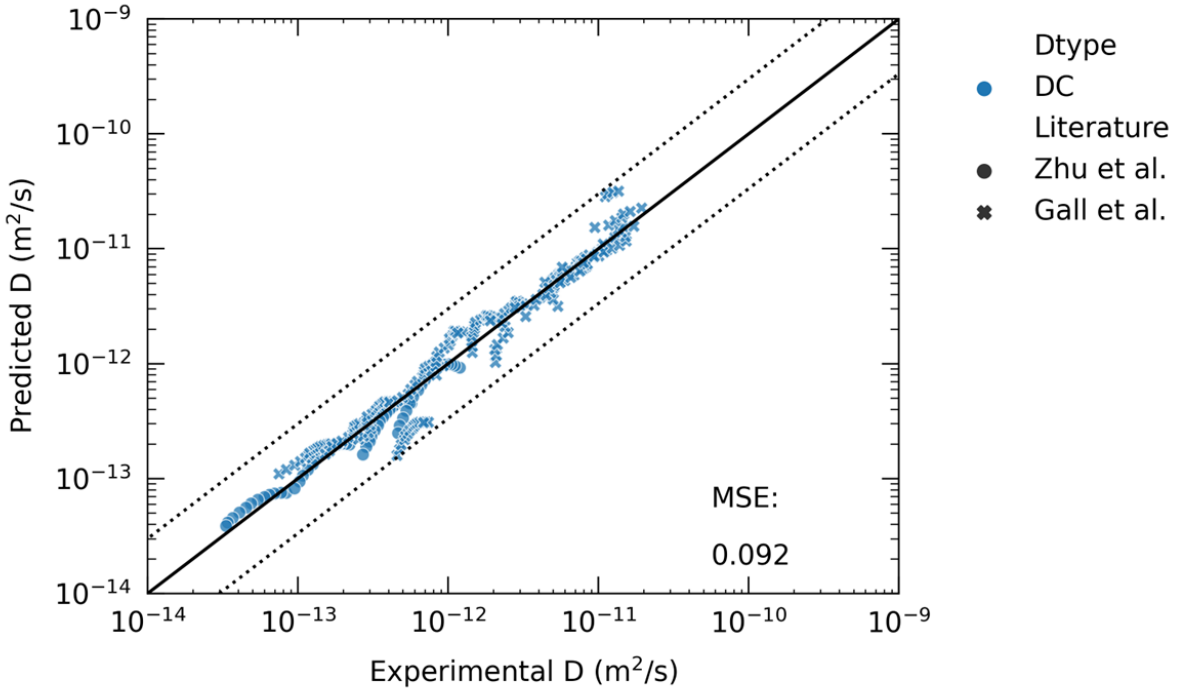

Figure 6.8 Predicted D versus experimental D for Hf-Ti system using Z-Z-Z binary model.

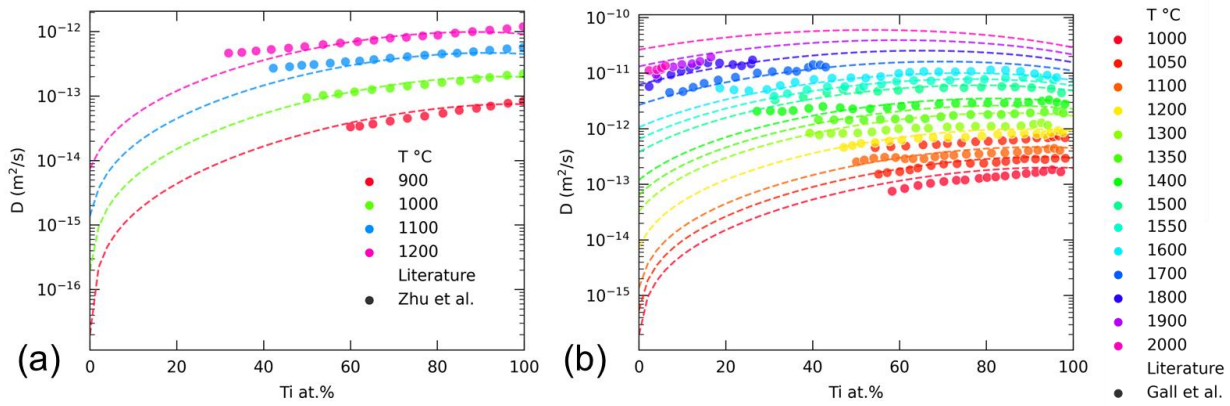

Figure 6.9 Fitting results for interdiffusion coefficients in Hf-Ti system.

6.3.3 Co-Mn

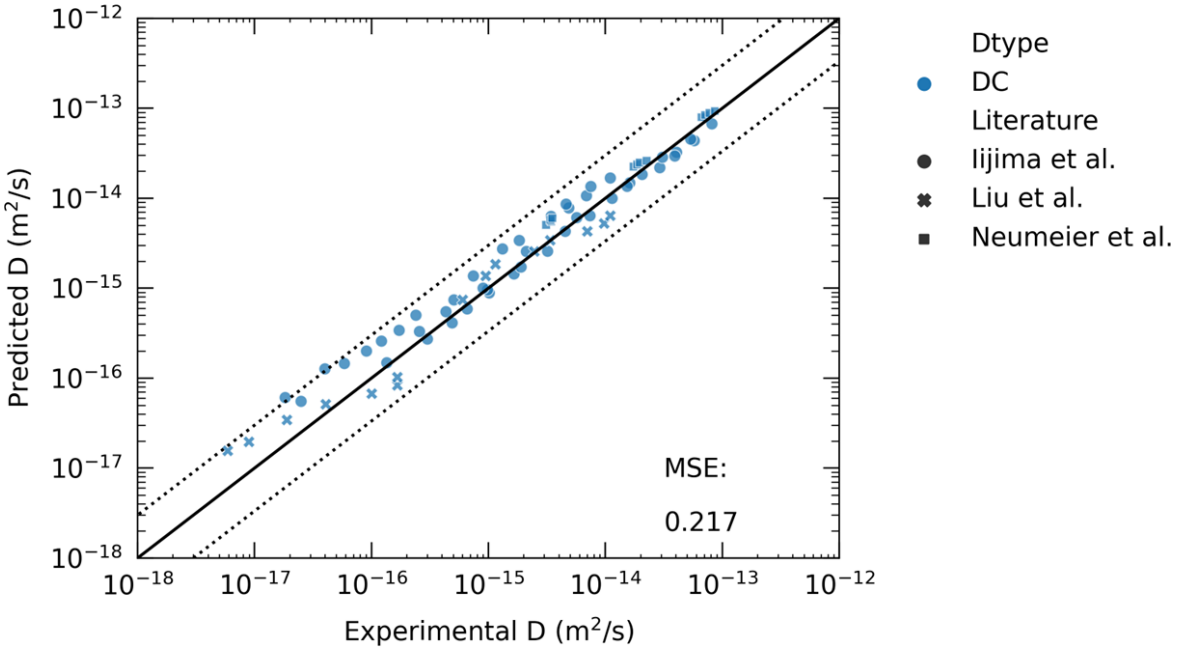

Figure 6.10 Predicted D versus experimental D for Co-Mn system using Z-Z-Z binary model.

Lijima et al. investigated the interdiffusion coefficients in the temperature range between 860 °C and 1150 °C using Co/Co-30.28Mn and Co/Co51.76 Mn diffusion couples [215]. They reported the frequency factor and activation energy of intrinsic diffusion coefficients at 33 at.% Mn. Neumeier et al. explored the interdiffusion behaviors in a composition range from 0.5 to 5.5 Mn at.% at 1100 °C, 1200 °C, and 1300 °C using Co/Co-6Mn diffusion couple [216]. The diffusivity of transition metal solutes in Co is generally smaller than that in Ni, which suggests a slower diffusion process in Co than in Ni, as reported by them. A mobility assessment was performed by Liu et al. on their experimental data at 800 °C and 1000 °C along with the data from other studies [217]. They used 5 parameters totally to optimize the model and obtained good fitting results.

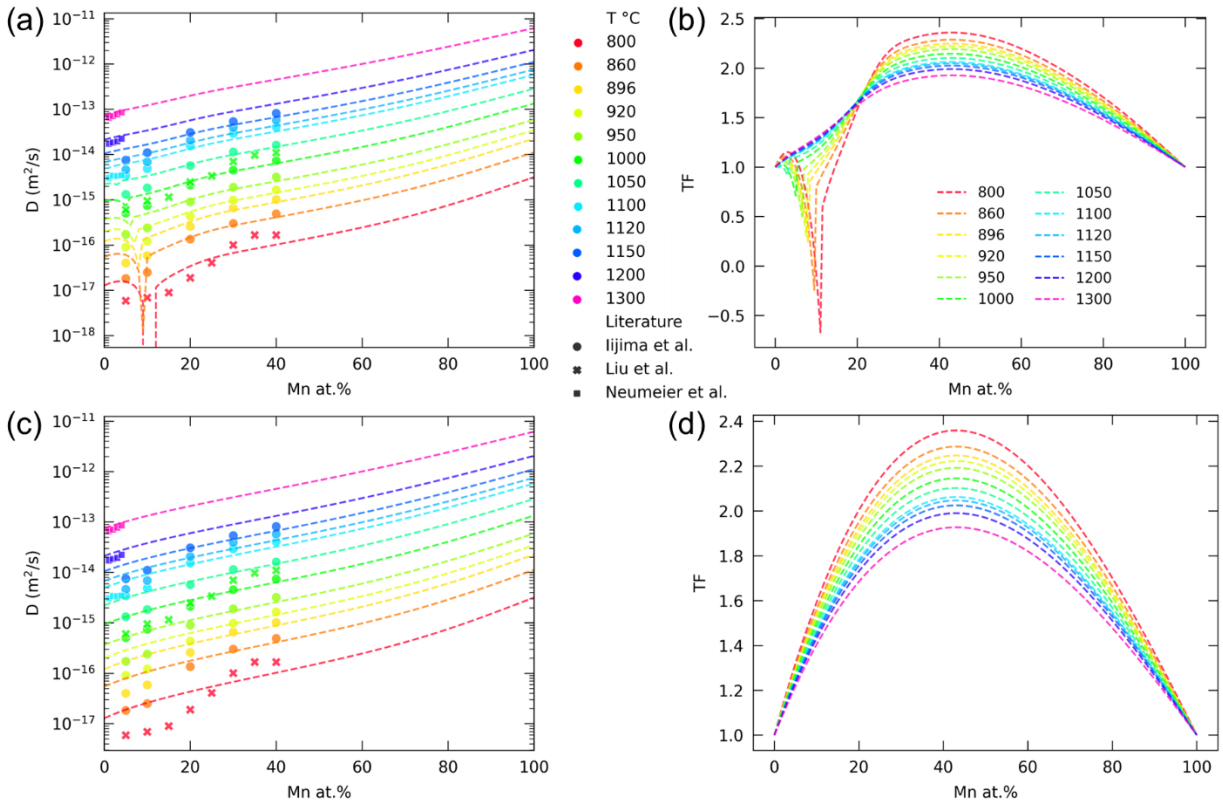

Figure 6.11 Fitting results for interdiffusion coefficients in Co-Mn system. (a) Fitting results and (b) thermodynamic factors using Thermo-Calc implemented TCNI11. (c) Fitting results and (d) thermodynamic factors using the database from literature after excluding magnetic terms [218].

We employed the TCNI11 implemented in Thermo-Calc to calculate the thermodynamic factor in Co-Mn system and got negative values near 10 at.% Mn, as shown in **Fig. 6.11(b)**. And therefore, a drastic drop to infinity shows up in the fitting results (**Fig. 6.11(a)**) because the negative diffusion coefficients are predicted and included in the natural logarithm function in **Eq. (6.5)**. This phenomenon is due to the assessed parameters describing effects of magnetism in the TCNI11 database. To avoid this case, the assessed database from literature excluding magnetic

parameters was adopted [218]. The newly fitting results are presented in **Fig. 6.11(c)** with recalculated thermodynamic factors in **Fig. 6.11(d)**. The fitting curves become smooth compared with that in **Fig. 6.11(a)**, better explaining the behaviors of interdiffusion coefficients. The interaction parameter we optimized is $\Phi_i^{A,B}$ = -20936.15 J/mol.

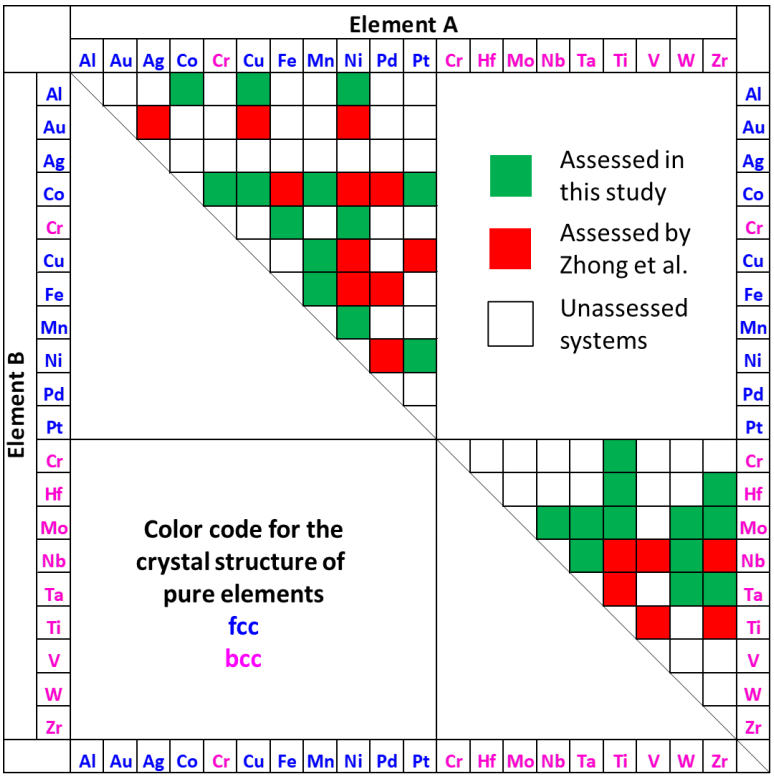

Figure 6.12 Summary of assessed systems by Zhong et al. and by this study.

In summary, we adopted the Z-Z-Z binary diffusion model to study the diffusion coefficients of 12 BCC binary systems and 13 FCC binary systems. Up to now, we have total 43 BCC or FCC systems (25 systems in this study + 18 systems in Zhong et al.). We will keep collecting the diffusion data on other systems (labeled in white color in **Fig. 6.12**) and provide the data to our collaborator to build reliable ML models to predict diffusion coefficients.

Chapter 7: The property measurement on Mo-Nb, Mo-Ta, Nb-Ta binary systems

7.1. Introduction

The diffusion-multiple approach enables high-throughput studies of the phase diagram and composition-structure-property relationships in binary, ternary, and high-order systems [2,2,5]. For example, the relationship between hardness and compositions was investigated in a Ni-Pt diffusion couple heat-treated at 900 °C for 1650 h [35]. A diffusion distance of around 160 microns from pure Ni to pure Pt was created in the diffusion couple and was helpful for the hardness measurement at locations with various compositions. It was found that the hardness

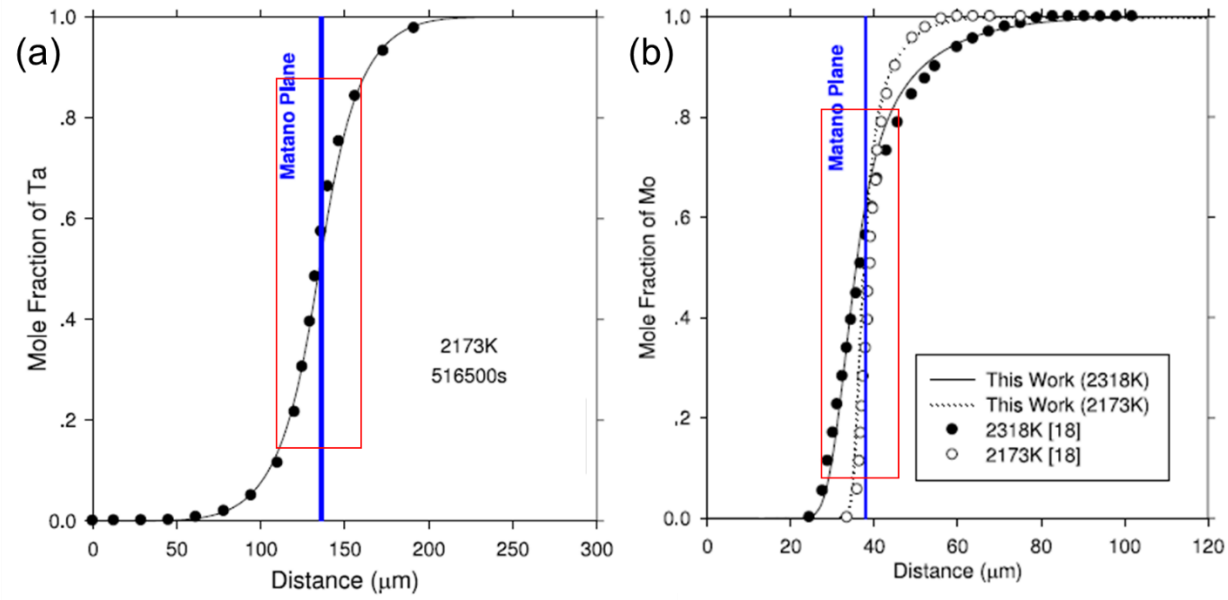

Figure 7.1 The calculated and experimental diffusion profiles in Mo-Ta diffusion couple annealed at 2173K for 516,500s.

of Ni-Pt alloys with intermediate compositions was higher than that of pure Ni or Pt due to the solution hardening mechanism. The diffusion multiple method is dictated by kinetics, and it requires appropriate annealing time and temperature to create composition change/gradient over a sufficiently long distance for the sluggish diffusion elements with low diffusion coefficients.

In the slow-diffusing system consisting of refractory elements, the number of data points we can measure in the diffusion zone is limited to describe the composition-property relationship sufficiently. For example, **Fig. 7.1(a)** represents the diffusion profile of Mo-Ta binary system at 1900 °C for 143.5 h [219]. In the rectangle enclosed area, the mole fraction of Ta changes from 0.15 to 0.85 over 50 μm, which is about 0.72 μm / 1 at.%. The spacing between two indents is usually 5 μm or even higher in the nanoindentation test. It can be easily deduced that we can measure the hardness every 7 at.%, which is about 15 data points for the hardness over the full range of composition. A steeper slope is shown in the diffusion profiles of Nb-Ta system in **Fig. 7.1(b)**. The number of data points we can obtain are limited to describe the property-composition relationship completely, so we need to increase either the temperature or diffusion time to get a smaller composition gradient over distance. However, it needs high-quality experimental facilities and a long experimental period, making it cost-ineffective.

Electron beam welding (EBW) uses a high-energy beam of electrons to melt the welded joint area to join metallic materials under a vacuum [220]. It is an efficient method of welding that is particularly useful for joining materials that are difficult to weld using other methods. EBW is often used in many different industrial fields: automotive, aerospace, mechanical and electrical power engineering, as well as in the production of medical implants since it has advantages in high-density heat input, low level of deformation, and less heat loss in the welding process compared with other heating sources or approaches [221–223]. One of many applications of

EBW is alloying, a dynamic process of melting and solidifying surface layers in a substrate [224–228]. The aluminum effect on the microstructures and mechanical properties of AZ-series alloys were studied using similar metals welding and dissimilar metals welding [227]. Grain coarsening and submicron-sized crystal precipitation were reported to contribute to the formation of the microstructure of the heat-affected zone in Mg-Al-Zn weldment. By melting the materials in a single pass or multiple passes, the compositions of the layers can be optimized to reach specific and desired characteristics and properties. The alloying process can help materials achieve a layered structure with various compositions in each layer, which is beneficial to the design of functional or structural materials with specific property demands on different parts of materials [229].

The composition-property measurement takes advantage of the diffusion process in the diffusion multiple, which is hard to be performed in the binary systems consisting of refractory elements with high melting points and low diffusivity. The EBW is a helpful tool to join two pieces of refractory metals with a certain thickness because of its high-energy and narrow electron beam [230]. Therefore, the EBW technology is leveraged to create a new experiment method to prepare binary couples with a long distance of composition variation, that is to say, a small composition gradient. This new method has been demonstrated in this study to obtain the composition-property (hardness) relationship in the Mo-Nb, Mo-Ta, and Mo-Ta binary systems.

7.2 Experimental procedures

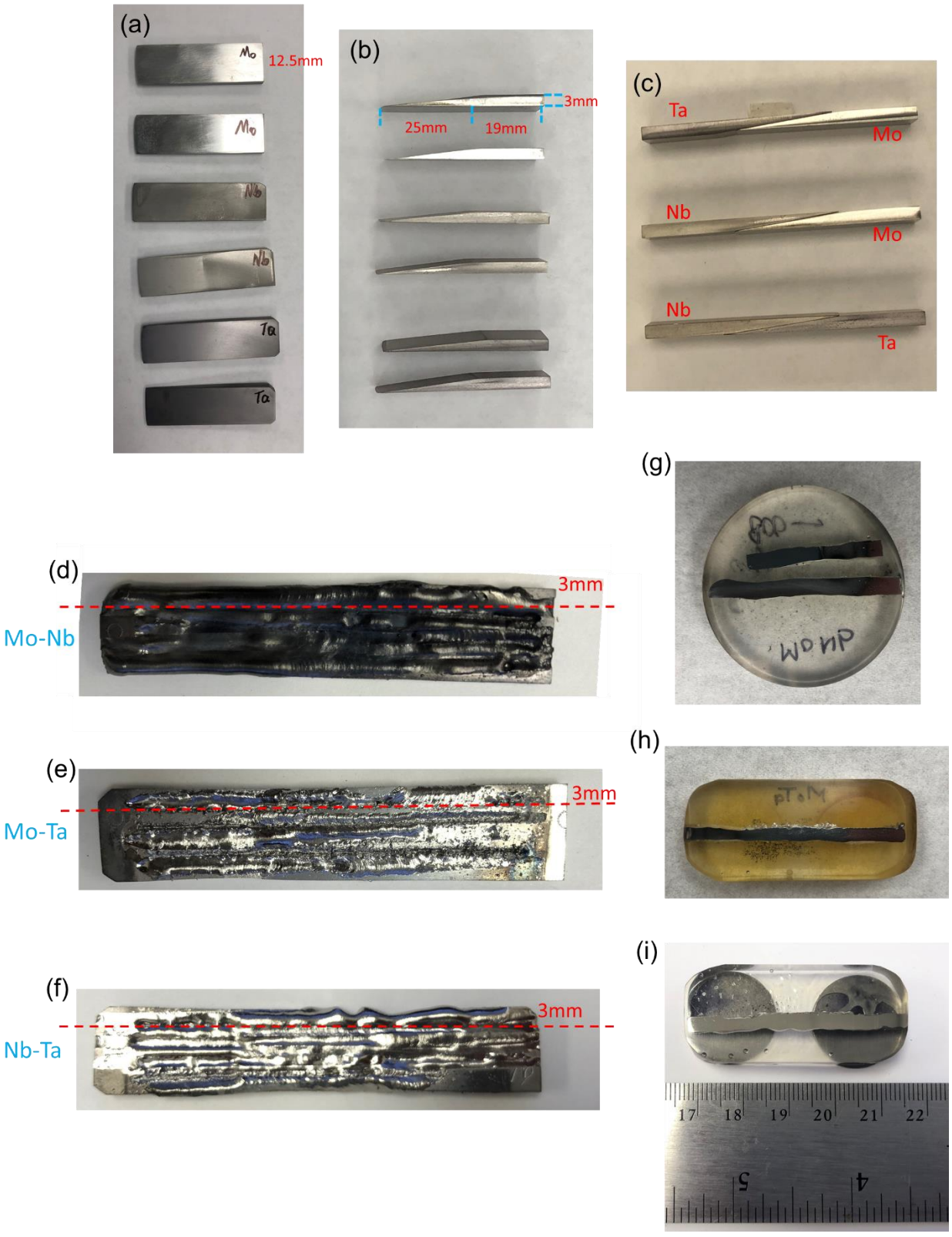

Figure 7.2 The experimental procedures of preparing the electron-beam (EB) welded macro-gradient samples. (a) and (b) are the top and side views of each metal piece. (c) is the arrangement of the metal pieces before EB welding. (d), (e), and (f) are the EB-welded macro-gradient samples for the Mo-Nb, Mo-Ta, and Nb-Ta binary systems, respectively. The red lines are the cutting lines for EDM machining. (g), (h), and (i) are the mounted samples for pieces cut from the macro-gradient samples for the Mo-Nb, Mo-Ta, and Nb-Ta binary systems, respectively.

The top and side views of six metal pieces made using electrical discharge machining (EDM) cutting from the macro-gradient samples, including 2 Mo, 2 Nb, and 2 Ta pieces, are presented in **Fig. 7.2(a)** and **(b)**. These pieces were ground up to 1200 grit using SiC paper. As annotated in the top piece in **Fig. 7.2(b)**, the left part of the metal piece is in a wedge shape with a tapered body for about 25 mm long. Its right part has a cubic body with a length of 19 mm. The width and thickness are 12.5 mm and 3 mm, respectively. To create a zone with mixing compositions, the tapered part of one piece is designed to join with the tapered part of another piece. And the corresponding arrangement of two pieces with different elements before performing joining is shown in **Fig. 7.2(c)**. In order to make the two metal pieces join and mix to reach homogeneity at each location, the EBW technique was employed with a beam of high-velocity electrons scanning the whole samples back and forth on top and bottom sides through multiple passes, whose scanning process is illustrated in **Fig. 7.3**. The composition of one element is expected to range from 0 to 100 atomic percent linearly over roughly 25mm distance in the joined tapered region after EBW processing. The joined materials after EBW are displayed in **Fig. 7.2(d)**, **(e)**, and **(f)**. Grooves formed in the joined samples, which is normal behavior because of the melting

and solidification process in the weld pool. It also indicates that multiple passes are necessary to produce homogeneous compositions at each location on its melting part at different locations from left to right of the joined macro-gradient sample. Then we cut 3 mm thick pieces from the joined materials following the red dashed lines and went through the standard metallographic sample preparation with a final polishing step using 0.05 µm silica suspension to prepare the samples shown in **Fig. 7.2(g)**, **(h)**, and **(i)** for our following materials property measurement. The Mo-Nb piece was broken into two halves accidentally during the EDM process, but it would not affect the property test. It is worthy to note that we cut some materials off at the two ends of the joined materials to make the mounted samples smaller since the materials are pure elements at the two ends. This cutting saved polishing time and had no adverse effects on the experimental results.

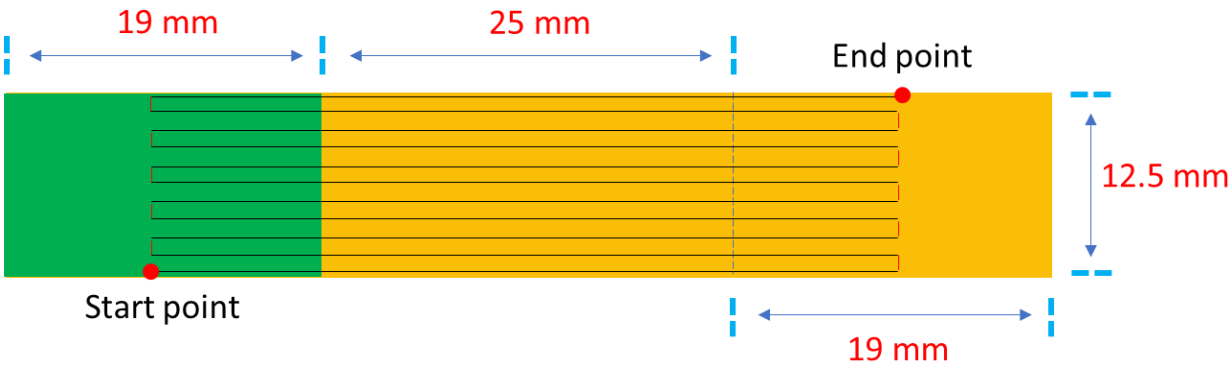

Figure 7.3 The EBW scanning strategy on the samples in a schematic diagram. The black line stands for the scanning directions back and forth with the marked start point and end point. The dimensions are the same as the prepared samples in the experiment.

The hardness test was performed using the TI-900 TriboIndenter with a loading force of 10 mN, a 10 second load time, a 10 second unload time, and a 250 μm interval between two indents. This test was repeated three times to collect more data at each equivalent location. The X-ray diffraction (XRD) with the 2θ angle from 0° to 90° was used to identify the crystal structure information based on Bragg's law at different locations on the samples and lattice parameters were extracted. Scanning electron microscope (SEM) and energy-dispersive spectroscopy (EDS) techniques were employed using the Tescan system to determine the microstructure and composition distribution of these three samples.

7.3 Results and summary

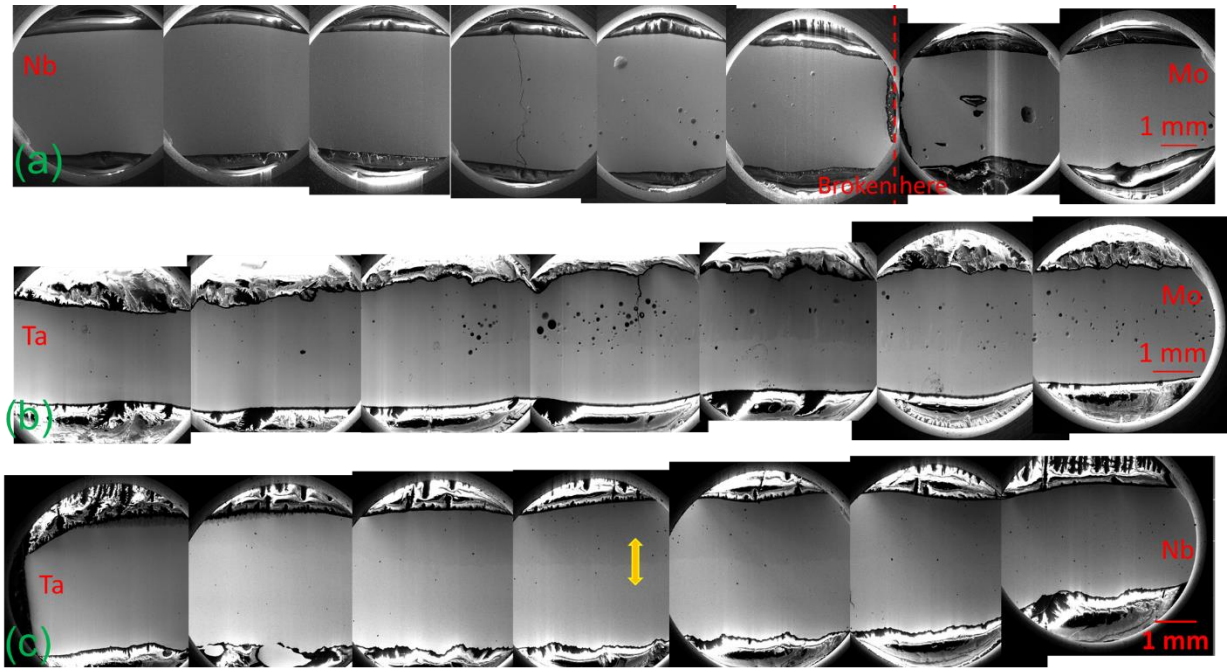

Figure 7.4 (a), (b), and (c) are montages of SEM images taken mainly across the composition mixing zone of the Mo-Nb, Mo-Ta, and Nb-Ta systems, respectively.

The montages of SEM SE images on the surface of the Mo-Nb, Mo-Ta, and Nb-Ta samples are presented in **Fig. 7.4(a)**, **(b)**, and **(c)**, respectively. The magnification was set to be very small to collect these SEM images. The EBW Mo-Nb sample exhibits porosity in the mixing composition region, which is lower than the porosity in the Mo-Ta sample and higher than that in the Nb-Ta sample. Some inclusions formed on the right side of the broken line on the Mo-Nb sample. In the SEM image of the Nb-Ta sample, a brightness contrast can be seen in the bidirectional arrow marked location, which leads to a composition difference of less than 10 at.% in the top half and bottom half regions. Inconsistent EB melting scans in the multiple passes of the EBW process could cause such a difference. The same phenomenon occurs in the Mo-Ta sample. In order to upgrade the surface quality with less porosity and fewer cracks, process parameter maps can be constructed by adjusting the parameters such as the accelerating voltage, beam current, vacuum levels, working distance, and welding speed [231–233]. In this work, the hardness and EDS tests were conducted on the less porous region to decrease the possible incorrect measurement results caused by the pores or cracks.

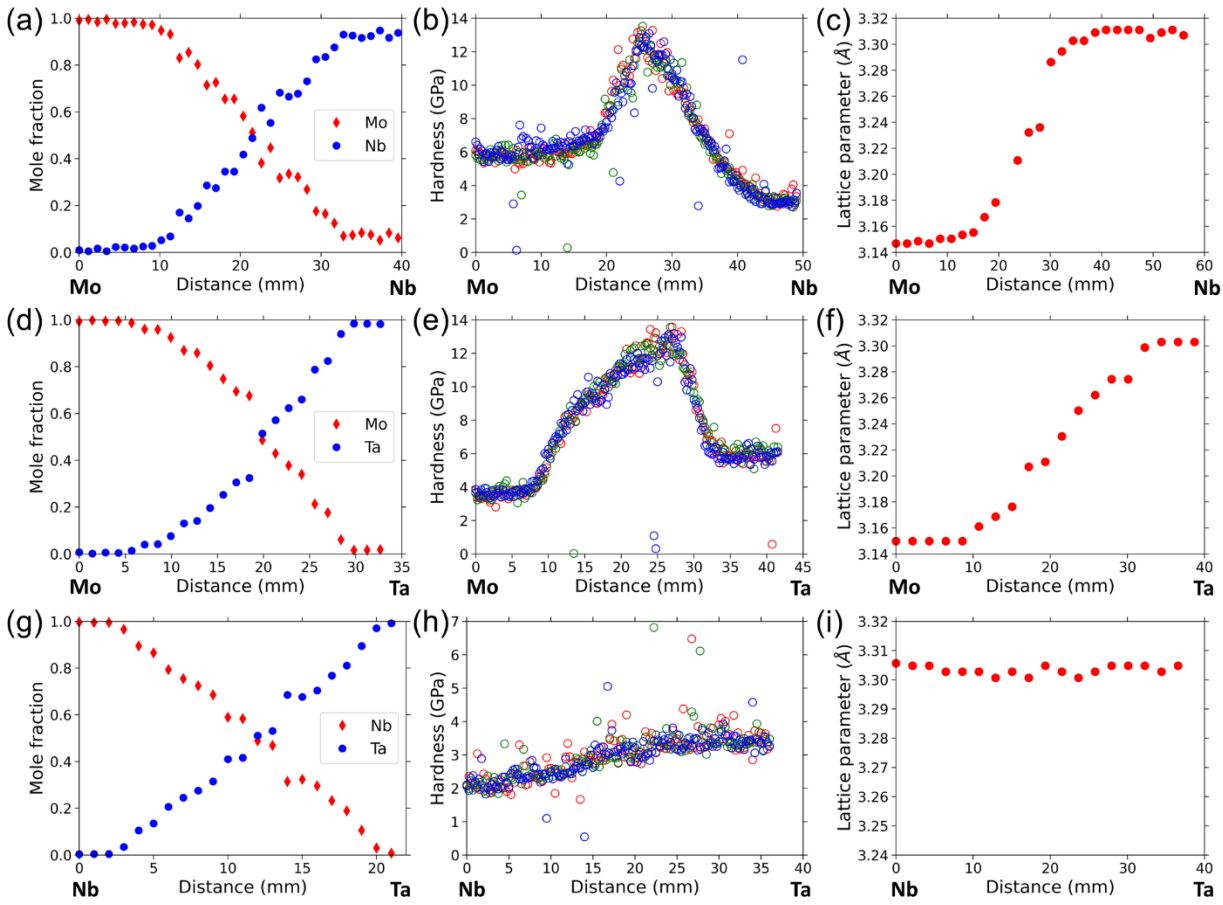

Figure 7.5 (a), (b) and (c) are the composition versus distance profiles, hardness versus distance profiles, and lattice parameter versus distance profiles for the Mo-Nb system, respectively. (d), (e), and (f) are for the Mo-Ta system. (g), (h), and (i) are for the Nb-Ta system. The compositions are from EDS, not WDS, and thus should be considered preliminary. The XRD lattice parameter data are also preliminary and may be further improved in a more detailed analysis in the future.

The composition at various locations was measured using EDS, and the corresponding results are shown in **Fig. 7.5(a)**, **(d)**, and **(g)** for the Mo-Nb, Mo-Ta, and Nb-Ta samples, respectively.

Overall, the composition presents a linear change following the distance from one end of pure element to the other end of another pure element, in accord with our expectations of the preparation method. It is worth noting that the composition of Nb did not reach 100 at.% in our measuring range, and it stayed at around 93 at.% at the right end of the profile in **Fig. 7.5(a)**. This could be attributed to the over-melting near the Nb end which causes the homogeneity in that area.

Three groups of tests were performed along the long-axis direction of the samples, and the corresponding hardness versus distance profiles are shown in **Fig. 7.5(b)**, **(e)**, and **(h)** for the Mo-Nb, Mo-Ta, and Nb-Ta systems, respectively. In the Mo-Nb and Mo-Ta systems, the solid solution hardening (SSH) effect results in the increase of hardness from the two ends towards the intermediate (composition) locations. However, no hardening phenomenon was observed in the Nb-Ta system, and the hardness follows a linear change from pure Nb to pure Ta side of the sample. Since the SSH mechanism is affected by the atomic size difference between the solutes and solvent, the small atomic-size misfit between Nb and Ta has only a trivial contribution to the hardening behavior at intermediate composition locations, which helps to explain the linear change of hardness in the Nb-Ta system [234,235].

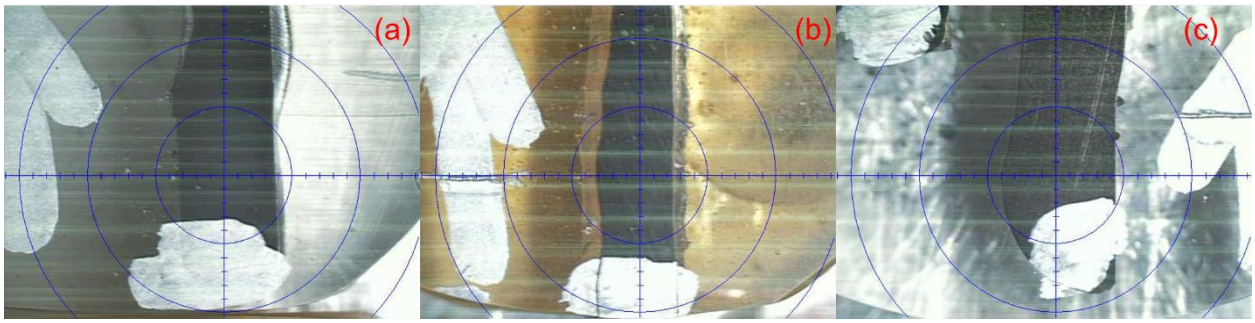

Figure 7.6 The experimental setup for XRD on samples (a) Nb-Ta, (b) Mo-Ta, (c) Mo-Nb. The measurement starts from the side of one pure element and following the white arrow to the other side with another element.

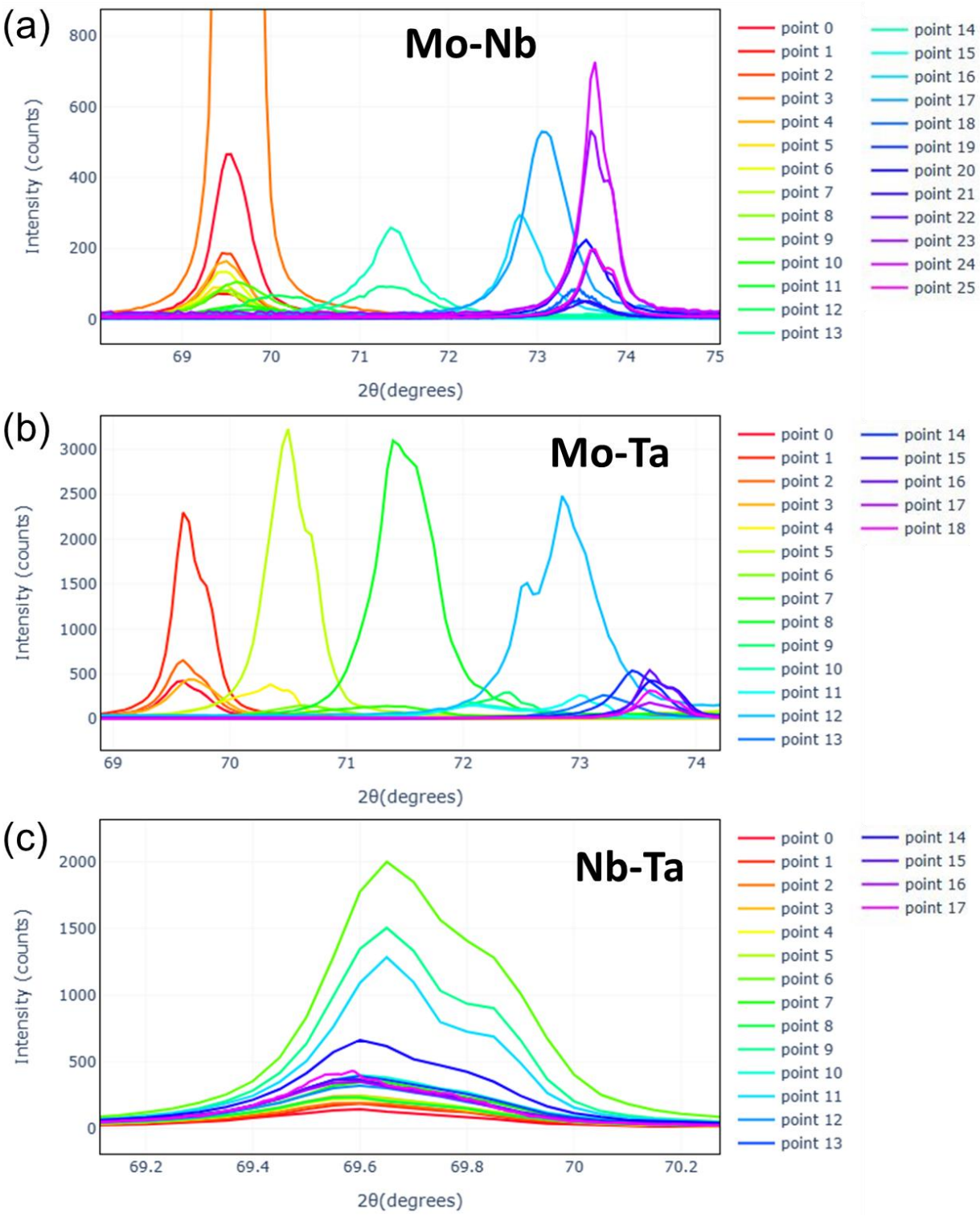

Figure 7.7 A part of XRD data in the range of 2θ from 68° to 75°.

The experimental setup of XRD for the samples is presented in **Fig. 7.6**, and the intensity-2θ profile for each binary system is presented in the three subplots of **Fig. 7.7**. These three targeted binary systems all present a complete solubility with a body-centered cubic structure. **Fig. 7.5(c)**, **(f)**, **(i)** are the lattice parameter versus distance profiles for the Mo-Nb, Mo-Ta, and Nb-Ta systems, respectively. The lattice parameter changes essentially linearly along the distance. From the composition-versus-distance, hardness-versus-distance, and lattice-parameter-versus-distance profiles, the composition-dependent hardness and lattice parameters can be extracted by interpolating these experimentally measured profiles.

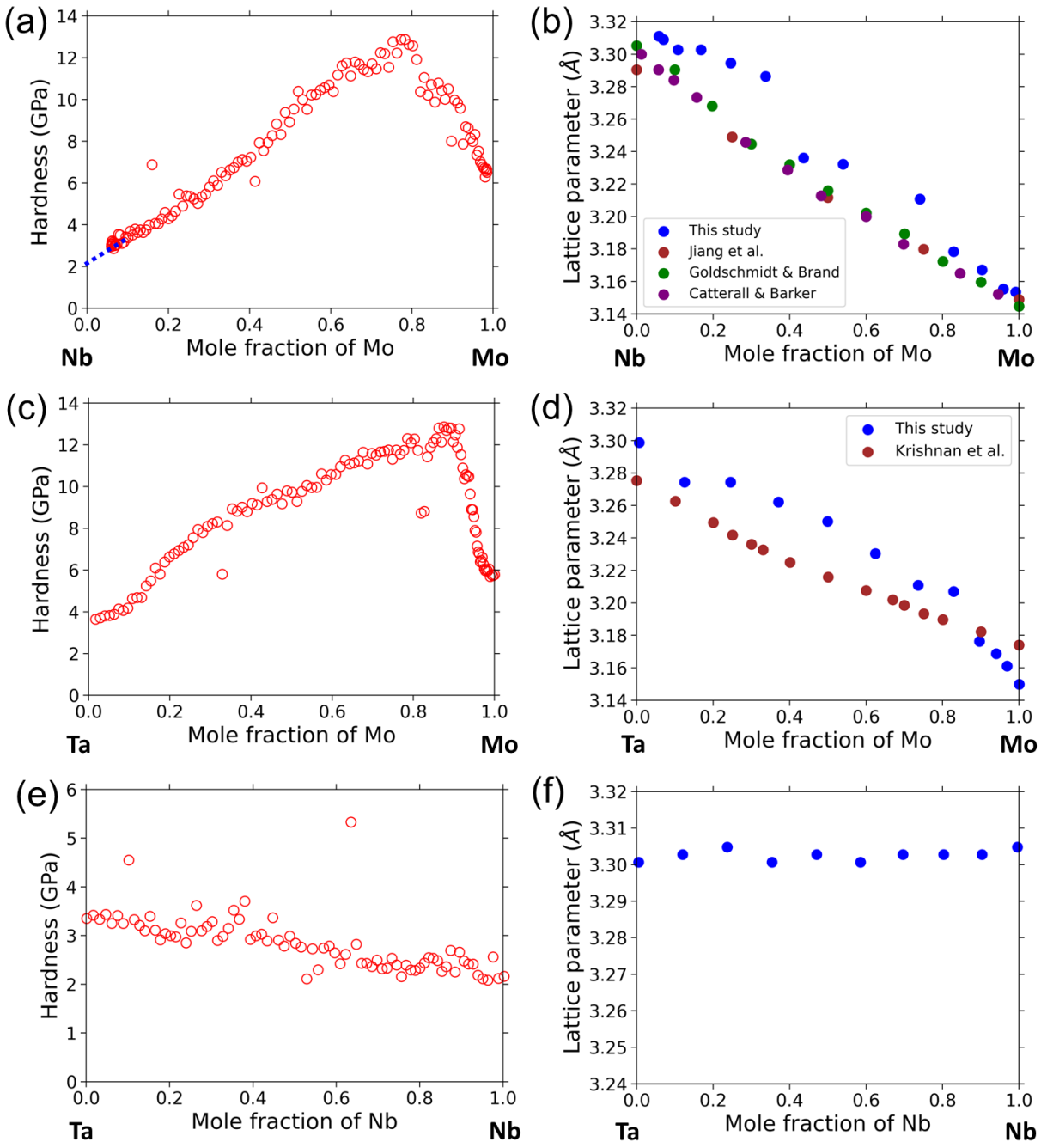

Figure 7.8 (a), and (b) are the hardness versus composition profiles, and lattice parameter versus composition profiles for the Mo-Nb system, respectively. (c) and (d) are for the Mo-Ta system. (e) and (f) are for the Nb-Ta system. The XRD lattice parameter data are preliminary and may be further improved in a more detailed analysis in the future. Some of the compositional data

reported in **Fig. 7.5** should be considered preliminary since EDS is not as accurate as the WDS analysis. In addition, the XRD lattice parameters are also preliminary. More careful analysis in the future may lead to more accurate data, and thus potential shifting of the hardness peak positions in this figure.

The composition-property relationship for the Mo-Nb, Mo-Ta, and Nb-Ta systems is presented in **Fig. 7.8(a)**, **(c)**, and **(e)**, respectively. The hardness test did not go all the way to the pure Nb side and stopped at 93 at.% Nb in the Mo-Nb sample due to the sample cutting. With a simple extrapolation shown by the blue dotted line, the hardness of pure Nb is ~2 GPa, consistent with the measured value of pure Nb in the Nb-Ta sample. The SSH mechanism significantly increases from the pure ends towards the intermediate compositions in Mo-Nb and Mo-Ta systems. The hardness reaches 12.7 GPa at the composition of 78 at.% Mo, increasing from pure Mo with a 6 GPa hardness and from pure Nb with a hardness of 2 GPa. Moreover, it can be seen that the SSH rate of solute Nb in solvent Mo is higher than that of solute Mo in solvent Nb. The maximal hardness is also 12.7 GPa in Mo-Ta sample at 88 at.% Mo. Therefore, the hardening rate of Ta is much higher than the hardening rate of Nb in Mo-based binary systems as it needs less amount of Ta to achieve the same hardness value. The Vickers hardness has a maximum at 62 at.% Mo in the Mo-Ta binary system according to the work of Stephens and Witzke [236], which is about 16 at.% deviation compared with this study. As discussed above, no SSH effect exists in the Nb-Ta binary system since the hardness changes linearly with the mole fraction of Nb. It is noted that since the compositions were obtained from EDS, not WDS, the hardness peak positions are subject to change when the more reliable WDS composition data become available.

Fig. 7.8(b), **(d)**, and **(f)** represent the composition-structure relationship for Mo-Nb, Mo-Ta, and Nb-Ta samples, respectively. A positive deviation from Vegard's law is observed in the Mo-Nb and Mo-Ta binary systems, while the literature data show a slightly negative deviation from Vegard's law [237–241]. The changing profile of lattice parameters along composition is hard to be determined as a linear trend since the data fluctuation is comparable to the lattice parameter difference between pure Nb and Ta. Our measured lattice parameter of Mo is ~ 3.15 Å by averaging from the values obtained on Mo-Nb and Mo-Ta samples, which is very close to the reported values in **Fig. 7.8(b)**. The measured lattice parameters of Nb and Ta are ~ 3.31 Å and 3.3 Å, about 0.3% and 0.7% deviation from the reported values, respectively. It is noted that the XRD lattice parameter data are preliminary and more rigorous results will be reported in the future.

In summary, a novel method of making macro-gradient samples using high-energy EBW was developed to study the composition-structure-property of refractory systems, and demonstrated for the Mo-Nb, Mo-Ta, and Nb-Ta binary systems. Composition-dependent hardness and lattice parameters were determined on the prepared samples and assessed by comparing them with the literature data. The solid solution hardening mechanism and the departure of composition-dependent lattice parameter from Vegard's law was studied in the Mo-Nb and Mo-Ta binary systems. This approach can create a shallow composition gradient over a long distance, enabling the high-throughput measurement of materials properties at various compositions for high-melting point (and thus slow diffusion) systems. We expect to expand this method to make samples for ternary or high-order systems to accelerate the property measurements of refractory systems in the future.

Chapter 8: Summary and conclusion remarks

Nanoindentation test was performed on the eight Mg-X (X = Al, Ca, Ce, Gd, Li, Sn, Y, Zn) liquid-solid diffusion couples. The hardening ability of these solutes in Mg is in the rank of $K_{Ce} > K_{Ca} > K_{Y} > K_{Gd} > K_{Zn} > K_{Al} > K_{Sn} > K_{Li}$. Despite having the highest solubility, Li exerts the slightest hardening effect in Mg. The rank of hardening coefficients obtained in this experimental study is consistent with microindentation results of Y, Gd, Zn, Al, and Sn solutes in Mg reported in the literature. The relationship between hardness and critical resolved shear stress was explored and it showed that the hardness coefficient increases with the increasing strengthening potency obtained from both literature experiment and first-principle calculations.

Even though diffusion couples could provide various composition gradients along the diffusion zone for mechanical and other properties measurements, preparation of diffusion couples consisting of refractory elements requires high temperature, high-quality furnaces and long-time annealing. To create a shallow composition gradient over a long distance, a novel method that uses electron beam welding of tapered and stacked wedge samples was developed to prepare the samples for refractory binary systems Mo-Nb, Mo-Ta, and Nb-Ta. EDS, XRD, and nanoindentation were used to measure the compositions, lattice parameters, and hardness at different locations of the macro-gradient samples. Then, the composition-dependent hardness and lattice parameters were mapped and assessed by comparing them with the literature data. The Mo-Nb and Mo-Ta systems present an obvious hardening effect at intermediate compositions above the hardness of the pure elements, while Nb-Ta shows no hardening effect at all. This phenomenon could be attributed to larger atomic size difference in the Mo-Nb and Mo-Ta systems. The composition-dependent lattice parameters deviate slightly from the Vegard's

law in the Mo-Nb and Mo-Ta systems. The lattice parameter of Nb and Ta are very close, resulting in a linear variation with composition. In the future, this approach could be applied to other refractory binary systems or ternary systems or even high-order systems. Some of the compositional data reported in this dissertation should be considered preliminary since EDS is not as accurate as the WDS analysis. In addition, the XRD lattice parameters are also preliminary. More careful analysis in the future may lead to more accurate data, and thus potential shifting of the hardness peak positions in **Fig.7.8**.

Led by Prof. Ichiro Takeuchi's group at UMD and Dr. A. Gilad Kusne at the National Institute of Standards and Technology (NIST), an autonomous materials search engine was developed to automatically measure the phase diagram of the thin-film Sn-Bi binary system. In this joint team, I performed thermodynamic modeling by integrating the thermodynamic model parameter optimization with the overall artificial intelligence (AI) program to allow on-the-fly optimization of the thermodynamic parameters of the phases to match the experimental observation each step on the way. The predicted the phase boundaries using assessed thermodynamic parameters are compared with the high-throughput experimental tests and improve the parameters as each data point is collected. This thermodynamic database is updated in each cycle via optimizing the parameters in Gibbs energy functions using newly measured compositions of phase equilibrium. The phase boundaries including solvus and liquidus near the Sn-rich side were mapped in about 5 hours through the interaction between computation and experiment, saving large amount of time, in contrast with the traditional grid mapping method. The mapped phase diagram of thin-film Sn-Bi is shifted in comparison with the phase boundaries of the Sn-Bi bulk alloy systems. The shift is reasonable considering the stress from the substrate, the fast evaporation rate during experiment, and their inherent two-dimensional crystal structure.

The AMASE method is very helpful in fast mapping the phase diagram of thin-film binary systems, which is promising in establishing a holistic and robust database for future use. Even though we demonstrated this is a useful method, it is noted that Sn-Bi is a simple system and difficulties could occur when mapping other more complex systems. To map other systems with intermediate or high eutectic temperature, a better XRD equipment with a wide range of temperature should be adopted. More Gibbs energy functions, or parameters should be added for the systems with intermetallics or magnetic systems, making the thermodynamic modeling process more complex.

CALPHAD and ML models were employed to predict the phase equilibrium of 2,436 experimental high entropy alloys (HEAs). The CALPHAD approach was only performed for 1,761 solid solutions (SSs) since it is incapable to predict the phase equilibrium with intermetallics (IMs) or amorphous (AM) phase. Both CALPHAD predictions and experimental results show that alloys prefer BCC/B2 over FCC at larger atomic size difference because BCC is less constrained than FCC. Alloys form single-phase BCC/B2 at VEC < 6.87 and single-phase FCC at VEC > 9.16, which agrees with prior findings for BCC/B2, but the condition VEC > 8 in previous literature was expanded. Four ML models, decision tree (DT), support vector machine (SVM), k-nearest neighbor (KNN), and artificial neural network (ANN) were adopted to make predictions on two datasets, one with the 1,761 SS only HEA compositions and the other with the entire 2,436 HEAs including AM and/or IM. The cross-validation (CV) accuracies achieve 90.4%, 94.1%, 93.8%, 89.7% for classifying BCC/B2, BCC/B2 + FCC, FCC with DT, KNN, SVM, and ANN models, respectively. By studying the input feature importance, VEC is identified as the most important feature in determining phase formation of SS. These trained models were used to predict the phase equilibrium of 66 selected bulk alloys from literature, and

the ANN model could reach 80.3% prediction accuracy, comparable to CALPHAD predictions. The CV accuracy reaches 92.9%, 96.3%, 96.9%, 92.3% for classification of SS, AM, SS + AM, IM phases using DT, KNN, SVM, and ANN models, respectively. The high CV accuracies for predicting the phase equilibrium of two datasets shows our ML models were well trained and tested. ΔH_{mix} and VEC were identified as two dominating factors for predicting the SS phase; and based on this learning, a simple straight line of $\Delta H_{mix} = 29 \times VEC - 247$ was determined, which can predict single-phase BCC/B2 and single-phase FCC at a 96.2% accuracy. $\Delta\chi$ and FBI are the two best features that improve the performance of ML models in predicting the phase formation in the full dataset. Our trained ML models will be used to predict phase equilibrium of available phase equilibrium data of other HEAs in the future.

The Z-Z-Z binary diffusion model developed by previous graduates in our group was employed to study the diffusion coefficients of 12 BCC binary systems (Cr-Ti, Hf-Ti, Hf-Zr, Mo-Nb, Mo-Ta, Mo-Ti, Mo-W, Mo-Zr, Nb-Ta, Nb-W, Ta-W, Ta-Zr) and 13 FCC binary systems (Al-Co, Al-Cu, Al-Ni, Co-Cu, Co-Mn, Co-Cr, Co-Pt, Cr-Fe, Cr-Ni, Cu-Mn, Fe-Mn, Mn-Ni, Ni-Pt). Three binary systems (BCC Mo-Ti and Hf-Ti, and FCC Co-Mn) were presented in detail to describe the process of optimizing the Z-Z-Z binary diffusion model. When there are no impurity diffusion coefficients available, we can extrapolate on the interdiffusion profiles to obtain them. Up to now, we have assessed a total of 43 single-phase BCC or single-phase FCC binary systems (25 systems in this study + 18 systems in the literature). We provided all assessed interaction parameters to our collaborator at Pittsburg University for ML studies. More data is needed to build reliable ML models to generate accurate predictions for the interaction parameters that are used for calculating diffusion coefficients. In a word, we will keep collecting more diffusion coefficient data of other binary systems.

The study of improving prediction ability of topological close-packed (TCP) phase stability in Ni-based superalloys is sponsored by National Science Foundation. It includes two parts of work, one is measuring phase diagram of ternary systems by our group, another one is performing thermodynamic assessments by the group from Penn State University. A new approach to mapping phase diagram of ternary systems was developed by WDS mapping to measure large amount of compositions on the triple junction areas. A Python package was developed to extract tie-line data, visualize the ternary diagram, and transform the structured phase equilibrium data to .json file. This approach can save expenses on measuring compositions, and also help identify phase interfaces by looking into their composition heatmaps. This approach was demonstrated to be correct in mapping the phase diagram of Fe-Nb-Ni system at 1100 °C by comparing the results from EPMA line scans and results from WDS mapping. This approach was further used to explore phase diagram of other ternary systems such as Cr-Nb-Ni, Co-Cr-Ta, Co-Cr-W, Co-Ni-Ta, and Co-Ni-W, generating large amount of phase equilibrium data. The ternary compound with a composition of 24Cr-30Nb-46Ni in Cr-Nb-Ni ternary system was identified to have a C14 Laves phase crystal structure based on the analysis of the detected diffraction patterns. Thermodynamic assessments were done on Fe-Nb-Ni and Cr-Nb-Ni systems, presenting good agreements between the predictions and experiments, especially for the intermetallics including TCP phases. The assessed interaction parameters from ternary systems will be used for the database of Ni-based superalloys to improve its prediction ability of the phase equilibrium with TCP phases.

Bibliography

[1] Mater. Genome Initiat. (2021).

[2] J. C. Zhao, Adv. Eng. Mater. **3**, 143 (2001).

[3] X. D. Xiang *et al.*, Science (80-.). **268**, 1738 (1995).

[4] M. L. Green *et al.*, Appl. Phys. Rev. **4**, (2017).

[5] J. C. Zhao, X. Zheng, and D. G. Cahill, Mater. Today **8**, 28 (2005).

[6] J. O. Andersson *et al.*, Calphad **26**, 273 (2002).

[7] U. R. Kattner, Jom **49**, 14 (1997).

[8] A. Jain *et al.*, APL Mater. **1**, 011002 (2013).

[9] R. Reiter, Lect. Notes Comput. Sci. (including Subser. Lect. Notes Artif. Intell. Lect. Notes Bioinformatics) **230 LNCS**, 153 (1986).

[10] Y. Liu *et al.*, J. Mater. Sci. Technol. **57**, 113 (2020).

[11] E. A. Guggenheim, Trans. Faraday Soc. **33**, 151 (1936).

[12] O. Redlich and A. T. Kister, Ind. Eng. Chem. **40**, 345 (1948).

[13] B. Sundman, H. L. Lukas, and and S. G. Fries, Cambridge Cambridge Univ. Press (2007).

[14] B. Sundman and J. Ågren, Solid State Commun. **37**, 297 (1981).

[15] F. Tang and B. Hallstedt, Calphad **55**, 260 (2016).

[16] H. Okamoto and T. B. Massalski, J. Phase Equilibria **14**, 316 (1993).

[17] C. Matano, Japanese J. Phys. **8**, 109 (1933).

[18] F. Sauer and V. Freise, Zeitschrift für Elektrochemie **66**, 353 (1962).

[19] C. Wagner, Acta Metall. **17**, 99 (1969).

[20] L. D. Hall, J. Chem. Phys. **21**, 87 (1953).

[21] Z. Chen, Q. Zhang, and J. C. Zhao, J. Open Res. Softw. **7**, 1 (2019).

[22] Q. Zhang and J. C. Zhao, Intermetallics **34**, 132 (2013).

[23] L. S. Darken, Trans. AIME **175**, 184 (1948).

[24] M. Hillert, CALPHAD **4**, 1 (1980).

[25] S. R. Safavian and D. Landgrebe, IEEE Trans. Syst. Man Cybern. **21**, 660 (1991).

[26] D. E. Knuth, Acta Inform. **1**, 14 (1971).

[27] T. M. Cover and P. E. Hart, IEEE Trans. Inf. Theory **13**, 21 (1967).

[28] J. M. Keller and M. R. Gray, IEEE Trans. Syst. Man Cybern. **4**, 580 (1985).

[29] P. E. Danielsson, Comput. Graph. Image Process. **14**, 227 (1980).

[30] C. Cortes and V. Vapnik, Mach. Learn. **20**, 273 (1995).

[31] R. P. Lippmann, IEEE ASSP Mag. **4**, 4 (1987).

[32] L. K. A. I. Hansen and P. Salamon, IEEE Trans. Pattern Anal. Mach. Intell. **12**, 993 (1990).

[33] J. C. Zhao, Annu. Rev. Mater. Res. **35**, 51 (2005).

[34] J. C. Zhao, Methods Phase Diagr. Determ. 246 (2007).

[35] J. C. Zhao, J. Mater. Res. **16**, 1565 (2001).

[36] J. C. Zhao, Metall. Mater. Trans. A Phys. Metall. Mater. Sci. **51**, 5006 (2020).

[37] J. C. Zhao, M. R. Jackson, and L. A. Peluso, Acta Mater. **51**, 6395 (2003).

[38] J. Allison, D. Backman, and L. Christodoulou, Jom **58**, 25 (2006).

[39] W. Yi Wang *et al.*, Comput. Mater. Sci. **158**, 42 (2019).

[40] Z. Chen, A Comprehensive Study of Diffusion and Modulus of Binary Systems within the Ti-Mo-Nb-Ta-Zr System, The Ohio State University, 2019.

[41] S. Cao, Determination of the Fe-Cr-Ni and Fe-Cr-Mo Phase Diagrams at Intermediate Temperatures Using a Novel Dual-Anneal Diffusion-Multiple Approach, The Ohio State University, 2013.

[42] W. Zhong, Measurement of Diffusion Coefficients of Nine Elements in Magnesium and Establishment of a Comprehensive Mobility Database for Lightweight Magnesium Alloys, The Ohio State University, 2019.

[43] Z. Chen, Z. K. Liu, and J. C. Zhao, Metall. Mater. Trans. A **49**, 3108 (2018).

[44] Z. Chen and J. C. Zhao, Materialia **2**, 63 (2018).

[45] S. Cao and J. C. Zhao, Acta Mater. **88**, 196 (2015).

[46] S. Cao and J. C. Zhao, J. Phase Equilibria Diffus. **37**, 25 (2016).

[47] W. Zhong and J. C. Zhao, Scr. Mater. **127**, 92 (2017).

[48] W. Zhong and J. Zhao, Metall. Mater. Trans. A **48**, 5778 (2017).

[49] W. Zhong and J. C. Zhao, Materialia **7**, 100353 (2019).

[50] W. Zhong *et al.*, Acta Mater. **189**, 214 (2020).

[51] W. Zhong and J. C. Zhao, Materialia **11**, 100674 (2020).

[52] W. Zhong and J. C. Zhao, Acta Mater. **201**, 191 (2020).

[53] A. Abdullah and A. Mohammed, Proc. 2018 Int. Conf. Hydraul. Pneum. - HERVEX 77 (2019).

[54] W. C. Oliver and G. M. Pharr, J. Mater. Res. **7**, 1564 (1992).

[55] W. C. Oliver and G. M. Pharr, J. Mater. Res. **19**, 3 (2004).

[56] B. L. Mordike and T. Ebert, Mater. Sci. Eng. A **302**, 37 (2001).

[57] M. Easton *et al.*, Jom **60**, 57 (2008).

[58] M. P. Staiger *et al.*, Biomaterials **27**, 1728 (2006).

[59] C. Kammerer, The Influence of Alloying Additions on Diffusion and Strengthening of Magnesium, University of Central Florida, 2015.

[60] A. Akhtar, Solid Solution Strengthening of Magnesium, THE UNIVERSITY OF BRITISH COLUMBIA, 1968.

[61] J. Nie, Metall. Mater. Trans. A **43**, (2012).

[62] S. K. Sahoo *et al.*, J. Mater. Eng. Perform. **24**, 2346 (2015).

[63] H. Somekawa and C. A. Schuh, J. Mater. Res. **27**, 1295 (2012).

[64] M. Ghazisaeidi, L. G. Hector, and W. A. Curtin, Acta Mater. **80**, 278 (2014).

[65] D. Buey, L. G. H. Jr, and M. Ghazisaeidi, Acta Mater. **147**, 1 (2018).

[66] C. H. Ca and A. Blake, Phys. stat. sol. **158**, 147 (2002).

[67] L. Gao, R. S. Chen, and E. H. Han, J. Alloys Compd. **481**, 379 (2009).

[68] L. Gao, R. S. Chen, and E. H. Han, J. Alloys Compd. **472**, 234 (2009).

[69] B. Q. Shi, R. S. Chen, and W. Ke, J. Alloy. Compd. J. **509**, 3357 (2011).

[70] C. H. Cáceres and D. M. Rovera, J. Light Met. **1**, 151 (2001).

[71] Y. Xu *et al.*, Magnes. Technol. 135 (2016).

[72] W. C. Oliver and G. M. Pharr, J. Mater. Res. **7**, 1564 (1992).

[73] R. Labusch, Acta Metall. **20**, 917 (1972).

[74] R. L. Fleisgher, Acta Metall. **9**, 996 (1961).

[75] A. G. Atkins and D. Tabor, J. Mech. Phys. Solids **13**, 149 (1965).

[76] J. A. Yasi, L. G. Hector, and D. R. Trinkle, Acta Mater. **58**, 5704 (2010).

[77] A. M. Minor *et al.*, Nat. Mater. **5**, 697 (2006).

[78] D. Lorenz *et al.*, Phys. Rev. B - Condens. Matter Mater. Phys. **67**, 1 (2003).

[79] G. I. TAYLOR, J. Inst. Met. **62**, (1938).

[80] C. Varvenne *et al.*, Acta Mater. **124**, 660 (2017).

[81] J. Wang *et al.*, Acta Mater. **170**, 155 (2019).

[82] F. Mordike, *Magnesium Technology* (2006).

[83] S. B. Kadambi, V. D. Divya, and U. Ramamurty, Metall. Mater. Trans. A **48**, 4574 (2017).

[84] K. Chen and K. P. Boyle, Phys. Status Solidi B **2095**, 2089 (2012).

[85] K. Durst *et al.*, Acta Mater. **55**, 6825 (2007).

[86] W. D. Nix and H. Gao, J. Mech. Phys. Solids **46**, 411 (1998).

[87] A. AKHTAR and E. TEGHTSOONIAN, Acta Metall. **17**, 1339 (1969).

[88] H. Yoshinaga and R. Horiuchi, Trans. JIM **4**, 134 (1963).

[89] A. Akhtar and E. Teghtsoonian, Philos. Mag. **25**, 897 (1972).

[90] J. Van Der Planken and A. Deruyttere, Acta Metall. **17**, 451 (1969).
[91] B. Lee, C. Oh, and J. Shim, J. Electron. Mater. **25**, (1996).
[92] M. H. Braga *et al.*, Calphad **31**, 468 (2007).
[93] J. Vizdal *et al.*, Calphad **31**, 438 (2007).
[94] D. V. Malakhov *et al.*, J. Phase Equilibria **21**, 514 (2000).
[95] T. Mousavi *et al.*, IEEE Trans. Appl. Supercond. **26**, 0 (2016).
[96] T. Mousavi *et al.*, Supercond. Sci. Technol. (2016).
[97] J. W. Yeh *et al.*, Adv. Eng. Mater. **6**, 299 (2004).
[98] M. H. Tsai and J. W. Yeh, Mater. Res. Lett. **2**, 107 (2014).
[99] A. Manzoni *et al.*, J. Alloys Compd. **552**, 430 (2013).
[100] H. Mao, H. L. Chen, and Q. Chen, J. Phase Equilibria Diffus. **38**, 353 (2017).
[101] C. Zhang *et al.*, Jom **64**, 839 (2012).
[102] T. M. Butler and M. L. Weaver, J. Alloys Compd. **691**, 119 (2017).
[103] H. L. Chen, H. Mao, and Q. Chen, Mater. Chem. Phys. **210**, 279 (2018).
[104] J. E. Saal *et al.*, Scr. Mater. **146**, 5 (2018).
[105] A. Karati *et al.*, Scr. Mater. **162**, 465 (2019).
[106] R. Feng *et al.*, Nat. Commun. **12**, 6 (2021).
[107] U. Mizutani, Surf. Prop. Eng. Complex Intermet. 323 (2010).
[108] S. Guo *et al.*, J. Appl. Phys. **109**, 103505 (2011).
[109] L. Jiang, Jom **72**, 2949 (2020).
[110] S. Yang *et al.*, Acta Mater. **192**, 11 (2020).
[111] S. Guo and C. T. Liu, Prog. Nat. Sci. Mater. Int. **21**, 433 (2011).
[112] O. N. Senkov *et al.*, Nat. Commun. **6**, 1 (2015).
[113] A. Inoue, Acta Mater. **48**, 279 (2000).
[114] X. Yang and Y. Zhang, Mater. Chem. Phys. **132**, 233 (2012).
[115] Y. F. Ye *et al.*, Scr. Mater. **104**, 53 (2015).
[116] J. H. Li and M. H. Tsai, Scr. Mater. **188**, 80 (2020).
[117] Y. Liu *et al.*, J Mater. **3**, 159 (2017).
[118] J. Wei *et al.*, InfoMat **1**, 338 (2019).
[119] J. M. Rickman *et al.*, Nat. Commun. **10**, 1 (2019).
[120] R. Ramprasad *et al.*, npj Comput. Mater. (2017).
[121] G. L. W. Hart *et al.*, Nat. Rev. Mater. **6**, 730 (2021).
[122] N. Islam, W. Huang, and H. L. Zhuang, Comput. Mater. Sci. **150**, 230 (2018).

[123] W. Huang, P. Martin, and H. L. Zhuang, Acta Mater. **169**, 225 (2019).
[124] R. Li *et al.*, Front. Mater. **7**, 1 (2020).
[125] Y. Chen *et al.*, Procedia Manuf. **37**, 299 (2019).
[126] A. Agarwal and A. K. Prasada Rao, Jom **71**, 3424 (2019).
[127] F. Tancret *et al.*, Mater. Des. **115**, 486 (2017).
[128] Y. V. Krishna, U. K. Jaiswal, and R. M. R, Scr. Mater. **197**, 113804 (2021).
[129] D. Q. Zhao *et al.*, Appl. Phys. Lett. **118**, (2021).
[130] Z. Pei *et al.*, npj Comput. Mater. **6**, (2020).
[131] Y. Zeng *et al.*, Mater. Des. **202**, 109532 (2021).
[132] R. Machaka, Comput. Mater. Sci. **188**, 110244 (2021).
[133] L. Zhang *et al.*, Mater. Des. **193**, 108835 (2020).
[134] Z. Zhou *et al.*, npj Comput. Mater. **5**, 1 (2019).
[135] S. A. Kube *et al.*, Acta Mater. **166**, 677 (2019).
[136] Y. Zhang *et al.*, Adv. Eng. Mater. **10**, 534 (2008).
[137] Y. Zhang, X. Yang, and P. K. Liaw, Jom **64**, 830 (2012).
[138] M. G. Poletti and L. Battezzati, Acta Mater. **75**, 297 (2014).
[139] S. Fang *et al.*, J. Non. Cryst. Solids **321**, 120 (2003).
[140] D. B. Miracle and O. N. Senkov, Acta Mater. **122**, 448 (2017).
[141] A. Takeuchi and I. Akihisa, Mater. Trans. **46**, 2817 (2005).
[142] A. Takeuchi and A. Inoue, Mater. Sci. Eng. A **304**–**306**, 446 (2001).
[143] A. R. Miedema, P. F. de Châtel, and F. R. de Boer, Phys. B+ c **100**, 1 (1980).
[144] K. N. Stevens, T. M. Cover, and P. E. Hart, IEEE Trans. Inf. Theory **13**, 21 (1967).
[145] J. M. Keller and M. R. Gray, IEEE Trans. Syst. Man Cybern. **SMC-15**, 580 (1985).
[146] D. E. Knuth, Acta Inform. **1**, 14 (1971).
[147] C. Cortes and V. Vapnik, Mach. Learn. **20**, 273 (1995).
[148] F. Pedregosa, R. Weiss, and M. Brucher, J. Mach. Learn. Res. **12**, 2825 (2011).
[149] Y. Li and W. Guo, Phys. Rev. Mater. **3**, 095005 (2019).
[150] H. Wu *et al.*, Comput. Mater. Sci. **134**, 160 (2017).
[151] Y. Zhang *et al.*, Acta Mater. **185**, 528 (2020).
[152] J.-C. Zhao and M. F. Henry, Adv. Eng. Mater. **4**, 501 (2002).
[153] R. Raghavan, K. C. Hari Kumar, and B. S. Murty, J. Alloys Compd. **544**, 152 (2012).
[154] A. Mangal and E. A. Holm, Integr. Mater. Manuf. Innov. **7**, 87 (2020).
[155] D. J. M. King *et al.*, Acta Mater. **104**, 172 (2016).

[156] D. Furrer and H. Fecht, Jom **51**, 14 (1999).

[157] B. Seiser, R. Drautz, and D. G. Pettifor, Acta Mater. **59**, 749 (2011).

[158] F. C. Frank and J. S. Kasper, Acta Crystallogr. **12**, 483 (1959).

[159] F. C. Frank and J. S. Kasper, Acta Crystallogr. **11**, 184 (1958).

[160] P. Caron and T. Khan, Aerosp. Sci. Technol. **3**, 513 (1999).

[161] R. Darolia, D. F. Lahrman, and R. D. Field, 255 (2012).

[162] T. M. Pollock and S. Tin, J. Propuls. Power **22**, 361 (2006).

[163] K. A. Christofidou *et al.*, Metall. Mater. Trans. A **49**, 3896 (2018).

[164] M. Xia *et al.*, Sci. Bull. **61**, 1013 (2016).

[165] N. G. Jones *et al.*, Mater. Sci. Technol. (United Kingdom) **30**, 1853 (2014).

[166] R. Otis and Z.-K. Liu, J. Open Res. Softw. **5**, 1 (2017).

[167] S. L. Chen *et al.*, Jom **55**, 48 (2003).

[168] N. Saunders, M. Fahrmann, and C. J. Samm, Roll. ROYCE PLC-REPORT-PNR 803 (2000).

[169] T. Keller *et al.*, Acta Mater. **139**, 244 (2017).

[170] Y. Hasebe *et al.*, Mater. Res. Soc. **1295**, (2011).

[171] K. P. Gupta, S. B. Rajendraprasad, and A. K. Jena, J. Alloy phase diagrams **2**, 53 (1986).

[172] Y. Du *et al.*, Calphad **29**, 140 (2005).

[173] A. A. Kodentsov and F. J. J. Van Loo, Monatshefte fur Chemie **143**, 1309 (2012).

[174] J. C. Zhao, Prog. Mater. Sci. **51**, 557 (2006).

[175] J. C. Zhao *et al.*, Jom **54**, 42 (2002).

[176] D. R. Snoeyenbos, D. A. Wark, and J. C. Zhao, Microsc. Microanal. **14**, 1276 (2008).

[177] A. A. Kodentsov, G. F. Bastin, and F. J. J. Van Loo, J. Alloys Compd. **320**, 207 (2001).

[178] Y. Hasebe, K. Hashimoto, and M. Takeyama, J. Japan Inst. Met. **75**, 265 (2011).

[179] J. M. Drapier, J. L. De Brouwer, and D. Coutsouradis, Cobalt **27**, 59 (1965).

[180] C. C. Zhao *et al.*, J. Alloys Compd. **608**, 118 (2014).

[181] P. Villars, *Pearson's Handbook* (1997).

[182] K. P. Gupta, J. Phase Equilibria Diffus. **26**, 93 (2005).

[183] K. P. Gupta, J. Phase Equilibria **24**, 190 (2003).

[184] Ž. Blažina and S. Pavković, J. less-common Met. **155**, 247 (2022).

[185] N. Bouliez *et al.*, J. Alloys Compd. **892**, (2022).

[186] J. M. Larson, R. Taggart, and D. H. Polonis, Metall. Mater. Trans. B **1**, 485 (1970).

[187] J. M. Walsh and M. J. Donachie, Metall. Trans. **4**, (1973).

[188] K. E. Poulsen, S. Rubaek, and E. W. Langer, Scr. Metall. **8**, 1297 (1974).

[189] R. G. Barrows and J. B. Newkirk, Metallography **5**, 515 (1972).

[190] K. P. Gupta, J. Phase Equilibria Diffus. **27**, 178 (2006).

[191] S. Y. Yang *et al.*, Trans. Nonferrous Met. Soc. China (English Ed. **21**, 2270 (2011).

[192] J. Sato, Thermodynamic Database of Co-Based Systems, Tohoku University, 2007.

[193] X. Zhang *et al.*, Int. J. Mater. Res. **104**, 836 (2013).

[194] B. Kaplan *et al.*, Calphad Comput. Coupling Phase Diagrams Thermochem. **50**, 59 (2015).

[195] P. Wang *et al.*, Calphad Comput. Coupling Phase Diagrams Thermochem. **73**, 102252 (2021).

[196] S. N. Nesterenko *et al.*, Vestn. Mosk. Univ. Seriya 2. Khimiya **21**, 275 (1980).

[197] H. Xu *et al.*, J. Alloys Compd. **425**, 153 (2006).

[198] R. K. Shaipov, E. Y. Kerimov, and E. M. Slyusarenko, J. Alloys Compd. **701**, 262 (2017).

[199] V. A. Baheti *et al.*, J. Alloys Compd. **622**, 1033 (2015).

[200] L. Zhu *et al.*, Intermetallics **93**, 20 (2018).

[201] C. Zhou *et al.*, Calphad **66**, 101649 (2019).

[202] V. S. Shipovskov, L. L. Meshkov, and E. M. Sokolo, Vestn. Mosk. Univ. Seriya II. Khimiya **22**, 74 (1981).

[203] J. Zhanpeng, G. Weiping, and Q. Caian, Mater. Sci. Eng. A **124**, 211 (1990).

[204] P. Cao, W. Gan, and D. Din, J. Cent. South Univ. Technol. **27**, 70 (1996).

[205] V. D. Divya, U. Ramamurty, and A. Paul, Metall. Mater. Trans. A **43**, 1564 (2012).

[206] W. Zhong, Q. Zhang, and J. C. Zhao, Acta Mater. **215**, 117077 (2021).

[207] Z. Wei *et al.*, Mater. Des. **198**, 109287 (2021).

[208] K. Majima and T. Isomoto, J. Japan Soc. Powder Metall. **29**, 18 (1982).

[209] W. Sprengel, T. Yamada, and H. Nakajima, Defect Diffus. Forum **143**–**147**, 431 (1997).

[210] L. Zhu *et al.*, J. Mater. Sci. **52**, 3255 (2017).

[211] B. Bian *et al.*, J. Phase Equilibria Diffus. **40**, 206 (2019).

[212] T. Heumann and R. Imm, Forschungsberichte des Landes NRW **2781**, 5 (1978).

[213] G. B. Kale and R. V. Patil, Mater. Trans. **35**, 439 (1994).

[214] G. LE Gall, D. Ansel, and J. Debuigne, Acta Met. **35**, 2297 (1987).

[215] Y. Iijima, O. Taguchi, and K. Hirano, Metall. Trans. A **8**, 991 (1977).

[216] S. Neumeier *et al.*, Acta Mater. **106**, 304 (2016).

[217] H. Liu *et al.*, Calphad **64**, 306 (2019).

[218] M. Noori and B. Hallstedt, Calphad **71**, 101793 (2020).

[219] Y. Liu *et al.*, Calphad **36**, 110 (2012).

[220] H. Schultz, *Electron Beam Welding* (Woodhead Publishing, 1993).

[221] M. S. Węglowski, S. Błacha, and A. Phillips, Vacuum **130**, 72 (2016).

[222] Z. Sun and R. Karppi, J. Mater. Process. Technol. **59**, 257 (1996).

[223] X. Liu *et al.*, Optik (Stuttg). **225**, 165720 (2021).

[224] D. Neagu, Nonconv. Technol. Rev. 31 (2010).

[225] W. Maurer *et al.*, Weld. World **56**, 85 (2012).

[226] J. Cheol Oh and S. Lee, Surf. Coatings Technol. **179**, 340 (2004).

[227] C. T. Chi *et al.*, Scr. Mater. **56**, 733 (2007).

[228] P. Ferro, A. Zambon, and F. Bonollo, Mater. Sci. Eng. A **392**, 94 (2005).

[229] Z. Hu *et al.*, Scr. Mater. **226**, 115197 (2023).

[230] D. L. Olson, B. Mishra, and D. W. Wenman, Miner. Process. Extr. Metall. Rev. **22**, 1 (2001).

[231] G. Angella *et al.*, Materials (Basel). **10**, 1 (2017).

[232] N. L. Richards, R. Nakkalil, and M. C. Chaturvedi, Metall. Mater. Trans. A **25**, 1733 (1994).

[233] S. F. Su *et al.*, Metall. Mater. Trans. A **33**, 1461 (2002).

[234] H. W. King, J. Mater. Sci. **1**, 79 (1966).

[235] L. A. Gypen and A. Deruyttere, Scr. Mater. **15**, 815 (1981).

[236] J. R. Stephens and W. R. Witzke, J. Less-Common Met. **29**, (1972).

[237] H. J. Goldschmidt and J. A. Brand, J. less-common Met. **3**, 44 (1961).

[238] C. Jiang *et al.*, Phys. Rev. B **69**, 1 (2004).

[239] J. A. Catterall and S. M. Barker, Plansee Proc. 577 (1964).

[240] R. Krishnan, S. P. Garg, and N. Krishnamurthy, J. Alloy Phase Diagrams **2**, 205 (1986).

[241] P. E. A. Turchi *et al.*, Phys. Rev. B **71**, 1 (2005).